

Electronic Thesis and Dissertation Repository

---

8-12-2020 3:00 PM

## New Model And Simulation Algorithm Of Nonstationary Non-gaussian Ground Motions Based On S-transform

Xizhong Cui, *The University of Western Ontario*

Supervisor: Hong, Hanping, *The University of Western Ontario*

A thesis submitted in partial fulfillment of the requirements for the Doctor of Philosophy degree in Civil and Environmental Engineering

© Xizhong Cui 2020

Follow this and additional works at: <https://ir.lib.uwo.ca/etd>



Part of the [Structural Engineering Commons](#)

---

### Recommended Citation

Cui, Xizhong, "New Model And Simulation Algorithm Of Nonstationary Non-gaussian Ground Motions Based On S-transform" (2020). *Electronic Thesis and Dissertation Repository*. 7221.  
<https://ir.lib.uwo.ca/etd/7221>

This Dissertation/Thesis is brought to you for free and open access by Scholarship@Western. It has been accepted for inclusion in Electronic Thesis and Dissertation Repository by an authorized administrator of Scholarship@Western. For more information, please contact [wlsadmin@uwo.ca](mailto:wlsadmin@uwo.ca).

## **Abstract**

The seismic ground motions are nonstationary stochastic processes and vary from site to site. The time histories of synthetic ground motions are used for nonlinear inelastic structural dynamic analysis since the historical records are limit or unavailable for a particular scenario seismic event. This is especially the case for structures with multiple supports. The characteristics of the nonstationary stochastic ground motions depend on the earthquake magnitude, fault mechanism, source-to-site distance, and local site conditions. The characteristics could be represented by time-frequency (dependent) power spectral density (TFPSD) and coherence functions. The assessment of such power spectral density and coherence functions are presented by using historical records and the S-transform – a Fourier transform with time localized and frequency-dependent windows – is carried out. New models of the TFPSD function and coherence function are presented. Also, new time-frequency spectral representation methods (TFSRMs) to simulate nonstationary stochastic processes are proposed. The TFSRM is developed by taking the advantages of the orthonormal basis functions in the discrete orthogonal S-transform (DOST) and the refined time-frequency representation obtained by using the S-transform. TFSRM can be used to simulate ground motions at a single site or multiple sites. They can also be used to simulate seismic ground motions conditioned on observed ground motions. TFSRM can cope with the time-varying lagged coherence function; this is not the case with the well-known spectral representation method (SRM).

Similar to the SRM, the direct use of TFSRM leads to Gaussian processes (stationary or nonstationary). However, there is indicates that the seismic ground motions may not be Gaussian. A new iterative power and amplitude correction algorithm is proposed to simulate nonstationary non-Gaussian stochastic processes. This procedure is successfully implemented and illustrated by numerical examples.

## **Keywords**

Nonstationary; non-Gaussian; stochastic processes; earthquake ground motion; spatial-varying; S-transform; discrete orthonormal S-transform; simulation; time-dependent coherence; time-dependent power spectral density function

## **Summary for Lay Audience**

Large earthquakes are rare but very destructive. The recorded ground motions during large earthquakes are scarce. The amplitude of ground movements in an earthquake is time-varying. Also, the frequency of the ground movement changes over time. The characteristics of the intensity and frequency contents for a ground motion record impact their destructiveness. This study is focused on the characterization of the frequency-dependent time-varying intensity. By using the identified characteristics, a new ground motion model is proposed. Also, new methods and algorithms are developed to generate synthetic ground motions that can be used to evaluate the response of structures subjected to severe earthquake excitations.

## **Co-Authorship Statement**

The materials presented in Chapters 2, 3, 4, 5, 6 and Appendix of the thesis have been published or submitted for potential publication in peer-reviewed journals.

A version of Chapter 2, that is co-authored by X.Z. Cui and H. P. Hong, is published in the Bulletin of Seismological Society of America.

A version of Chapter 3, that is co-authored by H. P. Hong and X.Z. Cui, is published in the Journal of Engineering Mechanics.

A version of Chapter 4, that is co-authored by X.Z. Cui and H. P. Hong, is submitted to a peer-reviewed journal for potential publication.

A version of Chapter 5, that is co-authored by X.Z. Cui and H. P. Hong, is submitted to a peer-reviewed journal for potential publication.

A version of Chapter 6, that is co-authored by X.Z. Cui and H. P. Hong, is submitted to a peer-reviewed journal for potential publication.

A version of Appendix C that is co-authored by H.P. Hong, X.Z. Cui, and D. Qiao is submitted to a peer-reviewed journal for potential publication.



## **Dedication**

To my dear parents Yongjun Cui and Qin Zong,  
my beloved wife Yuxi (Joy)  
and my naughty little boy Jayden

## **Acknowledgments**

Foremost, I would like to express my profound and sincere gratitude to my supervisor, Professor Hanping Hong, for his continuous support of my Ph.D. study. His insight and knowledge steered me in the past four years and showed me how to be a serious and admirable researcher and educator. I really enjoy every discussion we had and am always impressed by his active and intelligent but very precise thinking. I am honored to be one of his students and will always be. I would like to thank my thesis committee members and examiners, Professor Bitsuamlak, Professor Li, Professor Ren and Professor Zhou, for their constructive comments and suggestions. I would also like to extend my appreciation to my colleagues at Western and my friends in Canada and China. I would not have such a colorful life in Canada without them.

The financial support of the Natural Science and Engineering Research Council of Canada, the University of Western Ontario, and the China Scholarship Council are gratefully acknowledged.

Endless thanks and love to my parents Yongjun and Qin for encouraging me to come to Canada for further my study. I am lucky to be your son. For my naughty little boy, Jayden, sorry for not much accompany with you during the thesis preparation period. But you will have me whenever and wherever you need. Finally, I would like to say thanks to my beloved wife, Yuxi (Joy), for her understanding, supports, and accompany. You are and will always be my “joy” in the rest of my life.

# Table of Contents

<b>Abstract</b> .....	ii
<b>Summary for Lay Audience</b> .....	iii
<b>Co-Authorship Statement</b> .....	iv
<b>Acknowledgments</b> .....	vi
<b>Table of Contents</b> .....	vii
<b>List of Tables</b> .....	xi
<b>List of Figures</b> .....	xii
<b>List of Appendix</b> .....	xx
<b>List of symbols and abbreviations</b> .....	xxi
Chapter 1 .....	1
1 Introduction .....	1
1.1 Background.....	1
1.2 Objective and thesis organization .....	4
1.3 Format of the thesis.....	5
Reference.....	5
Chapter 2.....	9
2 Use of discrete orthonormal S-transform to simulate earthquake ground motions .....	9
2.1 Introduction.....	9
2.2 The S-transform and discrete orthonormal S-transform .....	11
2.3 Application of S-transform and DOST to ground motion records .....	16
2.3.1 Simulated records and their characteristics based on DOST .....	17
2.4 Conclusion .....	29
2.5 Data and Resources.....	29
Reference.....	29

Chapter 3.....	32
3 Time-frequency spectral representation models to simulate nonstationary processes and their use to generate ground motions .....	32
3.1 Introduction.....	32
3.2 The S-transform and discrete orthonormal S-transform .....	35
3.3 Two new time-frequency spectral representation models for nonstationary processes .....	39
3.4 Estimation of coherence and models to simulate multiple-support ground motions .....	42
3.5 Numerical assessment of time-frequency representation and simulation of ground motions.....	45
3.5.1 Evaluation of the time-frequency representation of recorded ground motions.....	45
3.5.2 Simulated records for a single site .....	52
3.5.3 Illustration of simulated records for multiple-support .....	54
3.6 Enhancement for increased fidelity in the time-frequency representation .....	58
3.7 Conclusion .....	63
3.8 Data availability statement.....	64
Reference.....	64
Chapter 4.....	67
4 A time-frequency representation model for seismic ground motions .....	67
4.1 Introduction.....	67
4.2 Time-frequency representation and simulation of ground motions using S-transform and discrete orthonormal S-transform .....	70
4.2.1 Time-frequency representation using S-transform .....	70
4.2.2 Simulation model and algorithm.....	72
4.3 Historical horizontal ground motion record components used to develop the TFPSD function .....	77
4.4 Development of the model for the TFPSD function.....	80

4.4.1	Time-frequency analysis of ground motions .....	80
4.4.2	Development of predicting equations for the model parameters .....	88
4.5	Use and validation of the proposed time and frequency power spectral density function .....	94
4.5.1	Illustration of the procedure to generate synthetic record components for scenario events .....	94
4.5.2	Comparison of PSA from the simulated records to ground motion models .....	96
4.5.3	Comparison of PSA from the simulated records to PSA from the selected historical records .....	98
4.6	Conclusion .....	99
4.7	Data and resources .....	99
	Reference.....	100
Chapter 5	.....	103
5	A time-frequency dependent coherence model for seismic ground motions.....	103
5.1	Introduction.....	103
5.2	Family of Fourier transforms for evaluating power spectral density and coherence functions.....	105
5.3	Estimation of TF-dependent spectra and coherence .....	111
5.3.1	Considered seismic ground motion records .....	111
5.3.2	Estimated coherence .....	112
5.3.3	Proposed TF-dependent lagged coherence model .....	118
5.4	Numerical example applications.....	126
5.4.1	Method to simulate ground motions for given target TFPSD functions.	126
5.4.2	Numerical examples.....	129
5.5	Summary and Conclusions .....	134
	Reference.....	135
Chapter 6	.....	139

6	An algorithm to simulate nonstationary and non-Gaussian stochastic processes at single or multiple sites .....	139
6.1	Introduction.....	139
6.2	The S-transform, discrete orthonormal S-transform, and energy distribution....	143
6.2.1	The S-transform and discrete orthonormal S-transform – a brief description.....	143
6.2.2	Energy distribution and lagged coherence .....	147
6.2.3	Sampling coherent noise.....	148
6.3	Extension of IPAC algorithm to simulate nonstationary non-Gaussian vector processes .....	149
6.4	Numerical validation and application of IPAC algorithm .....	154
6.4.1	Numerical validation for the case with time-independent lagged coherence .....	154
6.4.2	Numerical validation for the case with time-dependent lagged coherence .....	163
6.5	Summary and conclusions .....	169
	Reference.....	170
	Chapter 7.....	174
7	Summary remarks and future work.....	174
7.1	Summary remarks .....	174
7.2	Future work.....	176
	Appendix.....	177
	Curriculum Vitae .....	214

## List of Tables

Table 2.1: Considered recorded horizontal ground motions from large earthquakes.....	15
Table 2.2: Information of Mexican interplate earthquakes at CU station, UNAM. ....	26
Table 3.1: Mapping between $j$ and $(p, q; \beta)$ .....	37
Table 3.2: Selected records. ....	46
Table 4.1. Summary of the selected records and their corresponding events.....	79
Table 4.2. Fitted distribution parameters for the probability distribution models shown in Figure 4.8. ....	89
Table 4.3. Coefficients for the predicting equations shown in Eq. (4-32).....	93
Table 4.4. Correlation between total residuals of 8 parameters in normal space. ....	94
Table 5.1: Selected seismic events recorded on LSST array and SMART-1 array (see Liu and Hong (2016) for additional detail). ....	112
Table 5.2: Model parameters for the scenario event. The coefficients shown in the table represent a set of sampled coefficients simulated based on the ground motion model given in Chapter 4).....	132
Table 6.1: Simplification to the algorithm for the case where the marginal probability distribution of $x_k(t)/\sigma_k(t)$ is identical.....	153

## List of Figures

Figure 2.1: A few selected basis functions ( $N$  discrete points with time step  $\Delta_T = 0.01$ s) based on the octave sampling..... 14

Figure 2.2: Time and frequency varying amplitude and phase angle of coefficients calculated by using the S-transform and DOST for a record from the Loma Prieta earthquake. Rows 1 to 3 show the record, the results from the S-transform and the results from DOST. The same plotting format is used for Figures 2.3 to 2.6). ..... 18

Figure 2.3: Time and frequency varying amplitude and phase angle of coefficients calculated by using the S-transform and DOST for a record from the Kobe earthquake. .... 19

Figure 2.4: Time and frequency varying amplitude and phase angle of coefficients calculated by using the S-transform and DOST for a record from the Kocaeli earthquake. .... 20

Figure 2.5: Time and frequency varying amplitude and phase angle of coefficients calculated by using the S-transform and DOST for a record from the Michoacán earthquake. .... 21

Figure 2.6: Time and frequency varying amplitude and phase angle of coefficients calculated by using the S-transform and DOST for a record from the Wenchuan earthquake..... 22

Figure 2.7: Calculated mean of  $|x_S(f_p, t_q)|$ , Fourier amplitude and response spectrum of the simulated records are shown in the plots from left to right. .... 23

Figure 2.8: Samples of simulated records and their corresponding instantaneous amplitude. 24

Figure 2.9: Statistics of the amplitude of the DOST and Fourier transform of the simulated records. Columns 1 to 4 show the mean of  $|x_{DS}(f_p, t_q)|$ , the cov of  $|x_{DS}(f_p, t_q)|$ , Fourier spectrum and  $A(t)$  of the simulated 50 records. Rows 1 to 5 correspond to the use of Records 1 to 5 as the seed record. .... 25

Figure 2.10: Comparison of response spectra of simulated and seed records. .... 26



Figure 2.11: Time shifted horizontal record components for the records listed in Table 2.2, total energy of each record component  $E_T$ , average of the standardized amplitude of DOST coefficient, and a typical simulated record by using Eq. (2-11). The time shift is to ensure that the maximum value of the time varying variance are aligned at 20 s..... 28

Figure 2.12: Mean and coefficient of variation of the DOST amplitude of 200 simulated ground motion records. .... 28

Figure 3.1: Illustration of a few selected basis functions (for  $N$  discrete points with time step  $\Delta = 0.01$ s) for DOST..... 38

Figure 3.2: Time and frequency varying amplitude and phase angle of the DOST coefficients for a record from Wenchuan earthquake (Record 1 shown in Table 3.1)..... 47

Figure 3.3: Time and frequency varying amplitude and phase angle of the DOST coefficients for a record from Tohoku earthquake (Record 2 shown in Table 3.1). .... 48

Figure 3.4: Recording sites and time and frequency varying amplitude and phase angle of the DOST coefficients for records from Smart-1 arrays (see Table 3.1 for the considered records). .... 49

Figure 3.5: Estimated lagged coherence (the separation distance ( $d$ ) increases from left to right and from the first row to second row). .... 51

Figure 3.6: Estimated phase angle of coherence (the separation distance ( $d$ ) increases from left to right and from the first row to second row)..... 51

Figure 3.7: Illustration of typical simulated records, mean and coefficient of variation of the amplitude of the DOST coefficients and the response spectrum of the simulated records ( $S(j)$  from Wenchuan earthquake record shown in Figure 3.2 is used as the target). The second and third rows are based on Model-1 and Model-2, respectively..... 53

Figure 3.8: Illustration of typical simulated records, mean and coefficient of variation (COV) of the amplitude of the DOST coefficients and the response spectrum of the simulated records ( $S(j)$  from Tohoku earthquake record shown in Figure 3.3 is used as the target). The second and third rows are based on Model-1 and Model-2, respectively..... 54

Figure 3.9: Typical samples of simulated records by using Model-1 (left panel) and Model-2 (right panel).....	56
Figure 3.10: Average of the lagged coherence calculated from 50 sets of simulated records using Model-1. ....	57
Figure 3.11: Average of the lagged coherence calculated from 50 sets of simulated records using Model-2. ....	57
Figure 3.12: Typical samples of simulated ground motions at site I02 and M01 conditioned on records at sites C00 and I01 (for the site configuration and the conditioning records see Figure 3.4).....	58
Figure 3.13: Amplitude of the ST coefficients, $ x_s(f, \tau) $ , by considering Records 1 (left) and Record 2 (right).....	59
Figure 3.14: Flowchart to simulate ground motions at a site for given target TFPSD function obtained based on ST.....	61
Figure 3.15: Calculated $S_T(j)$ , typical sampled records, mean of amplitude of ST coefficients, and response spectrum of simulated records according to Option-A. The left and right panels are by considering Records 1 and 2, respectively.....	62
Figure 3.16: Empirical probability distributions of simulated samples at several selected times presented on the normal probability paper.....	63
Figure 4.1. a) The actual record and its corresponding velocity and displacement time histories; b) the amplitude of ST coefficients of the record; c) the TFPSD of the record.....	72
Figure 4.2. Procedure of simulating records by using TFSRM.....	74
Figure 4.3. a) A sample of simulated record and its velocity and displacement time histories; b) the statistics of PGA and PGV, c) PSA, d) AI and e) zero crossing rate of a00 simulated records to their corresponding targets. The seed or target record is shown in Figure 4.1. ....	76

Figure 4.4. a) A historical record (i.e., seed record) and its velocity and displacement time histories; b) its TFPSD; c) a sample of simulated record and its velocity and displacement time histories; d) statistics of PGA and PGV, e) PSA, f) AI and g) zero-crossing rate of the 100 simulated records to their corresponding targets. ....	77
Figure 4.5. Distribution of $M$ and $R_{rup}$ of selected records. ....	80
Figure 4.6. Time-frequency characteristics of the record component shown in Figure 4.1: a) Calculated normalized TFPSD function, b) the time-varying envelop function $A(\tau)$ , c) the PSD function, d) $\lambda_0(\tau)$ , e) $\lambda_1(\tau)/\lambda_0(\tau)$ , and f) $\lambda_2(\tau)/\lambda_0(\tau)$ . ....	81
Figure 4.7. Empirical cumulative distribution of the ratios $r_b$ and $r_c$ . ....	85
Figure 4.8. $r_b$ and $r_c$ versus of $M$ , $R_{rup}$ or $V_{S30}$ . ....	86
Figure 4.9. Cumulative distribution of each parameter and their corresponding fitted cumulative probability distribution function. ....	90
Figure 4.10. Compare of actual data and predicted values as functions of $M$ , $R_{rup}$ and $V_{S30}$ . ....	91
Figure 4.11. Residuals of inter- and intra-event for each parameter in normal space. ....	92
Figure 4.12. Sampled target TFPSD function, a sampled time history, the statistics of simulated TFPSD and PSA of the simulated records: a) Target $S_{S_x}(f, \tau)$ for a scenario event, b) a typical sampled record and its velocity and displacement time history, c) mean $S_{S_x}(f, \tau)$ of the samples, d) standard deviation of $S_{S_x}(f, \tau)$ of the samples, and e) calculated PSA of the sampled records. ....	96
Figure 4.13. Comparison of the calculated PSA to the median values and median +/- standard deviation predicted by using the GMMs from NGA-West2. ....	97
Figure 4.14. Comparison of trends of the calculated PSA from simulated records based on the proposed TFPSD model to the PSA of historical records described Table 4.1 ( $T_n$ represents the period). ....	98

Figure 5.1: Sampled record and estimated PSD functions by using FT, STFT, and ST: a) Sampled record, b) Comparison of the target and estimated PSD by using FT and ST, and c) Comparison of the target and estimated PSD by using STFT. .... 109

Figure 5.2: Layouts of LSST (right) and SMART1 (left) array located in Lotung, Taiwan. 112

Figure 5.3: Records from station FA1-1 and FA1-3 for SE-2, and estimated (doubled-sided) PSD, lagged coherence, and phase angle of coherence. .... 113

Figure 5.4: Estimated TFPSD (unit:  $\text{cm}^2/\text{s}^3$ ) and coherence by using STFT for the records shown in Figures 5.2a and 5.2b. The first and second rows show the results for  $h = 0.5$  and  $2.0$  s of the records at station FA1-1 of SE-2, respectively. The first column shows TFPSDF, the second column shows the TFSDF in detail, the third column depicts the lagged coherence between records FA1-1 and FA1-3, and the fourth column presents the phase angle of the coherence. .... 114

Figure 5.5: Effects of  $\kappa$  on the TFPSD (unit:  $\text{cm}^2/\text{s}^3$ ) and coherence functions by using ST for the two records shown in Figures 5.2a and 5.2b. The first, second, and third rows show the results for  $\kappa$  equal to 1, 2, and 3, respectively. The first column shows TFPSD, the second column shows the TFSDF in detail, the third column depicts the lagged coherence, and the fourth column presents the phase angle of the coherence..... 116

Figure 5.6: Records from the stations C00, I01, and M01 for the event SE-2, and estimated TFPSD and lagged coherence functions: a). Records and their TFPSD function (unit:  $\text{cm}^2/\text{s}^3$ ), b) lagged coherence function, and c) wrapped phase angles. .... 118

Figure 5.7. Records at stations I01, I06 and M01 from each of the 5 events listed in Table 1, and the calculated values of the lagged coherence. .... 118

Figure 5.8: Lagged coherence shown in Figure 5.5 and 5.6 plotted in  $f$ - $I$  domain. .... 119

Figure 5.9: Mean of the estimated  $|\gamma_s(f, I, d)|$  by considering records from the events listed in Table 5.1 and for selected  $d$  values. .... 123

Figure 5.10: a) Mean of $\tanh^{-1} \gamma_S(f, I, d) $ , and b) mean of $ \gamma_S(f, I, d) $ plotted in $f$ - $I$ domain by considering records described in Table 5.1 for different $d$ values ranging from 5 to 2000 m. ....	124
Figure 5.11: Comparison of the fitted model and samples for selected combinations of separation and intensity.....	125
Figure 5.12: Predicted $ \gamma_S(f, I, d) $ and $\tanh^{-1} \gamma_S(f, I, d) $ by using the empirical model shown in Eq. (5-17) with the estimated model parameters.....	126
Figure 5.13: Illustration of mapping from $S_{T, n_1 n_2}(f, \tau)$ to $S_{T, n_1 n_2}(j)$ : a) Target TFPSD function, b) Magnified view of TFPSD function for a portion of low frequency, c) discretization according to the time and frequency localization of DOST, and d) TFPSD associated with DOST representation. ....	129
Figure 5.14: Layout of the sites for the numerical example. ....	131
Figure 5.15: a) the target TFPSD; b) the target TF-dependent lagged coherence with $d$ equal to 100m, 200m, and 500m. and c) normalized intensity.....	133
Figure 5.16: a) A set of sample of simulated records using Eq (5-20) and Eq (5-21) with wave-passage effect considered; b) mean of TFPSD samples of Sites 3, 4, and 5; c) mean of lagged coherence of simulated samples between 3 pairs of sites with $d$ equal to 100m, 200m and 500m separately; d) standard deviation of TFPSD samples of Sites 3, 4, and 5; e) standard deviation of lagged coherence of simulated samples between 3 pairs of sites with $d$ equal to 100m, 200m and 500m separately. ....	134
Figure 6.1: IPAC algorithm to simulate nonstationary and non-Gaussian vector processes.	154
Figure 6.2: a). Layout of considered site; b) the target TFPSD; c) time-varying standard deviation that equals $\sqrt{\lambda_0(\tau)}$ . ....	156
Figure 6.3: a) Target time-independent lagged coherence in the $\tau$ - $f$ space and b) simulated coherent. ....	157

Figure 6.4: Lagged coherence between simulated noise shown in Figure 6.3b. ....	157
Figure 6.5: Simulated nonstationary Gaussian ground motions with time-independent lagged coherence and their spectral characteristics: a) sampled records, b) calculated lagged coherence; c) calculated TFPSD. ....	158
Figure 6.6: Simulated nonstationary Non-Gaussian ground motions with time-independent lagged coherence and their spectral characteristics: a) sampled records, b) calculated lagged coherence; c) calculated TFPSD. ....	161
Figure 6.7: Estimated statistics of the lagged coherence from the sampled noises and records: a) for coherence noises; b) for nonstationary Gaussian records, and c) for nonstationary non-Gaussian noises. ....	162
Figure 6.8: Estimated statistics of the TFPSD functions of the simulated ground motions: a) for simulated nonstationary Gaussian ground motions, and b) for simulated nonstationary non-Gaussian ground motions. ....	163
Figure 6.9: Target time-dependent lagged coherence and typical sampled noises with time-dependent coherence: a) target time-dependent lagged noise, and b) typical set of sampled noises. ....	165
Figure 6.10: Calculated lagged coherence by using the sampled noises shown in Figure 6.9b. ....	165
Figure 6.11: Simulated nonstationary Gaussian ground motions with time-dependent lagged coherence and their spectral characteristics: a) sampled records, b) calculated lagged coherence; c) calculated TFPSD. ....	166
Figure 6.12: Simulated nonstationary non-Gaussian ground motions with time-dependent lagged coherence and their spectral characteristics: a) sampled records, b) calculated lagged coherence; c) calculated TFPSD. ....	167
Figure 6.13: Estimated statistics of the lagged coherence from the sampled noises and ground motion records considering time-dependent target lagged coherence: a) for coherence noises; b) for nonstationary Gaussian records, and c) for nonstationary non-Gaussian noises; .....	168

Figure 6.14: Estimated statistics of the TFPSD functions using the simulated ground motions:  
a) for simulated nonstationary Gaussian ground motions, and b) for simulated nonstationary  
Gaussian ground motions..... 169

## List of Appendix

Appendix. A Expectation of TFPSD function of the proposed models for a single site .....	177
Appendix. B Expectation of TFPSD function of the proposed models for multiple-support	180
Appendix. C An algorithm to simulate nonstationary and non-Gaussian stochastic processes .....	182



# List of symbols and abbreviations

## Symbols

### Chapter 2

$\beta$	Width of the frequency band
$D_{[\beta]}$	Basis function of DOST
$\Delta_T$	Time increment
$E_T$	Total energy
$f_p$	Frequency index
$\phi$	Phase
$\Phi$	Phase of basis function
$\kappa$	Parameter to control window width
$N$	Length of signal
$m$	Octave sampling number
$\mu_{ET}$	Mean of $E_T$
$\theta_{pq}$	Independent uniformly distributed random phase
$t_q$	Time localization
$w$	Window function for S-transform
$x_{\mathcal{D}S}$	Coefficient of the DOST transform of $x(t)$
$x_{\mathcal{D}S-0}$	Average of the standardized DOST spectrum

$x_s$  Coefficient of the S-transform of  $x(t)$

$\hat{x}$  Fourier coefficient of  $x$

### Chapter 3

$A, B$  Fourier coefficients

$\beta$  Width of the frequency band

$C$  Covariance matrix

$Cov$  Covariance

$\Delta f$  Frequency increment

$\Delta$  Time increment

$D_1$  Basis function of DOST in single index form

$D_{[\beta]}$  Basis function of DOST

$F$  Coefficient vector

$F_{ob}$  Fourier coefficient vector of the observed record

$f_{ob}$  Sample of Fourier coefficient vector of the observed record

$F_{un}$  Fourier coefficient vector of unconditional simulated record

$F_{un|ob}$  Fourier coefficient vector of simulated records conditioned on observed records

$f_p$  Frequency index

$\phi$  Phase

$\Gamma$	Coherence
$\kappa$	The parameter to control window width
$L$	Cholesky decomposition
$m$	Octave sampling number
$\mu$	Mean
$n_{ob}$	Number of sites with observed records
$n$	Number of sites considered
$N$	Length of signal
$\theta$	Independent uniformly distributed random phase
$S_F$	One-sided power spectral density
$S$	Time-frequency power spectral density
$\Sigma$	Covariance
$S_T$	Target TFPSD
$S_{ES}$	Average TFPSD of simulated records
$t_q$	Time localization
$w$	Window function for S-transform
$\hat{x}$	Fourier coefficient of $x$
$x_{1,\mathcal{S}}$	Coefficient of the DOST transform of $x(t)$ in single index form
$x_{i,\mathcal{S}}$	ST coefficients of $i$ -th simulated record

$X_{ob}$	Observed record
$X_{un}$	Unconditional simulated record
$x_{TS}$	Target ST coefficient
$x_S$	Coefficient of the S-transform of $x(t)$
$x_{DS}$	Coefficient of the DOST transform of $x(t)$

#### Chapter 4

$a_{j,k}$	Model coefficients
$\beta$	Width of the frequency band
$D$	Effective duration
$\delta$	Parameters of the amplitude modulation function
$\delta_j$	Intraevent residual of $Z_j$
$D_k$	Constant for frequency conservation
$\Delta T$	Time increment
$E_T$	Total energy
$\eta_j$	The interevent residual of $Z_j$
$\varepsilon_j$	Total residual of $Z_j$
$F_b$	The parameter describes the bandwidth of PSD
$F_c$	The parameter describes the nominal frequency of PSD

$f_p$	Frequency index
$\gamma$	Parameters of the amplitude modulation function
$h$	The normalized squared amplitude modulation function
$\kappa$	The parameter to control window width
$\lambda_j$	$j$ -th moment
$m$	Octave sampling number
<b>M</b>	Moment magnitude
$N$	Length of signal
$v$	Normalized time
$Rrup$	Rupture distance
$r_b$	Decrease ratio of $F_b$
$r_c$	Decrease ratio of $F_c$
$S_{S_x}$	TFPSD of $x$ calculated based on ST
$S_{\mathcal{D}S_x}$	TFPSD defined based on DOST
$\theta$	Independent uniformly distributed random phase
$S_{ES}$	Average TFPSD of simulated records
$S_{0,S_x}$	Normalized TFPSD function
$\sigma_j$	Standard deviation of intraevent residual of $Z_j$
$\tau$	Time

$T$	Duration of record
$T_n$	Vibration period
$\tau_j$	Standard deviation of interevent residual of $Z_j$
$\tau_q$	Time localization
$t_q$	Time localization
$V_{S30}$	Shear-wave velocity of the top 30 m of soil
$w$	Window function for S-transform
$\hat{x}$	Fourier coefficient of $x$
$x_S$	Coefficient of the S-transform of $x(t)$
$Z_j$	Standard normally distributed random variable of $j$ -th model parameters
$z_j$	Value of $Z_j$

## Chapter 5

$a_1$	Parameter of coherence model
$a_2$	Parameter of coherence model
$a_3$	Parameter of coherence model
$a_4$	Parameter of coherence model
$b$	Parameter of coherence model
$c_1$	Parameter of coherence model

$c_2$	Parameter of coherence model
$D_{S_{n_1}}$	Normalization factor for ST
$D_{W_{n_1}}$	Normalization factor of STFT
$D_1$	Basis function of DOST
$d_0$	Parameter of coherence model
$d, d_{n_1, n_2}$	Separation between the recording sites for $x_{n_1}(t)$ and $x_{n_2}(t)$
$\Delta\tau$	Time increment
$E_T$	Model parameters of TFPSD
$\eta(\tau)$	Model parameters of TFPSD
$F_c(\tau)$	Model parameters of TFPSD
$g$	Window for STFT
$\kappa$	Parameter of window
$\gamma_{\mathcal{F}}$	Coherence calculated based on FT
$\gamma_W$	Coherence calculated based on STFT
$\gamma_{TS_{n_1, n_2}}$	Target coherence
$I_{W_{n_1}}$	Time-varying intensity of $x_{n_1}(t)$ calculated from STFT
$I_{S_{n_1}}$	Time-varying intensity of $x_{n_1}(t)$ calculated from ST
$I, I_{N_{n_1, n_2}}$	Normalized time-varying intensity for $x_{n_1}(t)$ and $x_{n_2}(t)$

$\mathbf{L}$	Cholesky decomposition of $\mathbf{M}_{ST}$
$\lambda_d$	Parameter of coherence model
$\lambda_I$	Parameter of coherence model
$\lambda_0(\tau)$	Model parameters of TFPSD
$M$	Width of window $W$
$\mathbf{M}_{ST}$	TFPSD matrix
$N_T$	Number of sets of samples
$x_{\mathcal{S}n_1}$	ST of $x_{n_1}(t)$
$x_{\mathcal{W}n_1}$	STFT of $x_{n_1}(t)$
$X_{n_1}$	stochastic processes
$x_{n_1}(t)$	A realization of $X_{n_1}$
$x_{\mathcal{F}n_1}$	Fourier transform of $x_{n_1}(t)$
$x_{init,n_1}$	Initial simulated records
$S_{\mathcal{F}n_1n_2}$	Double-sided cross PSD of $x_{n_1}(t)$ and $x_{n_2}(t)$ based on FT
$S_{\mathcal{W}n_1n_2}$	Double-sided cross TFPSD of $x_{n_1}(t)$ and $x_{n_2}(t)$ based on STFT
$\bar{S}_{\mathcal{F}n_1n_2}$	Smoothed double-sided cross PSD of $x_{n_1}(t)$ and $x_{n_2}(t)$
$S_{\mathcal{S}n_1n_2}$	Double-sided cross TFPSD of $x_{n_1}(t)$ and $x_{n_2}(t)$ based on ST
$S_{Tn_1n_2}$	Target TFPSD



$S_{ESn_1n_1}$	Average TFPSD of simulated records
$\theta_{\mathcal{F}}$	Phase of coherence $\gamma_{\mathcal{F}}$
$\theta_{\mathcal{W}n_1n_2}$	Phase of coherence $\gamma_{\mathcal{W}}$
$\theta_m$	Random phase
$T$	Duration of record
$v_{ap}$	Apparent velocity
$W$	Smoothing window for FT
$w$	Window for ST
$\zeta$	Bias

## Chapter 6

$\alpha$	Random shuffled phase
$a_1$	Parameter of time-dependent coherence model
$a_2$	Parameter of time-dependent coherence model
$a_3$	Parameter of time-dependent coherence model
$a_4$	Parameter of time-dependent coherence model
$A$	Parameter of time-independent coherence model
$\alpha_0$	Parameter of time-independent coherence model
$B$	Parameter of time-independent coherence model

$b$	Parameter of time-dependent coherence model
$c_1$	Parameter of time-dependent coherence model
$c_2$	Parameter of time-dependent coherence model
$D_k$	Constant for energy conservation in TFPSD
$\Delta_f$	Frequency increment
$\Delta_t$	Time interval
$D_{[\beta]}$	Basis functions of DOST
$d_0$	Parameter of time-dependent coherence model
$\varsigma$	Parameter for lagged coherence bias
$\eta$	Parameter of TFPSD
$F_b$	Parameter describe the bandwidth of PSD
$F_c$	Parameter describe the nominal frequency of PSD
$F_{X,t}$	Marginal CDF of $X$
$\phi_A$	Randomly assigned phase angle
$\phi$	Phase angle
$\phi_k$	Phase angle of Fourier coefficient for $x_k(t)$
$f_{X,t}$	Marginal probability density function
$\phi_0$	Phase of ST coefficient of white noise $w_0$
$\Gamma_{BiasXX}$	The biased coherence model

$\Gamma_{\mathcal{D}SXY}$	Coherence between $x$ and $y$ based on DOST
$\Gamma_{SXY}$	Coherence between $x$ and $y$ based on ST
$\Gamma_{XY}$	Coherence based on FT
$I_{kl}$	Average normalized time-varying ground motion intensity between site $k$ and $l$
$\kappa$	Parameter to control window width
$\mathbf{L}$	Lower triangle Cholesky decomposition matrix
$L_{km}$	( $k, m$ )-th element of the lower triangle matrix $\mathbf{L}$
$\lambda_0$	Parameter of target TFPSD
$\lambda_l$	Parameter of time-dependent coherence
$\lambda_d$	Parameter of time-dependent coherence
$N$	Length of $x$
$N_l$	Number of basis function employed in DOST in this thesis
$N_p$	Number of stochastic vector processes
$T$	Duration
$S_{\mathcal{F}XX}$	Auto PSD based on FT
$S_{\mathcal{F}XY}$	Cross PSD based on FT
$S_{\mathcal{D}SXY}$	Cross TFPSD between $x$ and $y$ based on DOST
$S_{SXY}$	Cross TFPSD between $x$ and $y$ based on ST

$S_s$	Target TFPSD defined based on ST
$p$	Probability level
$r_j$	Ranking of $p$
$\sigma$	Time-varying standard deviation
$\theta_m$	Independent and uniformly distributed random phase
$\theta_0$	Phase angle of ST coefficient of $w_0$
$\theta_k$	Phase angle of ST coefficient of $w_k$
$T$	Duration
$w(t)$	White noise
$\hat{x}$	Fourier coefficients of $x$
$x_s$	ST coefficient of $x$
$x_{1,s}$	ST coefficient
$x_{\mathcal{D}S}$	DOST coefficients of $x$
$x_{PC}$	Power corrected time series
$x_{AC}$	Amplitude corrected time series

### **Abbreviations**

$Cov$	Covariance
$COV$	Coefficient of variation

<i>CDF</i>	Cumulative density function
<i>DOST</i>	Discrete orthonormal Stockwell transform
<i>E-W</i>	East-West
<i>EPSD</i>	Evolutionary power spectral density
<i>FT</i>	Fourier transform
<i>FFT</i>	Fast Fourier transform
<i>GMM</i>	Ground motion model
<i>GGD</i>	Generalized Gaussian distribution
<i>IAAFT</i>	Iterative amplitude adjusted Fourier transform
<i>IPAC</i>	Iterative power and amplitude correction algorithm
<i>IPAC-M</i>	Iterative power and amplitude correction algorithm for multiple sites
<i>IMF</i>	Intrinsic mode function
<i>IST</i>	Inverse S-transform
<i>IES</i>	Institute of Earth Science
<i>LSST</i>	Lotung Large Scale Seismic Test
<i>MFW</i>	Modulated, and filtered white noise
<i>MODIF</i>	Modulated and intensity function adjusted
<i>N-S</i>	North-South
<i>NGA</i>	Next generation attenuation
<i>PSD</i>	Power spectral density

<i>PSA</i>	Pseudo-spectral acceleration
<i>PEER</i>	Pacific earthquake engineering research center
<i>REML</i>	Restricted maximum likelihood
<i>SE</i>	Seismic event
<i>SRM</i>	Spectral representation method
<i>STFT</i>	Short time Fourier transform
<i>ST</i>	Stockwell transform
<i>SMART</i>	Strong Motion Array in Taiwan
<i>TFSRM</i>	Time-frequency spectral representation method
<i>TSPSD</i>	Time scale power spectral density
<i>TFPSD</i>	Time-frequency power spectral density
<i>TF</i>	Time-frequency
<i>UNAM</i>	Universidad Nacional Autónoma de México
<i>WT</i>	Wavelet Transform

# Chapter 1

## 1 Introduction

### 1.1 Background

The evaluation of the seismic responses of structures and infrastructure systems subjected to earthquake excitation can be carried out by using the nonlinear inelastic dynamic analysis (i.e., the time-history analysis). The necessary input for such an analysis is the ground motion time history. The ground motion time history varies from seismic event to seismic event and from site to site. This variability is modeled by using a stochastic process (Newmark and Rosenblueth 1971; Zerva 2009). As the characteristics of the ground motions within a record vary in time, the motions are nonstationary. The nonstationary characteristics of the motions depend on the earthquake magnitude, fault mechanism, source-to-site distance, and local site conditions (Boore 2003; Sabetta and Pugliese 1996; Bozorgnia et al. 2014). A particular class of nonstationary stochastic processes, known as the evolutionary process (Priestley 1965), is commonly adopted to represent the ground motions.

For a given structure or infrastructure system with multiple supports, the ground motion time history for the nonlinear inelastic dynamic analysis may be selected from a database containing historical ground motion records. However, the available records are limited for a given combination of the magnitude, fault mechanism, source-to-site distance, and local site conditions. In some cases, no historical ground motion records may be available, and simulated records are used. Moreover, since the actual ground motion records that match the configuration of the multiple supports of a structure, such as a bridge and a latticed shell structure (Zanardo et al. 2002; Lupoi et al. 2005; Zerva 2009; Li et al. 2014), are unavailable, simulated seismic ground motions are required as well.

A target power spectral density (PSD) function or the evolutionary PSD (EPSD) function needs to be specified for simulating the ground motions for a single site. The commonly used PSD and EPSD models include the Kanai-Tajimi model, the Clough-

Penzien model, and the model given by Sabetta and Pugliese (1996). The assessment of the PSD or EPSD function is often carried out based on the ordinary Fourier transform or the short-time Fourier transform (STFT). A well-known drawback of STFT is that its application is associated with energy leakage. A narrow-width window results in a better resolution in the time domain but a reduced resolution in the frequency domain, and vice versa (Cohen 1995). As will be seen throughout the present thesis, this can be overcome by using the S-transform (Stockwell et al. 1996), which is a hybrid of STFT and wavelet transform. The S-transform provides the time-frequency resolution rather than the time-scale resolution offered by the continuous wavelet transform. It provides good resolution at lower frequency and time localization of the energy at high frequencies. Besides, the discrete orthonormal S-transform (Stockwell 2007) can be considered because of its orthogonal property.

Given the EPSD function, the simulation of ground motion record for a site can be carried out using the spectral representation method (SRM) (Shinozuka and Jan 1972; Shinozuka and Deodatis 1991; Liang et al. 2007). The method essentially represents the samples of the stochastic process by using the superposition of sine and cosine functions with an amplitude determined based on EPSD function and random phase angle. For the simulation of ground motions at multiple supports (or sites), in addition to the target EPSD function, the target spatial lagged coherence function needs to be specified. There are several well-known empirical spatial lagged coherence models proposed in the literature for ground motions, including the ones given by Luco and Wang (1986), Harichandran and Vanmarcke (1986), Hao et al. (1989) and Abrahamson et al. (1991). A review and discussion of the popular coherence models are given in Hong and Liu (2014), Konakli et al. (2014), and Liu and Hong (2015, 2016). The majority of the models were developed based on the records from the dense arrays in Taiwan (i.e., Lotung Large Scale Seismic Test (LSST) Array and Strong Motion Array in Taiwan (SMART)). It was shown that given the EPSD and the time-independent coherence, the simulation of records at multiple support could be carried out by using the SRM as well (Deodatis 1996).



It is noted that all the mentioned coherence models are time-independent, although there are indications that the coherence may likely depend on the amplitude of the ground motion (Qiao et al. 2020). In such a case, SRM is no longer applicable since it was shown in Priestley and Tong (1973) that the coherence between two evolutionary processes is time-independent. As studies on the vector processes with time-dependent coherence function for ground motions are scarce, the development of a time-dependent coherence model is required. Furthermore, the development of simulation algorithms for vector processes with a prescribed time-dependent coherence is needed.

It should be noted that the application of SRM leads to a Gaussian stochastic process. However, the Gaussian assumption of the ground motions was questioned in Kafali and Grigoriu (2003), and Radu and Grigoriu (2018). Radu and Grigoriu (2018) analyzed a large number of ground motion records and concluded that the marginal probability distribution of the amplitude of ground motions is highly non-Gaussian. Therefore, the non-Gaussian aspect needs to be considered in simulating ground motions as well.

A simple and straightforward approach to simulate the stationary non-Gaussian process is based on SRM and the probability distribution mapping (i.e., translation process) (Grigoriu 1998). One of the drawbacks of the approach is that the PSD of the simulated process may deviate from the target PSD function because of the probability distribution mapping. Several algorithms (Yamazaki and Shinozuka 1988; Gurley and Kareem 1997; Deodatis and Micaletti 2001; Masters and Gurley 2003) are proposed to correct this deviation. The iterative spectral correction algorithm proposed by Masters and Gurley (2003) is efficient; it is similar to the iterative amplitude adjusted Fourier transform (IAAFT) algorithm (Schreiber and Schmitz 1996, 2000), which is designed to generate surrogate for a given signal for statistical hypothesis testing. A clear difference between these two algorithms is how the prescribed target PSD function and cumulative distribution function (CDF) are calculated or assigned. The extension of IAAFT algorithm for generating a vector of surrogates is given in Schreiber and Schmitz (2000). The translation process has been extended for the nonstationary non-Gaussian process (Ferrante et al. 2005; Shields and Deodatis 2013, Wu et al. 2018). However, again, possible time-dependent coherence cannot be taken into account because the algorithm is

based on the evolutionary processes. It would be valuable to explore the possibility of extending the IAAFT algorithm to simulate the nonstationary non-gaussian vector processes.

## 1.2 Objective and thesis organization

The thesis is focused on developing new power spectral density models for ground motion records by considering time-frequency representation and new algorithms to simulate the nonstationary non-gaussian process and vector processes with time-dependent coherence. For the time-frequency representation of the ground motions, the S-transform, as well as the discrete orthonormal S-transform, will be used because of their excellent properties mentioned in the previous section.

The present thesis contains seven chapters and is organized according to the integrated manuscript format specified by the School of graduate and post-graduate studies. The subsequent six chapters are organized as follows.

Chapter 2 describes a model and method to simulate nonstationary ground motions at a site based on discrete orthonormal S-transform (DOST) for a given seed record or a given target time-frequency (dependent) PSD (TFPSD) function. The work is aimed at having a model and method that is bounded by the assumptions associated with the evolutionary process. The adequacy of the model and the simulation method is assessed in terms of the energy distribution in the time-frequency domain and in terms of the resulting response spectrum.

In Chapter 3, the modeling technique based on DOST proposed in Chapter 2 is extended to vector processes. Two methods are proposed to simulate nonstationary processes. The use of one of the methods to conditionally simulate ground motions is elaborated. Also, the incorporation of the time-frequency representation obtained from the S-transform in simulating nonstationary processes is presented and discussed so to increase the fidelity of the time-frequency representation.

Chapter 4 is focused on developing the TFPSD function for scenario seismic events and site conditions. More than 1500 historical ground motion records for strike-slip

records are used as the basis for the development. The proposed model requires 10 model parameters. Probabilistic models for the model parameters are proposed based on statistical analysis by considering both the inter- and intra-event variability.

In Chapter 5, the assessment of coherence is carried out using the records from the dense arrays (i.e., LSST and SMART). The assessment is focused on the time-dependency. It is shown that the coherence depends on the amplitude of the acceleration time history. A new time-dependent coherence model is proposed. The use of the proposed model to simulate nonstationary vector processes is illustrated.

Chapter 6 is concentrated on the characterization and simulation of the non-Gaussian aspect of the nonstationary process. In particular, an iterative power and amplitude correction algorithm is proposed to simulate the nonstationary non-Gaussian vector processes. The algorithm can be viewed as the extension of IAAFT and spectral correction algorithms. The extension incorporates the essential features of the IAAFT algorithm for generating a vector of surrogates. It considers both the time-independent coherence and time-dependent coherence. The algorithm is verified and illustrated by numerical examples.

Finally, a summary of the findings is presented. In addition, possible future research topics on the topic dealt with in this thesis are briefly highlighted.

### 1.3 Format of the thesis

This thesis is prepared in a manuscript format as specified by the School of Graduate and Postdoctoral Studies at the University of Western Ontario. Each chapter, except Chapters 1 and 7, is presented in a manuscript format with its own list of notations and references.

## Reference

- Abrahamson, N. A., Schneider, J. F., and Stepp, J. C. (1991). Empirical spatial coherency functions for application to soil-structure interaction analyses. *Earthquake spectra*, 7(1), 1-27.
- Boore, D. M. (2003). Simulation of ground motion using the stochastic method. *Pure and applied geophysics*, 160(3-4), 635-676.

- Bozorgnia, Y., Abrahamson, N. A., Atik, L. A., Ancheta, T. D., Atkinson, G. M., Baker, J. W., ... and Darragh, R. (2014). NGA-West2 research project. *Earthquake Spectra*, 30(3), 973-987.
- Cohen, L. (1995). *Time-frequency analysis*, Prentice-Hall, New Jersey, U.S.
- Deodatis, G. (1996). Non-stationary stochastic vector processes: seismic ground motion applications. *Probabilistic Engineering Mechanics*, 11(3), 149-167.
- Deodatis, G., and Micaletti, R. C. (2001). Simulation of highly skewed non-Gaussian stochastic processes. *Journal of engineering mechanics*, 127(12), 1284-1295.
- Ferrante, F. J., Arwade, S. R., and Graham-Brady, L. L. (2005). A translation model for non-stationary, non-Gaussian random processes. *Probabilistic engineering mechanics*, 20(3), 215-228.
- Grigoriu, M. (1998). Simulation of stationary non-Gaussian translation processes. *Journal of engineering mechanics*, 124(2), 121-126.
- Gurley, K., and Kareem, A. (1997). Analysis interpretation modeling and simulation of unsteady wind and pressure data. *Journal of Wind Engineering and Industrial Aerodynamics*, 69, 657-669.
- Harichandran, R. S., and Vanmarcke, E. H. (1986). Stochastic variation of earthquake ground motion in space and time. *Journal of Engineering Mechanics*, 112(2), 154-174.
- Hao, H., Oliveira, C. S., and Penzien, J. (1989). Multiple-station ground motion processing and simulation based on SMART-1 array data. *Nuclear Engineering and Design*. 111(3), 293-310.
- Hong, H. P., and Liu, T. J., (2014). Assessment of coherency for bidirectional horizontal ground motions and its application for simulating records at multiple stations. *Bulletin of the Seismological Society of America*, 104(5), 2491-2502.
- Konakli, K., Der Kiureghian, A., and Dreger, D. (2014) Coherency analysis of accelerograms recorded by the UPSAR array during the 2004 Parkfield earthquake. *Earthquake Engineering & Structural Dynamics* 43(5), 641-659.
- Kafali, C., and Grigoriu, M. (2003). Non-Gaussian model for spatially coherent seismic ground motions. *Proceedings of the ICASP9*.
- Lupoi, A., Franchin, P., Pinto, P. E., and Monti, G. (2005). Seismic design of bridges accounting for spatial variability of ground motion. *Earthquake engineering & structural dynamics*, 34(4 - 5), 327-348.
- Li, Y. G., Fan, F., and Hong, H. P. (2014). Effect of support flexibility on seismic responses of a reticulated dome under spatially correlated and coherent excitations. *Thin-Walled Structures*, 82, 343-351.
- Liang, J., Chaudhuri, S. R., and Shinozuka, M. (2007). Simulation of nonstationary stochastic processes by spectral representation. *Journal of Engineering Mechanics*, 133(6), 616-627.

- Luco, J. E., and Wong, H. L. (1986). Response of a rigid foundation to a spatially random ground motion. *Earthquake Engineering & Structural Dynamics*, 14(6), 891-908.
- Liu, T.J. and Hong, H.P. (2015). Simulation of horizontal ground motions with spatial coherency in two orthogonal horizontal directions. *Journal of Earthquake Engineering*, 19(5), 752-769.
- Liu, T. J., and Hong, H. P. (2016). Assessment of spatial coherency using tri-directional ground motions, *Journal of Earthquake Engineering*, 20(5), 773-794.
- Masters, F., and Gurley, K. R. (2003). Non-Gaussian simulation: cumulative distribution function map-based spectral correction. *Journal of engineering mechanics*, 129(12), 1418-1428.
- Newmark, N. M., and Rosenblueth, E. (1971). *Fundamentals of earthquake engineering*. Prentice-Hall. New Jersey. U.S.
- Priestley, M.B. (1965). Evolutionary spectra and non-stationary processes, *Journal of the Royal Statistical Society: Series B*, 27, 204–37.
- Priestley, M. B., and Tong, H. (1973). On the analysis of bivariate non - stationary processes. *Journal of the Royal Statistical Society: Series B (Methodological)*, 35(2), 153-166.
- Qiao, D., Zhi, X., Fan, F., and Hong, H. (2020). Estimation of Wavelet Coherence of Seismic Ground Motions. *Bulletin of the Seismological Society of America*, 110(2), 613-628.
- Radu, A., and Grigoriu, M. (2018). A site-specific ground-motion simulation model: application for Vrancea earthquakes. *Soil Dynamics and Earthquake Engineering*, 111, 77-86.
- Sabetta, F., and Pugliese, A. (1996). Estimation of response spectra and simulation of nonstationary earthquake ground motions. *Bulletin of the Seismological Society of America*, 86(2), 337-352.
- Stockwell, R. G., Mansinha, L., and Lowe, R. P. (1996). Localization of the complex spectrum: the S transform. *IEEE Transactions on Signal Processing*, 44(4), 998-1001.
- Stockwell, R. G. (2007). A basis for efficient representation of the S-transform. *Digital Signal Processing*, 17(1), 371-393.
- Shinozuka, M., and Deodatis, G. (1991). Simulation of stochastic processes by spectral representation. *Applied Mechanics Review*, 44(4) 191-204.
- Shinozuka, M., and Jan, C. M. (1972). Digital simulation of random processes and its applications. *Journal of sound and vibration*, 25(1), 111-128.
- Schreiber, T., and Schmitz, A. (2000). Surrogate time series. *Physica D: Nonlinear Phenomena*, 142(3-4), 346-382.
- Schreiber, T., and Schmitz, A. (1996). Improved surrogate data for nonlinearity tests. *Physical review letters*, 77(4), 635.

- Shields, M. D., and Deodatis, G. (2013). Estimation of evolutionary spectra for simulation of non-stationary and non-Gaussian stochastic processes. *Computer & Structures*, 126, 149–163.
- Wu, Y., Gao, Y., Zhang, N., and Zhang, F. (2018). Simulation of spatially varying non-gaussian and nonstationary seismic ground motions by the spectral representation method. *Journal of Engineering Mechanics*, 144(1), 04017143.
- Yamazaki, F., and Shinozuka, M. (1988). Digital generation of non-Gaussian stochastic fields. *Journal of Engineering Mechanics*, 114(7), 1183-1197.
- Zerva, A. (2009). Spatial variation of seismic ground motion: Modeling and engineering applications. *Nonlinear Dynamics*, 460.
- Zanardo, G., Hao, H., and Modena, C. (2002). Seismic response of multi - span simply supported bridges to a spatially varying earthquake ground motion. *Earthquake engineering & structural dynamics*, 31(6), 1325-1345.

## Chapter 2

# 2 Use of discrete orthonormal S-transform to simulate earthquake ground motions

## 2.1 Introduction

The seismic ground motions are nonstationary. A popular model for the ground motions is based on the uniformly modulated evolutionary process (Priestley 1965, 1981). The modulation function could be assessed based on the time-varying energy distribution. It involved in selecting records to be considered and choosing the best parametric or nonparametric model in the least-squares sense. The frequency characterization of the motions can be determined based on Fourier transform, leading to the average spectral composition and the power spectral density function. The model is practical as the simulation of the ground motions within such a modeling framework can be carried out using the spectral representation method (SRM) (Shinozuka and Jan 1972; Shinozuka and Deodatis 1991; Liang et al. 2007), where the phase angle is considered to be uniformly distributed. The amplitude modulation is used in the stochastic point source method and the stochastic finite-fault method (Atkinson et al. 2009; Boore 2009).

However, there are indications that the frequency content varies with time (i.e., the instantaneous frequency is a function of time). To cope with the time-varying frequency content, Yeh and Wen (1990) considered the use of the time transformation together with an evolutionary process to represent the ground motions and assumed that the time transformation can be determined based on the zero-crossing rate from the recorded ground motions. This results in that the instantaneous frequency of the ground motions is directly proportional to the time derivative of the time transformation function. Other nonstationary models for the modeling and simulating ground motions include those developed based on short-time Fourier transform (Liang et al. 2007), the Hilbert-Huang transform (Wen and Gu 2004; Gu and Wen 2007) and discrete wavelet transformation or wavelet packet transform (Iyama and Kuwamura 1999; Gurley and Kareem 1999; Yamamoto and Baker 2013). These simulation procedures can be viewed as record-based procedures. The use of the seed record based simulation technique to assess seismic

hazard was elaborated and shown in Gu and Wen (2007). For the hazard assessment at a site of interest, a seismic scenario event in an earthquake historical or synthetic catalogue that is applicable to the site is sampled, and the ground motion record is simulated based on a randomly selected seed record having the earthquake magnitude and epicentral distance matching the scenario event. This random selection of scenario event and ground motion simulation is repeated for each event within the catalogue, and the response spectrum for each simulated record is calculated and used to estimate the uniform hazard spectra. The use of the Hilbert-Huang transform takes advantage of the orthogonal basis formed by the intrinsic mode functions (IMFs) that are obtained based on the empirical mode decomposition. Each IMF appears as an amplitude modulated and frequency modulated signal. Some of the drawbacks of the empirical mode decomposition are discussed in Rato et al. (2008). The use of the short-time Fourier transform (STFT) that partitions the record into blocks of equal length, and then carries out Fourier transforms on each block is with leakage (Cohen 1995). The discrete wavelet transform (Daubechies 1992) provides good time resolution, but different dilations lead to overlapping spectral responses.

Instead of using the above-mentioned methods, one can use the S-transform (or Stockwell-transform) developed by Stockwell et al. (1996) (see also Pinnegar and Mansinha 2003; Stockwell 2007) to analyze the recorded ground motions. Differences among the S-transform to the Fourier transform, STFT, and wavelet transform are extensively discussed and illustrated in Stockwell et al. (1996), Stockwell (2007), and Ventosa et al. (2008). These references show that the S-transform provides frequency-dependent resolution with absolutely referenced phase information (i.e., the phase information refers to the argument of the cosinusoid at zero time as it is the case for Fourier transform) and the time average of the coefficients of the S-transform equals the Fourier coefficients. Unlike the continuous wavelet transform, the S-transform produces a time-frequency representation instead of a time-scale representation. The difference between the S-transform and STFT is that the window in STFT is independent of the frequency. However, similar to continuous wavelet transform and STFT, the S-transformation is a redundant representation in the time-frequency plane. A more efficient transform called discrete orthonormal S-transform (DOST) that localizes the



spectrum and retains the advantageous phase properties of the S-transform was proposed in Stockwell (2007).

In this chapter, a procedure to simulate nonstationary ground motions based on DOST is proposed based on a seed record or a given target amplitude of DOST coefficients. The adequacy of the simulated records is assessed in terms of the power distributed in time and frequency and the response spectrum. The basic formulation for the S-transform and DOST is summarized in the following section. This is followed by the numerical evaluation using DOST and the S-transform, showing the time-frequency decomposition and the phase angle of ground motions. Statistics of the amplitude of coefficients of the DOST, Fourier amplitude, time-varying power distribution and response spectrum of the simulated records are compared with those of seed records.

## 2.2 The S-transform and discrete orthonormal S-transform

The S-transform for a signal,  $x(t)$ , such as a ground motion record, is defined as (Stockwell et al. 1996; Pinnegar and Mansinha 2003; Stockwell 2007),

$$x_S(f, \tau) = \int_{-\infty}^{\infty} x(t)w(f, \tau - t)e^{-i2\pi ft} dt, \quad (2-1)$$

where  $x_S(f, \tau)$  is the coefficient of the S-transform of  $x(t)$ ,  $f$  and  $t$  are the frequency and time, and  $\tau$  is the center of the window function  $w(f, \tau - t)$ . The frequently selected window is the Gaussian one,

$$w(f, t) = \frac{|f|}{\sqrt{2\pi\kappa}} \exp\left(-\frac{f^2 t^2}{2\kappa^2}\right), \quad (2-2)$$

where  $\kappa$  a parameter that controls the number of oscillations in the effective width of the window. The use of this window with  $\kappa$  not equal to one in Eq. (2-1) is sometimes referred to as the generalized S-transform. The window for a given  $\kappa$  width is inversely proportional to the frequency.

The S-transform has several interesting properties as shown in Stockwell et al. (1996), Pinnegar and Mansinha (2003) and Stockwell (2007). Eq. (2-1) can be expressed in terms of the Fourier transform of  $x(t)$ ,  $\hat{x}(f)$ , resulting in

$$x_S(f, \tau) = \int_{-\infty}^{\infty} \hat{x}(\phi + f) e^{-\frac{2\pi^2 \phi^2 \kappa^2}{f^2}} e^{i2\pi\phi\tau} d\phi, \quad (2-3)$$

where,

$$\hat{x}(f) = \int_{-\infty}^{\infty} x(t) e^{-i2\pi ft} dt. \quad (2-4)$$

For  $x(t)$  that is evenly spaced in time with sampling interval  $\Delta_T$ , the discretized version of  $x_S(f, \tau)$  can be written as,

$$x_S(f_p, t_q) = \frac{1}{N\Delta_T} \sum_{j=0}^{N-1} e^{-\frac{2\pi^2 f_j^2 \kappa^2}{f_p^2}} \hat{x}(f_{j+p}) e^{i2\pi f_j t_q}, \quad (2-5)$$

where  $\hat{x}(f_p) = \Delta_T \sum_{j=0}^{N-1} x(t_j) e^{-i2\pi f_p t_j}$ ,  $t_j = j\Delta_T$ ,  $f_p = p / (N\Delta_T)$ ,  $p = 0, 1, \dots, N-1$ ,  $t_q = q\Delta_T$

and  $p = 0, 1, \dots, N-1$ .  $x_S(f_p, t_q)$  is referred to as a voice for a constant frequency  $f_p$ . The discrete equation to reconstruct the signal is given by,

$$x(t_j) = \frac{2}{N} \sum_{p=0}^{N-1} \sum_{q=0}^{N-1} |x_S(f_p, t_q)| \cos \left[ 2\pi f_p t_j + \phi(f_p, t_q) \right]. \quad (2-6)$$

where  $|x_S(f_p, t_q)|$  and  $\phi(f_p, t_q)$  are instantaneous amplitude (or DOST spectrum) and phase angle of  $x_S(f_p, t_q)$ . Since  $\phi(f_p, t_q)$  varies in time,  $x(t_j)$  shown in Eq. (2-6) is not expressed in terms of orthogonal basis functions. It must be emphasized that, at present, a record-based simulation algorithm with a theoretical foundation to generate ground motions by using the coefficients from the S-transform is unavailable. One may assume that the ground motions can be modeled as an evolutionary process with an amplitude

modulation defined by  $|x_s(f_p, t_q)|$ . However, this is not advisable as will be illustrated using numerical examples in the following sections.

An extension of the S-transform, the DOST is defined as (Stockwell 2007),

$$x_{\mathcal{D}S}(f_p, t_q) = 1/N \sum_{k=0}^{N-1} x(t_k) D_{[\beta]}(t_k; f_p, t_q), \quad (2-7)$$

where,

$$D_{[\beta]}(t_k; f_p, t_q) = \frac{ie^{-i\pi q} \{e^{-i2\pi(k/N-q/\beta)(p-\beta/2-1/2)} - e^{-i2\pi(k/N-q/\beta)(p+\beta/2-1/2)}\}}{\sqrt{\beta} 2\sin[\pi(k/N - q/\beta)]} \quad (2-8)$$

are the basis functions, and  $\beta$  indicates the width of the frequency band centred at the frequency indexed by  $p$  (i.e.,  $f_p$ ). The detail on the derivation of the basis functions is given in Stockwell (2007). As can be observed that the phase angle is absolutely referenced which distinguishes these basis functions from wavelets. The  $1/\sqrt{\beta}$  is necessary to ensure orthonormality of the basis functions. As indicated in Stockwell (2007) that rules must be applied to the sampling of the time-frequency space to ensure orthogonality. The suggested rules are that  $q = 0, 1, \dots, \beta - 1$ , and  $p$  and  $\beta$  must be selected so each Fourier frequency sample is used once and only once. Such rules are satisfied by using the octave sampling (which is similar in discrete wavelet transform) resulting in the orthonormal basis functions given by Eq. (2-7) with,

$$(p; q; \beta) = (2^{m-1} + 2^{m-2}; 0, 1, \dots, 2^{m-1} - 1; 2^{m-1}), \text{ for } m = 2, \dots, \log_2(N) - 1; \quad (2-9)$$

and  $p = 0, q = 0$  and  $\beta = 1$  for  $m = 0$ ; and  $p = 1, q = 0$  and  $\beta = 1$  for  $m = 1$ . An illustration of a few selected basis functions is shown in Figure 2.1. As can be observed from the figure, the basis functions in DOST are not dilations nor translations of a single function.

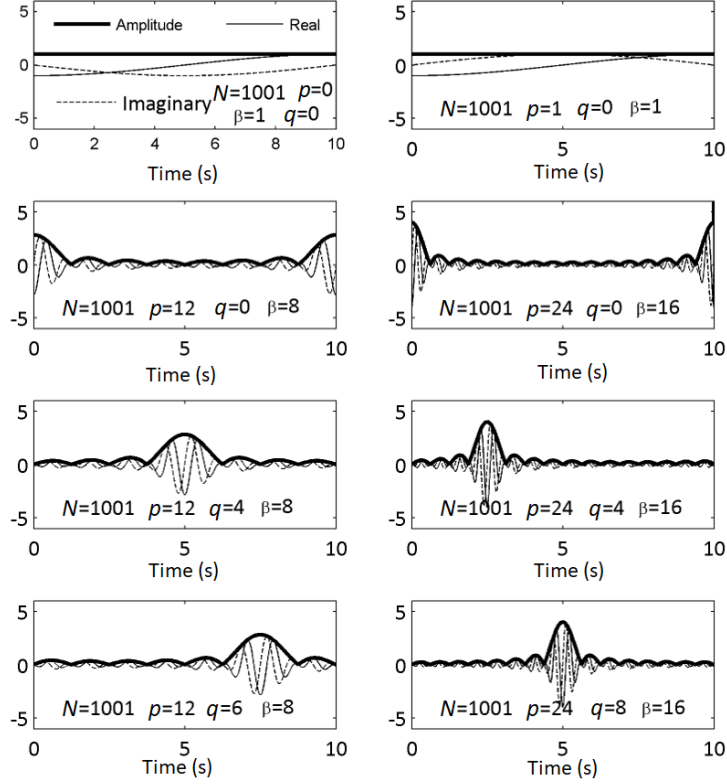


**Figure 2.1:** A few selected basis functions ( $N$  discrete points with time step  $\Delta_T = 0.01$ s) based on the octave sampling.

The equation to reconstruct  $x(t_k)$  is simply given by,

$$x(t_k) = \sum_{\text{for feasible } p, q} x_{\mathcal{D}S}(p, q) D_{[\beta]}(t_k; f_p, t_q), \quad k = 0, \dots, N-1, \quad (2-10)$$

where  $p$  and  $q$  are assigned as shown in Eq. (2-9). The use of the Fourier transform as well as fast Fourier transform for their evaluation that is given in Wang and Orchard (2009), Yan and Zhu (2011) and Battisti and Riba (2016) is employed in the thesis for the numerical analysis.

Given a ground motion record,  $x(t_k)$ , its coefficients of DOST can be calculated using Eq. (2-7). Since the octave sampling ensures the basis functions to be orthonormal, it is

proposed that a model to simulate the stochastic ground motions,  $X(t)$ , based on a seed record or target DOST spectrum can be written as,

$$X(t_k) = \text{Re} \left[ \sqrt{2} \sum_{\text{for feasible } p,q} |x_{\mathcal{DS}}(f_p, t_q)| D_{[\beta]}(t_k; f_p, t_q) e^{i\theta_{pq}} \right], \quad (2-11)$$

where  $\theta_{pq}$  are independent uniformly distributed between 0 to  $2\pi$  and  $\text{Re}[\ ]$  denotes the real part of its argument. Because of the orthogonality, the expected value of  $X(t)$ ,  $E(X(t_k))$ , is given by,

$$E(X(t_k)) = \text{Re} \left[ \sqrt{2} \sum_{\text{for feasible } p,q} |x_{\mathcal{DS}}(f_p, t_q)| D_{[\beta]}(t_k; f_p, t_q) E \left( e^{i\theta_{pq}} \right) \right] = 0, \quad (2-12)$$

and covariance  $\text{Cov}(X(t_j)X(t_k))$ ,

$$\begin{aligned} \text{Cov}(X(t_j)X(t_k)) = \\ \sum_{\text{for feasible } p,q} |x_{\mathcal{DS}}(f_p, t_q)|^2 |D_{[\beta]}(t_j; f_p, t_q)| |D_{[\beta]}(t_k; f_p, t_q)| \cos \left( \Phi(t_j; f_p, t_q) - \Phi(t_k; f_p, t_q) \right) \end{aligned} \quad (2-13)$$

in which  $\Phi(t_k; f_p, t_q)$  is the time-varying phase angle of the basis function  $D_{[\beta]}(t_j; f_p, t_q)$ .

The variance is given by Eq. (13) by letting  $t_j = t_k$ . This results in

$$\sum_{\text{for feasible } p,q} |x_{\mathcal{DS}}(f_p, t_q)|^2 \text{ equals } (1/N) \sum_{k=0}^{N-1} x^2(t_k) \text{ so it is consistent with the seed record.}$$

**Table 2.1:** Considered recorded horizontal ground motions from large earthquakes

Record #	Earthquake	Date	Moment magnitude	Station Name
1	Loma Prieta, U.S.	1989.10.18	6.9	Gilroy Array #1
2	Kobe, Japan	1995.01.16	6.9	KJMA
3	Kocaeli, Turkey	1999.08.17	7.6	Gebez
4	Michoacán, Mexico	1985.09.19	8.0	CU
5	Wenchuan, China	2008.05.12	7.9	Qingping

## 2.3 Application of S-transform and DOST to ground motion records

Five real records from large earthquakes are selected and listed in Table 2.1. Each record listed in the table is used as the seed record to test the proposed model. By applying the S-transform and DOST, the obtained amplitude and phase angle of the coefficients of the S-transform and of DOST are shown in Figures 2.2 to 2.6. For the S-transform,  $\kappa = 1$  is considered. As can be observed that the time-frequency resolution obtained from the DOST is coarse as compared to that obtained using the S-transform because of the octave sampling used in DOST. The areas where the amplitudes of the coefficients of DOST attain their large values are almost the same as those of the S-transform. The time-frequency characteristics of the seed records differ.

As mentioned previously, although the theoretical foundation for a simple to use simulation algorithm based on the S-transform is unavailable, one may assume that  $X(t)$  can be modeled as an evolutionary process with an amplitude modulation defined by  $|x_S(f_p, t_q)|$ . This and the use of SRM lead to,

$$x(t) = \text{Re} \sqrt{2} \sum_{p=0}^{N-1} |x_S(f_p, t_q)| \sqrt{2\Delta f} \cos(2\pi f_p t + \phi_p), \quad (2-14)$$

where  $f_p$  is uniformly distributed between 0 to  $2\pi$ .

By using this model, and  $|x_S(f_p, t_q)|$  shown in Figure 2.2, 50 ground motion records are simulated. The mean of  $|x_S(f_p, t_q)|$  obtained by using the S-transform and the amplitude of the Fourier transform for the simulated records are shown on the left and middle plots in Figure 2.7. In addition, the response spectra of the simulated and the seed records are calculated and shown on the right plot in Figure 2.7. A comparison of the results shown in Figure 2.7 to that presented in Figure 2.2 indicates that the mean of  $|x_S(f_p, t_q)|$  from the simulated records deviates from  $|x_S(f_p, t_q)|$  of the seed record. The middle plot implies that there is energy deficiency in the simulated records as compared to the seed record while the right plot indicates that the mean of the response spectra for

the simulated records is smaller than that of the seed record. Therefore, the usefulness of taking  $|x_s(f_p, t_q)|$  as the amplitude modulation function is questionable. Note that there is large variability in the Fourier amplitude of the simulated records. This is a typical feature of the SRM and is consistent with that observed in Liu and Hong (2015)

The observed deficiency is likely due to the neglect of the time and frequency-dependent phase angle or the time-varying instantaneous frequency. The time-dependent frequency could be taken into account using time transformation (i.e., uniformly modulated frequency). In such a case, the simulation must take into account the effect of time transformation on the frequency (Yeh and Wen 1990; Hong 2016) in order to use SRM to simulate records. Assessment of the time transformation based on the zero-crossing rate is extensively discussed in Yeh and Wen (1990) and Alamilla et al. (2001).

### 2.3.1 Simulated records and their characteristics based on DOST

Using the proposed simulation procedure and considering each record listed in Table 2.1 as the seed record, a sample of simulated record and its corresponding amplitude of the coefficients of DOST are presented in Figure 2.8. Comparison of the simulated records to the seed records shown in Figures 2.2 to 2.6 and 2.8 indicates that in all cases, the simulated follows the time-varying amplitude of the ground motions closely. A comparison of results shown in Figures 2.2 to 2.6 and 2.8 also indicates that the amplitude of the coefficients of DOST of the simulated records follows that of seed records. Note that the plots shown in Figure 2.8 show that the amplitude of DOST coefficients (or DOST spectrum) of the sampled records vary in time and frequency. However, similar to the plots for the seed records shown in Figures 2.2 to 2.6, the variation of the frequency content does not follow a simple identifiable pattern, suggesting the non-stationarity of ground motions in both amplitude and frequency.

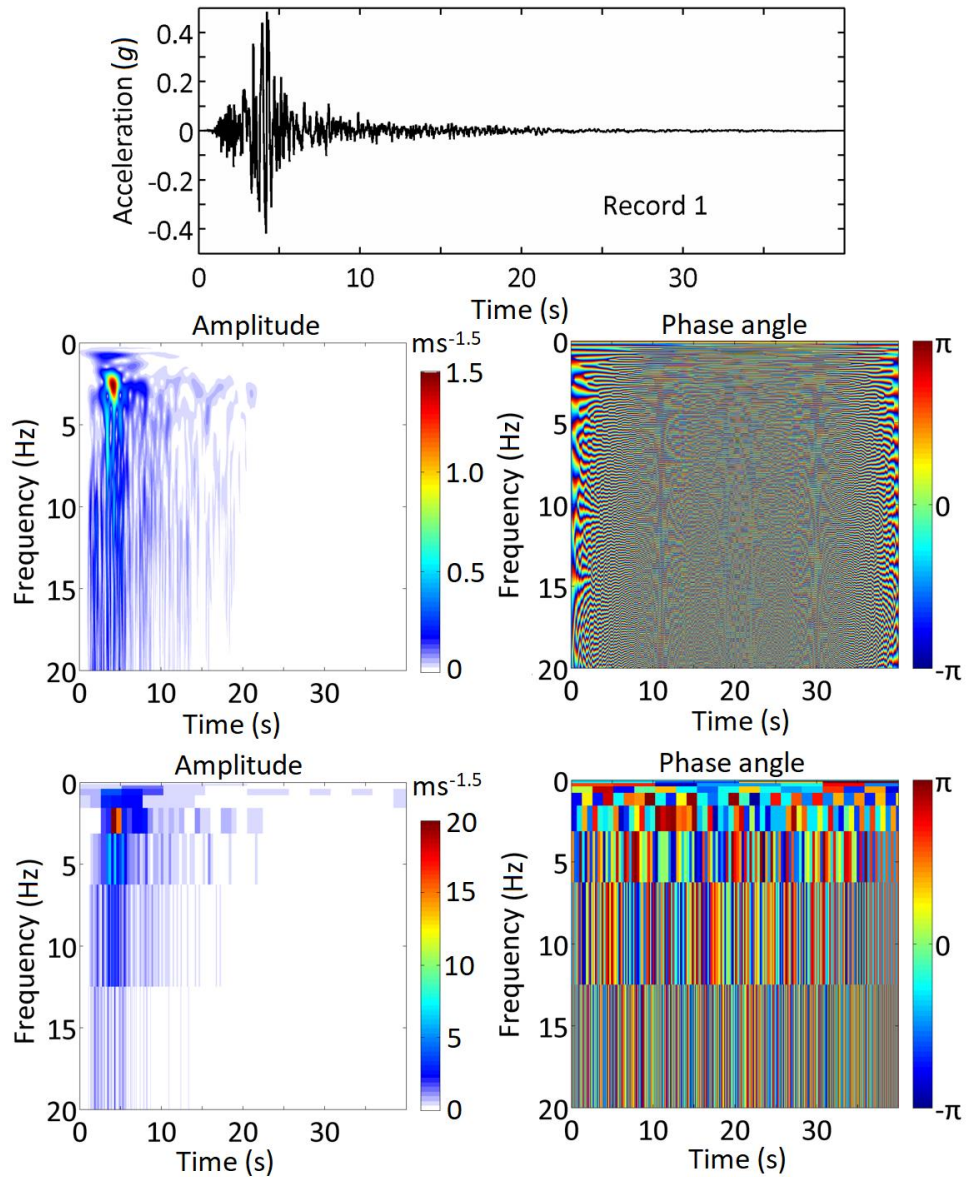


**Figure 2.2:** Time and frequency varying amplitude and phase angle of coefficients calculated by using the S-transform and DOST for a record from the Loma Prieta earthquake. Rows 1 to 3 show the record, the results from the S-transform and the results from DOST. The same plotting format is used for Figures 2.3 to 2.6).



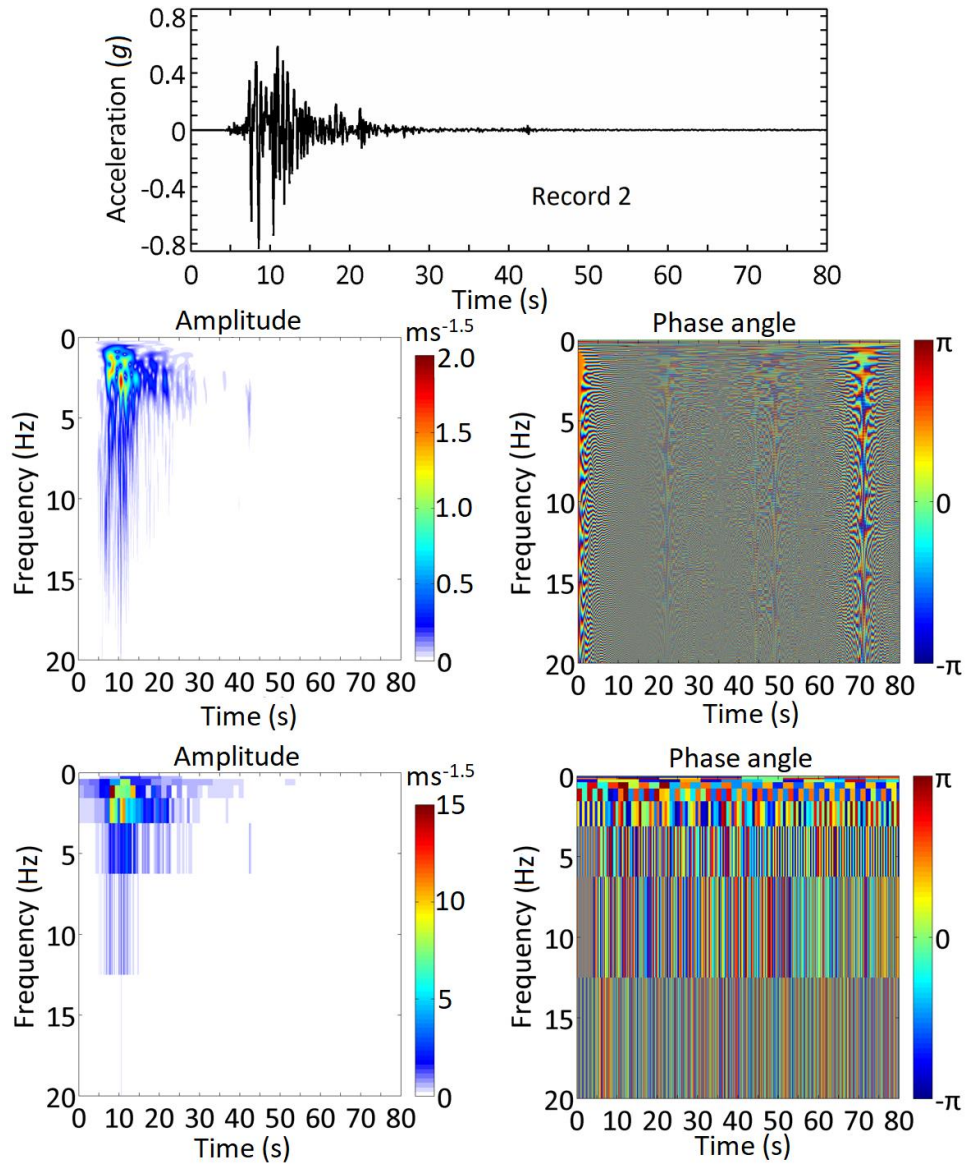


**Figure 2.3:** Time and frequency varying amplitude and phase angle of coefficients calculated by using the S-transform and DOST for a record from the Kobe earthquake.

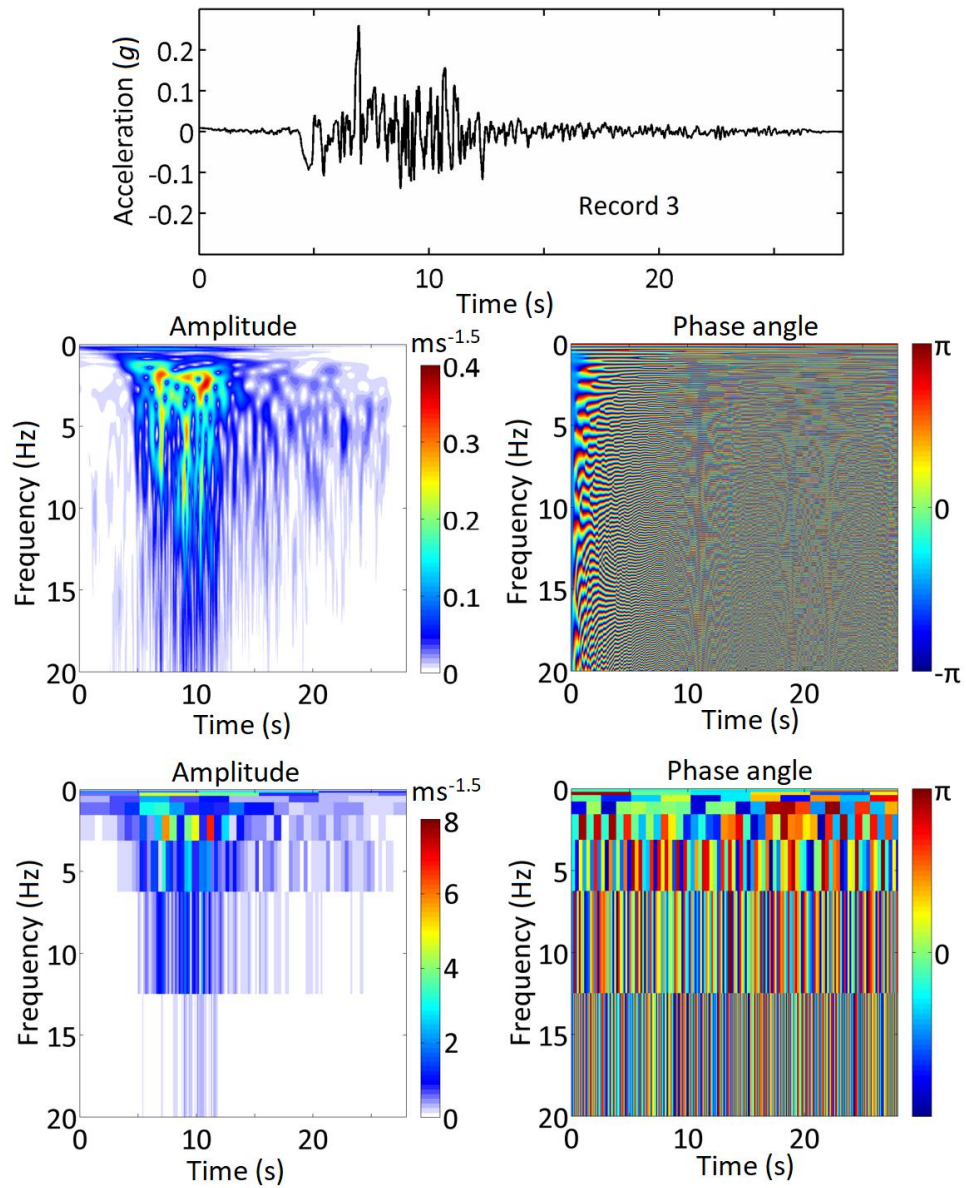


**Figure 2.4:** Time and frequency varying amplitude and phase angle of coefficients calculated by using the S-transform and DOST for a record from the Kocaeli earthquake.

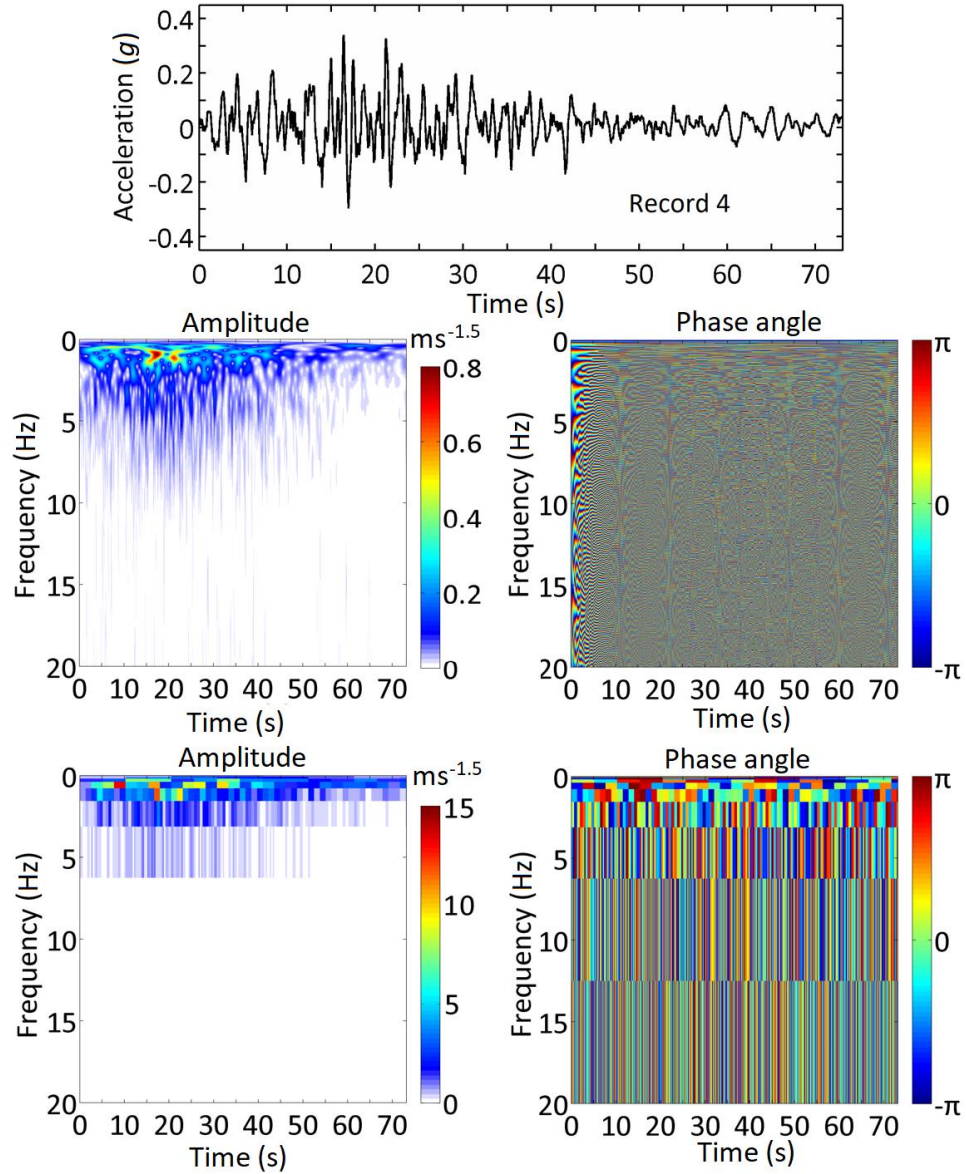


**Figure 2.5:** Time and frequency varying amplitude and phase angle of coefficients calculated by using the S-transform and DOST for a record from the Michoacán earthquake.

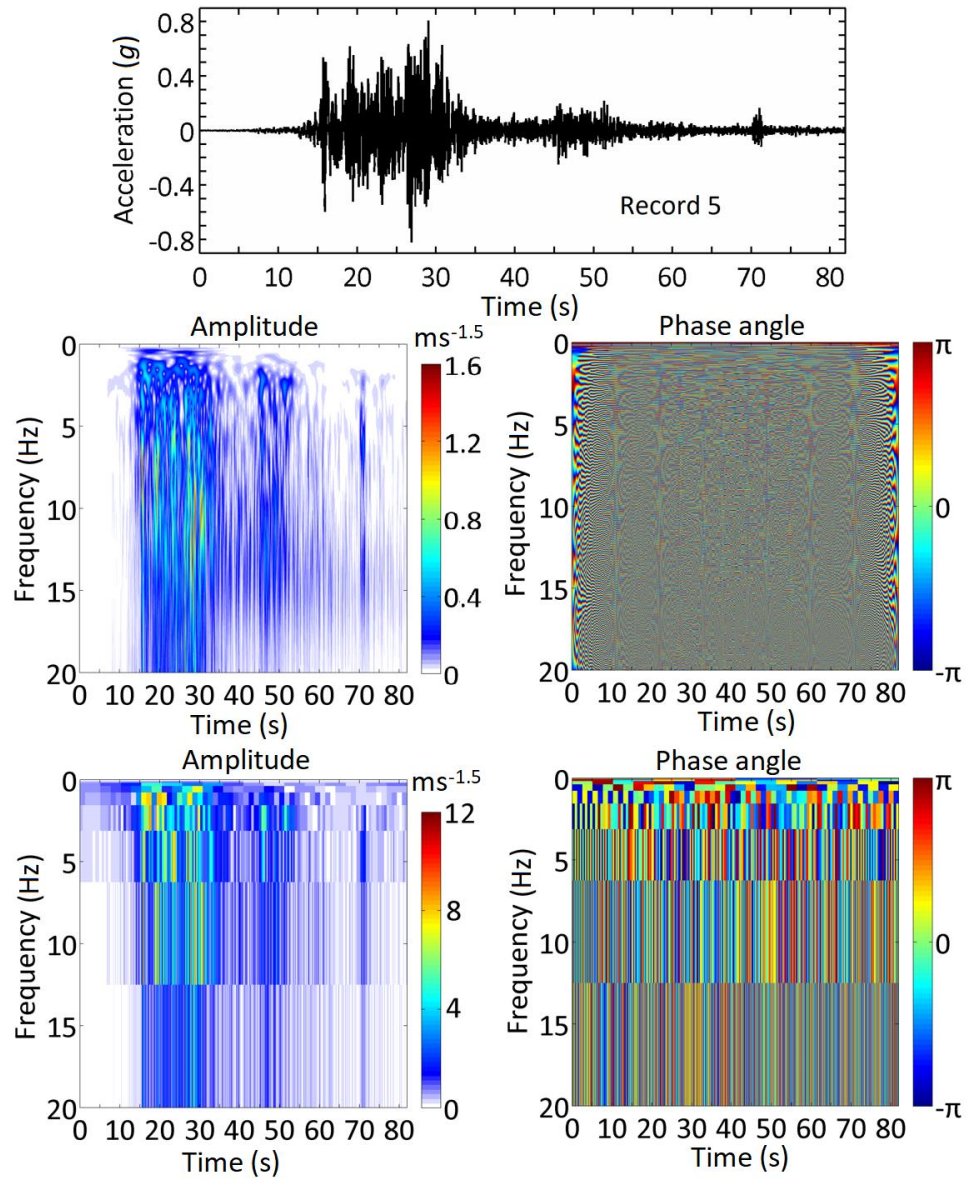


**Figure 2.6:** Time and frequency varying amplitude and phase angle of coefficients calculated by using the S-transform and DOST for a record from the Wenchuan earthquake.

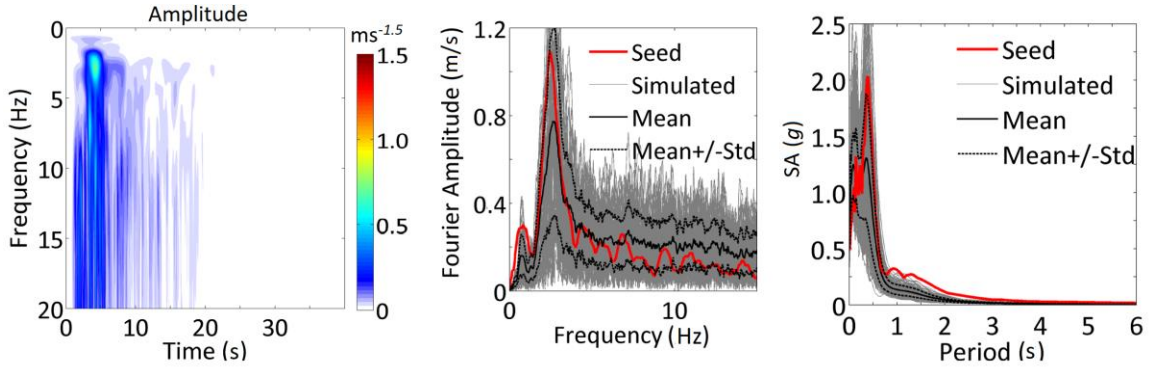


**Figure 2.7:** Calculated mean of  $|x_s(f_p, t_q)|$ , Fourier amplitude and response spectrum of the simulated records are shown in the plots from left to right.

To quantify the differences between the simulated records and the seed records, 50 records are simulated for each seed record. The statistics of the amplitude of the coefficients of DOST and the Fourier amplitude spectra of the simulated records as well as the time-varying square root of energy distribution, denoted as  $A(t)$ , are presented in Figure 2.9. The Figure shows that the mean of  $|x_{\mathcal{D}S}(f_p, t_q)|$  for the simulated records agrees well with those of the corresponding seed records. Also, on average, the mean of the amplitude of Fourier coefficients of the simulated records agrees well with those of the corresponding seed records. However, there is a clear difference between the mean of the Fourier amplitude of the simulated records and that of the seed records as well. The former tends to remain constant for segments of frequencies which is attributed to the use of octave sampling in the DOST. The magnitude of coefficient of variation (COV) of  $|x_{\mathcal{D}S}(f_p, t_q)|$  is similar to the COV values of Fourier coefficients that can be inferred from the plots. The magnitude of the COV is also similar to that of Fourier coefficients of simulated records that is observed in the literature (Liu and Hong 2015, 2016) if the ground motions are modeled as a uniformly modulated evolutionary process and SRM is used for simulation – such a large COV is also observed in Figure 2.7 when the SRM is used. The mean of the time-varying power distribution of the simulated records follows closely to those of seed records.



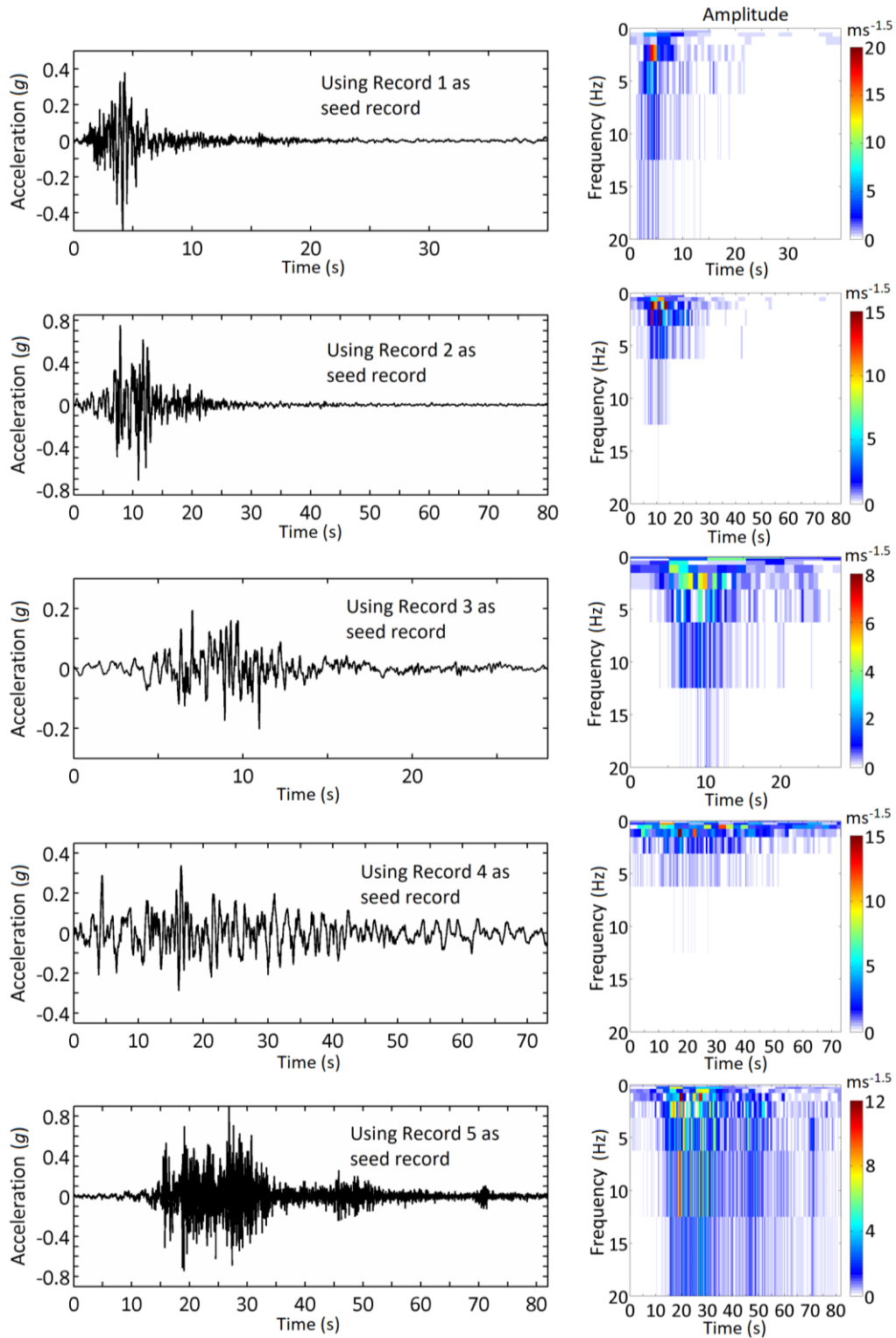


**Figure 2.8:** Samples of simulated records and their corresponding instantaneous amplitude.

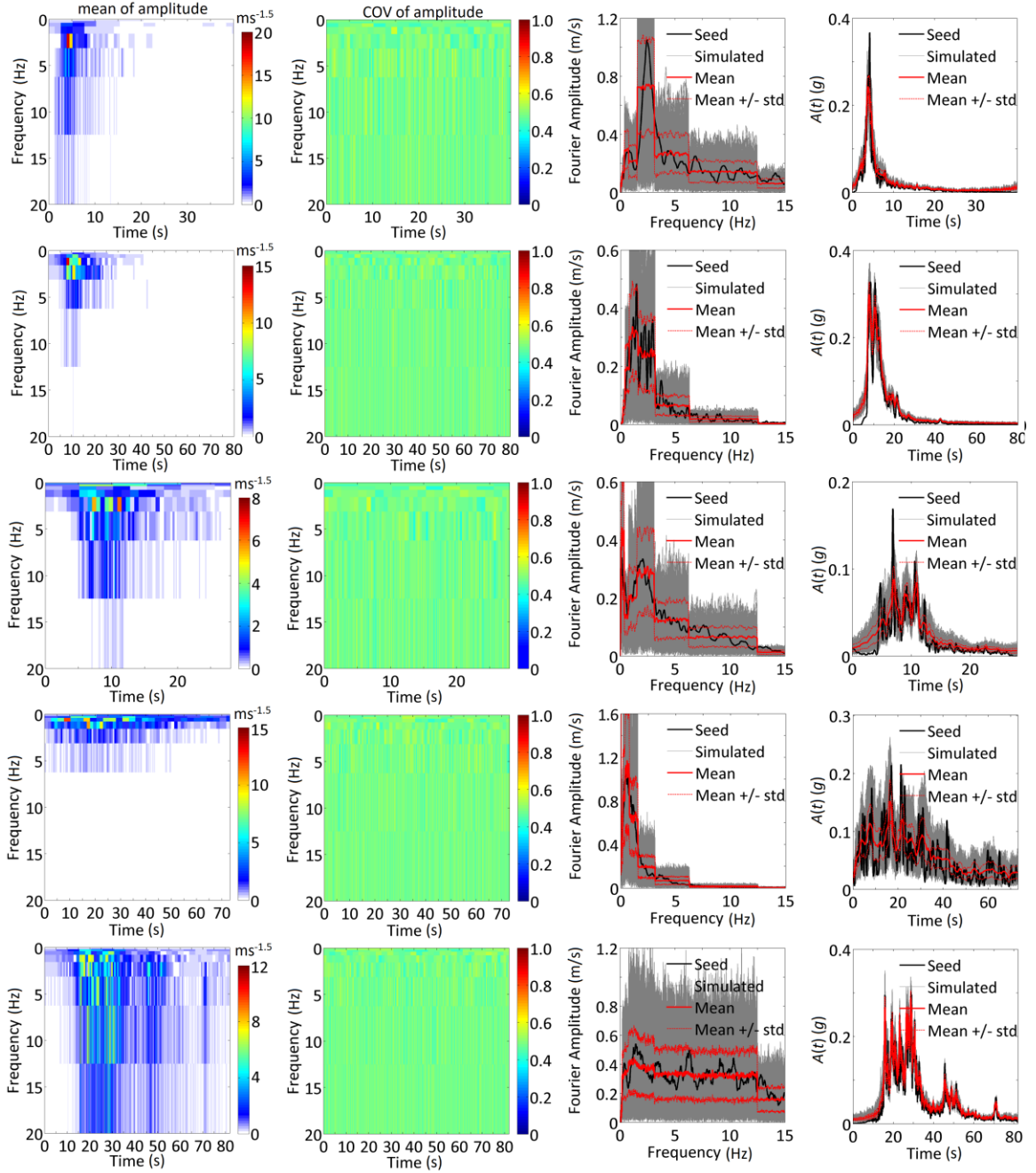


**Figure 2.9:** Statistics of the amplitude of the DOST and Fourier transform of the simulated records. Columns 1 to 4 show the mean of  $|x_{\mathcal{D}S}(f_p, t_q)|$ , the cov of  $|x_{\mathcal{D}S}(f_p, t_q)|$ , Fourier spectrum and  $A(t)$  of the simulated 50 records. Rows 1 to 5 correspond to the use of Records 1 to 5 as the seed record.

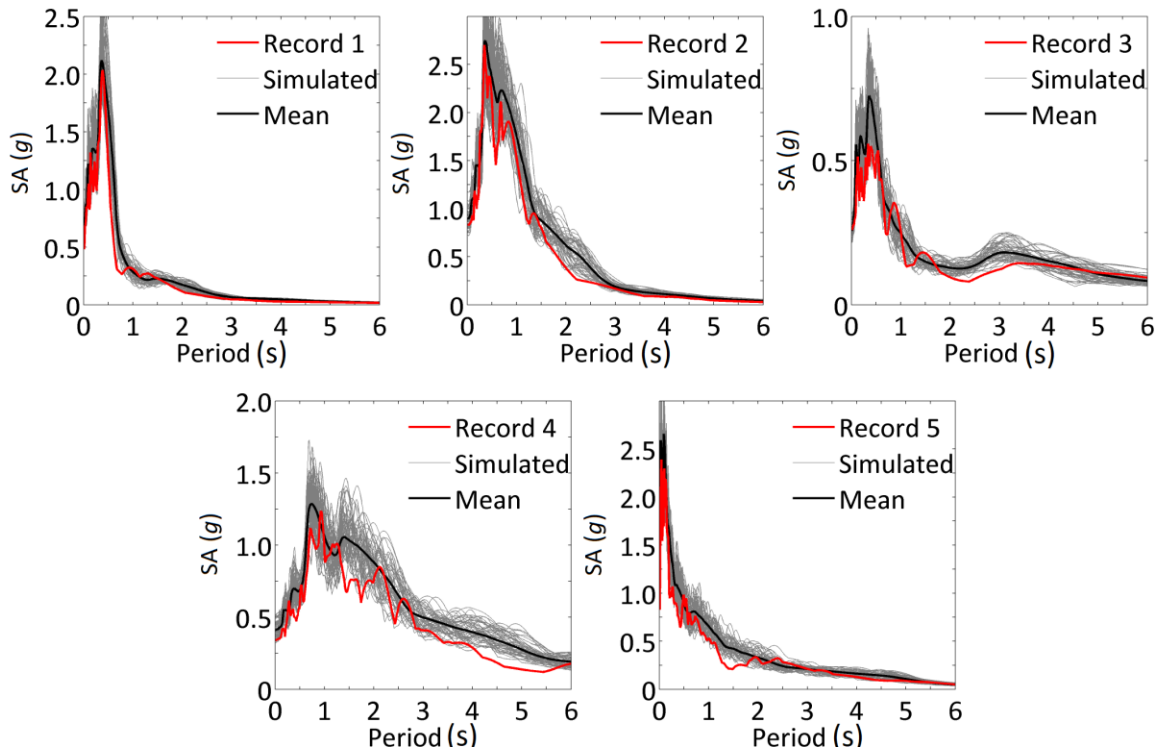


**Figure 2.10:** Comparison of response spectra of simulated and seed records.

**Table 2.2:** Information of Mexican interplate earthquakes at CU station, UNAM.

Event No.	Date	<b>M</b>	<i>H</i> (km)	Lat. N.	Long. W.
1	14/03/1979	7.6	28	17.49	101.26
2	25/04/1989	6.9	19	16.60	99.40
3	31/05/1990	6.1	16	17.11	100.89
4	07/06/1982	7.0	24	16.26	98.51
5	14/09/1995	7.3	22	16.31	98.88
6	19/09/1985	8.0	15	18.08	102.94
7	24/10/1993	6.7	19	16.54	98.98
8	29/11/1978	7.8	19	16.00	96.69
9	11/12/2012	6.5	58	17.84	99.98



Since the simulated records are used for structural analysis, the response spectra of the simulated and seed records are calculated and presented in Figure 2.10. The Figure indicates that, on average, the response spectra of the simulated records follow those of the seed records.

To further test the proposed model for simulating ground motions based on a target DOST spectrum, consider a set of records listed in Table 2.2. These records are from interpolate seismic events and recorded at the CU station, UNAM, Mexico. First, the time-varying variance of the horizontal record components is calculated. Based on the calculated values, each record is time-shifted such that the maximum value of the time-varying variance is aligned at 20 s as shown in Figure 2.11. The DOST is applied to the time-shifted records, the obtained DOST spectrum is then standardized with respect to its corresponding total energy  $E_T$ . The average of the standardized DOST spectrum,  $x_{\mathcal{D}S-0}(f_p, t_q)$ , as well as the  $E_T$  of each horizontal record component is also presented in Figure 2.11, where  $\mu_{ET}$  represents the mean of  $E_T$ . Using  $\mu_{ET}x_{\mathcal{D}S-0}(f_p, t_q)$  as the target DOST spectrum and Eq. (2-11), a typical simulated record is shown in Figure 2.11 as well, illustrating the time-varying characteristics.

By simulating 200 records and applying the DOST to the simulated records, the obtained mean of DOST spectrum (or amplitude of the DOST coefficients) is shown in Figure 2.12. The calculated mean agrees well to the target  $\mu_{ET}x_{\mathcal{D}S-0}(f_p, t_q)$  which is shown in Figure 2.11. Also shown in Figure 2.12 are the COV value of DOST spectrum for the simulated records and the response spectrum of the simulated records. Again, the magnitude of the coefficient of variation is consistent with those observed Figures 2.7 and 2.9.

It must be emphasized that although the development of an earthquake magnitude and epicentral distance dependent ground motion model for the DOST spectrum is beyond the scope of this chapter, such a model together with the proposed model for simulating stochastic ground motions can be valuable to assess seismic hazard and risk. The model development could be carried out following similar steps given in Sabetta and Pugliese (1996) and in Alamilla et al. (2001).

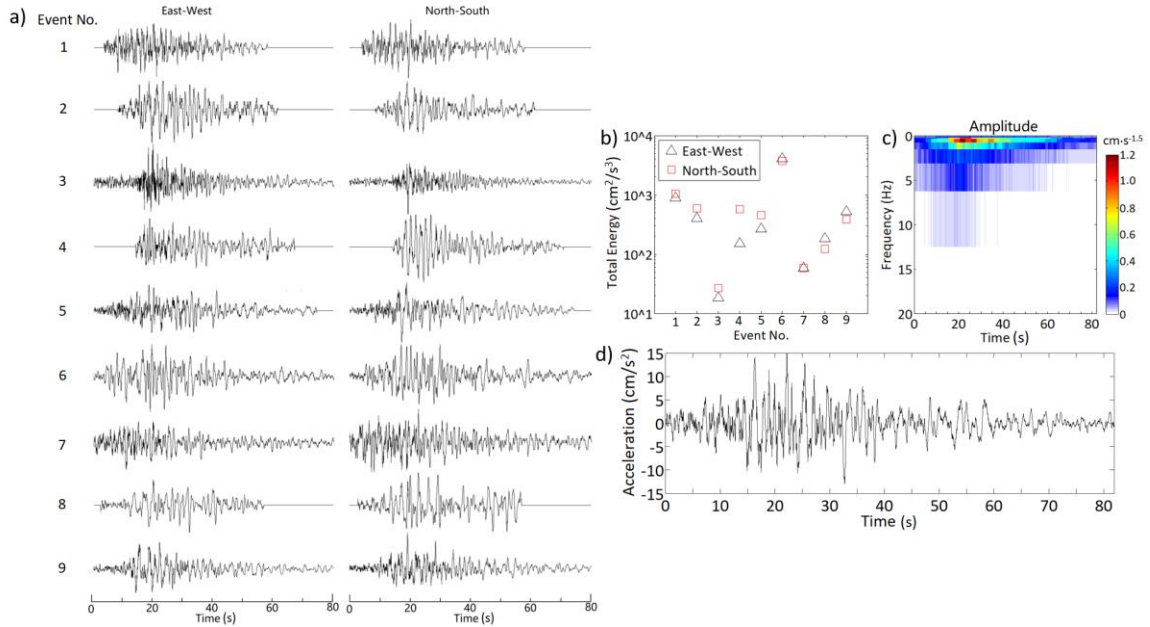


**Figure 2.11:** Time-shifted horizontal record components for the records listed in Table 2.2, the total energy of each record component  $E_T$ , average of the standardized amplitude of DOST coefficient, and a typical simulated record by using Eq. (2-11). The time shift is to ensure that the maximum value of the time-varying variance is aligned at 20 s.

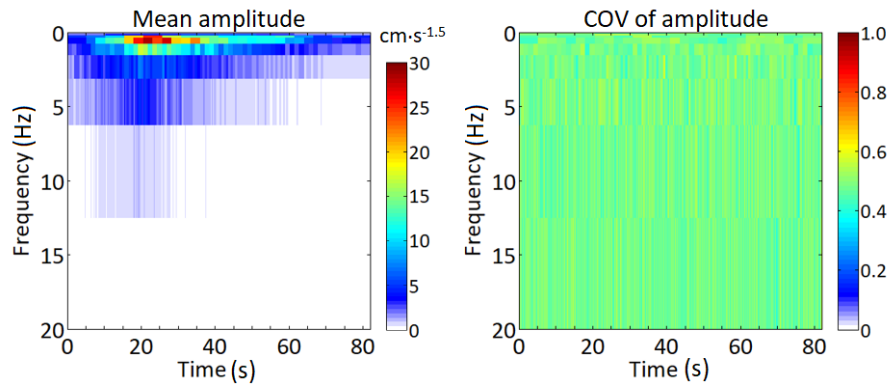


**Figure 2.12:** Mean and coefficient of variation of the DOST amplitude of 200 simulated ground motion records.

## 2.4 Conclusion

A very simple to use record-based approach to simulate ground motion records based on the DOST is proposed. It is shown that although the time-frequency resolution obtained from DOST for the recorded ground motions is coarse as compared to that obtained using the S-transform, its use clearly identifies the energy distribution in time and frequency. The time-frequency representation instead of a time-scale representation obtained from wavelet transformation facilitates the understanding of the ground motion records.

The comparison of the time-frequency resolution, Fourier spectrum, time-varying power distribution and response spectrum of the simulated and seed records indicates that the proposed simulation equation is useful for practical applications.

Numerical results also show that representing the ground motions as an evolutionary process with the amplitude modulation function equal to the amplitude of the coefficients of the S-transform has questionable value.

## 2.5 Data and Resources

There five records listed in Table 2.1. Records 1 to 3 are from obtained from <https://ngawest2.berkeley.edu>, Record 4 and those shown in Table 2.2 are obtained from <http://aplicaciones.iingen.unam.mx/AcelerogramasRSM/Inicio.aspx>, and Record 5 is obtained from <http://www.csmnc.net>. They are last access on May, 2019.

## Reference

- Alamilla, J., Esteva, L., Garcia-Perez, J., and Diaz-Lopez, O. (2001). Evolutionary properties of stochastic models of earthquake accelerograms: Their dependence on magnitude and *distance*, *Journal of Seismology*, **5**(1), 1-21.
- Atkinson, G. M., Assatourians, K., Boore, D. M., Campbell, K., and Motazedian, D. (2009). A guide to differences between stochastic point-source and stochastic finite-fault simulations, *Bull. Seismol. Soc. Am.*, **99**(6), 3192-3201.
- Battisti, U., and Riba, L. (2016). Window-dependent bases for efficient representations of the Stockwell transform, *Applied and Computational Harmonic Analysis*, **40**(2), 292-320.

- Boore, D.M. (2009). Comparing stochastic point-source and finite-source ground-motion simulations: SMSIM and EXSIM, *Bull. Seismol. Soc. Am.*, **99**(6): 3202-3216.
- Cui, X.Z., and Hong, H.P. (2020). Use of Discrete Orthonormal S - Transform to Simulate Earthquake Ground Motions. *Bull. Seismol. Soc. Am.*, **110**(2), 565-575.
- Cohen, L. (1995). *Time-frequency analysis*, Prentice Hall, Vol. 778.
- Daubechies, I. (1992). *Ten lectures on wavelets*, Siam, Vol. 61.
- Gu, P., and Wen, Y. K. (2007). A record-based method for the generation of tridirectional uniform hazard-response spectra and ground motions using the Hilbert-Huang transform, *Bull. Seismol. Soc. Am.*, **97**(5), 1539-1556.
- Gurley, K., and Kareem, A. (1999). Applications of wavelet transforms in earthquake, wind and ocean engineering, *Eng. Struct.*, **21**(2), 149-167.
- Hong, H. P. (2016). Modeling of nonstationary winds and its applications, *J. Eng. Mech.*, **142**(4), 04016004.
- Iyama, J., and Kuwamura, H.(1999). Application of wavelets to analysis and simulation of earthquake motions, *Earthquake Eng. Struct. Dynam.*, **28**(3), 255-272.
- Liang, J., Chaudhuri, S. R., and Shinozuka, M. (2007). Simulation of nonstationary stochastic processes by spectral representation, *J. Eng. Mech.*, **133**(6), 616-627.
- Liu, T.J. and Hong, H.P. (2015). Simulation of horizontal ground motions with spatial coherency in two orthogonal horizontal directions. *Journal of Earthquake Engineering*, **19**(5), 752-769.
- Liu, T. J., and Hong, H. P. (2016). Assessment of spatial coherency using tri-directional ground motions, *J. Earthquake Eng.*, **20**(5), 773-794.
- Pinnegar, C. R., and Mansinha, L. (2003). The S-transform with windows of arbitrary and varying shape, *Geophysics*, **68**(1), 381-385.
- Priestley, M.B. (1965). Evolutionary spectra and non-stationary processes, *J. R. Stat Soc B*, **27**, 204–37.
- Priestley, M.B. (1981). *Spectral analysis and time series*, New York: Academic.
- Rato, R. T., Ortigueira, M. D., and Batista, A. G. (2008). On the HHT, its problems, and some solutions, *Mech. Syst. Signal Process*, **22**(6), 1374-1394.
- Sabetta, F., and Pugliese, A. (1996). Estimation of response spectra and simulation of nonstationary earthquake ground motions. *Bulletin of the Seismological Society of America*, **86**(2), 337-352.
- Shinozuka, M., and Jan, C.M. (1972). Digital simulation of random processes and its applications, *J. Sound Vib.*, **25**(1): 111-128.
- Shinozuka, M., and Deodatis, G. (1991). Simulation of stochastic processes by spectral representation, *Appl. Mech. Rev.*, **44**(4), 191-204.
- Stockwell, R. G. (2007). A basis for efficient representation of the S-transform. *Digit. Signal Process.*, **17**(1), 371-393.

- Stockwell, R. G., Mansinha, L., and Lowe, R. P. (1996). Localization of the complex spectrum: the S transform, *IEEE Trans. Signal Process.*, **44**(4), 998-1001.
- Ventosa, S., Simon, C., Schimmel, M., Dañobeitia, J. J., and Mànuel, A. (2008). The S-transform from a wavelet point of view, *IEEE Trans. Signal Process.*, **56**(7), 2771-2780.
- Wang, Y., and Orchard, J. (2009). Fast discrete orthonormal Stockwell transform, *SIAM J. Sci. Comput.*, **31**(5), 4000-4012.
- Wen, Y. K., and Gu, P. (2004). Description and simulation of nonstationary processes based on Hilbert spectra, *J. Eng. Mech.*, **130**(8), 942-951.
- Yamamoto, Y., and Baker, J. W. (2013). Stochastic model for earthquake ground motion using wavelet packets, *Bull. Seismol. Soc. Am.*, **103**(6), 3044-3056.
- Yan, Y., and Zhu, H. (2011). The generalization of discrete Stockwell transforms, *2011 19th IEEE European Signal Processing Conference*, 1209-1213.
- Yeh, C.H., and Wen, Y.K. (1990). Modeling of nonstationary ground motion and analysis of inelastic structural response, *Struct. Safety*, **8**(1-4), 281-298.

## Chapter 3

### 3 Time-frequency spectral representation models to simulate nonstationary processes and their use to generate ground motions

#### 3.1 Introduction

Many of the models used to model and simulate the nonstationary stochastic processes are based on the evolutionary spectral theory advanced by Priestley (1965, 1981) and Priestley and Tong (1973). In such a case, the nonstationary stochastic process is known as the evolutionary stochastic process and is characterized by the evolutionary power spectral density function. Such a spectral function, at least, requires the assignment of the amplitude modulation function. The evolutionary stochastic process is often used to represent the seismic ground motions (Newmark and Rosenblueth 1971; Clough and Penzien 2003), winds (Simiu and Scanlan 1996) and waves (Ochi 2005). Simulation of an evolutionary stochastic process can be conveniently carried out using the spectral representation method (SRM) (Shinozuka and Jan 1972; Shinozuka and Deodatis 1996; Liang et al. 2007). Although the use of time-frequency dependent amplitude modulation function is considered in the context of an evolutionary stochastic process, the potential frequency modulation (i.e., modulating the frequency) is often neglected even though there is evidence that the instantaneous frequency of ground motions varies with time (Grigoriu et al. 1988; Yeh and Wen 1989; Alamilla et al. 2001). Yeh and Wen (1989) proposed a model by considering frequency modulation, where the modulation function is assessed based on time-varying zero-crossing rate. The model is attractive for its simplicity, but its extension and use to non-uniform frequency modulation could be difficult. The application of this model results in that the recorded ground motions with a constant sampling time interval becomes a time series with unevenly spaced time step in the new timescale. It seems that the evaluation of the power spectral density function using the (ordinary) Fourier transform by considering this aspect is not fully addressed in the mentioned references. Other models include the one proposed by Conte and Peng (1997), where the superposition of several amplitude-modulated stochastic processes is

used to represent the seismic ground motions.

Besides the use of the results from the Fourier transform to characterize the ground motions, the use of other signal processing techniques such as the short-time Fourier transform (STFT) (Cohen 1995), wavelet transform (Daubechies 1992) and Hilbert-Huang transform (Huang and Wu 2008; Wen and Gu 2004) in dealing with the seismic ground motions have been considered in the literature. For example, Liang et al. (2007) compared the time-frequency characteristics of the ground motions obtained by using the STFT and other transforms. Basu and Gupta (1998), Iyama and Kuwamura (1999), Gurley and Kareem (1999), Spanos and Failla (2004), Hancock et al. (2006) and Yamamoto and Baker (2013) employed the continuous wavelet transform, discrete wavelet transform, and wavelet packet transform to described the ground motions in time-scale representation. The application of the continuous wavelet transform leads to the time-scale representation with high fidelity. The representation, however, is highly redundant, and the decomposed signal is not presented in an easy to use superposition in terms of orthogonal basis functions for simulation. The use of discrete wavelet transform and wavelet packet transform has lead to simulation models for nonstationary processes (Gurley and Kareem 1999; Spanos and Failla 2004; Yamamoto and Baker 2013). The feasibility to extend some of the mentioned models to simulate nonstationary ground motions at multiple-support with time-frequency dependent coherence is not explored.

The advantages and shortcomings of the STFT and wavelet transform are well discussed in Cohen (1995), Daubechies (1992), Percival and Walden (2000) and Stockwell (2007). For example, the use of STFT is associated with leakage (Cohen 1995). The use of discrete wavelet transform with different dilations has overlapping spectral responses, and the function of the phase in the wavelet representation is not well understood as compared to that in the Fourier transform (Stockwell 2007). Instead of using the mentioned transforms, an alternative transform, the S-transform (or Stockwell-transform) (Stockwell et al. 1996; Pinnegar and Mansinha 2003) and discrete orthonormal S-transform (DOST) (Stockwell 2007) can be considered. These transforms differ from the STFT and wavelet transform (Stockwell et al. 1996; Stockwell 2007; Battisti and Riba 2016). The application of these transforms to records or signals

provides a time-frequency representation, which is in contrast to the application of the wavelet transform resulting in a time-scale representation. The S-transform provides frequency-dependent resolution with the phase angle referring to the argument of the sinusoid at zero time that is consistent with the Fourier transform. The S-transform leads to a redundant representation in the time-frequency plane, which is similar to the continuous wavelet transform and STFT. DOST is an efficient transform that localizes the spectrum and retains the advantageous phase properties of the S-transform. Its application results in that the signal can be represented as the superposition of scaled orthonormal basis functions.

In this chapter, two simulation models within the framework of the time-frequency spectral representation method are proposed to simulate nonstationary stochastic processes. The models are based on the DOST and S-transform. One of the models considers the phase angles are uncertain, while the second one considers the amplitudes associated with real and imaginary parts of the orthonormal basis functions are uncertain. Both models are simple to use. The first one is simple to interpret and implement. The second one can be used for conditional simulation. The advantages of the proposed models are that they implicitly include the amplitude and frequency modulations for the nonstationary stochastic process, hence avoid the difficulty in assessing non-uniform amplitude modulation and frequency modulation to be used with the application of the evolutionary stochastic process. The incorporation of the time-frequency representation obtained from the S-transform in the model is elaborated so to increase the fidelity of the time-frequency representation. Throughout this chapter, the exposition and use of the proposed models are focused on the seismic ground motions at the single and multiple-support, although the models can be applied to nonstationary processes such as the winds and waves as well. The adequacy of the models is shown through theoretical derivation and numerical examples.

The development of the proposed models is given after a quick summary of the S-transform and DOST in the next section. The parallel between the models developed based on the (frequency) spectral representation method (Shinozuka and Jan 1972; Shinozuka and Deodatis 1991; Kameda and Morikawa 1994; Liang et al. 2007, Chen et



al. 2018) and the proposed models in this chapter is drawn. The incorporation of time-frequency representation obtained from the S-transform to enhance the proposed models is elaborated and illustrated by numerical examples.

### 3.2 The S-transform and discrete orthonormal S-transform

In this section, a summary of the S-transform (ST) and DOST is presented. ST proposed by Stockwell et al. (1996) is,

$$x_s(f, \tau) = \int_{-\infty}^{\infty} x(t)w(f, \tau-t)e^{-i2\pi ft} dt, \quad (3-1)$$

where  $x_s(f, \tau)$  denotes the ST coefficient of  $x(t)$ ,  $f$  and  $t$  are the frequency and time similar in the Fourier transform, and  $\tau$  is the center of the window function  $w(f, \tau-t)$ , which will be discussed further. The transform provides a time-frequency representation of the signal  $x(t)$ . The signal can be reconstructed using,

$$x(t) = \int_{-\infty}^{\infty} \left[ \int_{-\infty}^{\infty} x_s(f, \tau) d\tau \right] e^{i2\pi ft} df. \quad (3-2)$$

Similar to the continuous wavelet transform, ST provides a redundant representation which is inefficient. The time-frequency power spectral density (TFPSD) function can be defined based on  $x_s(f, \tau)$ . However, an algorithm to simulate signals such that their expected TFPSD function equal to that obtained from  $x_s(f, \tau)$  of a seed signal or a target TFPSD is unavailable at present. This perhaps is partly due to that the use of ST does not lead to  $x(t)$  that is expressed as the sum of the product of  $x_s(f, \tau)$  and the orthogonal basis functions.

To achieve maximum representation efficiency, DOST that takes a time series of  $N$  points to the time-frequency representation with  $N$  points was proposed in Stockwell (2007). DOST is based on  $N$  orthonormal basis functions,  $D_{[\beta]}(t_k; p, q)$ , and is given by,

$$x_{\mathcal{D}S}(p, q) = \left(1/N\right) \sum_{k=0}^{N-1} x(t_k) D_{[\beta]}(t_k; p, q), \quad (3-3)$$

where  $x_{\mathcal{D}S}(p, q)$  is the DOST coefficient,  $x(t_k)$  denotes the sampled  $x(t)$  at the discrete points  $t_k = k\Delta$ ,  $p$  is an index of the center of a frequency band  $f_p = p/(N\Delta)$ ,  $q$  is an index for the time localization  $t_q = q\Delta$ ,

$$D_{[\beta]}(t_k; p, q) = \frac{ie^{-i\pi q} \{e^{-i2\pi(k/N-q/\beta)(p-\beta/2-1/2)} - e^{-i2\pi(k/N-q/\beta)(p+\beta/2-1/2)}\}}{\sqrt{\beta} 2 \sin[\pi(k/N - q/\beta)]}, \quad (3-4)$$

and  $\beta$  indicates the width of the frequency band centred at the frequency indexed by  $p$  (i.e.,  $f_p$ ). For  $D_{[\beta]}(t_k; p, q)$  to be orthogonal, Stockwell (2007) suggested that  $q = 0, 1, \dots, \beta - 1$ , and  $p$  and  $\beta$  must be selected so each Fourier frequency sample is used once and only once, which can be achieved by using the octave sampling. This lead to,

$$(p; q; \beta) = (0; 0; 1), \text{ for } m = 0; \quad (3-5)$$

$$(p; q; \beta) = (1; 0; 1), \text{ for } m = 1; \quad (3-6)$$

and,

$$(p; q; \beta) = (2^{m-1} + 2^{m-2}; 0, 1, \dots, 2^{m-1} - 1; 2^{m-1}), \text{ for } m = 2, \dots, \log_2(N) - 1. \quad (3-7)$$

where  $m$  is the octave number. Unlike in the continuous wavelet transform, the basis functions in DOST are not dilations nor translations of a single function. An illustration of some of the basis functions is presented in Figure 3.1. According to Eqs. (3-5) to (3-7), there are  $N_1 = N/2$  basis functions. Wang and Orchard (2009) showed that if the same  $\tau$  value is used, the basis function for  $p$  is conjugate symmetric to that for  $-p$ . The DOST coefficients for a real-valued signal are conjugate symmetric about  $p = 0$ . Therefore,  $x(t_k)$  can be reconstructed using,

$$x(t_k) = \sum_{\text{for feasible } p, q} x_{\mathcal{D}S}(p, q) D_{[\beta]}(t_k; f_p, t_q), \quad k = 0, \dots, N-1, \quad (3-8)$$

where the asterisk denotes the complex conjugate;  $p$  and  $q$  are assigned as shown in Eqs. (3-5) to (3-7) and  $p$  can be both positive and negative. The DOST coefficients and the basis functions in this equation are presented in double-indexed (i.e., matrix form). To simplify the notation, and to consider the mapping of the indices between  $j$  ( $1 \leq j \leq N/2$ ) and  $(p, q; \beta)$  with  $p \geq 0$  shown in Table 3.1. Due to the complex conjugate property of the basis functions with respect to  $p$ , the complex conjugate property of basis function about  $j = N/2+1$  can also be used for obtaining the basis function with  $j$  from  $N/2+2$  to  $N$  and the basis function of  $j = N/2+1$  is identical to that of  $j = 1$ . Eq. (8) is rewritten as,

$$x(t_k) = \sqrt{2} \sum_{j=1}^{N/2} \text{Re} \left[ x_{1_{\mathcal{D}S}}(j) D_1^*(t_k; j) \right], \quad k = 0, \dots, N-1, \quad (3-9)$$

where  $x_{1_{\mathcal{D}S}}(j) = \sqrt{2} x_{\mathcal{D}S}(p, q)$  and  $D_1^*(t_k; j) = D_{[\beta]}^*(t_k; p, q)$  are used to present the basis functions in a single-index or vector form. It is emphasized that the mapping between  $j$  and  $(p, q; \beta)$  is not unique and is used to simplify the notation only. Throughout the remaining part of this chapter, the single- or double-indexed presentations are used interchangeably to facilitate the exposition of the derivation and results. The use of the Fourier transform as well as the fast Fourier transform to evaluate the ST, DOST and their inverses is given in Wang and Orchard (2009), Yan and Zhu (2011) and Battisti and Riba (2016).

**Table 3.1:** Mapping between  $j$  and  $(p, q; \beta)$ .

$M$	$j \longleftrightarrow (p, q; \beta)$			
0	$1 \longleftrightarrow (0, 0; 1)$			
1	$2 \longleftrightarrow (1, 0; 1)$			
2	$3 \longleftrightarrow (3, 0; 2)$		$4 \longleftrightarrow (3, 1; 2)$	
3	$5 \longleftrightarrow (6, 0; 4)$	$6 \longleftrightarrow (6, 1; 4)$	$7 \longleftrightarrow (6, 2; 4)$	$8 \longleftrightarrow (6, 3; 4)$
	...			

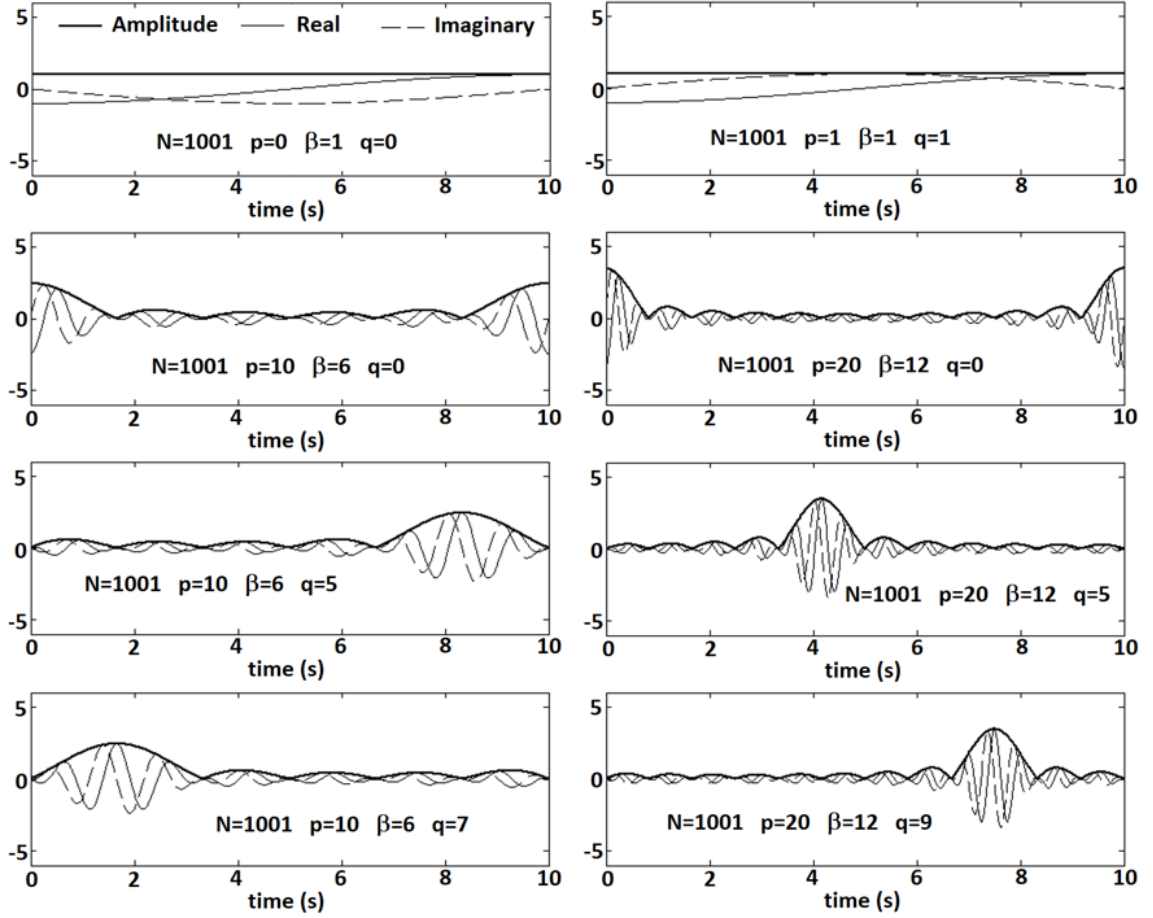


**Figure 3.1:** Illustration of a few selected basis functions (for  $N$  discrete points with time step  $\Delta = 0.01$ s) for DOST.

The one-sided TFPSD function of  $x(t)$  based on the DOST coefficients is defined as,

$$S(p, q) = 2x_{\mathcal{D}_S}(p, q)x_{\mathcal{D}_S}^*(p, q), \quad (3-10a)$$

or,

$$S(j) = x_{1_{\mathcal{D}_S}}(j)x_{1_{\mathcal{D}_S}}^*(j) = |x_{1_{\mathcal{D}_S}}(j)|^2, \quad (3-10b)$$

where  $S(j) \equiv S(p, q)$  represents the one-sided TFPSD function for the center of the frequency band  $f_p$  and the time localization  $t_q$ ; the relation between  $j$  and  $(p, q; \beta)$  is the

same as shown in Table 3.1. Eq. (10b) indicates that the amplitude of the DOST coefficient,  $|x_{1\text{DOST}}(j)|$ , equals  $\sqrt{S(j)}$ .

### 3.3 Two new time-frequency spectral representation models for nonstationary processes

In this section, two models that can be used to model and simulate nonstationary stochastic processes are described. These models are based on the orthonormal basis function used in DOST. Given that the target DOST coefficients or DOST coefficients of an actual record  $x(t_k)$ , a model to simulate the nonstationary stochastic ground motions,  $X(t)$ , was proposed in Chapter 2. The model according to the above-adopted notation is written as,

$$X(t_k) = \sqrt{2} \sum_{j=1}^{N_1} \sqrt{S(j)} \operatorname{Re} \left[ D_1(t_k; j) e^{i\theta(j)} \right], \quad k = 0, \dots, N-1, \quad (3-11)$$

where  $\theta(j)$  is independent and uniformly distributed between 0 to  $2\pi$ , and  $\operatorname{Re}(\cdot)$  denotes the real part of its argument. The use of  $D_1$  or  $D_1^*$  in Eq. (3-11) is equivalent in terms of simulation. The model, which will be referred to as Model-1, takes advantage of the orthonormal basis functions associated with octave sampling. Adequacy of the model was assessed by comparing the coefficients of DOST, Fourier coefficients, the energy distribution in time, TFPSD function and response spectrum of the seed and the simulated records.

To better understand the format of the model shown in Eq. (3-11), it is noteworthy that the format presented in Eq. (3-11) is similar to one of the formats used in SRM (Shinozuka and Jan 1972), which is expressed as the sum of  $\sqrt{2} \sqrt{S_F(f_j) \Delta f} \operatorname{Re} \left[ e^{i2\pi f_j t} e^{i\theta(j)} \right]$ , where  $S_F(f)$  is the (one-sided) power spectral density function obtained from the ordinary Fourier analysis and  $f_j$  are non-negative frequencies in Hz. The orthogonal basis functions in SRM are  $e^{i2\pi f_j t}$  and in Model-1 are  $D_1(t_k; j)$ . However, it must be emphasized that  $\exp(i2\pi f_j t)$  represents stationary oscillatory

behaviour and  $D_1(t_k; j)$  provides nonstationary characteristics as illustrated in Figure 3.1.

It is straightforward to show that the expectation of  $X(t_k)$ ,  $E(X(t_k))$ , is given by,

$$E(X(t_k)) = \sqrt{2} \sum_{j=1}^{N_1} \sqrt{S(j)} \operatorname{Re} \left[ D_1(t_k; j) E \left( e^{i\theta(j)} \right) \right] = 0, \quad (3-12)$$

and the covariance  $\operatorname{Cov}(X(t_{k_1})X(t_{k_2}))$  by considering  $\theta(j)$  that are independent and uniformly distributed between 0 to  $2\pi$  is,

$$\operatorname{Cov}(X(t_{k_1})X(t_{k_2})) = \sum_{j=1}^{N_1} S(j) |D_1(t_{k_1}; j)| |D_1(t_{k_2}; j)| \cos \left( \phi(t_{k_1}; j) - \phi(t_{k_2}; j) \right), \quad (3-13)$$

in which  $E(\ )$  denotes the expectation,  $\phi(t_k, j) = \tan^{-1} \left( \frac{\operatorname{Im}(D_1(t_k; j))}{\operatorname{Re}(D_1(t_k; j))} \right)$  is the time and frequency-dependent phase angle and  $\operatorname{Im}(\ )$  denotes the imaginary part of its argument.

The variance can be obtained from Eq. (3-13) by letting  $t_{k_1} = t_{k_2}$ . This results in  $\sum_{j=1}^N S(j)$

which equals  $(1/N) \sum_{k=0}^{N-1} x^2(t_k)$  based on the Parseval theorem. Therefore, on average, the

simulated records are consistent with the seed record. In addition, it can be shown that by letting  $X_{1_{\mathcal{D}S}}(j)$  representing the DOST coefficients of  $X(t_k)$ , it can be shown that (see Eq. (A7) in Appendix A),

$$E \left\{ X_{1_{\mathcal{D}S}}(j) X_{1_{\mathcal{D}S}}^*(j) \right\} = S(j), \quad (3-14)$$

which indicates that the expectation of the TFPSD function of the sampled records from Model-1 equals the target TFPSD function  $S(j)$ .

The model presented in Eq. (3-11) is very simple to use. However, similar to the case of SRM, it is difficult, if not impossible, to extend it to conditionally incoherent simulate multiple stochastic processes. To formulate a model for the conditional simulation of

ground motions at multiple-support, it is noted that the model based on SRM for such a purpose is represented by the sum of  $a_j \cos(2\pi f_j t) + b_j \sin(2\pi f_j t)$  (Kameda and Morikawa 1994), where  $a_j$  and  $b_j$  are considered to be zero-mean normal variates with the standard deviation equal to  $\sqrt{S_F(f_j)\Delta f}$ , where  $S_F(f)$  is one-sided PSD function and  $\Delta f$  is a frequency increment. The above and Eq. (9) suggests that by using the basis functions in DOST the following model, referred to as Model-2, could be considered to simulate nonstationary ground motions,

$$X(t_k) = \sum_{j=1}^{N_1} \left\{ A_j \operatorname{Re}[D_1(t_k; j)] + B_j \operatorname{Im}[D_1(t_k; j)] \right\}, \quad (3-15)$$

where  $A_j$  and  $B_j$  are independent zero-mean normal variates with the standard deviation equal to  $\sqrt{S(j)}$ . Also,  $E(A_j A_k)$ ,  $E(B_j B_k)$ ,  $E(A_j B_k)$  and  $E(B_j A_k)$  are assumed to be equal to zero if  $j$  is not equal to  $k$ . The mean and covariance of  $X(t)$  modeled by this model, are given by,

$$E(X(t_k)) = E \left\{ \sum_{j=1}^{N_1} A_j \operatorname{Re}[D_1(t_k; j)] + B_j \operatorname{Im}[D_1(t_k; j)] \right\} = 0, \quad (3-16)$$

and,

$$\begin{aligned} \operatorname{Cov}(X(t_{k_1})X(t_{k_2})) &= E \left\{ \left[ \sum_{j_1=1}^{N_1} A_{j_1} \operatorname{Re}[D_1(t_{k_1}; j_1)] + B_{j_1} \operatorname{Im}[D_1(t_{k_1}; j_1)] \right] \right. \\ &\quad \left. \times \left[ \sum_{j_2=1}^{N_1} A_{j_2} \operatorname{Re}[D_1(t_{k_2}; j_2)] + B_{j_2} \operatorname{Im}[D_1(t_{k_2}; j_2)] \right] \right\}, \quad (3-17) \\ &= \sum_{j=1}^{N_1} S(j) |D_1(t_{k_1}; j)| |D_1(t_{k_2}; j)| \cos(\phi(t_{k_1}; j) - \phi(t_{k_2}; j)) \end{aligned}$$

which is the same as Eq. (3-13). Similar to the case for Model-1, it can be shown that the expectation of the TFPSD function of the records sampled according to Model-2 equals the target TFPSD function  $S(j)$  (see Eq. (A8) in Appendix A). The above mathematical proofs show that the expectation of the simulated signal by using the proposed models

equals zero and the expectation of the TFPSD function of the simulated signal equals its target. Moreover, based on the central limit theorem  $X(t_k)$  presented in Eqs. (3-11) and (3-15) is Gaussian.

### 3.4 Estimation of coherence and models to simulate multiple-support ground motions

The procedure to assess lagged coherence and extension of the two models described in the previous section to model and simulate coherent nonstationary stochastic processes are presented in this section. Moreover, the use of Model-2 for conditional simulation is also formulated.

Given two records  $x_{n_1}(t)$  and  $x_{n_2}(t)$  for the same seismic event with wave passage effect removed (Der Kiureghian 1996), their DOST coefficients, denoted as  $x_{n_1, \mathcal{D}\mathcal{S}}(j)$  and  $x_{n_2, \mathcal{D}\mathcal{S}}(j)$  (i.e.,  $x_{n_1, \mathcal{D}\mathcal{S}}(p, q)$  and  $x_{n_2, \mathcal{D}\mathcal{S}}(p, q)$ ), can be evaluated. Similar to the definition of the TFPSD function (see Eqs. (3-10a) and (3-10b)), its crossed version for two processes  $x_{n_1}(t)$  and  $x_{n_2}(t)$ ,  $S_{n_1 n_2}(j)$  (i.e.,  $S_{n_1 n_2}(p, q)$ ), is defined as,

$$S_{n_1 n_2}(j) = x_{n_1, \mathcal{D}\mathcal{S}}(j) x_{n_2, \mathcal{D}\mathcal{S}}^*(j). \quad (3-18)$$

$S_{n_1 n_1}(j)$  and  $S_{n_2 n_2}(j)$  are defined analogously. The coherence is then defined as,

$$\Gamma_{n_1 n_2}(j) = \frac{\mathcal{S}[S_{n_1 n_2}(j)]}{\sqrt{\mathcal{S}[S_{n_1 n_1}(j)] \mathcal{S}[S_{n_2 n_2}(j)]}}, \quad (3-19)$$

where  $\mathcal{S}[\ ]$  denotes the smoothing operator,  $|\Gamma_{n_1 n_2}(j)|$  is known as lagged coherence, and

$$\phi_{n_1 n_2}(j) = \tan^{-1} \left( \frac{\text{Im}(\Gamma_{n_1 n_2}(j))}{\text{Re}(\Gamma_{n_1 n_2}(j))} \right), \quad (3-20)$$

is the phase spectrum. The smoothing is necessary and the reason is similar to that for



the analysis based on Fourier transform, where the calculated coherence equals one if no smoothing is applied (Zerva 2009). The same issue and the need for smoothing also arise in the use of the wavelet transform (Torrence and Compo 1998). For simplicity of the implementation of the smoothing, the smoothing operation can be carried out based on the double-indexed representation of the TFPSD function  $S_{n_1 n_2}(p, q)$  rather than single-indexed  $S_{n_1 n_2}(j)$ .

First, by considering the time-frequency dependent coherence, Model-1 shown in Eq. (3-11) is extended to simulate multiple-support ground motions. To model the  $n \times 1$  vector of stochastic processes,  $\mathbf{X}(t)$ , representing the ground motions at  $n$  supports or recording stations, the  $n \times n$  TFPSD matrix  $\mathbf{S}(j)$  with the  $(n_1, n_2)$ -th element  $S_{n_1 n_2}(j)$  is decomposed into  $\mathbf{L}(j)\mathbf{L}^H(j)$  based on Cholesky decomposition where  $\mathbf{L}(j)$  is the lower triangle matrices and the superscript denotes the conjugate transpose (i.e., Hermitian matrix). This leads to that the  $n_1$ -th element of the stochastic process within  $\mathbf{X}(t)$  is given by,

$$X_{n_1}(t_k) = \sqrt{2} \sum_{m=1}^{n_1} \sum_{j=1}^{N_1} \text{Re} \left[ L_{n_1 m}(j) D_1(t_k; j) e^{i\theta_m(j)} \right], \quad (3-21)$$

where  $n_1 = 1, \dots, n$ ,  $L_{n_1 m}$  denotes the  $(n_1, m)$ -th element of the lower triangle matrix  $\mathbf{L}(j)$  and  $\theta_m(j)$  are independent and uniformly distributed between 0 and  $2\pi$ . Sampling  $\theta_m(j)$ , hence  $X_{n_1}(t_k)$ , by using Eq. (3-21), is a straight forward task.

It can be shown that the mean of  $X_{n_1}(t_k)$  equals zero and that the expectation of the TFPSD function of the simulated records is the same as their targets (see Appendix B).

By considering Model-2 shown in Eq. (3-15), the  $n_1$ -th element of the stochastic process is given by,

$$X_{n_1}(t_k) = \sum_{j=1}^N A_{n_1 j} \text{Re} [D_1(t_k; j)] + B_{n_1 j} \text{Im} [D_1(t_k; j)], \quad (3-22)$$

where  $A_{n_1 j}$  and  $B_{n_1 j}$  are model parameters. Let

$\mathbf{F}_{n_1} = [A_{n_1,1}, A_{n_1,2}, \dots, A_{n_1,N}, B_{n_1,1}, B_{n_1,2}, \dots, B_{n_1,N}]^T$  and  $\mathbf{F} = [\mathbf{F}_1^T, \mathbf{F}_2^T, \dots, \mathbf{F}_n^T]^T$ , where the  $n \times (2N_1)$  variables in  $\mathbf{F}$  are zero mean correlated normal variates and the superscript  $T$  denotes the transpose. The covariance matrix of  $\mathbf{F}$ ,  $\mathbf{C}_{FF}$ , is formed by  $n \times n$  submatrices

$\mathbf{C}_{F_{n_1}F_{n_2}}$ ,  $n_1, n_2 = 1, \dots, n$ , where  $\mathbf{C}_{F_{n_1}F_{n_2}} = \begin{bmatrix} \mathbf{C}_{A_{n_1}A_{n_2}} & \mathbf{C}_{A_{n_1}B_{n_2}} \\ \mathbf{C}_{B_{n_1}A_{n_2}} & \mathbf{C}_{B_{n_1}B_{n_2}} \end{bmatrix}$  is a  $2N_1 \times 2N_1$  matrix. In  $\mathbf{C}_{FF}$ ,

$E(A_{n_1j}A_{n_2j}) = E(B_{n_1j}B_{n_2j}) = \sqrt{\mathcal{S}[2S_{n_1n_1}(j)]\mathcal{S}[2S_{n_2n_2}(j)]}\Gamma_{n_1n_2}(j)$ , and the remaining elements are equal to zero. Since the mean of each element in  $\mathbf{F}$  equals zero, and the covariance matrix of  $\mathbf{F}$  is known, the elements in  $\mathbf{F}$  can be simulated based on the Gaussian properties (Anderson 2003). Using the simulated values of  $A_{n_1j}$  and  $B_{n_1j}$ , a sample of nonstationary ground motions  $X_{n_1}(t_k)$  can be calculated using Eq. (3-22).

If  $n_{ob}$  processes,  $\mathbf{X}_{ob}(t)$ , within  $\mathbf{X}(t)$  are already observed while the remaining ones in  $\mathbf{X}_{un}(t)$  are to be simulated (i.e.,  $\mathbf{X}(t) = [(\mathbf{X}_{ob}(t))^T, (\mathbf{X}_{un}(t))^T]^T$ ), let  $\mathbf{F} = [\mathbf{F}_{ob}^T, \mathbf{F}_{un}^T]^T$ , where  $\mathbf{F}_{ob} = [\mathbf{F}_1^T, \mathbf{F}_2^T, \dots, \mathbf{F}_{n_{ob}}^T]^T$  and  $\mathbf{F}_{un} = [\mathbf{F}_{n_{ob}+1}^T, \mathbf{F}_{n_{ob}+2}^T, \dots, \mathbf{F}_n^T]^T$ . The matrix  $\mathbf{C}_{FF}$  is partitioned accordingly as,

$$\mathbf{C}_{FF} = \begin{bmatrix} \mathbf{C}_{F_{oo}} & \mathbf{C}_{F_{ou}} \\ \mathbf{C}_{F_{uo}} & \mathbf{C}_{F_{uu}} \end{bmatrix}, \quad (3-23)$$

with the sizes  $\begin{bmatrix} (n_{ob} \times 2N_1) \times (n_{ob} \times 2N_1) & (n_{ob} \times 2N_1) \times ((n - n_{ob}) \times 2N_1) \\ ((n - n_{ob}) \times 2N_1) \times (n_{ob} \times 2N_1) & ((n - n_{ob}) \times 2N_1) \times ((n - n_{ob}) \times 2N_1) \end{bmatrix}$ .  $\mathbf{C}_{F_{oo}}$  in

Eq. (23) consists of  $n_{ob} \times n_{ob}$  submatrix  $\mathbf{C}_{F_jF_k}$ ,  $j, k = 1, \dots, n_{ob}$ , and,  $\mathbf{C}_{F_{ou}}$ ,  $\mathbf{C}_{F_{uo}}$ , and  $\mathbf{C}_{F_{uu}}$  are defined analogously. The coefficients in  $\mathbf{F}_{ob}$ ,  $\mathbf{f}_{ob} = [f_1^T, f_2^T, \dots, f_{n_{ob}}^T]^T$ , are calculated using the observed records and according to Eq. (3-14). The variables in  $\mathbf{F}_{un}$  conditioned on  $\mathbf{F}_{ob} = \mathbf{f}_{ob}$ ,  $\mathbf{F}_{un|ob}$ , are also jointly Gaussian distributed with the mean  $\boldsymbol{\mu}_{\mathbf{F}_{un|ob}}$  and the covariance matrix  $\boldsymbol{\Sigma}_{\mathbf{F}_{un|ob}}$  given by (Anderson 2003),

$$\boldsymbol{\mu}_{\mathbf{F}_{un|ob}} = \mathbf{C}_{F_{uo}} \mathbf{C}_{F_{oo}}^{-1} \mathbf{f}_{ob}, \quad (3-24)$$

and,

$$\Sigma_{F_{un}|ob} = C_{F_{uu}} - C_{F_{uo}} C_{F_{oo}}^{-1} C_{F_{ou}}. \quad (3-25)$$

Using the simulated coefficients  $A$  and  $B$  (with subscripts) in  $F_{un}$  according to this joint probability distribution, samples of the stochastic processes  $X_{un}(t)$  can be evaluated using Eq. (3-22). It is emphasized again that similar to the case by using the SRM, the extension of Model-1 for conditional simulation is unavailable

### 3.5 Numerical assessment of time-frequency representation and simulation of ground motions

Numerical examples are presented in the following subsections to illustrate the time-frequency representation of recorded ground motions based on DOST. Examples by using the TFPSD functions obtained from the records as the target TFPSD function to generate synthetic ground motions are also presented.

#### 3.5.1 Evaluation of the time-frequency representation of recorded ground motions

For the numerical analysis and illustration, six records from three earthquakes listed in Table 3.2 are considered. By applying DOST, the time-frequency representation of the records are presented in Figures 3.2 to 3.4 in terms of amplitude and phase angle of the DOST coefficients.

These figures show that the amplitude of the DOST coefficient, which equals the square-root of the TFPSD function as mentioned earlier, varies in time and frequency. In Figure 3.2, the large values of  $|x_{DOST}(p, q)|$  occur around 10 s which coincides with the large amplitude of the recorded ground motions. The energy concentration around 32 s coincides with the second group of the large amplitudes of waves shown in the time history. Such identification of energy concentration in time is lost if the ordinary Fourier analysis is carried out. Also, the Figure shows that the energy concentration is around 2 Hz. Similarly, the time-frequency region where the energy concentration or large

$|x_{DST}(p, q)|$  values are localized can be identified from Figures 3.3 and 3.4 for each considered record. In other words, the energy concentration can be clearly identified by using DOST, although the resolution by using DOST is not as refined as those that could be obtained by using the S-transform which will be discussed shortly. A comparison of the results presented in Figures 3.2 to 3.4 indicates that the energy distribution in time and frequency differs from record to record and earthquake to earthquake. In all cases, no clear pattern can be identified from the plots of the phase angle of the DOST coefficients.

**Table 3.2:** Selected records.

Record	Event name, and date	Station name	Moment magnitude
1	Wenchuan, China 2008.05.12	Wolong	7.9
2	Tohoku, Japan 2011.03.11	Hitachi	9.0
3		C00	
4		I01	
5	SMART-1, 1986.11.14	I02	6.10
6		M01	

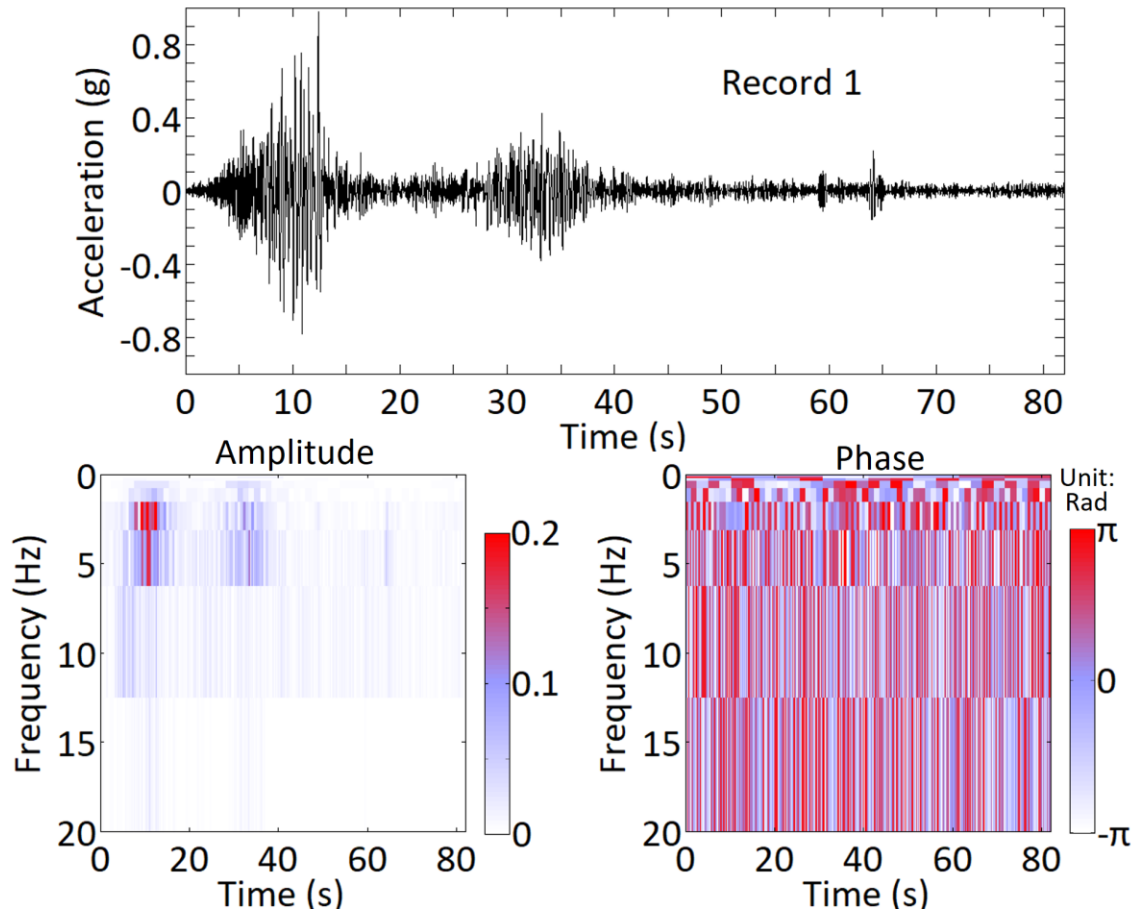


**Figure 3.2:** Time and frequency varying amplitude and phase angle of the DOST coefficients for a record from the Wenchuan earthquake (Record 1 shown in Table 3.1).

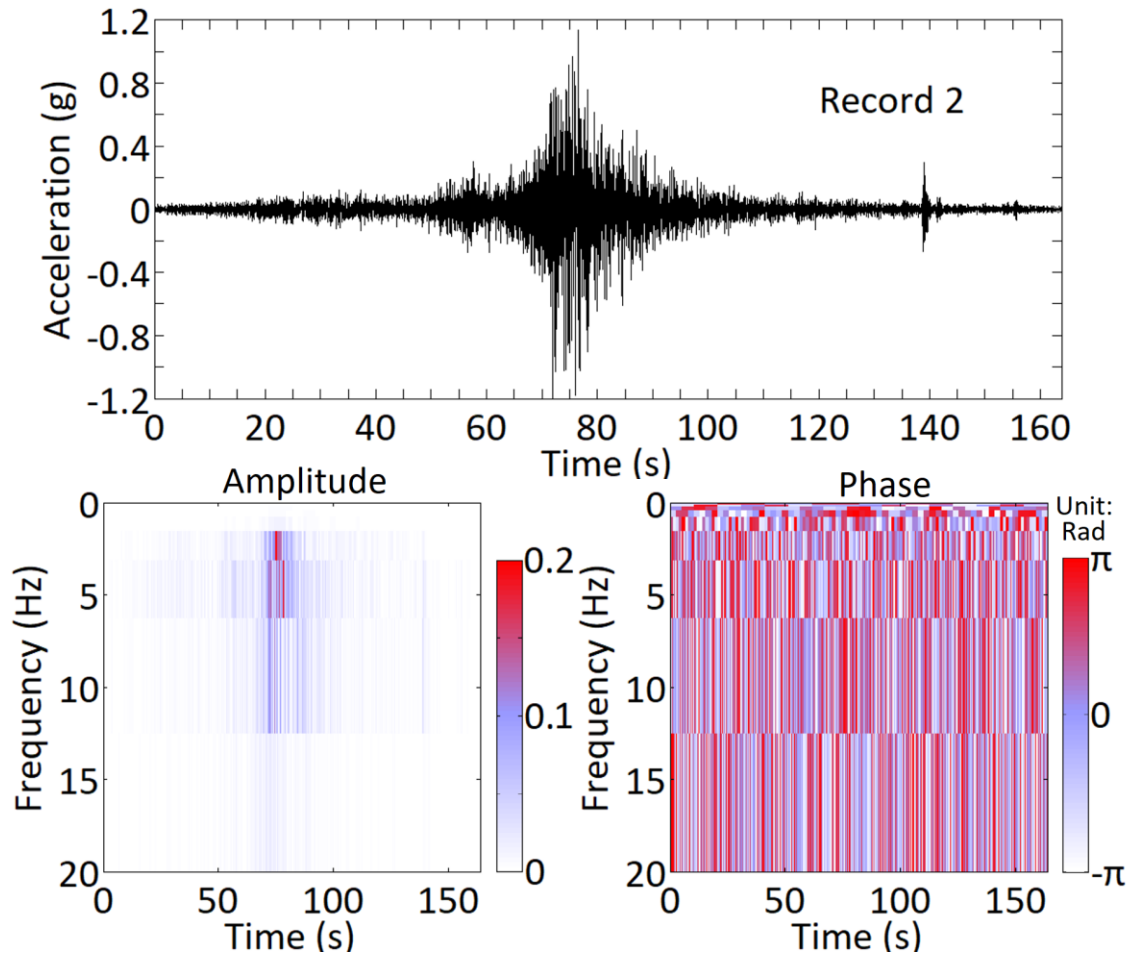


**Figure 3.3:** Time and frequency varying amplitude and phase angle of the DOST coefficients for a record from the Tohoku earthquake (Record 2 shown in Table 3.1).

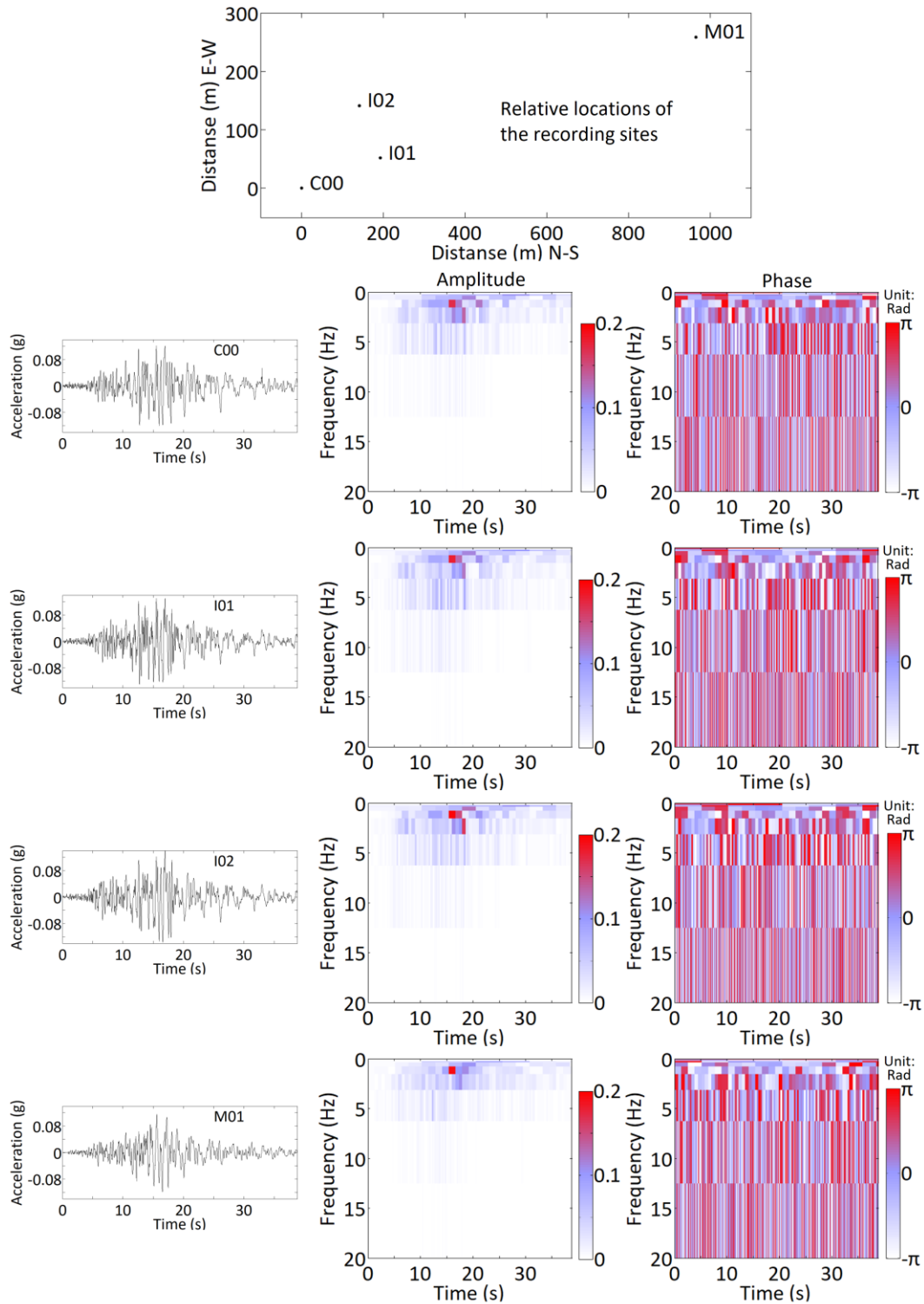


**Figure 3.4:** Recording sites and time and frequency varying amplitude and phase angle of the DOST coefficients for records from Smart-1 arrays (see Table 3.1 for the considered records).

The results presented in Figure 3.4 indicate that there are similarities of the time-frequency representation of the closely spaced records from the same earthquake. This similarity is quantified by using the coherence calculated by using Eq. (3-19). The obtained lagged coherence and the phase angle are shown in Figures 3.5 and 3.6, respectively. For the calculation, similar to Torrence and Compo (1998), the box window is used along the frequency index by considering immediate neighbouring frequency indices and the Gaussian window with a standard deviation of 1 is used along the time index by considering up to the third-order neighbours. The plots in Figure 3.5 indicate that lagged coherence varies in both time and frequency. The lagged coherence within the time interval of 10 to 20 s is greater as compared to those for the remaining time interval. This time interval is associated with more intense ground motions as shown in Figure 3.4 and the region with a large amplitude of the DOST coefficients. This observed trend cannot be detected based on results from the Fourier transform. As the separation or frequency increases the lagged coherence decreases. This observation is consistent with the results obtained based on the Fourier analysis (Harichandran and Vanmarcke 1986; Hao et al. 1989; Zerva 2009; Hong and Liu 2014; Liu and Hong 2016).

Results in Figure 3.6 indicate that the phase angle of coherence varies significantly in time and frequency, especially as frequency increases. However, it seems that for a very short separation and low frequency, the phase angle is nearly zero.



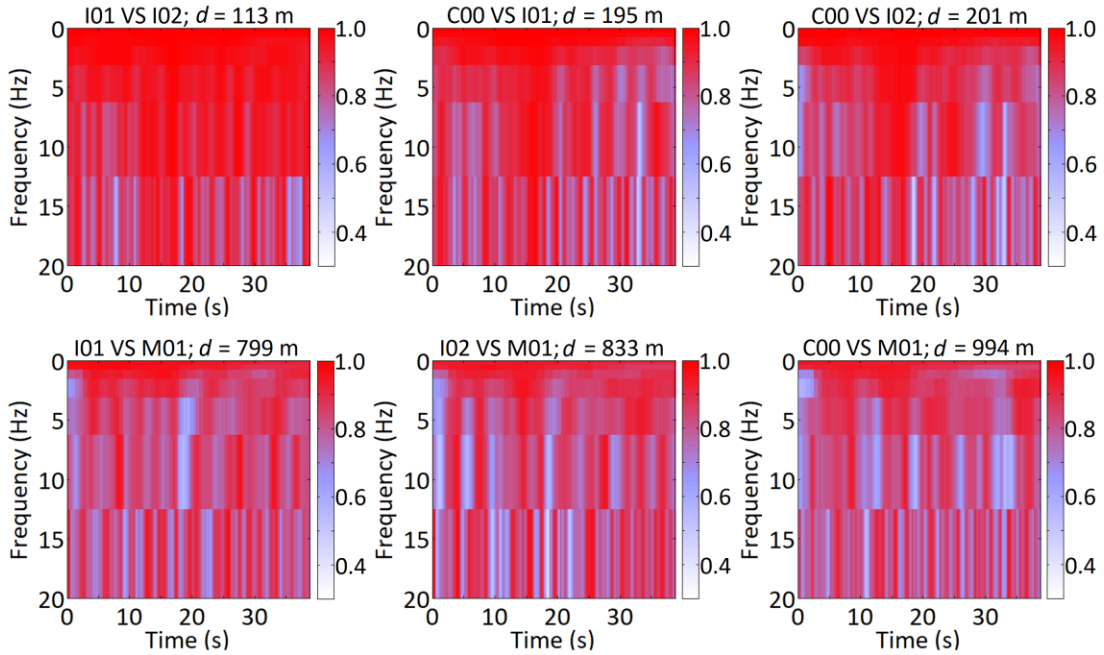


**Figure 3.5:** Estimated lagged coherence (the separation distance ( $d$ ) increases from left to right and from the first row to second row).

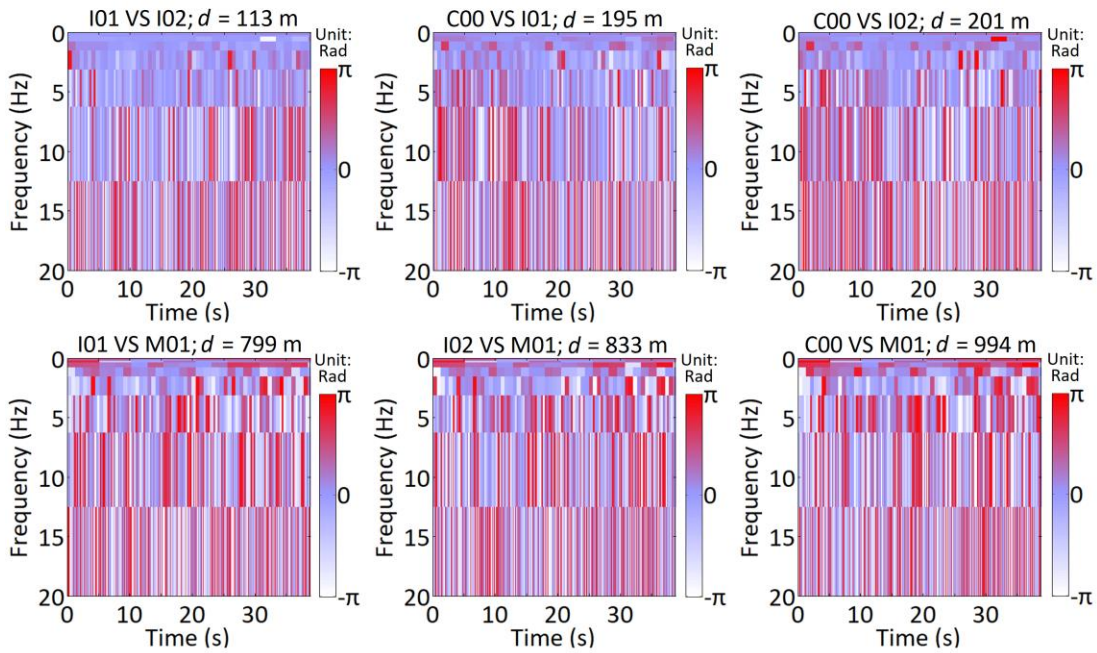


**Figure 3.6:** Estimated phase angle of coherence (the separation distance ( $d$ ) increases from left to right and from the first row to second row).

### 3.5.2 Simulated records for a single site

By using the TFPSD function calculated from Eq. (3-10) for the Record shown in Figure 3.2 as the target TFPSD function, samples of the ground motion records are simulated by using Model-1 shown in Eq. (3-11) and Model-2 in Eq. (3-15). A typical simulated record by using each model is shown in Figure 3.7. These samples resemble well the seed record shown in Figure 3.2. The process of simulating records is repeated 50 times. The DOST coefficients and the response spectrum of the simulated records are calculated. The mean and coefficient of variation (COV) of  $|x_{1,2\sigma}(j)|$  and the response spectra are shown in Figure 3.7 as well. A comparison of the mean of  $|x_{1,2\sigma}(j)|$  to the target presented in Figure 3.2 indicates that they are in very good agreement. The COV is within about 0.5. The plots of the response spectra of the simulated records compared to the response spectrum calculated by using the target record presented in Figure 3.2 indicates that the mean of the former matches well the response spectrum of the target record. A comparison of the results from Model-1 and Model-2 indicates that the performance of these two models is very similar and consistent. The difference in terms of the mean of the TFPSD function of the simulated records by using Model-1 and Model-2 is practically equal to zero. The observed variability from a simulated record to a simulated record is significant as can be observed from the COV of  $|x_{1,2\sigma}(j)|$  and the standard deviation of the response spectra of the simulated records. Such large variability is also observed by using the models based on SRM (Hong and Liu 2014; Liu and Hong 2016).

The analysis carried out for the results presented in Figure 3.7 is repeated by using the  $S(j)$  from the record shown in Figure 3.3 as the target. In this case, the results are presented in Figure 3.8. The observations made from Figure 3.7 are equally applicable to the results presented in Figure 3.8.

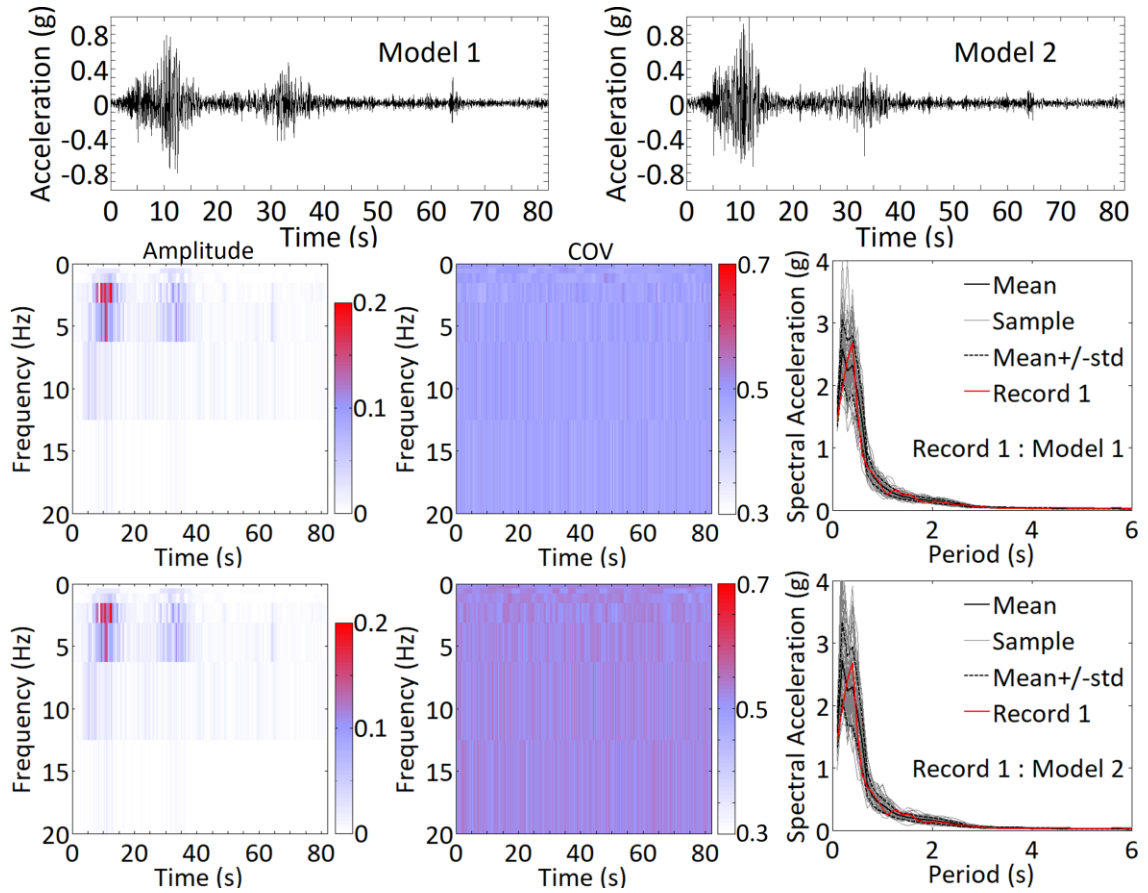


**Figure 3.7:** Illustration of typical simulated records, mean and coefficient of variation of the amplitude of the DOST coefficients and the response spectrum of the simulated records ( $S(j)$  from the Wenchuan earthquake record shown in Figure 3.2 is used as the target). The second and third rows are based on Model-1 and Model-2, respectively.

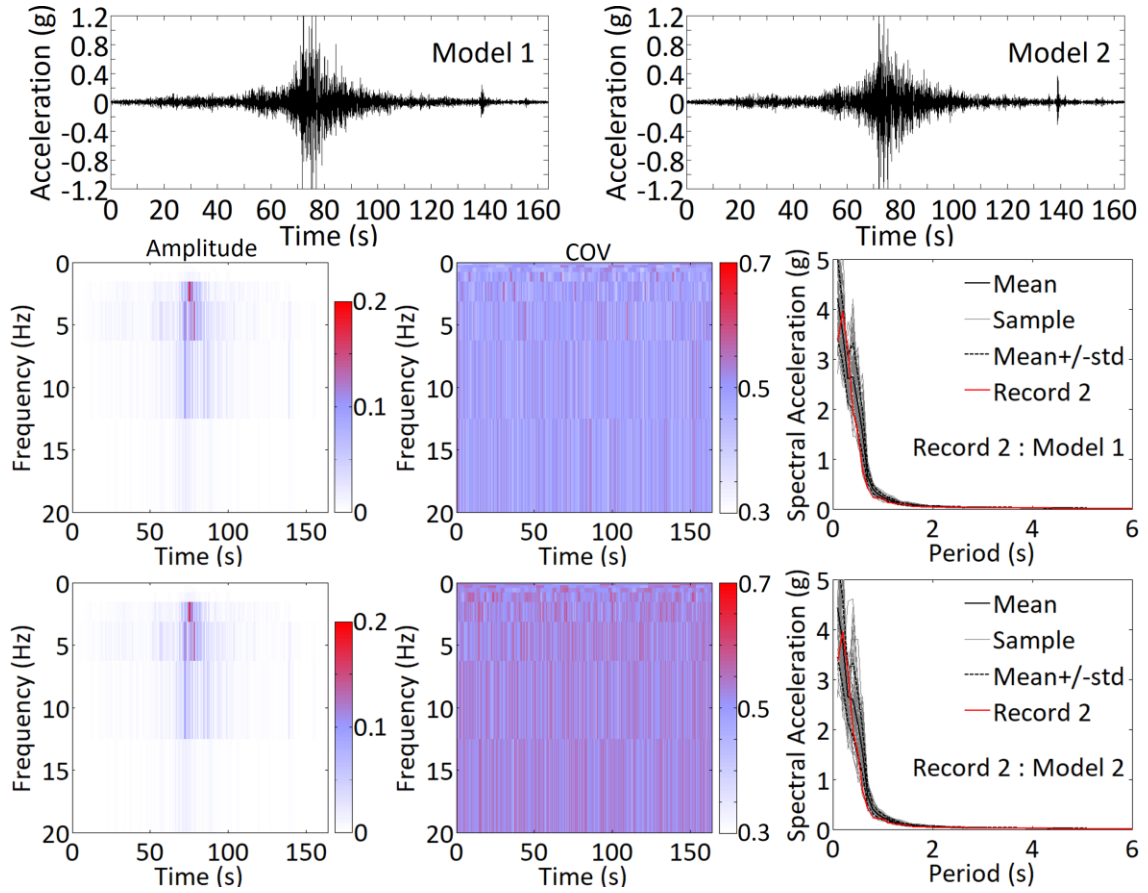


**Figure 3.8:** Illustration of typical simulated records, mean and coefficient of variation (COV) of the amplitude of the DOST coefficients and the response spectrum of the simulated records ( $S(j)$  from Tohoku earthquake record shown in Figure 3.3 is used as the target). The second and third rows are based on Model-1 and Model-2, respectively.

### 3.5.3 Illustration of simulated records for multiple-support

Both the proposed Model-1 and Model-2 for the case of multiple-support (see Eqs. (3-21) and (3-22)) are used to simulate ground motions at multiple-support at site C00, I01, I02 and M01 illustrated in Figure 3.4. By using the TFPSD obtained for Record 3 listed in Table 3.2 (i.e.,  $|x_{1DS}(j)|^2$  where  $|x_{1DS}(j)|$  is already presented in Figure 3.4) as the target TFPSD function and the lagged coherence depicted in Figure 3.5 as the target lagged coherence, two sets of typical simulated records are presented in Figures 3.9. As

can be observed, these records mimic the records presented in Figure 3.4 that are used to obtain the target TFPSD function. By carrying out the simulation 50 times using each model, and carrying out coherence analysis for the simulated records, the obtained means of the lagged coherence are presented in Figure 3.10 if Model-1 is used for simulation and in Figure 3.11 if Model-2 is used for simulation. A comparison of the means shown in Figures 3.10 and 3.11 to the target lagged coherence shown in Figure 3.5 indicates that the former approximates well to the latter in both time and frequency. Such a matching in time and frequency cannot be achieved based on the evolutionary stochastic process and SRM since, according to Priestley and Tong (1973), the lagged coherence of the evolutionary processes are time-independent.

Finally, to illustrate the proposed conditional simulation approach,  $|x_{1,2s}(j)|$  from Records 3 and 4 (i.e., at Site C00 and I01 shown in Figure 3.4) are used as the conditioning coefficients in Eqs. (3-23) to (3-25), and samples of simulated records at Sites I02 and M01 identified in Figure 3.4 are simulated. A typical set of simulated records is illustrated in Figure 3.12, indicating that they resemble well the conditioning samples. To save space, no additional statistics of the simulated records are presented.

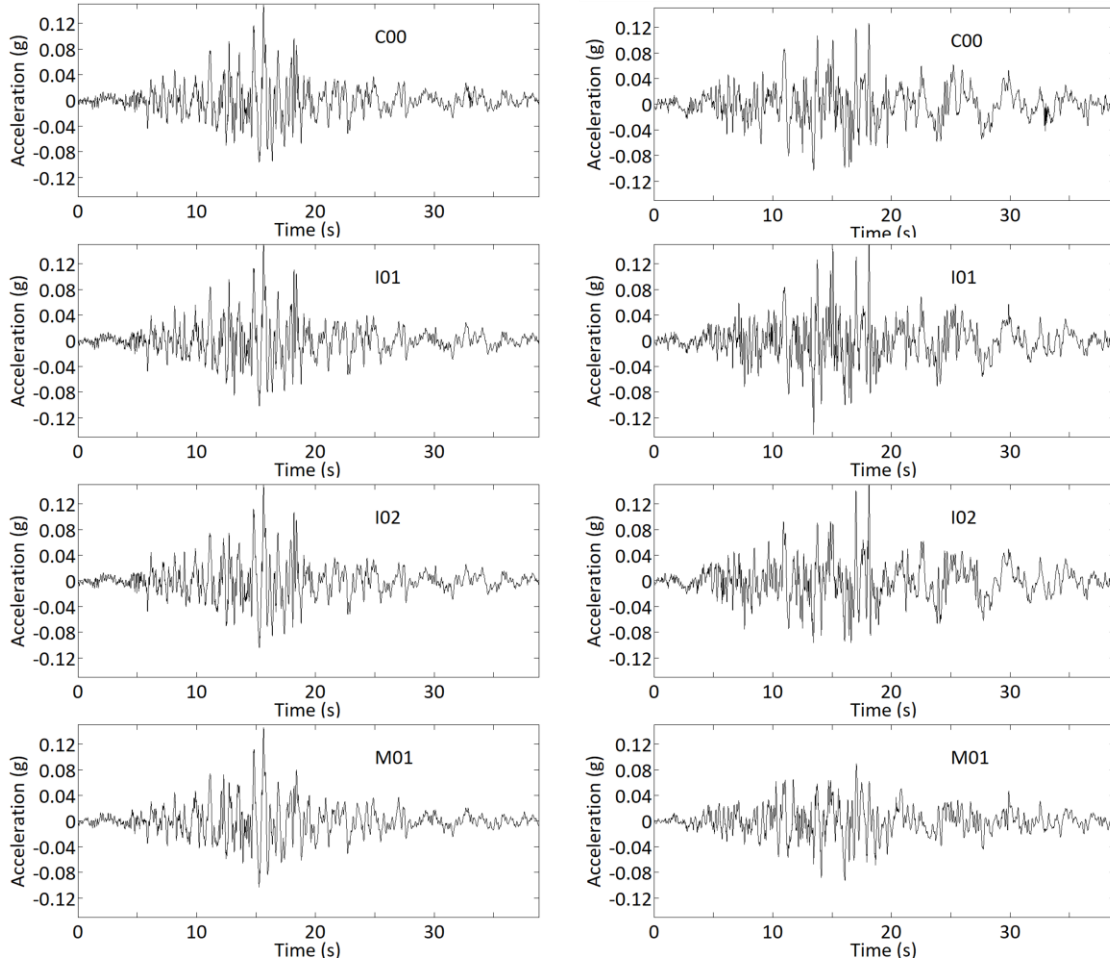


**Figure 3.9:** Typical samples of simulated records by using Model-1 (left panel) and Model-2 (right panel).

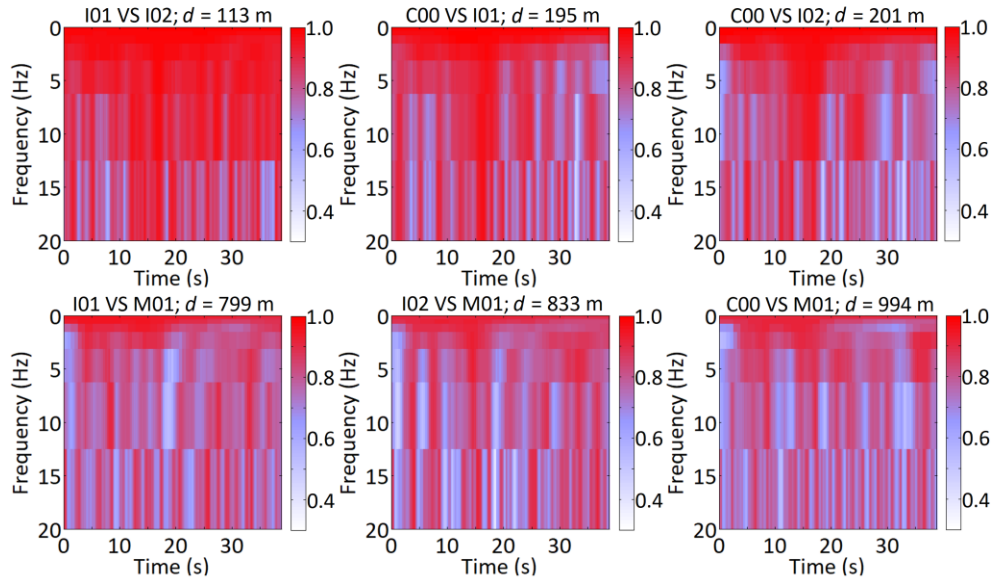


**Figure 3.10:** Average of the lagged coherence calculated from 50 sets of simulated records using Model-1.

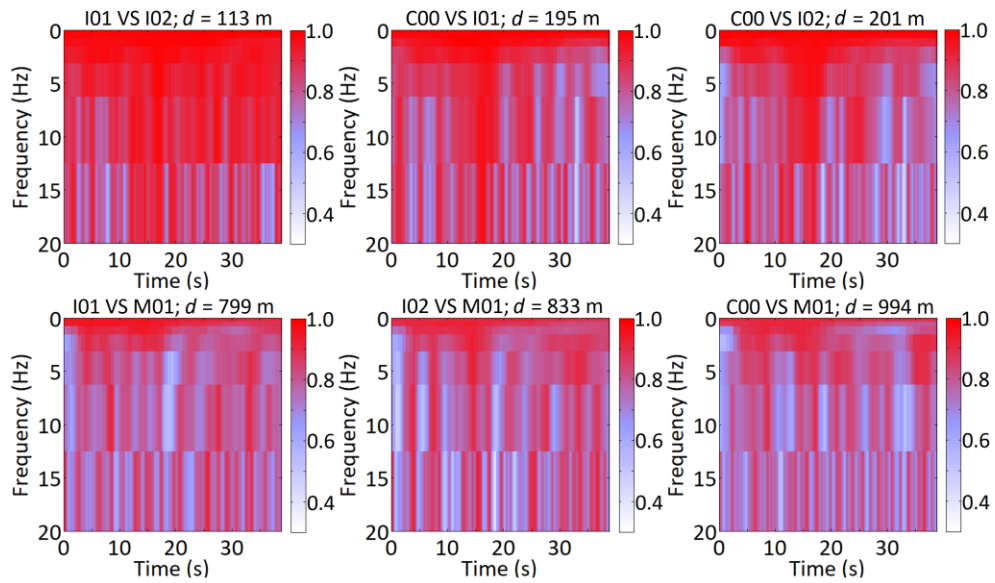


**Figure 3.11:** Average of the lagged coherence calculated from 50 sets of simulated records using Model-2.

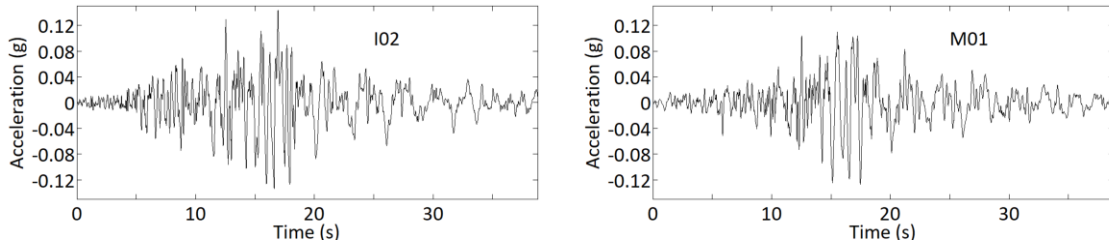


**Figure 3.12:** Typical samples of simulated ground motions at site I02 and M01 conditioned on records at sites C00 and I01 (for the site configuration and the conditioning records see Figure 3.4).

### 3.6 Enhancement for increased fidelity in the time-frequency representation

In this section, an approach to enhance the fidelity of time-frequency representation of the simulated records is proposed. The approach relies on the use of the ST and its inverse, together with the two simulation models described in the previous sections.

The results presented in Figures 3.2 to 3.4 indicate that the time-frequency representation obtained from DOST is relatively coarse because of the use of octave sampling. This problem can be overcome by using ST defined in Eq. (3-1). The general window function  $w(f, \tau - t)$  suggested for the ST is (Stockewell et al. 1996; Pinnegar and Mansinha 2003),

$$w(f, t) = \frac{|f|}{\sqrt{2\pi\kappa}} \exp\left(-\frac{f^2 t^2}{2\kappa^2}\right). \quad (3-26)$$

where  $\kappa$  is a parameter for the time- and frequency-dependent window.



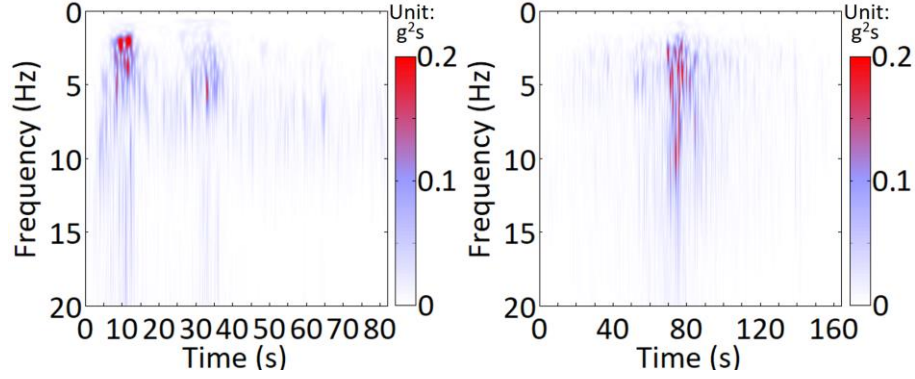


**Figure 3.13:** Amplitude of the ST coefficients,  $|x_s(f, \tau)|$ , by considering Records 1 (left) and Record 2 (right).

By applying  $\kappa = 1$  to Records 1 and 2 listed in Table 3.2, the obtained amplitude of the ST coefficients is presented in Figure 3.13. The results indicate that they provide time-frequency representation with higher fidelity than those shown in Figures 3.2 and 3.3 that are obtained from DOST. Therefore, it is of interest to develop models such that the expectation of the TFPSD function of the simulated records equal to the two-sided target TFPSD function that can be obtained by using ST for nonstationary stochastic processes of interest. To achieve this objective, first, note that the target TFPSD function, denoted as  $S_T(f, \tau) = |x_{TS}(f, \tau)|^2 / (D_\kappa |f|)$ , with the corresponding amplitude of the ST coefficients  $|x_{TS}(f, \tau)|$ , could be assigned based on the TFPSD function calculated from a seed record or the statistics of the TFPSD function from a set of records, and by ensuring the energy preservation, where  $D_k$  is the energy preserving constant (Hong 2020). By partitioning the time-frequency domain according to DOST (see Table 3.1),  $S_T(f, \tau)$  within each partition is then integrated and used as the modified target TFPSD function  $S_T(j)$ , where  $j$  is defined according to Table 3.1.

Using  $S_T(j)$  as the target TFPSD function, simulation of the nonstationary stochastic processes can be carried out by using Model-1 or Model-2 (i.e., Eq. (11) or (15)). Based

on the derivations and numerical results given in the previous section and in Appendix A, it is clear that the mean of the TFPSD function of the simulated records obtained by using DOST equals its target but differs from  $S_T(f, \tau)$ . Several options to enhance the time-frequency fidelity of the simulated records could be explored to reduce such a difference. For example, as Option-A, one could apply ST to the simulated  $i$ -th record,  $x_i(t_k)$ , leading to  $x_{iS}(f, \tau)$  and its corresponding  $S_i(f, \tau) = |x_{iS}(f, \tau)|^2 / (D_\kappa |f|)$ . By simulating a number of records  $x_i(t_k)$ , the average of  $S_i(f, \tau)$  of the simulated records,  $S_{ES}(f, \tau)$ , can be evaluated. By scaling  $x_{iS}(f, \tau)$  using  $\sqrt{S_T(f, \tau) / S_{ES}(f, \tau)}$  and using the scaled value in Eq. (3-2), the enhanced  $i$ -th simulated record is obtained. A flowchart illustrating this procedure is depicted in Figure 3.14. This can be expressed in the following mathematical form,

$$x(t_k) = IST \left[ \sqrt{S_T(f, \tau) / S_{ES}(f, \tau)} \square ST(x_i(t_k) \text{ from Eq. (11) or Eq. (15)}) \right], \quad (3-27)$$

where  $\square$  denotes the point by point multiplication in  $f$ - $\tau$  domain, and  $ST$  and  $IST$  denote the ST and inverse ST. As Option-B, one may iteratively apply Option-A such that the time-frequency representation of the (finally) simulated record is within a specified tolerance of the target TFPSD function.

To illustrate the adequacy of using Option-A to simulate records, consider that the target TFPSD can be assigned based on those obtained from Record 1 or Record 2, where the amplitude of the ST coefficients of these two records is already shown in Figure 3.13. Using the target TFPSD function and considering the time-frequency partition according to DOST,  $S_T(j)$  is calculated and shown in Figure 3.13. Following the flowchart depicted in Figure 3.14 (i.e., Eq. (3-27)), records are simulated. Typical sampled records, the means of the amplitude of ST coefficients of simulated records, and response spectra of the simulated records are also presented in Figure 3.15 by considering both Model-1 and Model-2. The match to the response spectrum of Record 1 and Record 2 is improved as compared to those shown in Figures 3.7 and 3.8. Most importantly, the average time-frequency representation of the simulated records shown in Figure 3.15 agrees well with their corresponding target shown in Figure 3.13.

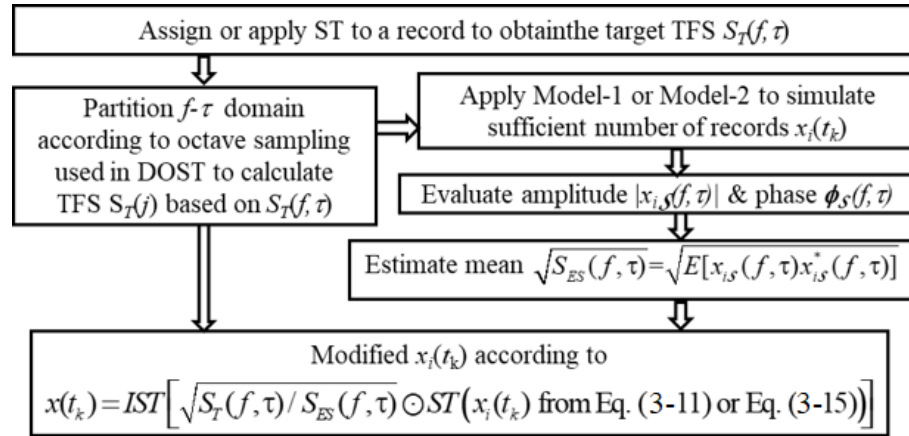


**Figure 3.14:** Flowchart to simulate ground motions at a site for given target TFPSD function obtained based on ST.

A final point that deserves discussion is whether the simulated records following the flowchart shown in Figure 3.14 is Gaussian. As mentioned earlier, the direct use of Model-1 and Model-2 results in the simulated records to be Gaussian. However, after adjustment according to Eq. (3-27), it is unknown if such property still holds since the theoretical proof is unavailable at present. However, by collecting the samples, at selected times, of simulated records corresponding to the numerical analysis carried out for Figure 3.15, their empirical probability distributions are plotted on the normal probability in Figure 3.16. The plots suggest that the samples could be considered as Gaussian.

Although the possible extensions similar to Option-A to simulate ground motions at multiple-support and the assessment of the adequacy of using Option-B are of interest, they are left for a future investigation.

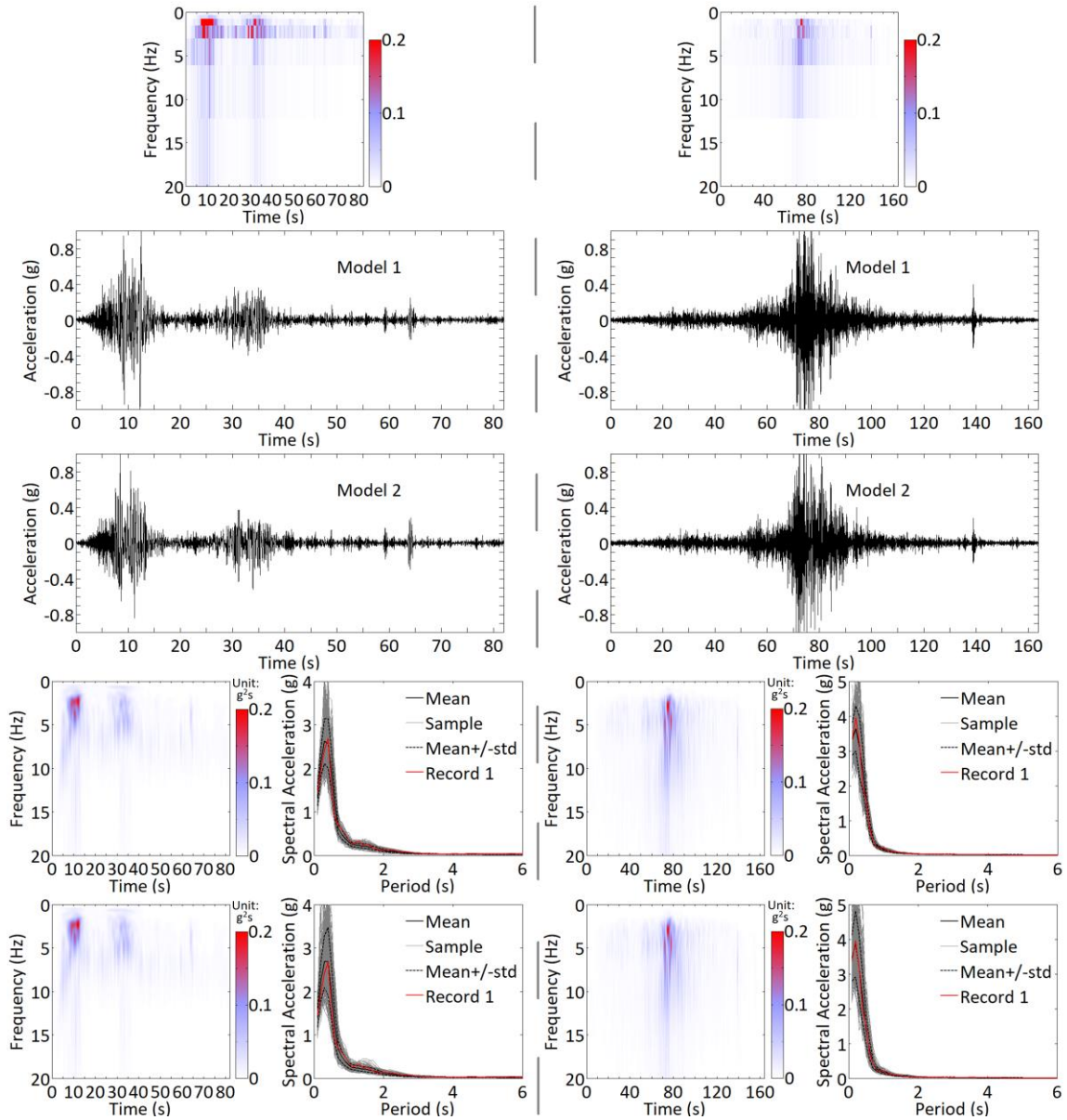


**Figure 3.15:** Calculated  $S_T(j)$ , typical sampled records, mean of amplitude of ST coefficients, and response spectrum of simulated records according to Option-A. The left and right panels are by considering Records 1 and 2, respectively.

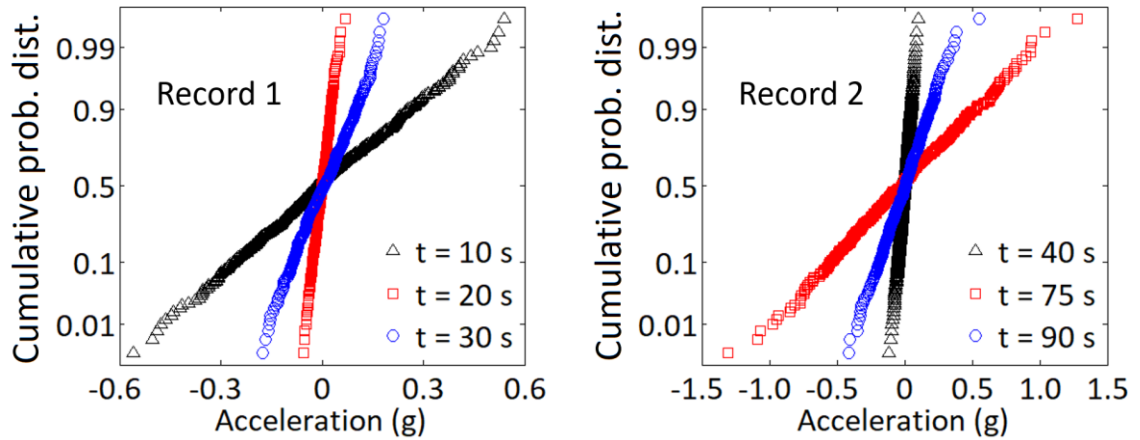


**Figure 3.16:** Empirical probability distributions of simulated samples at several selected times presented on the normal probability paper.

### 3.7 Conclusion

Two new time-frequency spectral representation models to simulate ground motions at single or multiple sites are proposed. The models are developed based on time-frequency representation obtained from the discrete orthonormal S-transform. They consider time-frequency dependent coherence and can be easily understood by drawing the parallel of the proposed models to those well-known models developed based on the (Fourier) spectral representation method. The models explicitly consider amplitude modulation and frequency modulation functions that are embedded in the time-frequency spectral representation. One of the models explicitly emphasizes the role of the random phase angle in modeling the nonstationary stochastic processes while the other brings out explicitly the uncertainty in the processes through the random amplitudes associated with the real and imaginary parts of the orthonormal basis functions. The formulation to conditionally simulate multi-support seismic ground motions is also given based on the proposed model with uncertain amplitudes. As can be observed from the formulation of the proposed models, their use is no more sophisticated or difficult than that of the models based on the well-known spectral representation method.

Numerical analysis carried out by using the proposed model indicates that the models can be successfully implemented to simulate nonstationary ground motions for a given target TFPSD function. Overall, the average time-frequency representation and response spectrum of the simulated records are in agreement with those of the targets.

A drawback of using the DOST is that the time-frequency resolution obtained from DOST is coarser than that obtained by using the S-transform. An enhancement of the proposed models to simulate ground motions at a site by incorporating the information obtained from the S-transform is also presented (see Eq. (3-27)). Numerical results indicate that such an extension could improve the simulated records to match the target response spectrum.

### 3.8 Data availability statement

The records shown in Table 3.2 are extracted from <http://www.csmnc.net>; <http://www.kyoshin.bosai.go.jp> and the Data Management Center for Strong Motion Seismology of the Institute of Earth Science (IES), Taiwan.

### Reference

- Alamilla, J., Esteva, L., Garcia-Perez, J., and Diaz-Lopez, O. (2001). "Evolutionary properties of stochastic models of earthquake accelerograms: Their dependence on magnitude and distance." *J. Seismol.*, 5(1), 1-21.
- Anderson, T. W. (2003). *An Introduction to Multivariate Statistical Analysis*, Wiley, Chichester, U.K.
- Basu, B., and Gupta, V. K. (1998). "Seismic response of SDOF systems by wavelet modeling of nonstationary processes." *J. Eng. Mech.*, 124(10), 1142-1150.
- Battisti, U., and Riba, L. (2016). "Window-dependent bases for efficient representations of the Stockwell transform." *Applied and Computational Harmonic Analysis.*, 40(2), 292-320.
- Chen, J., Song, Y., Peng, Y., and Spanos, P. D. (2018). "Simulation of homogeneous fluctuating wind field in two spatial dimensions via a joint wave number–frequency power spectrum." *J. Eng. Mech.* 144(11), 04018100.
- Clough, R. W., and Penzien, J. (2003). *Dynamics of Structures*, Computers and Structures, Inc., Berkeley, Calif.
- Cohen, L. (1995). *Time-frequency analysis*, Prentice-Hall, New Jersey, U.S.

- Conte, J. P., and Peng, B. F. (1997). "Fully nonstationary analytical earthquake ground-motion model." *J. Eng. Mech.* 123(1), 15-24.
- Daubechies, I. (1992). *Ten lectures on wavelets*, Siam, Philadelphia, U.S.
- Der Kiureghian A. (1996). "A coherency model for spatially varying ground motions." *Earthquake Eng. Struct. Dynam.*, 25(1), 99-111.
- Grigoriu, M., Ruiz, S. E., and Rosenblueth, E. (1988). "The Mexico earthquake of September 19, 1985—Nonstationary models of seismic ground acceleration." *Earthquake Spectra*, 4(3), 551-568.
- Gurley, K., and Kareem, A. (1999). "Applications of wavelet transforms in earthquake, wind and ocean engineering." *Eng. Struct.*, 21(2), 149-167.
- Hancock, J., Watson-Lamprey, J., Abrahamson, N. A., Bommer, J. J., Markatis, A., McCoy, E., and Mendis, R. (2006). "An improved method of matching response spectra of recorded earthquake ground motion using wavelets." *J. of Earthq. Eng.*, 10(spec01), 67-89.
- Hao, H., Oliveira, C. S., and Penzien, J. (1989). "Multiple-station ground motion processing and simulation based on SMART-1 array data." *Nucl. Eng. Des.*, 111(3), 293-310.
- Harichandran, R. S., and Vanmarcke, E. H. (1986). "Stochastic variation of earthquake ground motion in space and time." *J. Eng. Mech.*, 112(2), 154-174.
- Hong, H.P. (2020) Response and first passage probability of linear elastic SDOF systems subjected to nonstationary stochastic excitation modeled through S-Transform, Report to BLWT-1-2020, Boundary Layer Wind Tunnel Laboratory, the University of Western Ontario.
- Hong, H. P., and Liu, T. J., (2014). "Assessment of coherency for bidirectional horizontal ground motions and its application for simulating records at multiple stations." *Bull. Seismol. Soc. Am.*, 104(5), 2491-2502.
- Huang, N. E., and Wu, Z. (2008). "A review on Hilbert-Huang transform: Method and its applications to geophysical studies." *Rev. Geophys.*, 46(2), 1-23.
- Iyama, J., and Kuwamura, H. (1999). "Application of wavelets to analysis and simulation of earthquake motions." *Earthquake Eng. Struct. Dynam.*, 28(3), 255-272.
- Kameda, H., and Morikawa, H. (1994). "Conditioned stochastic processes for conditional random fields." *J. Eng. Mech.*, 120(4), 855-875.
- Liang, J., Chaudhuri, S. R., and Shinozuka, M. (2007). "Simulation of nonstationary stochastic processes by spectral representation." *J. Eng. Mech.*, 133(6), 616-627.
- Liu, T. J., and Hong, H. P. (2016). "Assessment of spatial coherency using tri-directional ground motions." *J. Earthquake Eng.*, 20(5), 773-794.
- Newmark, N.M., and Rosenblueth, E. (1971). *Fundamentals of Earthquake Engineering*, Prentice-Hall, Englewood Cliffs, N.J.
- Ochi, M. K. (2005). *Ocean waves: the stochastic approach*, Cambridge University Press, Cambridge, U.K.

- Percival, D. B., and Walden, A. T. (2000). *Wavelet Methods for Time Series Analysis*. Cambridge University Press.
- Pinnegar, C. R., and Mansinha, L. (2003). "The S-transform with windows of arbitrary and varying shape." *Geophysics*, 68(1), 381-385.
- Priestley, M. B. (1965). "Evolutionary spectra and non-stationary processes." *J. R. Stat Soc B.*, 27, 204-37.
- Priestley, M. B. (1981). *Spectral analysis and time series*, New York: Academic, New York, U.S.
- Priestley, M. B., and Tong, H. (1973). "On the analysis of bivariate non-stationary processes." *J. Roy. Stat. Soc. B.*, 35(2), 153-166.
- Shinozuka, M., and Deodatis, G. (1991). "Simulation of stochastic processes by spectral representation." *Appl. Mech. Rev.*, 44(4), 191-204.
- Shinozuka, M., and Jan, C. M. (1972). "Digital simulation of random processes and its applications." *J. Sound Vib.*, 25(1), 111-128.
- Simiu E., and Scanlan R H. (1996). *Wind effects on Structures: fundamentals and applications to design. Third edition*, JohnWiley & Sons, Inc., NewYork, U.S.
- Spanos, Pol D., and Failla, G. (2004). "Evolutionary spectra estimation using wavelets." *J. Eng. Mech.*, 130(8), 952-960.
- Stockwell, R. G. (2007). "A basis for efficient representation of the S-transform. " *Digit. Signal Process.*, 17(1), 371-393.
- Stockwell, R. G., Mansinha, L., and Lowe, R. P. (1996). "Localization of the complex spectrum: the S transform." *IEEE Trans. Signal Process.*, 44(4), 998-1001.
- Torrence, C., and Compo, G.P. (1998). "A practical guide to wavelet analysis." *Bull. Seismol. Soc. Am.*, 79(1), 61-78.
- Wang, Y., and Orchard, J. (2009). "Fast discrete orthonormal Stockwell transform." *SIAM J. Sci. Comput.*, 31(5), 4000-4012.
- Wen, Y. K., and Gu, P. (2004). "Description and simulation of nonstationary processes based on Hilbert spectra." *J. Eng. Mech.*, 130(8), 942-951.
- Yamamoto, Y., and Baker, J. W. (2013). "Stochastic model for earthquake ground motion using wavelet packets." *Bull. Seismol. Soc. Am.*, 103(6), 3044-3056.
- Yan, Y., & Zhu, H. (2011). "The generalization of discrete stockwell transforms." In 2011 19th IEEE. Eur. Signal Pr. Conf. IEEE., 1209-1213.
- Yeh, C. H., and Wen, Y. K. (1990). "Modeling of nonstationary ground motion and analysis of inelastic structural response." *Struct. Safety*, 8(1-4), 281-298.
- Zerva, A. (2009). *Spatial variation of seismic ground motion. Modeling and engineering applications*, " CRC Press, Florida, U.S.



## Chapter 4

### 4 A time-frequency representation model for seismic ground motions

#### 4.1 Introduction

Reliability analysis and risk modelling of structures subjected to seismic loading require the use of a large number of ground motions with various specific seismic scenarios. As the number of historical ground motion records are limited and cannot always match the given scenarios, simulated ground motion records are used. For the simulation, the ground motion is treated as a nonstationary stochastic process. A popular stochastic model is based on the evolutionary theory (Priestley 1965), assuming that the nonstationary stochastic process can be obtained by applying a slowly-varying amplitude modulation function to a stationary stochastic process defined by a power spectral density (PSD) function. A process modeled in such a manner is characterized by the evolutionary PSD (EPSD) function that is a function of the amplitude modulation function. A realization of the evolutionary stochastic process can be simulated using the spectral representation method (SRM) (Shinozuka and Jan 1972; Shinozuka and Deodatis 1991; Liang et al. 2007). Models of the EPSD function that depends on the seismic source and site characteristics were developed in Sabetta and Pugliese (1996) and Pousse et al. (2006). For the assessment of the EPSD function, they used the short-time Fourier transform (STFT), as suggested by Priestley (1965). A well-known drawback of STFT is that its application is associated with energy leakage. A narrow-width window results in a better resolution in the time domain but a reduced resolution in the frequency domain, and vice versa (Cohen 1995). In addition, STFT could provide good time resolution at high frequency or good frequency resolution at low frequency but not both since it uses fixed window length.

Yeh and Wen (1990) (Grigoriou et al. 1988) applied the time transformation to take into account potential time-varying frequency, resulting in the ground motion record that is characterized by a time-frequency dependent PSD function, which should not be treated as a time and frequency dependent amplitude modulation function in the context

of SRM. This was illustrated in Hong (2016) for the amplitude and frequency modulated nonstationary process. Modelling of ground motions with time transformation was also considered in Alamilla et al. (2001), and a set of model parameters for the power spectral density (PSD) function and for time transformation was developed based on Mexican ground motions. These parameters are functions of magnitude and epicentral distance. Other models used to model and simulate the nonstationary stochastic ground motions with time-varying amplitude and frequency include the use of superposition of multiple evolutionary processes (Conte and Peng 1997; Vlachos et al. 2018), the application of wavelet packet transform (Yamamoto and Baker 2013), the use of a modulated, and filtered white noise (MFW) process with the time- and frequency-varying characteristics of the filter (Rezaeian and Der Kiureghian 2010), and the use of the time-frequency spectral representation method (TFSRM) (Cui and Hong 2020; Hong and Cui 2020) which is based on the combined use of the S-transform (ST) and discrete orthonormal S-transform (DOST) (Stockwell et al. 1996; Pinnegar and Mansinha 2003; Stockwell 2007).

If the ground motions are represented by the superposition of multiple evolutionary processes, the number of parameters for the model increases as the number of the evolutionary processes increases. For example, the model reported in Vlachos et al. (2018) involves 18 model parameters. The use of the wavelet package transform, which provides a time-scale representation, overcomes the coarse time-scale representation obtained from the discrete wavelet transform. However, it is still a discrete representation. The model proposed in Yamamoto and Baker consists of 13 model parameters. The MFW model is very adaptive, and the identification of the model parameters can be carried out directly in the time domain. However, the selection of the time-varying functional forms for the filter is not a straightforward task for practical applications. Simplifying assumptions, such as that the time-varying frequency of the filter is a linear function of time and the damping ratio for the filter can be considered as constant, may be assumed to reduce the number of required model parameters (Rezaeian and Der Kiureghian 2010). The combined use of ST and DOST to model and simulate the nonstationary stochastic process is a new technique; it takes advantage of the high fidelity of time-frequency representation of ST and the orthogonal property of the basis

functions in DOST. However, the development of a model of the TFPSD function based on ST for the scenario seismic events has not been reported.

ST is viewed as a hybrid of continuous wavelet transform and STFT (Stockwell et al. 1996; Pinnegar and Mansinha 2003). It combines the good features of STFT and continuous wavelet transform; it can be interpreted as an STFT but with a frequency-dependent sliding window or as a phase-corrected continuous wavelet transform. It provides the time and frequency representation with the phase angle that has the interpretation consistent with the Fourier transform. The use of ST leads to both good time resolution at high frequency and good frequency resolution at low frequency. DOST is an efficient transform that localizes the spectrum and retains the advantageous phase properties of the S-transform (Stockwell 2007). Both ST and DOST are widely used for signal and image processing.

In this study, a model for the TFPSD function for scenario seismic events and site conditions is proposed. The proposed model requires 10 model parameters, where the regression equations for the model parameters are obtained by considering both the inter- and intra-event variability. The proposed model is developed based on 1504 historical records. In the next sections, a brief description of ST and DOST is given, and the newly developed simulation model based on ST and DOST is summarized. The criteria used to select records and the characteristics of the selected records used to develop the model are given, and the procedure used to assess the model parameters as well as the resulting model parameters are then presented. This is followed by an illustration of using the proposed model to simulate ground motions and by a comparison of the pseudo-spectral acceleration obtained from the simulated ground motions obtained using the proposed model to that predicted by using several ground-motion models (GMMs) from NGA-West2 (Ancheta et al. 2014) and to that of the considered actual records used in this study.

## 4.2 Time-frequency representation and simulation of ground motions using S-transform and discrete orthonormal S-transform

### 4.2.1 Time-frequency representation using S-transform

Given the ground motion record component  $x(t)$ , the ST application of ST (Stockwell et al. 1996) results in,

$$x_s(f, \tau) = ST(x(t)) = \int_{-\infty}^{\infty} x(t)w(f, \tau-t)e^{-i2\pi ft} dt, \quad (4-1)$$

where  $ST(\cdot)$  denotes the S-transform,  $i = \sqrt{-1}$ ,  $x_s(f, \tau)$  denotes the ST coefficient of  $x(t)$ , providing a time-frequency representation;  $f$  and  $\tau$  are the frequency and time similar in the Fourier transform; and  $\tau$  is the center of the window function  $w(f, \tau-t)$  defined by,

$$w(f, \tau-t) = \frac{|f|}{\sqrt{2\pi\kappa}} \exp\left(-\frac{f^2(\tau-t)^2}{2\kappa^2}\right), \quad (4-2)$$

in which  $\kappa$  is a parameter for the transformation and can be taken equal to one. The inverse ST (IST), denotes as  $IST(\cdot)$ , can be expressed as,

$$x(t) = IST(x_s(f, \tau)) = \int_{-\infty}^{\infty} \left[ \int_{-\infty}^{\infty} x_s(f, \tau) d\tau \right] e^{i2\pi ft} df. \quad (4-3)$$

For computational efficiency, the discrete version of Eqs. (4-1) and (4-3) for discretized  $x(t)$  sampled with sampling interval  $\Delta T$ , can be expressed as (Yan and Zhu 2011; Battisti and Riba 2016),

$$x_s(f_p, \tau_q) = \sum_{j=0}^{N-1} \exp\left(-\frac{2\pi^2 f_j^2 \kappa^2}{f_p^2}\right) \hat{x}(f_{j+p}) e^{i2\pi f_j \tau_q}, \quad (4-4)$$

and,

$$x(t_j) = IFFT_{f_p} \left( \sum_q x_S(f_p, \tau_q) \right), \quad (4-5)$$

where  $\hat{x}(f_p) = \sum_{j=0}^{N-1} x(t_j) e^{-i2\pi f_p t_j}$  or  $\hat{x}(f_p) = FFT_{t_j} (x(t_j))$  is the Fourier coefficient of  $x(t)$ ;  $t_j = j\Delta_T$  ;  $f_p = p / (N\Delta_T)$  ;  $p = 0, 1, \dots, N-1$  ;  $\tau_q = q\Delta_T$  ;  $q = 0, 1, \dots, N-1$  ;  $x_S(f_p, \tau_q) = IFFT_{f_j} \left( N\hat{x}(f_{p+j}) \exp(-2\pi^2 f_j^2 \kappa^2 / f_p^2) \right)$ ; and  $FFT()$  and  $IFFT()$  denote the FFT and the inverse FFT of its argument.

The single-sided TFPSD function of  $x(t)$  can be defined as (Hong and Cui 2019; Hong 2020),

$$S_{S_x}(f, \tau) = 2 \frac{x_S(f, \tau) x_S^*(f, \tau)}{D_\kappa f}, \quad f \geq 0, \quad (4-6)$$

where  $D_\kappa = \int_{-\infty}^{\infty} \exp(-(2\pi\kappa(\zeta-1))^2) \frac{d\zeta}{|\zeta|}$  is a constant that can be evaluated numerically and is well approximated by  $1/\sqrt{4\pi\kappa^2}$  (its use leads to a relative error less than 1.4% for  $\kappa = 1$  since the numerical integration leads to a value of 0.286); the superscript \* denotes the complex conjugate. Throughout the present study,  $\kappa = 1$  is considered. The use of Eq. (4-6) ensures the energy conservation, that is,

$$E_T = \int_0^T x^2(t) dt = \int_0^\infty \left[ \int_0^T S_{S_x}(f, \tau) d\tau \right] df \quad (4-7)$$

where  $E_T$  denotes the total energy and  $T$  is the duration of  $x(t)$ . It must be emphasized that  $x_S(f, \tau) x_S^*(f, \tau)$  must not be treated as the amplitude modulation function in the context of SRM since the use of  $x_S(f, \tau) x_S^*(f, \tau)$  is not energy preserving. Although  $S_{S_x}(f, \tau)$  could be used in SRM, however, in such a case, it cannot be used to simulate the time-dependent incoherent ground motions at multiple sites - a point that was already extensively discussed in Hong and Cui (2020). For this reason and to maintain the

consistency of using ST, TFSRM (Cui and Hong 2020; Hong and Cui 2020) rather than SRM is to be used to simulate ground motions for a given  $S_{S_x}(f, \tau)$  in the following.

An illustration of the ST coefficients, TFPSD function, and  $E_T$  for a record component (E-W component recorded at Tarzana - Cedar Hill in the 1992 Landers earthquake) shown in Figure 4.1 is given in the same figure. As can be observed from the figure, ST can be used to characterize complex ground motions in the time and frequency domain. In the same figure, the time histories of the displacement and velocity corresponding to the actual ground acceleration record are presented.

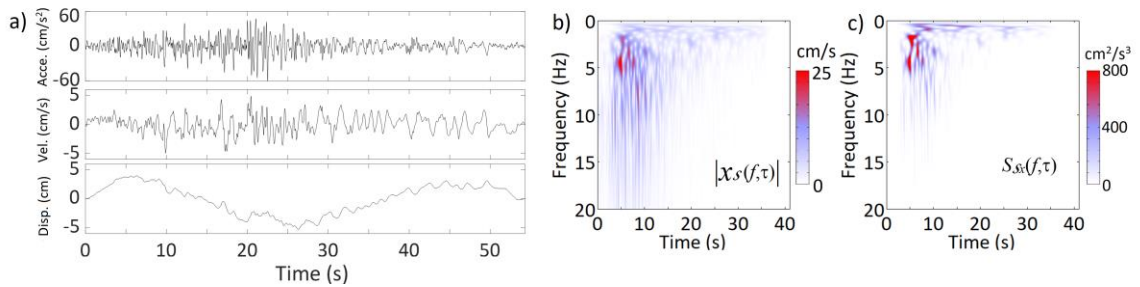


**Figure 4.1.** a) The actual record and its corresponding velocity and displacement time histories; b) the amplitude of ST coefficients of the record; c) the TFPSD of the record.

## 4.2.2 Simulation model and algorithm

Since ST, similar to the continuous wavelet transform, provides an inefficient redundant representation, a simple and efficient model by directly using IST to simulate ground motions for a given TFPSD function is unavailable. However, by taking advantage of the orthogonal basis in discrete orthonormal S transform (DOST) (Stockwell 2007), the procedure to simulate the records based on TFSRM (Cui and Hong 2020; Hong and Cui 2019) for a given target TFPSD function are shown in Figure 4.2. More specifically, the steps are as follows:

- a) Discretize the time-frequency space of the TFPSD function in cells according to the time and frequency localization of DOST. The indices  $p$  and  $q$  for the center of a frequency band  $f_p = p/(N\Delta)$ , and the time localization  $t_q = q\Delta$ , are selected based on octave sampling (Stockwell 2007), where for the octave number  $m$ ,

$$(p; q; \beta) = \begin{cases} (0; 0; 1), & \text{for } m = 0 \\ (1; 0; 1), & \text{for } m = 1 \\ (2^{m-1} + 2^{m-2}; 0, 1, \dots, 2^{m-1} - 1; 2^{m-1}), & \text{for } m = 2, \dots, \log_2(N) - 1 \end{cases}, \quad (4-8)$$

where  $\beta$  indicates the width of the frequency band centred at the frequency indexed by  $p$ . An illustration of using the calculated  $S_{S_x}(f, \tau)$  presented in Figure 4.1 as the target TFPSD function to evaluate  $S_{\mathcal{D}S_x}(f_p, \tau_p)$  is presented in Panels a) and b) in Figure 4.2

- b) Let  $S_{\mathcal{D}S_x}(f_p, \tau_p)$  denote the integral of  $S_{S_x}(f, \tau)$  for the  $(p, q)$ -th cell, and sample  $N_T$  records according to,

$$x_j(t_k) = \sqrt{2} \sum_{\text{all } (p,q)} \sqrt{S_{\mathcal{D}S_x}(f_p, \tau_p)} \operatorname{Re} \left[ D_{[\beta]}(t_k; f_p, \tau_p) e^{i\theta(p,q)} \right], \quad k = 0, \dots, N-1, \quad (4-9)$$

where  $x_j(t_k)$ ,  $j = 1, \dots, N_T$ , denotes the  $j$ -th simulated record,  $\theta(p, q)$  are independent and uniformly distributed between 0 to  $2\pi$ , and

$$D_{[\beta]}(t_k; f_p, \tau_p) = \frac{ie^{-i\pi q} \{e^{-i2\pi(k/N-q/\beta)(p-\beta/2-1/2)} - e^{-i2\pi(k/N-q/\beta)(p+\beta/2-1/2)}\}}{\sqrt{\beta} 2 \sin[\pi(k/N - q/\beta)]}, \quad (4-10)$$

are the orthonormal basis functions for DOST. An illustration of the simulated record, according to Eq. (4-9), is presented in Panel c) in Figure 4.2 by considering  $N_T = 100$ .

- c) As DOST provides a relatively coarse time-frequency representation, the  $j$ -th simulated record is adjusted for increased fidelity using,

$$x_j(t_k) = IST \left[ \sqrt{S_{S_x}(|f|, \tau) / S_{ES}(|f|, \tau)} \square ST(x_j(t_k) \text{ from Eq. (9)}) \right], \quad (4-11)$$

where  $\square$  denotes the point by point multiplication in the  $f$ - $\tau$  domain and  $S_{ES}(f, \tau)$  represents the average of the TFPSD function of the  $N_T$  simulated records in Step b). For illustration purposes, the adjusted record, according to Eq. (4-11), is depicted in Panel d) in Figure 4.2.

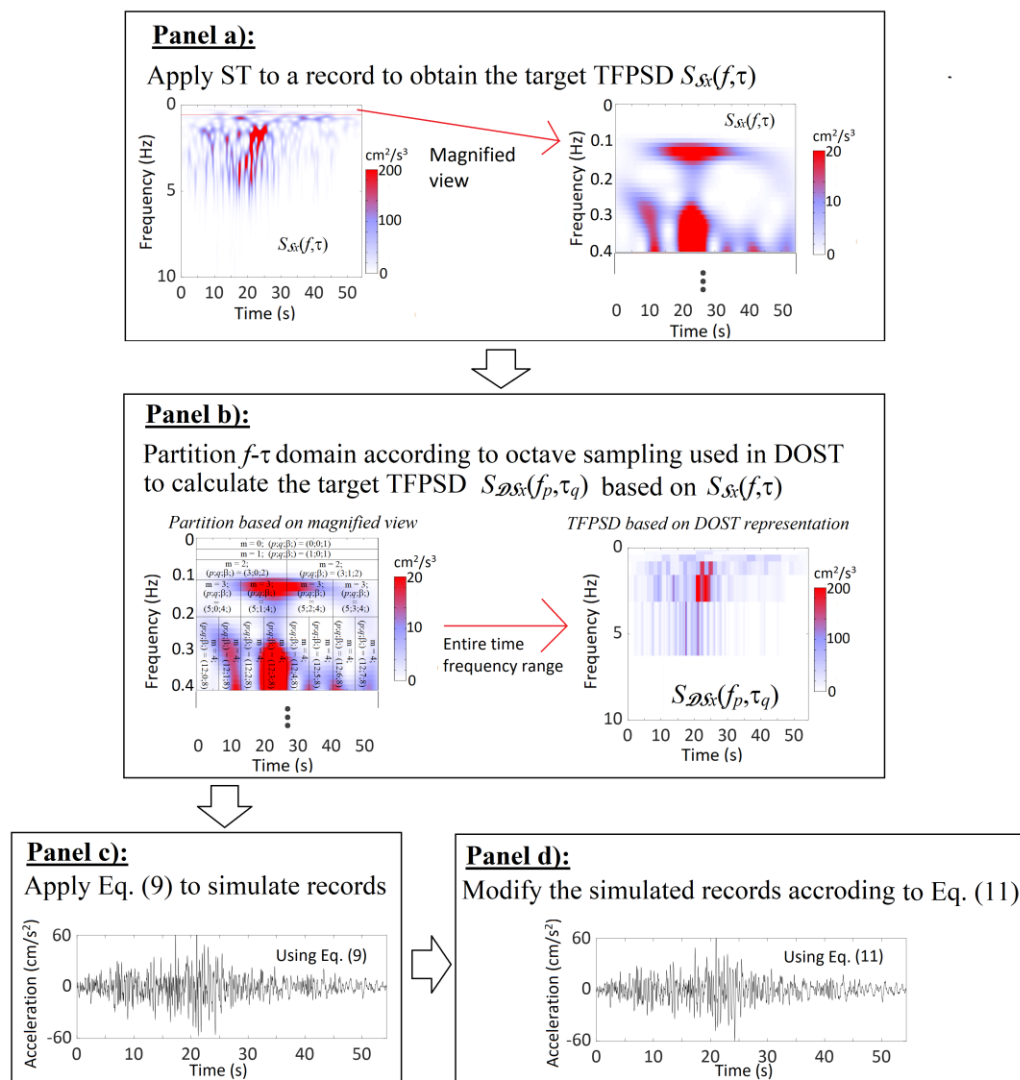


**Figure 4.2.** Procedure of simulating records by using TFSRM.



As can be observed from Figures 4.1 and 4.2,  $S_{\mathcal{S}_x}(f_p, \tau_p)$  is coarser than  $S_{\mathcal{S}_x}(f, \tau)$ , and the sampled records resemble closely the record used to calculate  $S_{\mathcal{S}_x}(f, \tau)$ . To show the adequacy of this simulation method, 100 records are sampled by following the above steps with the target  $S_{\mathcal{S}_x}(f, \tau)$  as shown Figure 4.1. A typical simulated record and its corresponding velocity and displacement time histories are illustrated in Figure 4.3. Since a sample-to-sample comparison of a stochastic process is not relevant, the peak ground acceleration (PGA), peak ground velocity (PGV), pseudo-spectral acceleration (PSA), Arias intensity (AI) and zero-crossing rate for each of the sampled records are calculated. The obtained statistics of the samples are presented in Figure 4.3 and compared with those corresponding to the seed record depicted in Figure 4.1. In all cases, the average values of PGA, PGV, PSA, AI, and zero-crossing rate follow closely to their targets. The slight differences between the mean of PGA and the seed record and mean of PGV to the seed record are attributed to the use of only 100 samples and the possible non-Gaussian effect. The latter is because the TFSRM, similar to the well-known SRM, generates the Gaussian process while the seed record is may not be Gaussian. In fact, by normalizing  $x(t_j)$  of the seed record to its uniform amplitude modulation function that is obtained according to the evolutionary theory (Priestley 1965), the kurtosis coefficient of the normalized values equals 2.87, which deviates from 3.0 that corresponds to a Gaussian process. To further illustrate the TFSRM, the same analysis is carried out for the E-W record component recorded at Salton City in the 1992 Big Bear-01 earthquake. This record component having a kurtosis coefficient of 2.53 is shown in Figure 4.4. The obtained results are also presented in Figure 4.4, indicating that the observations made to Figure 4.3 are equally applicable to these results. In all cases, the close match of the PSA, AI, and zero-crossing rate validates the usefulness of TFSRM for engineering applications.

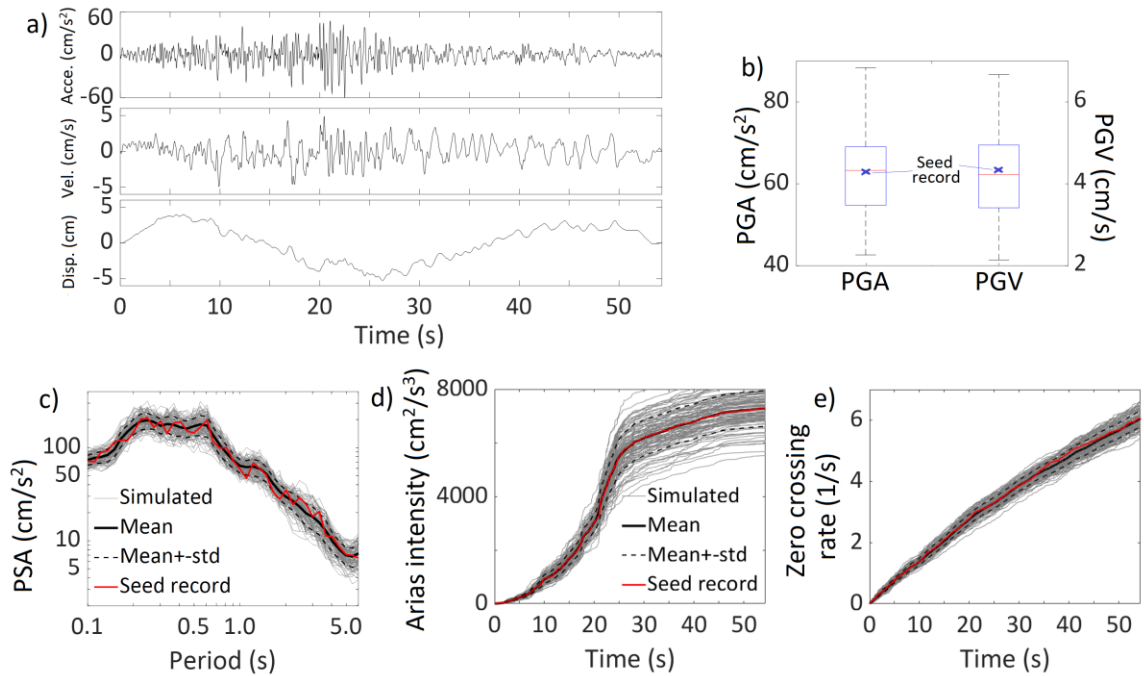


**Figure 4.3.** a) A sample of simulated record and its velocity and displacement time histories; b) the statistics of PGA and PGV, c) PSA, d) AI and e) zero crossing rate of a00 simulated records to their corresponding targets. The seed or target record is shown in Figure 4.1.

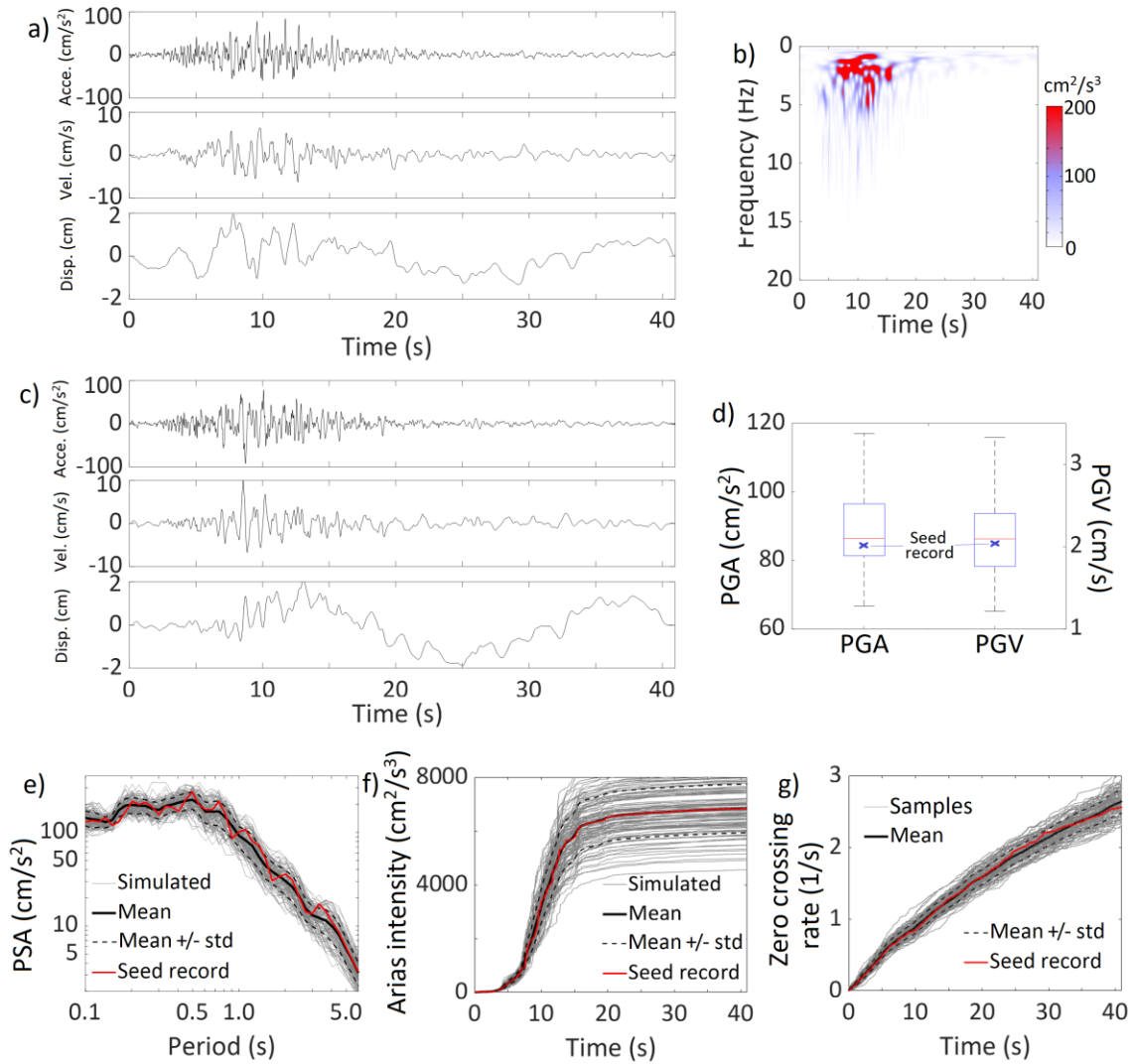


**Figure 4.4.** a) A historical record (i.e., seed record) and its velocity and displacement time histories; b) its TFPSD; c) a sample of simulated record and its velocity and displacement time histories; d) statistics of PGA and PGV, e) PSA, f) AI and g) zero-crossing rate of the 100 simulated records to their corresponding targets.

### 4.3 Historical horizontal ground motion record components used to develop the TFPSD function

The PEER NGA-West2 database contains a large number of ground motion records. The database included records from different earthquake types, source parameters, and

recording sites. For most cases, the three commonly used seismic source parameters and site condition, that are the earthquake moment magnitude  $\mathbf{M}$ , the rupture distance (i.e., the closest distance from the recording site to the fault area)  $R_{rup}$ , and the shear-wave velocity of the top 30 m of soil at the site  $V_{S30}$ , are available for each record. It is noted that the criteria used to select the records to develop ground motion models vary by different studies (Sabetta and Pugliese 1996; Alamilla et al. 2001; Pousse et al. 2006; Rezaeian and Der Kiureghian 2010; Yamamoto and Baker 2013; Vlachos et al. 2018). The criteria adopted for selecting records in the present study are:

- 1)  $\mathbf{M}$  is greater than 4.5 and  $R_{rup}$  is between 10 and 300 km so to exclude the low-intensity records and the near-fault records;
- 2)  $V_{S30}$  is between 180 m/s and 1500 m/s so to represent the site Classes B, C and D only as defined by UBC (1997); and,
- 3) Only free-field records from strike-slip fault earthquakes, which are considered as mainshocks, are included if there are at least five records from the same event.

The application of the above criteria resulted in 1504 records, each with two horizontal components. These records are from 31 events, as indicated in Table 4.1. The distribution of  $\mathbf{M}$  and  $R_{rup}$  associated with the selected records is depicted in Figure 4.5. Each record component is plotted, inspected, and baseline corrected. Before each record component is used, the segments of the record component with the first 0.5% and the last 0.5% of  $E_T$  are removed to eliminate the padded zeros from the processing and some non-earthquake noise.

**Table 4.1.** Summary of the selected records and their corresponding events.

Earthquake Name	Year	Magnitude	No. of pairs of records
"Coyote Lake"	1979	5.74	5
"Imperial Valley-06"	1979	6.53	16
"Imperial Valley-07"	1979	5.01	8
"Livermore-01"	1980	5.80	13
"Morgan Hill"	1984	6.19	19
"Chalfant Valley-02"	1986	6.19	10
"Superstition Hills-02"	1987	6.54	7
"Landers"	1992	7.28	65
"Big Bear-01"	1992	6.46	37
"Kobe Japan"	1995	6.90	16
"Kocaeli Turkey"	1999	7.51	22
"Duzce Turkey"	1999	7.14	15
"Hector Mine"	1999	7.13	69
"Yountville"	2000	5.00	20
"Big Bear-02"	2001	4.53	40
"Mohawk Val Portola"	2001	5.17	6
"Gulf of California"	2001	5.70	12
"CA/Baja Border Area"	2002	5.31	8
"Gilroy"	2002	4.90	34
"Nenana Mountain Alaska"	2002	6.70	35
"Denali Alaska"	2002	7.90	249
"Big Bear City"	2003	4.92	67
"Chi-Chi Taiwan-04"	1999	6.20	226
"Landers"	1992	7.28	8
"Hector Mine"	1999	7.13	43
"Bam Iran"	2003	6.60	21
"Parkfield-02 CA"	2004	6.00	64
"Molise-01 Italy"	2002	5.70	12
"El Mayor-Cucapah Mexico"	2010	7.20	279
"Joshua Tree CA"	1992	6.10	5
"Darfield New Zealand"	2010	7.00	73

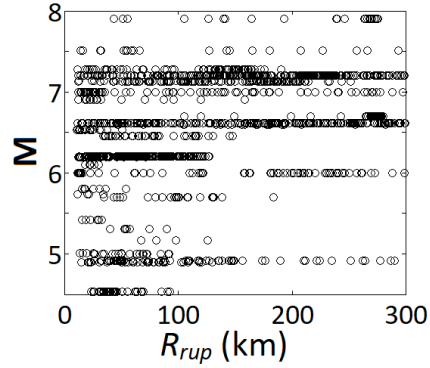


**Figure 4.5.** Distribution of  $M$  and  $R_{rup}$  of selected records.

## 4.4 Development of the model for the TFPD function

### 4.4.1 Time-frequency analysis of ground motions

To develop a probabilistic model of  $S_{s_x}(f, t)$  based on a set of ground motion records, first, the normalized TFPD function  $S_{s_x}(f, \tau)$ , denoted as  $S_{0s_x}(f, \tau)$ , is evaluated for each record component,

$$S_{0s_x}(f, \tau) = S_{s_x}(f, \tau) / E_T, \quad (4-12)$$

An illustration of the calculated  $S_{0s_x}(f, \tau)$  for the record component depicted in Figure 4.1 is shown in Figure 4.6a. The PSD function (i.e., integral of  $S_{s_x}(f, \tau)$  over the time) equals the integral of  $S_{s_x}(f, \tau)$  over the time, and the time-varying envelop function  $A(\tau)$  is defined as the square-root of the integral of  $S_{s_x}(f, \tau)$  over the frequency. The calculated SA and  $A(\tau)$  are presented in Figures 4.6b and 4.6c.

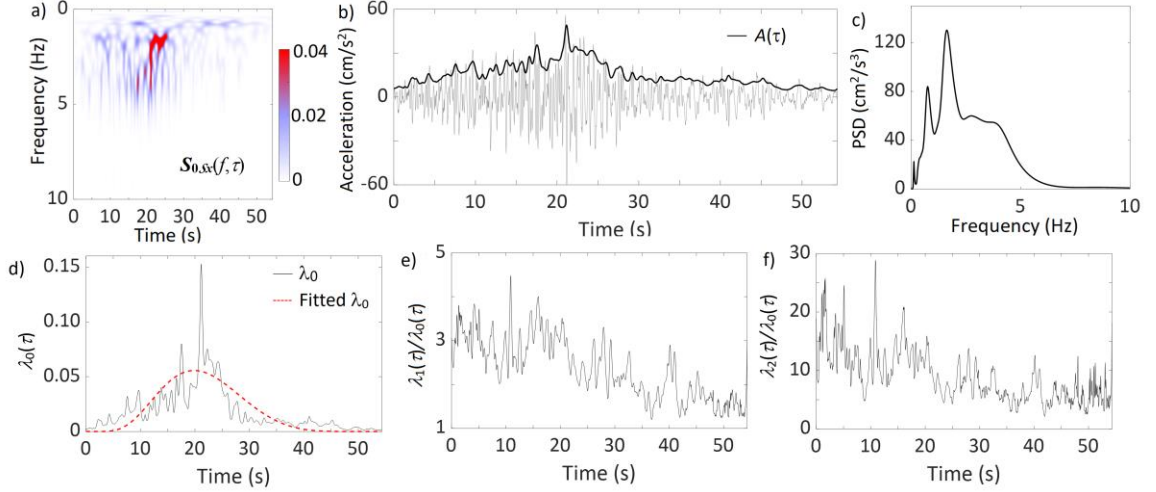


**Figure 4.6.** Time-frequency characteristics of the record component shown in Figure 4.1: a) Calculated normalized TFPSD function, b) the time-varying envelop function  $A(\tau)$ , c) the PSD function, d)  $\lambda_0(\tau)$ , e)  $\lambda_1(\tau)/\lambda_0(\tau)$ , and f)  $\lambda_2(\tau)/\lambda_0(\tau)$ .

To see the time-varying characteristics of the signal  $x(t)$ , moments of  $S_{0,S_x}(f, \tau)$  over the frequency domain for a given time  $\tau$  can be evaluated,

$$\lambda_j(\tau) = \int f^j S_{0,S_x}(f, \tau) df, j = 0, 1, 2; \quad (4-13)$$

where  $\lambda_j(\tau)$  denotes the  $j$ -th moment of the normalized TFPSD function.  $\lambda_0(\tau)$  represents the distributed energy in time; its square-root value represents the time-varying envelop function of the process.  $\lambda_1(\tau)/\lambda_0(\tau)$  and  $\lambda_2(\tau)/\lambda_0(\tau)$  represents the first and second moments of  $S_{0,S_x}(f, \tau)/\lambda_0(\tau)$ , respectively, where the use of this normalization ensures that the area under the curve  $S_{0,S_x}(f, \tau)/\lambda_0(\tau)$  for a given value of  $\tau$  equal to unit. The normalization facilitates the selection of a parametric model for  $S_{0,S_x}(f, \tau)/\lambda_0(\tau)$  since it may be interpreted as a probability density function, and many of the well-known probability density functions can be considered as the candidate parametric model, where the model fitting can be facilitated by using the method of

moments or the maximum likelihood method. For example, by considering  $S_{0,S_x}(f, \tau)$  shown in Figure 4.6a, the calculated  $\lambda_0(\tau)$ ,  $\lambda_1(\tau)/\lambda_0(\tau)$  and  $\lambda_2(\tau)/\lambda_0(\tau)$  are shown in Figures 4.6d to 4.6f, respectively. The plots indicate that the variations in time for all three parameters are significant.

Several probability density functions are considered as the candidate models to fit  $S_{0,S_x}(f, \tau)/\lambda_0(\tau)$ , and it was found that the lognormal model provides a better fit. The choice of the lognormal model is further justified since it was shown in Sabetta and Puliese (1996) and in Pousse et al. (2006) that it can be adequate but for the far-field ground motions. By adopting the lognormal model,

$$S_{S_x}(f, \tau) = \frac{E_T \lambda_0(\tau)}{f \sqrt{2\pi} \eta(\tau)} \exp \left[ -\frac{1}{2} \left( \frac{\ln f - \ln F_c(\tau) + \eta^2(\tau)/2}{\eta(\tau)} \right)^2 \right], \quad (4-14)$$

where

$$\eta(\tau) = \sqrt{\ln[1 + F_b^2(\tau) / F_c^2(\tau)]}, \quad (4-15)$$

$$F_b(t) = \left[ \lambda_2(\tau) / \lambda_0(\tau) - (\lambda_1(\tau) / \lambda_0(\tau))^2 \right]^{1/2}, \quad (4-16)$$

and

$$F_c(\tau) = \lambda_1(\tau) / \lambda_0(\tau), \quad (4-17)$$

These model parameters can be obtained based on regression analysis. As mentioned earlier that the developed model for  $S_{S_x}(f, \tau)$  cannot and must not be used in the context of SRM because the evaluation  $S_{S_x}(f, \tau)$  included both the frequency modulation and the amplitude modulation.

$\lambda_0(\tau)$  could be viewed as the squared amplitude modulation function. A preliminary analysis indicates that it could be as,



$$\lambda_0(\tau) = h(v)/T, \quad (4-18)$$

where

$$h(v) = \frac{\delta}{\sqrt{2\pi v(1-v)}} \exp\left[-\frac{1}{2}\left(\gamma + \delta \ln \frac{v}{1-v}\right)^2\right], \quad (4-19)$$

where  $v = v(\tau) = \tau/T$  represent the normalized time;  $T$  is the duration of the record;  $\gamma$  and  $\delta$  are the model parameters, and the mathematical form for  $h(v)$  is the Johnson SB distribution (Hahn and Shapiro 1967). The parameters  $\gamma$  and  $\delta$  can be determined by carrying out regression analysis. An illustration of such a fitting is depicted in Figure 4.6a. The results presented in the figure indicates that the use of the model shown in Eq. (4-18) can adequately represent the energy distribution in time. The Johnson SB distribution is flexible and can approximate well the lognormal and gamma distributions, which were used to model  $\lambda_0(\tau)$  in Sabetta and Pugliese (1996) and Rezaeian and Der Kiureghian (2010). Also, the mathematical model  $\lambda_0(\tau)$  only requires three parameters (i.e.,  $\gamma$ ,  $\delta$ ,  $T$ ). This number of parameters is the same as that used for the models considered in Sabetta and Pugliese (1996) and Pousse et al. (2006), and Rezaeian and Der Kiureghian (2010) but less than that used for the models considered in Alamilla et al. (2001) and Vlachos et al. (2016).

Let  $\tau_P$  denote the time at which the cumulative energy of the record component equals fraction  $P$  of the total energy. By definition,  $v_P = \tau_P/T$ . Since the energy distribution in  $v$  is modeled using the Johnson SB distribution, it can be shown that

$$v_P = \exp\left[\left(\Phi^{-1}(P) - \gamma\right)/\delta\right] / \left\{1 + \exp\left[\left(\Phi^{-1}(P) - \gamma\right)/\delta\right]\right\}, \quad (4-20)$$

where  $\Phi^{-1}(\bullet)$  is the inverse cumulative normal distribution function. To find regression models for  $\gamma$ ,  $\delta$ ,  $T$  as functions of seismic source and site characteristics, it is noted that the effective duration of ground motion defined as  $D = \tau_{0.95} - \tau_{0.05}$  is often used in the literature (Trifunac and Brady 1975). Therefore, if a value of  $D$  can be determined from

a regression model, by definition  $T$  can be calculated from,

$$T = D / (v_{0.95} - v_{0.05}), \quad (4-21)$$

The assessment of the predicting models for  $\gamma$ ,  $\delta$ , and  $D$  is to be discussed shortly.

By using the values of  $\lambda_1(\tau)/\lambda_0(\tau)$  and  $\lambda_2(\tau)/\lambda_0(\tau)$  such as those shown in Figure 4.6, it was found that  $F_c(\tau)$  and  $F_b(\tau)$  could be approximated by using,

$$F_b(\tau) = b_1 \exp[-b_2 \tau / T] + b_3, \quad (4-22)$$

and,

$$F_c(\tau) = c_1 \exp[-c_2 \tau / T] + c_3, \quad (4-23)$$

where  $c_j$  and  $b_j$  ( $j = 1, 2, 3$ ) are model parameters that can be determined based on the regression analysis. These considered models are slightly more sophisticated than those used by Sabetta and Pugliese (1996), which assumed  $F_b$  and  $F_c$  as linear functions of time.

However, an analysis aimed at developing a set of predicting equations for  $c_i$  and  $b_i$  was unsuccessful by considering the records described in Table 4.1 because of very large scatter associated with some of the predicting equations. As an alternative, values of  $F_b(0)$ ,  $F_b(T)$ ,  $F_c(0)$  and  $F_c(T)$ , denoted with simplified notations  $F_{b,0}$ ,  $F_{b,T}$ ,  $F_{c,0}$  and  $F_{c,T}$ , respectively, are calculated using the model shown in Eqs. (4-22) and (4-23) fitted to each record component. Moreover, the ratios defined as,

$$r_y = \frac{F_y(0) - F_y(T/2)}{F_y(0) - F_y(T)}, \text{ for } y = b \text{ or } c \quad (4-24)$$

are calculated based on the fitted model as well for each record component. As will be shown that the six parameters  $c_i$  and  $b_i$  can be determined for given values of  $F_{b,0}$ ,  $F_{b,T}$ ,  $F_{c,0}$ ,  $F_{c,T}$ ,  $r_b$ , and  $r_c$ .

Before developing predicting equations for  $(F_{b,0}, F_{b,T}, F_{c,0}, F_{c,T}, r_b, r_c)$ , a statistical analysis of  $r_b$  and  $r_c$  is carried out. By presenting the samples of  $r_b$  and samples of  $r_c$  obtained from all the considered record components in empirical distribution form as shown in Figure 4.7, it was observed that  $r_b$  and  $r_c$  are between 0.495 and 0.505 for about less than 20% of the cases, and  $r_b$  and  $r_c$  are less than 0.495 for about less than 0.2% of the cases. Note that because of the adopted model shown in Eqs. (4-22) and (4-23), values of  $r_b$  and  $r_c$  cannot be exactly equal to 0.5 since  $r_b$  or  $r_c = 0.5$  corresponds to the linear model. As  $r_b$  equal to 0.5 and  $r_c$  equal to 0.5 imply that  $F_c(\tau)$  and  $F_b(\tau)$  can be adequately approximated by a linear function, respectively, this suggests that only for about less than 20% of all the considered record component,  $F_b(\tau)$  and  $F_c(\tau)$  could be approximated well by linear functions. The cases for  $r_b$  or  $r_c$  that are less than 0.5 correspond to when  $F_b(\tau)$  and  $F_c(\tau)$  are increase functions of  $\tau$ . The cases for  $r_b > 0.5$  or  $r_c > 0.5$  correspond to when  $F_b(\tau)$  and  $F_c(\tau)$  are decreasing functions of  $\tau$ .

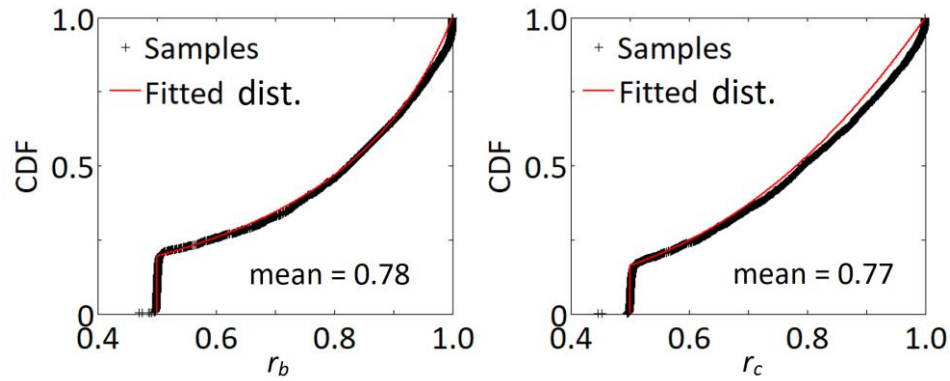


**Figure 4.7.** Empirical cumulative distribution of the ratios  $r_b$  and  $r_c$ .

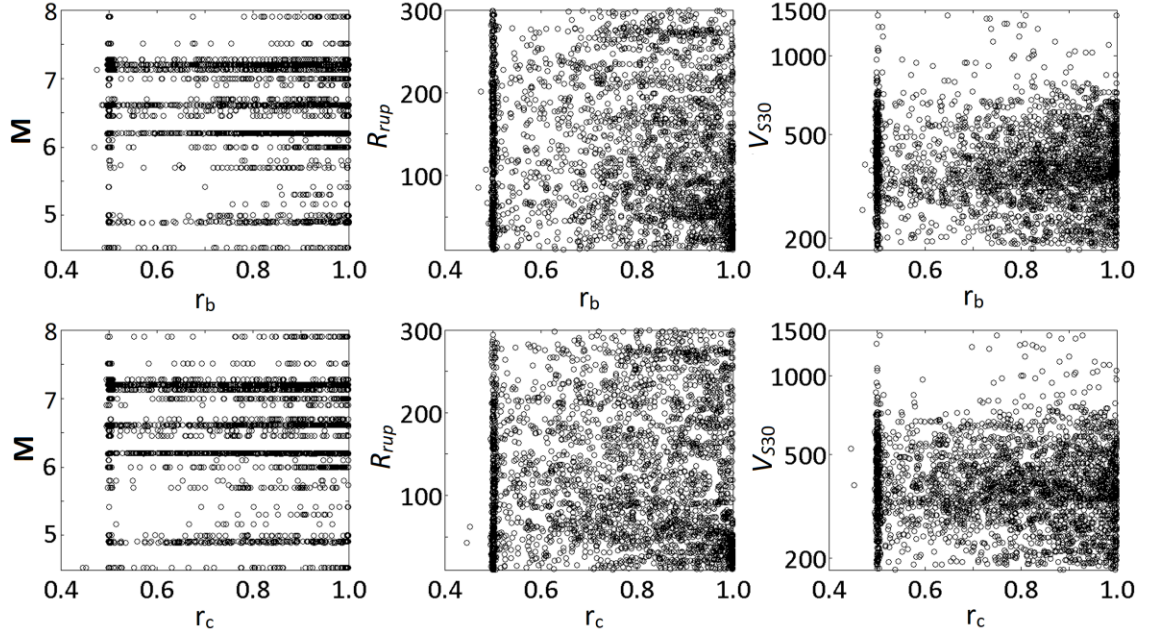


**Figure 4.8.**  $r_b$  and  $r_c$  versus of  $\mathbf{M}$ ,  $R_{rup}$  or  $V_{S30}$ .

To investigate whether  $r_b$  and  $r_c$  are functions of  $\mathbf{M}$ ,  $R_{rup}$  or  $V_{S30}$ , plots of  $r_b$  and  $r_c$  versus of  $\mathbf{M}$ ,  $R_{rup}$  or  $V_{S30}$  are presented in Figure 4.8. These plots show that there are no clear trends that can be used to develop predicting models for  $r_b$  and  $r_c$  as functions of  $\mathbf{M}$ ,  $R_{rup}$  or  $V_{S30}$ . Consequently, in the remaining part of the present study, it is assumed that  $r_c$  and  $r_b$  can be treated as random variables and independent of  $\mathbf{M}$ ,  $R_{rup}$  or  $V_{S30}$ . More specifically, the following quantile functions,

$$r_b(P) = \begin{cases} 0.5 & 0 < P < 0.195 \\ \frac{\ln P - 0.500P + 2.965}{2.465} & 0.195 \leq P < 1 \end{cases}, \quad (4-25)$$

and,

$$r_c(P) = \begin{cases} 0.5 & 0 < P < 0.162 \\ \frac{\ln P + 0.741P + 4.138}{4.879} & 0.162 \leq P < 1 \end{cases}, \quad (4-26)$$

are used to model  $r_b$  and  $r_c$ , where  $r_b(P)$  is quantile function of  $r_b$ ,  $r_c(P)$  is the quantile

function of  $r_c$ , and  $P$  denotes the probability (values of  $P$  in Eqs. (4-25) and (4-26) can differ). The adequacy of the quantile functions are illustrated in Figure 4.7. The linear correlation coefficient between  $r_b$  and  $r_c$  equals to 0.44, which is small.  $r_b$  and  $r_c$  are assumed to be independent in the following.

Given values of  $(F_{b,0}, F_{b,T}, r_b)$ , if  $r_b$  is not equal to 0.5,  $b_j$ ,  $j = 1, 2$ , and 3, can be calculated using,

$$b_1 = \frac{r_b^2 (F_{b,0} - F_{b,T})^2}{(2r_b - 1)(F_{b,0} - F_{b,T})}, \quad (4-27)$$

$$b_2 = -2 \ln \left( \frac{1 - r_b}{r_b} \right), \quad (4-28)$$

and,

$$b_3 = \frac{F_{b,0} F_{b,T} - F_{b,0}^2}{(2r_b - 1)(F_{b,0} - F_{b,T})}, \quad (4-29)$$

The model shown in Eq. (4-22) is then defined. If  $r_b$  equals 0.5, Eq. (4-22) is replaced by the following linear model.

$$F_b(\tau) = F_{b,0} - (F_{b,0} - F_{b,T})\tau/T, \quad (4-30)$$

Similarly,  $c_j$ ,  $j = 1, 2$ , and 3, can be calculated by using Eqs. (4-27) to (4-30) but with  $c$  replaced by  $b$ .

In summary, there are 10 model parameters for the proposed model shown in Eq. (4-14). Two parameters ( $r_b$  and  $r_c$ ) are already models using Eqs. (4-25) and (4-26), the remaining 8 parameters, which is included in the  $8 \times 1$  vector  $\mathbf{X}$ , where  $\mathbf{X} = (E_T, D, \gamma, \delta, F_{b,0}, F_{b,T}, F_{c,0}, F_{c,T})^T$ , the superscript denotes the transpose, and the  $j$ -th element in  $\mathbf{X}$ ,  $X_j$ , represents the  $j$ -th parameter in the vector. The total number of parameters is comparable or less than that for the models proposed in Sabetta and Pugliese (1996), Alamilla et al. (2001), and Pousse et al. (2006), Rezaeian and Der Kiureghian (2010), and

Vlachos et al. (2018). According to the above, the values of these eight model parameters for each record can be calculated by:

- a) Applying ST to  $x(t)$  as shown in Eq. (4-4) but using the FFT;
- b) Calculating the TFPSD function according to Eq. (4-6), and evaluate  $E_T$  using Eq. (4-7), effective duration  $D$ , and  $\lambda_j(\tau)$ ,  $j = 0, 1, 2$ ,
- c) Fitting model shown in Eq. (4-18) to the calculated  $\lambda_0(\tau)$  to find  $\gamma$  and  $\delta$ ; and,
- d) Fitting the model  $F_c(\tau)$  and  $F_b(\tau)$  defined by Eqs. (4-22) and (4-23) to the values of  $F_c(\tau)$  and  $F_b(\tau)$  calculated according to Eqs. (4-16) and (4-17), and calculate  $F_{b,0}$ ,  $F_{b,T}$ ,  $F_{c,0}$ ,  $F_{c,T}$ ,  $r_b$  and  $r_c$  (the modelling of  $r_b$  and  $r_c$  is already presented in the above).

#### 4.4.2 Development of predicting equations for the model parameters

By carrying out the analysis described in Steps a) to d) for each record component, the samples of  $\mathbf{X}$  are obtained. These samples are used to develop predicting equations for  $\mathbf{X}$  as functions of  $\mathbf{M}$ ,  $R_{rup}$ , and  $V_{S30}$ . For the development, first, a distribution fitting for each  $X_j$  is carried out. It was observed that they do not always follow a normal distribution, as shown in Figure 4.9. The probabilistic models shown in the figure for each parameter  $P_j$  are selected based on the Akaike information criterion (AIC and AICc) (Akaike 1970; Burnham and Anderson 2002) and by considering several commonly used probabilistic distribution models as candidate models. The plots shown in the figure show that the selected distribution models provide a good fit to the empirical data for the model parameters. The equations and model parameters of the fitted distributions are shown in Table 4.2.

**Table 4.2.** Fitted distribution parameters for the probability distribution models shown in Figure 4.8.

Distribution	Probability density function of $X$ , $f(x)$	$X$	Fitted model parameters
Lognormal	$\frac{1}{x\beta\sqrt{2\pi}} \exp\left(-\frac{(\ln x - \alpha)^2}{2\beta^2}\right),$	$E_T$	$(\alpha, \beta) = (6.73, 2.35)$
		$\delta$	$(\alpha, \beta) = (0.18, 0.23)$
Truncated lognormal	$\frac{\frac{1}{x\beta\sqrt{2\pi}} \exp\left(-\frac{(\ln x - \alpha)^2}{2\beta^2}\right)}{\Phi\left(\frac{\ln U - \alpha}{\beta}\right) - \Phi\left(\frac{\ln L - \alpha}{\beta}\right)}, L \leq x \leq U,$	$D$	$(\alpha, \beta, L, U) = (3.38, 0.63, 2.5, 150).$
Johnson SU	$\frac{\alpha}{\beta\sqrt{2\pi}} \frac{\exp\left(-\frac{1}{2}\left(\nu + \alpha \sinh^{-1}\left(\frac{x - \xi}{\beta}\right)\right)^2\right)}{\sqrt{1 + \left(\frac{x - \xi}{\beta}\right)^2}},$	$\gamma$	$(\nu, \alpha, \xi, \beta) = (-3.53, 2.72, -1.21, 1.28)$
Weibull	$\frac{\beta}{\alpha} \left(\frac{x}{\alpha}\right)^{\beta-1} \exp\left(-\left(\frac{x}{\alpha}\right)^\beta\right),$	$F_{b,0}$	$(\alpha, \beta) = (6.56, 2.87)$
Gamma	$\frac{1}{\Gamma(\alpha)\beta^\alpha} x^{\alpha-1} \exp\left(-\frac{x}{\beta}\right),$	$F_{b,T}$	$(\alpha, \beta) = (2.18, 1.27)$
		$F_{c,0}$	$(\alpha, \beta) = (5.45, 1.10)$
Frechet	$\frac{1}{\beta} \exp\left(-\left(1 + \xi \frac{x - \alpha}{\beta}\right)^{-\frac{1}{\xi}}\right) \left(1 + \xi \frac{x - \alpha}{\beta}\right)^{-1 - \frac{1}{\xi}},$	$F_{c,T}$	$(\xi, \alpha, \beta) = (0.38, 0.80, 1.42)$

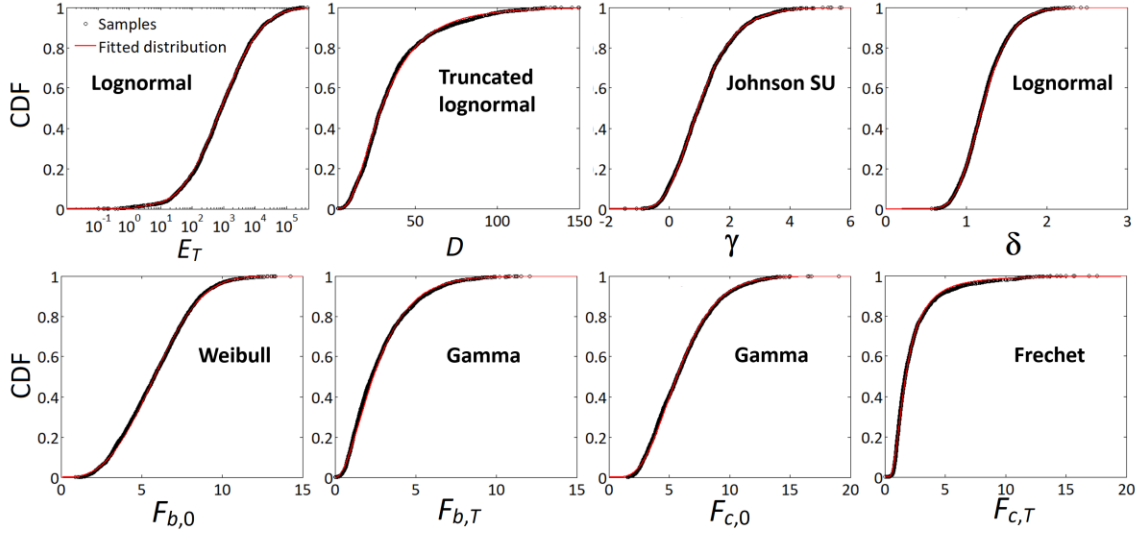


**Figure 4.9.** Cumulative distribution of each parameter and their corresponding fitted cumulative probability distribution function.

To develop the predicting equations, similar to others (e.g., Rezaeian and Der Kiureghian 2010; Vlachos et al. 2018), first, the random variables  $X_j$  are mapped to the normal space based on their marginal probability distribution functions. The multivariate regression analysis is then carried. More specifically, the value of  $X_j$ ,  $x_j$ , is mapped to the normal space using,

$$z_j = \Phi^{-1}[F_j(x_j)], \quad (4-31)$$

where  $F_j(\bullet)$  represents the fitted cumulative probability distribution function of  $X_j$  and  $\Phi^{-1}[\bullet]$  is the inverse of the standard normal distribution function, and  $z_j$  is the value of the standard normally distributed random variable  $Z_j$ .

In the normal space, it is considered that the predicting equations can take the following mathematical forms,

$$Z_j = \begin{cases} a_{j,1} + a_{j,2}\mathbf{M} + a_{j,3} \ln R_{rup} + a_{j,4} \ln V_{S30} + \varepsilon_j, & \text{for } j = 1, 2 \\ a_{j,1} + a_{j,2}\mathbf{M} + a_{j,3}\mathbf{M} \ln(R_{rup}) + a_{j,4} \ln V_{S30} + \varepsilon_j, & \text{for } j = 3, \dots, 8 \end{cases} \quad (4-32)$$



where  $a_{j,k}$ ,  $k = 1, \dots, 4$ , are the model coefficients of  $Z_j$ , and  $\varepsilon_j$  are zero-mean residuals. The residual  $\varepsilon_j$  equals the sum of the zero-mean interevent residual  $\eta_j$  and intraevent residual  $\delta_j$  with their standard deviation represented by  $\tau_j$  and  $\sigma_j$ , respectively. The mathematical forms considered are typical of those used to develop simple GMMs. The consideration of the spatial correlation (Goda and Hong (2008) and residuals that depend on  $\mathbf{M}$ ,  $R_{rup}$  or  $V_{S30}$  (e.g., Boore et al. 2014) are beyond the scope of the present study. This simplified treatment is consistent with the model development discussed in the introduction section. For the regression analysis, the restricted maximum likelihood method (REML) implemented in MATLAB is used (Patterson and Thompson 1971). The obtained model parameters, as well as the residuals, are shown in Table 4.3.

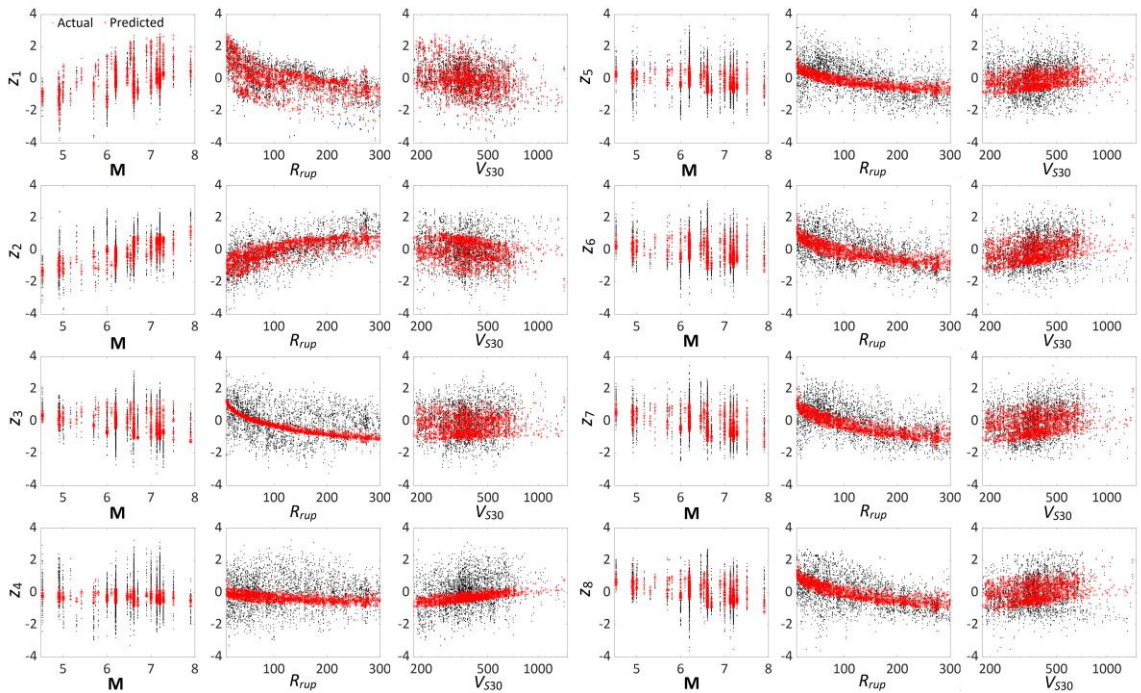


**Figure 4.10.** Compare of actual data and predicted values as functions of  $\mathbf{M}$ ,  $R_{rup}$  and  $V_{S30}$ .

The model coefficients presented in Table 4.3 indicate that all the predicted values are increasing function of  $\mathbf{M}$  and are decreasing function of  $\ln(R_{rup})$  or  $\mathbf{M}\ln(R_{rup})$ . All the predicted  $z_j$ , except  $z_1$  and  $z_2$ , increase as  $V_{S30}$  increases. By using the obtained model coefficients, the predicted values of  $Z_j$  as functions of  $\mathbf{M}$ ,  $R_{rup}$  or  $V_{S30}$  are compared to the samples in Figure 4.10. The plots indicate that the considered predicting models follow adequately to the trends of the samples. As can be observed that  $z_1$  (i.e., mapped values of  $E_T$ ) increases with increased  $\mathbf{M}$ , and decreased  $R_{rup}$  and  $V_{S30}$ . The same trends are observed for  $z_2$  that represents the mapped  $D$ , except that  $z_2$  is a decreased function of  $R_{rup}$ . The trends of both  $F_b(\tau)$  and  $F_c(\tau)$  at the beginning and the end of records to  $\mathbf{M}$ ,  $R_{rup}$  or  $V_{S30}$  are very similar; they decrease as  $\mathbf{M}$  or  $R_{rup}$  increases, and they increase with increasing  $V_{S30}$ . The predicted value of  $Z_3$  is sensitivity to  $R_{rup}$ ;  $z_4$  is an increasing function of  $V_{S30}$ . The predicted values of  $Z_5$  to  $Z_8$  (i.e., mapped  $F_{b,0}$ ,  $F_{b,T}$ ,  $F_{c,0}$ ,  $F_{c,T}$ ) are decreasing functions of  $R_{rup}$ .

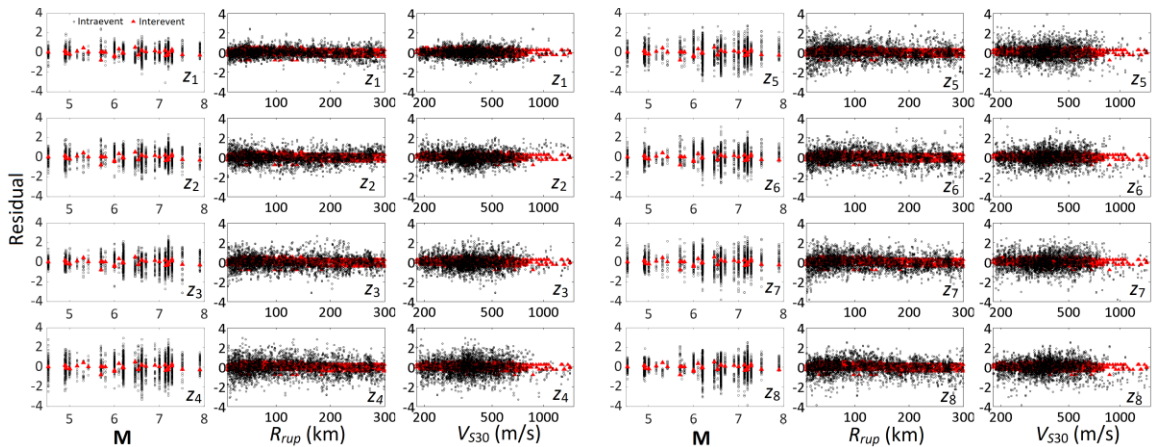


**Figure 4.11.** Residuals of inter- and intra-event for each parameter in normal space.

Table 4.3 shows that the standard deviation of the interevent residual is smaller or comparable to the intraevent residuals for the considered predicting equations.  $\eta_j$  and  $\delta_j$  for each record component are shown in Figure 4.11. As can be observed from the figure, the residuals are relatively consistent for ranges of values of  $\mathbf{M}$ ,  $R_{rup}$  and  $V_{S30}$ . The

correlation coefficient between  $\varepsilon_j$  and  $\varepsilon_k$  for  $j \neq k$  are calculated and shown in Table 4.4. The correlation coefficient between a pair of variables  $\varepsilon_j$  and  $\varepsilon_k$  for  $j \neq k$  is weak, except that the absolute value of the correlation coefficient is greater than 0.5 only for four pairs of variables  $(\varepsilon_2, \varepsilon_4)$ ,  $(\varepsilon_3, \varepsilon_4)$ ,  $(\varepsilon_5, \varepsilon_7)$  and  $(\varepsilon_6, \varepsilon_8)$ . The negative correlation coefficient between  $(\varepsilon_2, \varepsilon_4)$  suggests that a decreased  $D$  is associated with increased  $\delta$ ; hence, a more peaked amplitude modulation function. The positive correlation between  $(\varepsilon_3, \varepsilon_4)$  indicates that the location of the large amplitude modulation is shifted toward higher values of  $\tau$  if  $\delta$  is increased. The positive correlation coefficient between  $(\varepsilon_5, \varepsilon_7)$  implies that the mean and coefficient of variation over frequency (see Eq. (4-16) and Eq. (4-17)) for  $S_{s_x}(f, \tau)$  at  $\tau = 0$  are positively related. A similar observation can be made at  $\tau = T$  based on the positive coefficient between  $(\varepsilon_6, \varepsilon_8)$ .

It must be emphasized that since the processed records used are for the magnitude ranging from 4.5 to 8, rupture distance between 10 and 300 km,  $V_{S30}$  between 180 and 1500 m/s, and frequency ranging from 0 to 20 Hz, the developed TFPSD model is considered to be adequate only for these mentioned ranges.

**Table 4.3.** Coefficients for the predicting equations shown in Eq. (4-32).

	$a_{j,1}$	$a_{j,2}$	$a_{j,3}$	$a_{j,4}$	$\tau_j$	$\sigma_j$
$Z_1$	1.947	0.880	-0.927	-0.590	0.215	0.432
$Z_2$	-2.402	0.502	0.490	-0.526	0.605	0.580
$Z_3$	-0.535	0.378	-0.104	0.154	0.682	0.670
$Z_4$	-3.378	0.128	-0.032	0.533	0.656	0.623
$Z_5$	-2.546	0.249	-0.072	0.496	0.468	0.775
$Z_6$	-4.376	0.418	-0.098	0.753	0.530	0.699
$Z_7$	-2.459	0.253	-0.099	0.604	0.474	0.743
$Z_8$	-2.410	0.228	-0.087	0.596	0.483	0.742

**Table 4.4.** Correlation between total residuals of 8 parameters in normal space.

	$Z_1$	$Z_2$	$Z_3$	$Z_4$	$Z_5$	$Z_6$	$Z_7$	$Z_8$
$Z_1$	1	-0.215	0.186	0.272	-0.145	-0.007	0.032	0.221
$Z_2$		1	-0.075	<b>-0.565</b>	0.021	-0.472	-0.106	-0.505
$Z_3$			1	<b>0.509</b>	-0.038	0.193	0.186	0.120
$Z_4$				1	0.111	0.344	0.275	0.340
$Z_5$					1	0.133	<b>0.630</b>	-0.073
$Z_6$						1	0.431	<b>0.784</b>
$Z_7$							1	0.241
$Z_8$								1

## 4.5 Use and validation of the proposed time and frequency power spectral density function

### 4.5.1 Illustration of the procedure to generate synthetic record components for scenario events

The generation of synthetic ground motions for given seismic source and site characteristics is straight forward. For example, by considering  $\mathbf{M} = 7$ ,  $R_{rup} = 60$  km and  $V_{S30} = 450$  m/s, the calculated values of  $z_j$ ,  $j=1\dots, 8$ , are equal to [0.707, -0.095, 0.071, -0.143, 0.164, 0.342, 0.165, 0.334] by using Eq. (4-32) and the model coefficients shown in Table 4.3 but without considering the effect of residuals. By adding a set of sampled values of  $\varepsilon_j$ , that jointly normally distributed with the variance equal to  $(\tau_j^2 + \sigma_j^2)$  and correlation coefficient shown in Table 4.4, a sample of  $z_j$ ,  $j=1\dots, 8$ , for the considered scenario seismic event is obtained, which equals [0.785, -0.615, -0.120, 0.480, -1.64, -0.29, 2.36, 1.01]. The use of these values and Eq. (4-31) with the fitted distribution model parameters shown in Table 4.2 results in  $(E_T, D, \gamma, \delta, F_{b,0}, F_{b,T}, F_{c,0}, F_{c,T}) = [5287, 19.85, 0.85, 1.33, 2.34, 1.90, 13.70, 3.45]$ . Samples of  $r_b$  and  $r_c$  are calculated using the quantile functions shown in Eqs. (4-25) and (4-26). In particular,  $r_b$  and  $r_c$  equal to (0.98, 0.91) are used to emphasize the time-varying amplitude and frequency characteristics. Using the values of  $(E_T, D, \gamma, \delta, F_{b,0}, F_{b,T}, F_{c,0}, F_{c,T}, r_b, r_c)$ ,  $S_{S_x}(f, \tau)$  shown in Eq. (4-14) for the considered scenario event becomes,

$$S_{S_x}(f, \tau) = \frac{5287\lambda_0(\tau)}{f\sqrt{2\pi\eta(\tau)}} \exp\left[-\frac{1}{2}\left(\frac{\ln f - \ln F_c(\tau) + \eta^2(\tau)/2}{\eta(\tau)}\right)^2\right], \quad (4-33)$$

where

$$\eta(\tau) = \sqrt{\ln\left[1 + \left(\frac{0.436\exp(-0.24\tau) + 1.90}{10.36\exp(-0.12\tau) + 3.35}\right)^2\right]}, \quad (4-34)$$

$$F_c(\tau) = 10.36\exp(-0.12\tau) + 3.35, \quad (4-35)$$

$$\lambda_0(\tau) = \frac{1}{T} \times \frac{1.33}{\sqrt{2\pi\nu(1-\nu)}} \exp\left[-\frac{1}{2}\left(0.85 + 1.33\ln\frac{\nu}{1-\nu}\right)^2\right], \quad (4-36)$$

$T = 38.79$  (s), and  $\nu = \tau/38.79$ .

The values of  $S_{S_x}(f, \tau)$  shown in Eq. (4-33) is presented in Figure 4.12a. By applying the simulation model described in Eq. (4-11), a typical sampled record component is shown in Figure 4.12b. The mean and standard deviation of  $S_{S_x}(f, \tau)$  based on 500 simulated record components are shown in Figures 4.12c and 4.12d. The mean compares adequately to the target  $S_{S_x}(f, \tau)$ . The PSA for each sampled record component is calculated and illustrated in Figure 4.12e. The mean and mean +/- one standard deviation of the PSA for the sampled records are also shown in Figure 4.12e. The magnitude of the variability of the PSA calculated from the simulated ground motions in log scale is relatively consistent for the considered vibration period.

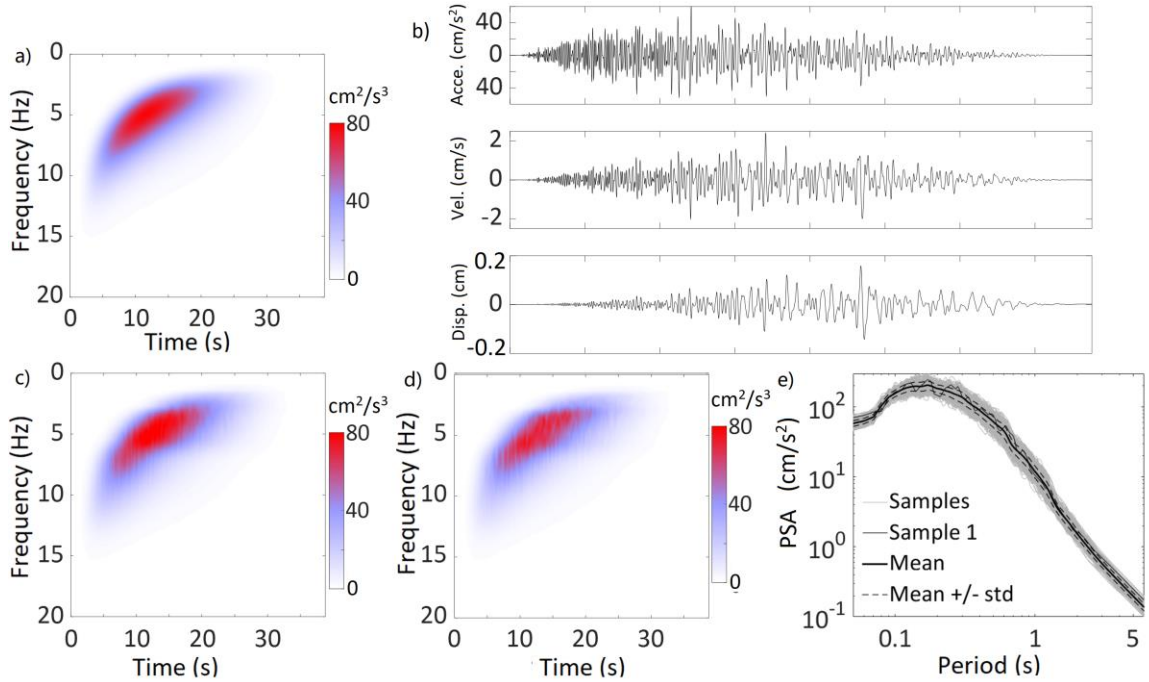


**Figure 4.12.** Sampled target TFPSD function, a sampled time history, the statistics of simulated TFPSD and PSA of the simulated records: a) Target  $S_{S_x}(f, \tau)$  for a scenario event, b) a typical sampled record and its velocity and displacement time history, c) mean  $S_{S_x}(f, \tau)$  of the samples, d) standard deviation of  $S_{S_x}(f, \tau)$  of the samples, and e) calculated PSA of the sampled records.

#### 4.5.2 Comparison of PSA from the simulated records to ground motion models

In an effort to validate the proposed model for  $S_{S_x}(f, \tau)$ , 500 records are simulated for selected values of  $\mathbf{M}$ ,  $R_{rup}$ , and  $V_{S30}$  by applying the procedure used for the illustrative example. PSA for each sampled record component is obtained and shown in Figure 4.13. The figure also shows the predicted median values, as well as the median +/- one standard deviation, by using GMMs from NGA-West2 developed by Abrahamson et al. (2014); Boore et al. (2014); Campbell and Bozorgnia (2014); Chiou and Youngs (2014), referred to as ASK14, BSSA14, CB14, and CY14, respectively. The comparison in

Figure 4.13 shows that for all cases, the median curves of the calculated PSA from the simulated records agree well with the predicted values by using the four mentioned GMMs. The standard deviations obtained based on the developed model are also comparable to those associated with GMMs from NGA-West2. The differences that can be observed from the plots are attributed to that the records used in the present study to develop the model for  $S_{s_x}(f, \tau)$  differ from those employed in developing the four GMMs. The comparison also suggests that the proposed  $S_{s_x}(f, \tau)$  and the simulation procedure are adequate.

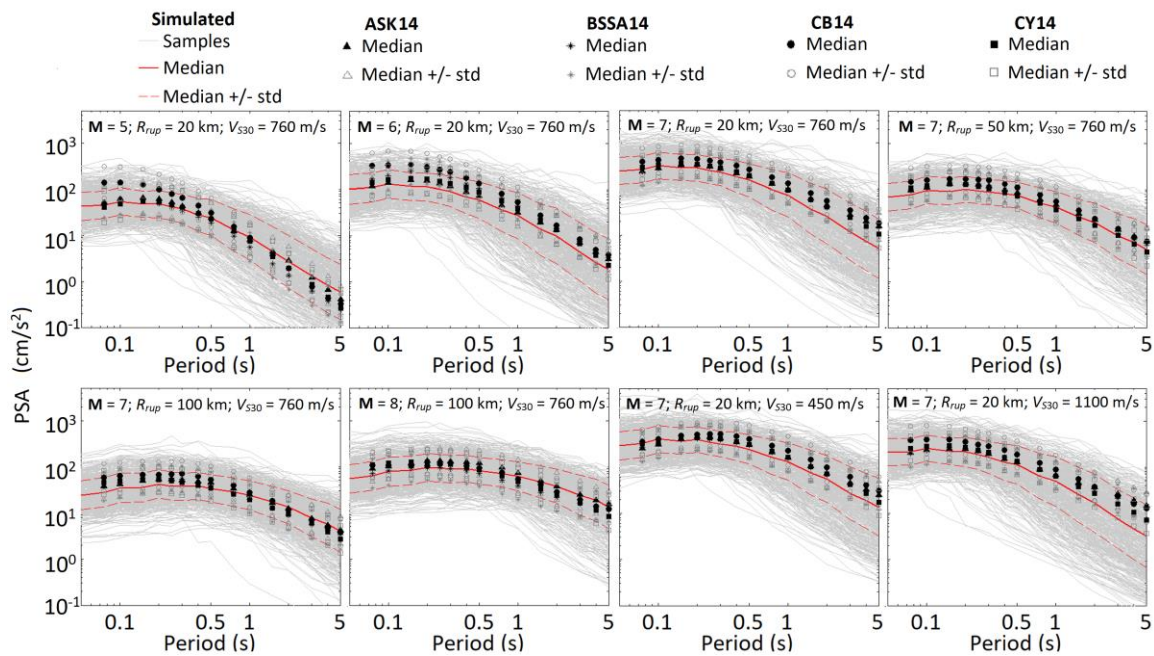


**Figure 4.13.** Comparison of the calculated PSA to the median values and median +/- standard deviation predicted by using the GMMs from NGA-West2.

Note that the probabilistic seismic hazard analysis (PSHA) for a site or a region incorporates the information on seismicity, magnitude-recurrence relations, and GMMs (e.g., McGuire 1995; Hong et al. 2006). One may adopt a TFPSD model, such as the one proposed in the present study, instead of using GMMs, to carry out PSHA. This



approach has the advantage of providing both the synthetic records as well as PSA instead of only PSA. The synthetic records are useful to evaluate the nonlinear inelastic structural responses.

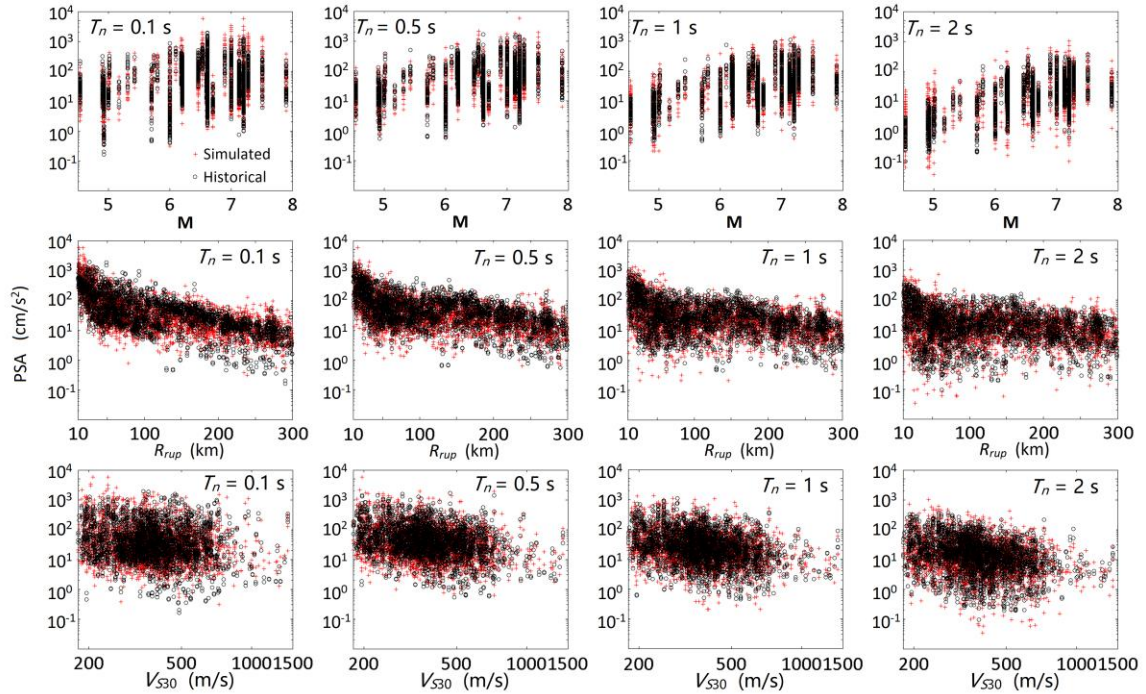


**Figure 4.14.** Comparison of trends of the calculated PSA from simulated records based on the proposed TFPSD model to the PSA of historical records described Table 4.1 ( $T_n$  represents the period).

#### 4.5.3 Comparison of PSA from the simulated records to PSA from the selected historical records

To further validate the proposed model for the TFPSD, a record is simulated for each of the combinations of  $\mathbf{M}$ ,  $R_{rup}$ , and  $V_{S30}$  that correspond to the considered records listed in Table 1. PSA values of the simulated records for the vibration period  $T_n$  equal to 0.1, 0.5, 1 and 2s are calculated and are plotted versus  $\mathbf{M}$ ,  $R_{rup}$ , and  $V_{S30}$ , separately, and



compared with those obtained from the actual records, as shown in Figure 4.14. The plots again indicate that the proposed  $S_{j_x}(f, \tau)$  and the simulation procedure are adequate since the overall trends of PSA from the proposed model reflect adequately those obtained from the actual records.

## 4.6 Conclusion

A model for the time-frequency power spectral density (TFPSD) function for scenario seismic source and site conditions is proposed. The model for the TFPSD has 10 model parameters. Predicting equations for these model parameters are developed by using 1504 selected historical ground motion records from strike-slip fault earthquakes.

The development of the model for TFPSD is based on the S-transform that has good time-frequency resolution since it uses a frequency-dependent window. Unlike some of the models available in the literature (i.e., evolutionary power spectral density models for the ground motions), the developed model implicitly considers both the amplitude modulation and frequency modulation. The use of the proposed TFPSD function to simulate ground motions for seismic source and site conditions is illustrated by applying a simulation model that is developed based on the discrete orthonormal S-transform and S-transform.

The adequacy of the proposed TFPSD function for the ground motions is investigated by comparing the spectral acceleration estimated from the simulated record components to the predicted PSA by using ground motion models from NGA-West2 and to the PSA from the considered historical records. These comparisons show that they agree well.

## 4.7 Data and resources

The records listed in Table 4.1 are from <https://ngawest2.berkeley.edu>. The website is last accessed on November 15, 2019.

## Reference

- Alamilla, J., Esteva, L., García-Pérez, J., and Diaz-Lopez, O. (2001). Simulating earthquake ground motion at a site, for given intensity and uncertain source location. *J. Seismol.*, **5**(4), 475-485.
- Akaike, H. (1970). Statistical predictor identification. *Ann. I. Stat. Math.*, **22**(1), 203-217.
- Anderson, D. R., and Burnham, K. P. (2002). Avoiding pitfalls when using information-theoretic methods. *J. Wildlife Manage.*, 912-918.
- Ancheta, T. D., Darragh, R. B., Stewart, J. P., Seyhan, E., Silva, W. J., Chiou, B. S. J., ... and Kishida, T. (2014). NGA-West2 database. *Earthq. Spectra*, **30**(3), 989-1005.
- Abrahamson, N. A., Silva, W. J., and Kamai, R. (2014). Summary of the ASK14 ground motion relation for active crustal regions. *Earthq. Spectra*, **30**(3), 1025-1055.
- Battisti, U., and Riba, L. (2016). Window-dependent bases for efficient representations of the Stockwell transform. *Appl. Comput. Harmon. A.*, **40**(2), 292-320.
- Boore, D. M., Stewart, J. P., Seyhan, E., and Atkinson, G. M. (2014). NGA-West2 equations for predicting PGA, PGV, and 5% damped PSA for shallow crustal earthquakes. *Earthq. Spectra*, **30**(3), 1057-1085.
- Campbell, K. W., and Bozorgnia, Y. (2014). NGA-West2 ground motion model for the average horizontal components of PGA, PGV, and 5% damped linear acceleration response spectra. *Earthq. Spectra*, **30**(3), 1087-1115.
- Chiou, B. S. J., and Youngs, R. R. (2014). Update of the Chiou and Youngs NGA model for the average horizontal component of peak ground motion and response spectra. *Earthq. Spectra*, **30**(3), 1117-1153.
- Conte, J. P., and Peng, B. F. (1997). Fully nonstationary analytical earthquake ground-motion model. *J. Eng. Mech.*, **123**(1), 15-24.
- Cohen, L. (1995). *Time-frequency analysis*, Prentice-Hall, New Jersey, U.S.
- Cui, X. Z., and Hong, H. P. (2020). Use of Discrete Orthonormal S-Transform to Simulate Earthquake Ground Motions. *Bull. Seismol. Soc. Am.* **XX**, 1–11, doi: 10.1785/0120190212
- Goda, K., and Hong, H. P. (2008). Spatial correlation of peak ground motions and response spectra. *Bull. Seismol. Soc. Am.*, **98**(1), 354-365.
- Grigoriu, M., Ruiz, S. E., and Rosenblueth, E. (1988). The Mexico earthquake of September 19, 1985—Nonstationary models of seismic ground acceleration. *Earthquake Spectra*, **4**(3), 551-568.
- Hong, H. P., Goda, K., and Davenport, A. G. (2006). Seismic hazard analysis: a comparative study. *Canadian Journal of Civil Engineering*, **33**(9), 1156-1171.
- Hong, H. P. (2016). Modeling of nonstationary winds and its applications. *Journal of Engineering Mechanics*, **142**(4), 04016004.

- Hong, H. P. (2020). Response and first passage probability of SDOF systems subjected to nonstationary stochastic excitation modeled through S-Transform. *Structural Safety*, In press.
- Hong, H. P., and Cui, X. Z. (2020). Time–Frequency spectral representation models to simulate nonstationary processes and their use to generate ground motions. *Journal of Engineering Mechanics*, 146(9), 04020106.
- Hahn, G. J., and Shapiro, S. S. (1967). *Statistical models in engineering*, John Wiley, New York, U.S.
- Liang, J., Chaudhuri, S. R., and Shinozuka, M. (2007). Simulation of nonstationary stochastic processes by spectral representation. *J. Eng. Mech.*, **133**(6), 616-627.
- McGuire, R. K. (1995). Probabilistic seismic hazard analysis and design earthquakes: closing the loop. *Bulletin of the Seismological Society of America*, 85(5), 1275-1284.
- Pousse, G., Bonilla, L. F., Cotton, F., and Margerin, L. (2006). Nonstationary stochastic simulation of strong ground motion time histories including natural variability: Application to the K-net Japanese database. *Bull. Seismol. Soc. Am*, **96**(6), 2103-2117.
- Priestley, M. B. (1965). Evolutionary spectra and non-stationary processes. *J. Roy. Stat. Soc. B. Met.*, **27**(2), 204-229.
- Pinnegar, C. R., and Mansinha, L. (2003). The S-transform with windows of arbitrary and varying shape. *Geophysics*, **68**(1), 381-385.
- Patterson, H. D., and Thompson, R. (1971). Recovery of inter-block information when block sizes are unequal. *Biometrika*, **58**(3), 545-554.
- Rezaeian, S., and Der Kiureghian, A. (2010). Simulation of synthetic ground motions for specified earthquake and site characteristics. *Earthq. Eng. Struct. D.*, **39**(10), 1155-1180.
- Stockwell, R. G., Mansinha, L., and Lowe, R. P. (1996). Localization of the complex spectrum: the S transform. *IEEE Trans. Signal Process.*, **44**(4), 998-1001.
- Stockwell, R. G. (2007). A basis for efficient representation of the S-transform. *Digit. Signal Process.*, **17**(1), 371-393.
- Shinozuka, M., and Jan, C. M. (1972). Digital simulation of random processes and its applications. *J. Sound Vib.*, **25**(1), 111-128.
- Shinozuka, M., and Deodatis, G. (1991). Simulation of Stochastic Processes by Spectral Representation. *Appl. Mech. Rev. (ASCE)*, **44**(4): 191–204.
- Sabetta, F., and Pugliese, A. (1996). Estimation of response spectra and simulation of nonstationary earthquake ground motions. *Bull. Seismol. Soc. Am*, **86**(2), 337-352.
- Trifunac, M. D., and Brady, A. G. (1975). A study on the duration of strong earthquake ground motion. *Bull. Seismol. Soc. Am*, **65**(3), 581-626.
- UBC (1997): *Uniform building code*. In International Conference of Building Officials, Whittier, CA.

- Yeh, C. H., and Wen, Y. K. (1990). Modeling of nonstationary ground motion and analysis of inelastic structural response. *Struct. Saf.*, **8**(1-4), 281-298.
- Vlachos, C., Papakonstantinou, K. G., and Deodatis, G. (2018). Predictive model for site specific simulation of ground motions based on earthquake scenarios. *Earthq. Eng. Struct. D.*, **47**(1), 195-218.
- Yamamoto, Y., and Baker, J. W. (2013). Stochastic model for earthquake ground motion using wavelet packets. *Bull. Seismol. Soc. Am.*, **103**(6), 3044-3056.
- Yan, Y., and Zhu, H. (2011). The generalization of discrete stockwell transforms. *In 2011 19th Eur. Signal Pr. Conf.*, IEEE, 1209-1213.

## Chapter 5

### 5 A time-frequency dependent coherence model for seismic ground motions

#### 5.1 Introduction

There are several well-known empirical lagged spatial coherence models for ground motions in the literature, including the ones given by Luco and Wang (1986), Harichandran and Vanmarcke (1986), Hao et al. (1989) and Abrahamson et al. (1991). A review and discussion of the coherence models are given in Hong and Liu (2014), Konakli et al. (2014), and Liu and Hong (2015, 2016). A common characteristic of the models that are developed for the ground motions along the same horizontal record component orientation is that the lagged coherence decreases exponentially with increasing separation or increasing frequency. The majority of the models were developed based on the records from the dense arrays in Taiwan (i.e., Lotung Large Scale Seismic Test (LSST) Array and Strong Motion Array in Taiwan (SMART)). The assessment of the lagged coherence for horizontal record components along the same orientation and for the vertical record components was presented in Chiu et al. (1995) using records from the SMART project. Their results indicate that the lagged coherence for the vertical record components is consistently lower than that for the horizontal record components. The same trends observed based on records from Taiwan were observed by using California records (Konakli et al. 2014). The assessment of the lagged coherence for record components along two orthogonal horizontal orientation was reported in Hong and Liu (2014) and Liu and Hong (2015). Some of the most interesting findings are that the statistics of the lagged coherence are insensitive to the orientations of the orthogonal horizontal excitations with respect to the principal axes (defined based on Arias intensity) and that the lagged coherence along the two horizontal principal axes is similar to that along two random but orthogonal horizontal orientations. In addition, a spatial coherence model by using the tri-directional ground motions was proposed in Liu and Hong (2016).

In all the above-mentioned studies, it is noted that the evaluation of the lagged

coherence was carried out using the ordinary Fourier transform (FT) and that the proposed spatial coherence models are functions of frequency and separation but independent of time. If the ground motions at different sites are modeled as the amplitude modulated evolutionary processes (Priestley 1965; Priestley and Tong 1973), the use of a time-independent lagged coherence is adequate since this agrees with the adopted theoretical model. The ground motions based on such a case can be simulated using the spectral representation method (Shinozuka and Jan 1972; Shinozuka and Deodatis 1996).

If the ground motions are modeled as the amplitude and frequency modulated evolutionary processes (Grigoriu, Ruiz, and Rosenblueth 1988; Yeh and Wen 1990), where the frequency modulation is achieved through non-linear time transformation, it can be shown that the lagged coherence of the nonstationary processes modeled in such a manner (Heredia-Zavoni and Santa-Cruz 2000; Hong 2016) depends on time. Also, Conte and Peng (1997) considered the ground motions at a site can be expressed as the superposition of several amplitude modulated subprocesses; in such a case, the lagged coherence between the ground motions at different sites could also be time-dependent. However, to the authors' knowledge, a time-frequency dependent (TF-dependent) empirical parametric lagged coherence model is unavailable in the literature, although an evaluation of the lagged coherence by using the continuous wavelet transform was assessed by applying complex Morlet wavelet in Abbas and Tezcan (2019, 2020) and by applying generalized Morse wavelet in Qiao et al. (2020). Abbas and Tezcan (2020) proposed a non-parametric model using the relevance vector machine modeling technique, where the weights and kernel widths were given only for the time up to 5 s.

The main objectives of the present study are to evaluate the TF-dependent lagged coherence, to develop an empirical TF-dependent lagged coherence model, and to show its application in simulating the spatially varying ground motions. The remainder of the paper is organized as follows. Section 2 provides a summary of the family of Fourier transforms used to estimate power spectral density and coherence functions. More specifically, it includes the FT, time-dependent windowed Fourier transform (i.e., short-time Fourier transform (STFT)) (Cohen 1995), and TF-dependent windowed Fourier

transform – the S-transform (ST) (Stockwell et al. 1996; Pinnegar and Mansinha 2003; Stockwell 2007). The summary provides the basis for discussing the characteristics of these transforms as well as possible bias in the calculated PSD by using these transforms. Section 3 describes the estimation of TF-dependent coherence and the proposed empirical TF-dependent lagged coherence model. In section 4, the use of the proposed TF-dependent coherence model to simulate the ground motions at multiple sites by using a recently developed ground motion simulation technique (Cui and Hong 2020a; Hong and Cui 2020) based on the ST and discrete orthonormal S-transform (DOST) (Stockwell 2007) is shown. Finally, the conclusions are presented in Section 5.

## 5.2 Family of Fourier transforms for evaluating power spectral density and coherence functions

The three techniques considered for evaluating spectra and coherence in this chapter are the ordinary Fourier analysis (Jenkins and Watts 1969; Newland 2012), the windowed Fourier analysis (Priestley 1965, 1988; Cohen 1995), and the S-transform (Stockwell et al. 1996).

Consider that the samples of the stochastic processes  $X_{n_1}(t)$  at the spatial points  $\mathbf{p}_{n_1}$ ,  $n_1 = 1, \dots, n$ , denoted as  $x_{n_1}(t)$ , are obtained. The FT of  $x_{n_1}(t)$ , and its inverse used in this chapter are,

$$x_{\mathcal{F}n_1}(f) = \int_{-\infty}^{+\infty} x_{n_1}(t) e^{-i2\pi ft} dt, \quad (5-1)$$

and,

$$x_{n_1}(t) = \int_{-\infty}^{+\infty} x_{\mathcal{F}n_1}(f) e^{i2\pi ft} df. \quad (5-2)$$

where  $x_{\mathcal{F}n_1}(f)$  denotes the Fourier transform of  $x_{n_1}(t)$ ,  $f$  is the frequency in Hz, and  $x_{\mathcal{F}n_1}(f) = x_{\mathcal{F}n_2}^*(-f)$ . If  $x_{n_1}(t)$  is given in the discrete form, the use of discrete FT and the fast Fourier transform (FFT) can be used to evaluate the Fourier coefficients (Jenkins and Watts 1969; Newland 2012).

The double-sided power spectral density (PSD) function,  $S_{\mathcal{F}n_1n_2}(f)$  is then calculated using (Zerva 2009),

$$S_{\mathcal{F}n_1n_2}(f) = x_{\mathcal{F}n_1}(f)x_{\mathcal{F}n_2}^*(f)/T, \quad (5-3)$$

where the subscript \* denotes the complex conjugate, and  $T$  is the duration of the sampled processes.  $S_{\mathcal{F}n_1n_2}(f)$  represents the auto and cross PSD functions for  $n_1 = n_2$  and  $n_1 \neq n_2$ , respectively. The square root of the integral of  $S_{\mathcal{F}n_1n_2}(f)$  over the frequency is referred to as the intensity of  $x_{n_1}(t)$ .

The smoothed auto and cross PSD functions need to be used to estimate the coherence between  $x_{n_1}(t)$  and  $x_{n_2}(t)$ ,  $\gamma_{\mathcal{F}}(f)$ , (Zerva 2009),

$$\gamma_{\mathcal{F}}(f) = \bar{S}_{\mathcal{F}n_1n_2}(f) / \sqrt{\bar{S}_{\mathcal{F}n_1n_1}(f)\bar{S}_{\mathcal{F}n_2n_2}(f)}, \quad (5-4)$$

where the bar above a symbol represents the smoothing operator applied to that symbol. The absolute value of  $\gamma_{\mathcal{F}}(f)$ ,  $|\gamma_{\mathcal{F}}(f)|$ , is known as the lagged coherence and the phase angle of the coherence  $\theta_{\mathcal{F}}(f)$  equals  $\tan^{-1}(\text{Im}(\gamma_{\mathcal{F}}(f))/\text{Re}(\gamma_{\mathcal{F}}(f)))$ , in which  $\text{Im}()$  and  $\text{Re}()$  denote the imaginary and real parts of its argument, respectively. As the values of  $x_{n_1}(t)$  and  $x_{n_2}(t)$  are often reported at discrete and evenly spaced values to  $t, t_p$  ( $p=1, \dots, N$ ), the  $S_{\mathcal{F}n_1n_2}(f)$  and its smoothed version,  $\bar{S}_{\mathcal{F}n_1n_2}(f_k)$ , are calculated at discrete frequencies  $f_k$ , by using,

$$\bar{S}_{\mathcal{F}n_1n_2}(f_k) = \sum_{m=-M}^{+M} W(m\Delta f)S_{\mathcal{F}n_1n_2}(f_k + m\Delta f), \quad (5-5)$$

where  $f_k = k\Delta f$ ,  $\Delta f$  is the frequency increment and equals to  $1/T$ , and  $W(m\Delta f)$  is the window with  $2M+1$  points. The commonly used window includes the boxcar, Hanning, Hamming windows (Jenkins and Watts 1969).



A stationary process can be characterized by using the PSD function that is obtained based on FT. However, the use of FT is not effective for the nonstationary processes since the analysis does not provide information on the time-varying aspect of the process or the PSD function. An alternative is to treat the nonstationary process as evolutionary processes and use the Fourier analysis but for the windowed time history (i.e., STFT) (Priestley 1965). More specifically, for a given sample of a stationary process,  $x_{n_1}(t)$ , the application STFT leads to,

$$x_{w_{n_1}}(f, \tau) = \int_{-\infty}^{\infty} x_{n_1}(u) g(\tau - u) e^{-i2\pi fu} du \quad (5-6)$$

where  $\tau$  denotes the time of interest, and the window  $g(u) = 1/(\sqrt{2h})$  for  $|u| \leq h$  with the window size  $h$  that is much smaller than  $T$  (Priestley 1965). Similar to the application of discrete FT to a signal given in the discrete form (i.e.,  $x_{n_1}(t)$  is given at  $t$  equal to  $t_p = (p-1) \times \Delta t$ ,  $p = 1, \dots, N$ ), the calculation of  $x_{w_{n_1}}(f, \tau)$  in Eq. (5-6) can be carried out at  $t_p$  and  $f_k$  using FFT (Jenkins and Watts 1969; Cohen 1995; Newland 2012).

The time-frequency (dependent) PSD (TFPSD) function,  $S_{w_{n_1 n_2}}(f, \tau)$ , is defined as,

$$S_{w_{n_1 n_2}}(f, \tau) = x_{w_{n_1}}(f, \tau) x_{w_{n_2}}^*(f, \tau) / \left( \sqrt{D_{w_{n_1}}} \sqrt{D_{w_{n_2}}} \right), \quad (5-7)$$

where  $S_{w_{n_1 n_2}}(f, \tau) = S_{w_{n_1 n_2}}^*(-f, \tau)$ ,  $D_{w_{n_1}}$  and  $D_{w_{n_2}}$  are the normalization factor in ensuring the integration of  $S_{w_{n_1 n_1}}(f, \tau)$  over the time and frequency domain equal to the integration of  $S_{\mathcal{F}_{n_1 n_1}}(f)$  over the frequency domain (i.e., variance). In other words,  $D_{w_{n_1}}$  is defined by,

$$D_{w_{n_1}} = \int_{\Omega_{f, \tau}} x_{w_{n_1}}(f, \tau) x_{w_{n_1}}^*(f, \tau) df d\tau / \left( T \int_{\Omega_f} S_{\mathcal{F}_{n_1 n_1}}(f) df \right), \quad (5-8)$$

where  $\Omega$  with subscripts denotes the integration over the domain of the subscripts. It can

be shown that  $D_{w_{n_1}}$  equals unity. However, in practical applications, since Eq. (5-6) is always applied to a signal with finite length, and in discrete form, there is a wrap-around effect on  $D_{w_{n_1}}$ . In such a case, a renormalization is needed to ensure energy conservation.

Eq. (5-7) provides the auto TFPSD function if  $n_1 = n_2$  and cross TFPSD function if  $n_1 \neq n_2$ . Analogously to the ordinary Fourier analysis, the square root of the integration of  $S_{w_{n_1 n_2}}(f, \tau)$  over the frequency for a given value of  $\tau$ ,

$$I_{w_{n_1}}(\tau) = \left[ \int_{-\infty}^{\infty} S_{w_{n_1 n_1}}(f, \tau) df \right]^{1/2}. \quad (5-9)$$

is referred to as the time-varying intensity of  $x_{n_1}(t)$ .

The TF-dependent coherence function,  $\gamma_w(f_k, \tau_r)$ , is defined as,

$$\gamma_{w_{n_1 n_2}}(f, \tau) = \bar{S}_{w_{n_1 n_2}}(f, \tau) / \sqrt{\bar{S}_{w_{n_1 n_1}}(f, \tau) \bar{S}_{w_{n_2 n_2}}(f, \tau)}, \quad (5-10)$$

where  $\bar{S}$  is the smoothed  $S$  with a time-frequency window. The lagged coherence equals  $|\gamma_{w_{n_1 n_2}}(f, \tau)|$ , and the phase angle of the coherence  $\theta_{w_{n_1 n_2}}(f, \tau)$  equals  $\tan^{-1}[\text{Im}(\gamma_w(f, \tau)) / \text{Re}(\gamma_w(f, \tau))]$ . The numerical calculation of the smoothed TFPSD functions is to be elaborated shortly.

Note that as the width of the window increases, the STFT provides better resolution at the low frequencies, but the resolution in time decreases, leading to a reduced temporal resolution. Moreover, a well-known drawback of STFT is energy leakage (Cohen 1995). To illustrate the effect of the window width on the estimated PSD function, consider a stochastic process that is defined by  $S(f) = (1 + 0.0225f^2) / [(1 - 0.25f^2)^2 + 0.0225f^2]$ , representing a (doubled-sided) Kanai-Tajimi model (Clough and Penzien 1995). By using this PSD function, a sample of the stationary process with the duration equal to

40.95 s and time increment of 0.01 s is simulated by using the spectral representation method. The simulated record is shown in Figure 5.1a. The evaluation of the PSD function of the simulated record is carried out by using the ordinary Fourier transform (see Eq. (5-3)) and shown in Figure 5.1b. By using STFT and applying Eq. (5-7),  $S_{w_{n_1, n_1}}(f, \tau)$  is obtained for  $h = 0.5$  and 2 s. The PSD function obtained by integrating  $S_{w_{n_1, n_1}}(f, \tau)$  over the time domain is also presented in Figure 5.1c. As shown in Figure 5.1b, the smoothed PSD obtained based on FT matches the target PSD well; the unsmoothed PSD function fluctuates around the target PSD function. The results presented in Figure 5.1c indicate that the PSD function obtained based on STFT is close to the target if  $h$  is large, but deviates from the target if the window width is small.

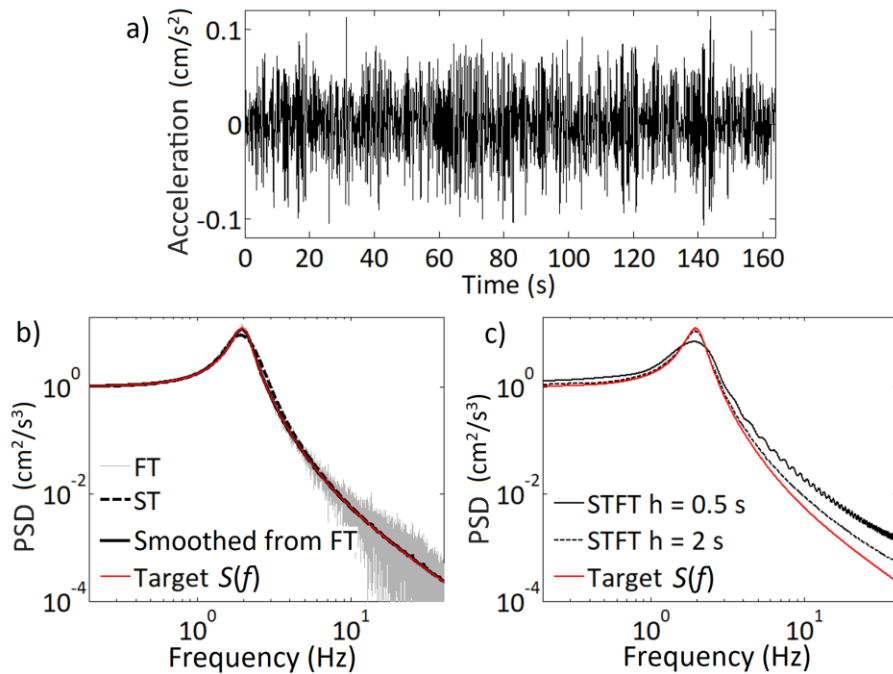


**Figure 5.1:** Sampled record and estimated PSD functions by using FT, STFT, and ST: a) Sampled record, b) Comparison of the target and estimated PSD by using FT and ST, and c) Comparison of the target and estimated PSD by using STFT.

To have better resolution, unless otherwise indicated, the numerical evaluation of the coherence in this chapter is to be carried out using ST (Stockwell et al. 1996) (i.e., Fourier transform with the TF-dependent window) defined as,

$$x_{S_{n_1}}(f, \tau) = ST(x_{n_1}(t)) = \int_{-\infty}^{\infty} x_{n_1}(t) w(f, \tau - t) e^{-i2\pi ft} dt, \quad (5-11)$$

where  $x_{S_{n_1}}(f, \tau)$  is the ST coefficient of  $x_{n_1}(t)$ ,  $ST(\cdot)$  denotes the S-transform, and the TF-dependent window  $w(f, \tau - t)$  is given by,

$$w(f, \tau - t) = \frac{|f|}{\sqrt{2\pi\kappa}} \exp\left(-\frac{f^2(\tau - t)^2}{2\kappa^2}\right). \quad (5-12)$$

in which  $\kappa$  is a parameter of the window. The inverse ST transform,  $IST(\cdot)$ , is given by,

$$x_{n_1}(t) = IST(x_{S_{n_1}}(f, \tau)) = \int_{-\infty}^{\infty} \left[ \int_{-\infty}^{\infty} x_{S_{n_1}}(f, \tau) d\tau \right] e^{i2\pi ft} df. \quad (5-13)$$

showing that the integration of the ST coefficients over time equals the Fourier coefficients. Similar to FT and STFT, the evaluation of the ST coefficient for the discrete time series can be carried out at  $(t_p, f_k)$  by using FFT (Yan and Zhu 2011; Battisti and Riba 2016).

In this case, the definition of the TFPSD  $S_{S_{n_1 n_2}}(f, \tau)$ , time-varying intensity  $I_{S_{n_1}}(\tau)$ , and the TF-dependent coherence  $\gamma_{S_{n_1 n_2}}(f, \tau)$  are defined using Eqs. (5-7), (5-9) and (5-10) except that the subscript  $\mathcal{W}$  is replaced by  $\mathcal{S}$  and Eq. (7) is replaced by

$$S_{S_{n_1 n_2}}(f, \tau) = x_{S_{n_1}}(f, \tau) x_{S_{n_2}}^*(f, \tau) / \left( \sqrt{D_{S_{n_1}}} \sqrt{D_{S_{n_2}}} f \right). \quad (5-14)$$

where  $S_{S_{n_1 n_2}}(f, \tau) = S_{S_{n_1 n_2}}^*(-f, \tau)$ ,  $f$  in the denominator is necessary to ensure the energy conservation for  $n_1 = n_2$ , and  $D_{S_{n_1}}$  can be evaluated numerical and can be approximated

by  $1/\left(\kappa\sqrt{4\pi}\right)$  with an error less than 1.3% for  $\kappa = 1$  (Hong 2020). As an example, for the sampled record shown in Figure 5.1a, by applying Eq. (5-14) and integrating  $S_{S_{n_1 n_1}}(f, \tau)$  over the time domain, the obtained PSD function is also presented in Figure 5.1b. The comparison shown in the figure indicates that the obtained PSD function matches the target PSD function well.

## 5.3 Estimation of TF-dependent spectra and coherence

### 5.3.1 Considered seismic ground motion records

For the evaluation of the TF-dependent coherence, sets of ground motions recorded from the LSST and SMART-1 arrays for several seismic events that were used and discussed in Liu and Hong (2016) are considered in the following. The sets of records are listed in Table 5.1 for easy reference; the location of the arrays is depicted in Figure 5.2. Similar to their study, the baseline correction and fourth-order Butterworth filter with low-cut corner frequency equal to 0.2 Hz are applied to the records, and the wave passage effect is removed from the paired records within the LSST array or within the SMART-1 array to assess the coherence. The consideration of the paired records only within the LSST array or within the SMART-1 array is because the sampling rate is 0.005 for the former and 0.01 s for the latter. In addition, only the records for the sensors oriented in the same horizontal direction (i.e., East-West (E-W) or North-South (N-S)) are considered.

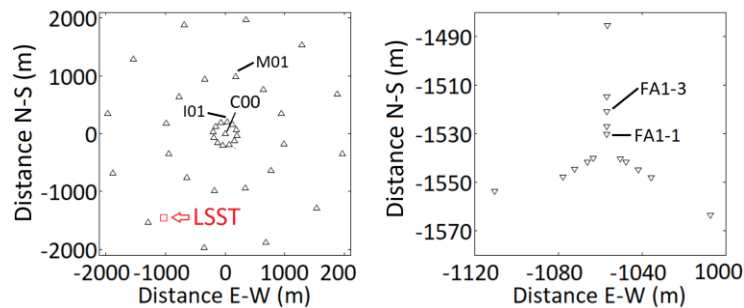


**Figure 5.2:** Layouts of LSST (right) and SMART1 (left) array located in Lotung, Taiwan.

**Table 5.1:** Selected seismic events recorded on LSST array and SMART-1 array (see Liu and Hong (2016) for additional detail).

Seismic Event	Data (YY,MM,DD)	Lat. ( $^{\circ}$ )	Lon. ( $^{\circ}$ )	Mag. ( $M_L$ )	Event No.*	
					LSST	SMART-1
SE-1	1985.10.26	121.84	24.42	4.7	2	37
SE-2	1986.01.16	121.97	24.77	6.1	4	39
SE-3	1986.05.20	121.60	24.09	6.2	7	40
SE-4	1986.07.30	121.80	24.64	5.8	12	43
SE-5	1986.11.14	121.84	24.00	6.8	16	45

### 5.3.2 Estimated coherence

To show the differences in the estimated coherence by using the three mentioned transforms in the previous section, and to identify a few salient features of the frequency-dependent coherence versus the TF-dependent coherence, consider a pair of records shown in Figures 5.3a and 5.3b with separation distance equal to 5 m. The time-varying intensity of the record  $I_{s_{n_1}}(\tau)$  that is also shown in the plots will be discussed shortly.

By applying FT, the obtained PSD functions, the lagged coherence and phase angle of the coherence are shown in Figures 5.3c to 5.3e. Since the use of different windows with the same window width leads to the similar results (Zerva 2009), for simplicity and without loss generality, a boxcar window with  $M = 15$  (see Eq. (5-5)) is used throughout this chapter for the numerical evaluation of the smoothed spectra and coherence if the FT is used. As can be observed from the plots, the PSD functions from the two records are similar, and the lagged coherence decreases with increasing frequency, a trend that is reported already in the literature (e.g., Luco and Wang 1986; Harichandran and Vanmarcke 1986, Hao et al. 1989).

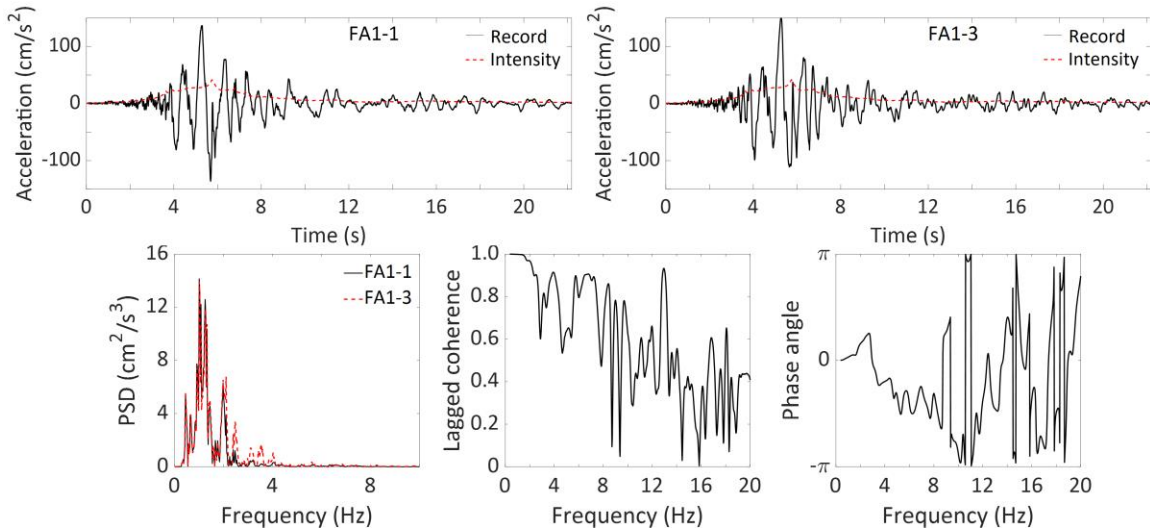


**Figure 5.3:** Records from station FA1-1 and FA1-3 for SE-2, and estimated (doubled-sided) PSD, lagged coherence, and phase angle of coherence.

If the STFT shown in Eq. (5-6) is employed for the pair of records shown in Figures 5.3a and 3b, the obtained results are shown in Figure 5.4.  $h$  equals 0.5 s and 2 s are considered to see the effect of  $h$  in the windowed Fourier transform on the estimated spectra and coherence. Before the evaluation of the cross PSD function using the windowed Fourier transform, one of the paired records is time-shifted such that the sum of the product of records after the shift is maximized. This is aimed at eliminating the wave passage effect and is done throughout the remaining analysis. Similar to the case based on the ordinary Fourier analysis, for simplicity, a boxcar window is used to estimate the smoothed spectra employed in calculating the coherence. The widths of the boxcar along the frequency axis and along the time axis are taken equal to 31 points for the numerical analysis in the following if STFT defined in Eq. (5-6) or ST defined in Eq. (5-11) are employed. The results presented in Figure 5.4 show that the use of STFT provides time and frequency localization of the energy of the records and coherence. This overcomes the drawback of using FT, which only provides the frequency characterization of the energy and lagged coherence. The plots of the TFPSD functions

show the time localization of the energy of the records. As  $h$  increases, the time localization of the energy is smeared over the time axis, and the resolution in time is decreased. This is expected, as explained earlier. It emphasizes that the resolution at the low frequencies deteriorates by using a narrower window because the long waves are better represented by records with long durations. The resolution at the high frequencies deteriorates by using a wider window because the increased window width cannot capture the temporal resolution of high frequencies waves. The calculated lagged coherence is sensitive to the window width  $h$ .

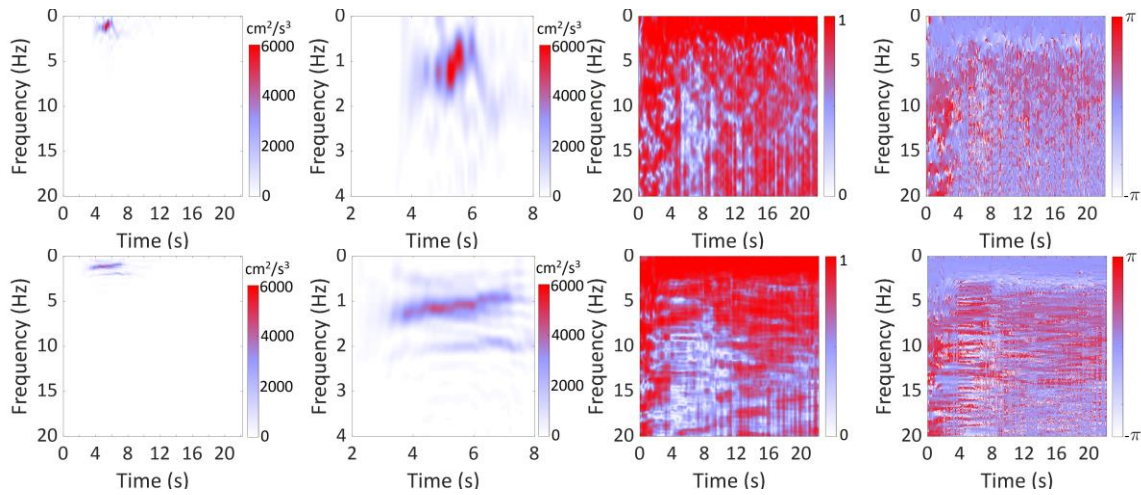


**Figure 5.4:** Estimated TFPSD (unit:  $\text{cm}^2/\text{s}^3$ ) and coherence by using STFT for the records shown in Figures 5.2a and 5.2b. The first and second rows show the results for  $h = 0.5$  and  $2.0$  s of the records at station FA1-1 of SE-2, respectively. The first column shows TFPSDF, the second column shows the TFPSDF in detail, the third column depicts the lagged coherence between records FA1-1 and FA1-3, and the fourth column presents the phase angle of the coherence.

By applying ST, the calculated TFPSD and the TF-dependent coherence for the two records shown in Figures 5.3a and 5.3b are shown in Figure 5.5. For the analysis,  $\kappa = 1, 2,$  and  $3$  are employed to illustrate the effect of the “bandwidth” parameter  $\kappa$  on the



estimated TF-dependent spectra and coherence. As can be observed from Figure 5.5, the increase in  $\kappa$  leads to decreased resolution of the TFPSD in time. However, the differences in the obtained TFPSD functions can be large by using  $\kappa$  equal 1 and 3. It appears that the estimated lagged coherence is much less sensitive to the value of  $\kappa$ . There are differences between the results shown in Figures 5.4 and 5.5. The energy shown in Figure 5.5 for frequencies lower than about 4 Hz is more widely spread in time than that in Figure 5.4. These observations show the advantages of using ST: it provides good resolution at lower frequency and time localization of the energy at high frequencies. Based on the above discussion, the use of the ordinary Fourier transform and STFT will not be considered further in the following numerical analysis. Moreover, since the use of different  $\kappa$  values can lead to different TFPSD and lagged coherence functions, the results obtained by using different  $\kappa$  values are not interchangeable. In the following, only  $\kappa = 1$  is considered to keep the numerical analysis to a manageable size, so to concentrate on the characterization of the TF-dependent coherence.

To identify the effect of the separation of the recording stations on the coherence, consider three records from the same seismic event that are shown in Figures 5.6a to 5.6c. The calculated time-varying intensity of the record  $I_{S_{n_i}}(\tau)$  is also included in each of the plots. The separation between C00 and I01, between I01 and M01 and between C00 and M01 are 200, 800, and 1000 m, respectively. The analysis that is carried out for the results presented in Figure 5.5 is repeated by using the three records shown in Figure 5.6. The obtained TFPSD and lagged coherence functions of the paired records among the three records are also shown in Figure 5.6. Note that the lagged coherence in the low frequencies for C00-M01, and I01-M01 is lower than that in the high frequencies for the time interval around 10 to 15 seconds. It was attributed to the sample-to-sample variability, as will be seen, this observed trend differs from that observed based on the average values of lagged coherence. As can be observed from the figure, the energy concentration in time is consistent with the time-varying  $I_{S_{n_i}}(\tau)$ . In all cases, the PSD and lagged coherence depend on time and frequency. Most importantly, the time dependency of the lagged coherence shown in Figure 5.6 is much more pronounced as compared to that shown in Figure 5.5. It suggests that the time dependency of the lagged

coherence for separation greater than 100 m should not be neglected, and the magnitude of lagged coherence depends on  $I_{S_{n_1}}(\tau)$ . The results also show that the lagged coherence decreases as the separation increases.

To further illustrate the time-dependency of the lagged coherence to the time-varying intensity, frequency, and separation, the analysis that is carried for the results presented in Figure 6 is repeated by considering the records recorded at station I01, I06, and M01 of the 5 events listed in Table 1. The calculated time-varying intensity, as well as the lagged coherence, are shown in Figure 7. The plots in the figure indicate that the lagged coherence for each event between the same paired records differs. This is viewed as the sample-to-sample variability. However, in general, the average of the lagged coherence decreases with increasing frequency or with decreasing separation. Most importantly, the average of the lagged coherence is larger at high-intensity values.

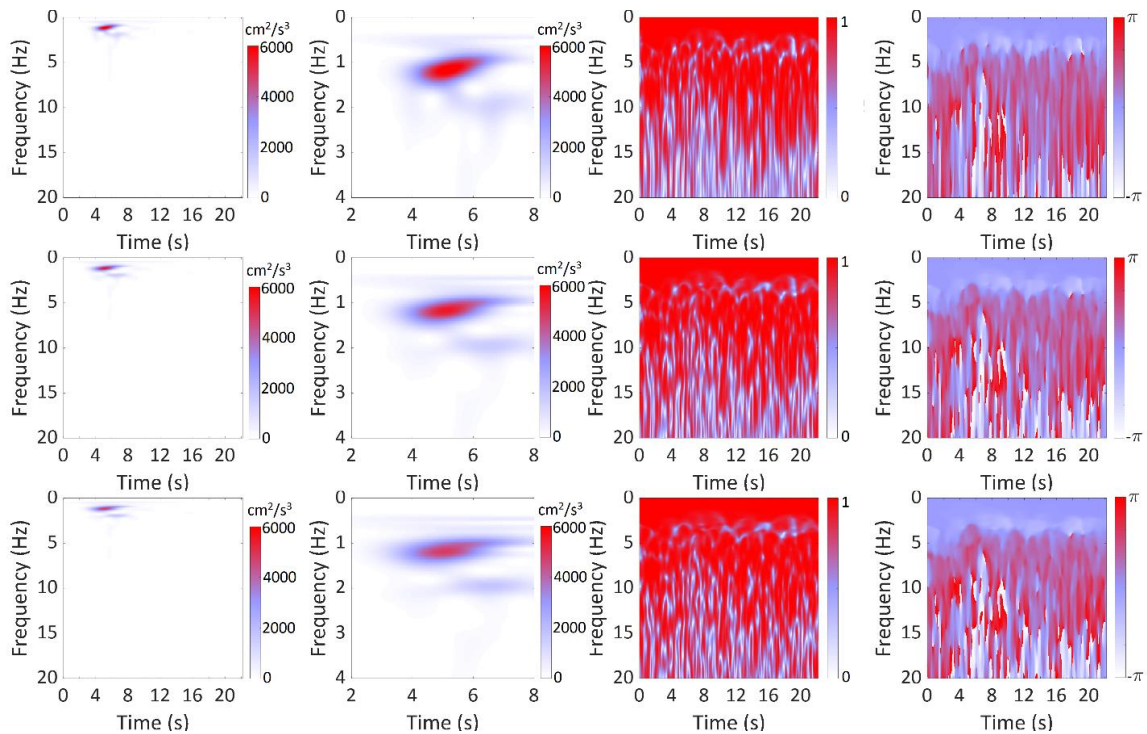


**Figure 5.5:** Effects of  $\kappa$  on the TFPSD (unit:  $\text{cm}^2/\text{s}^3$ ) and coherence functions by using ST for the two records shown in Figures 5.2a and 5.2b. The first, second, and third rows show the results for  $\kappa$  equal to 1, 2, and 3, respectively. The first column shows TFPSD,

the second column shows the TFSDF in detail, the third column depicts the lagged coherence, and the fourth column presents the phase angle of the coherence.

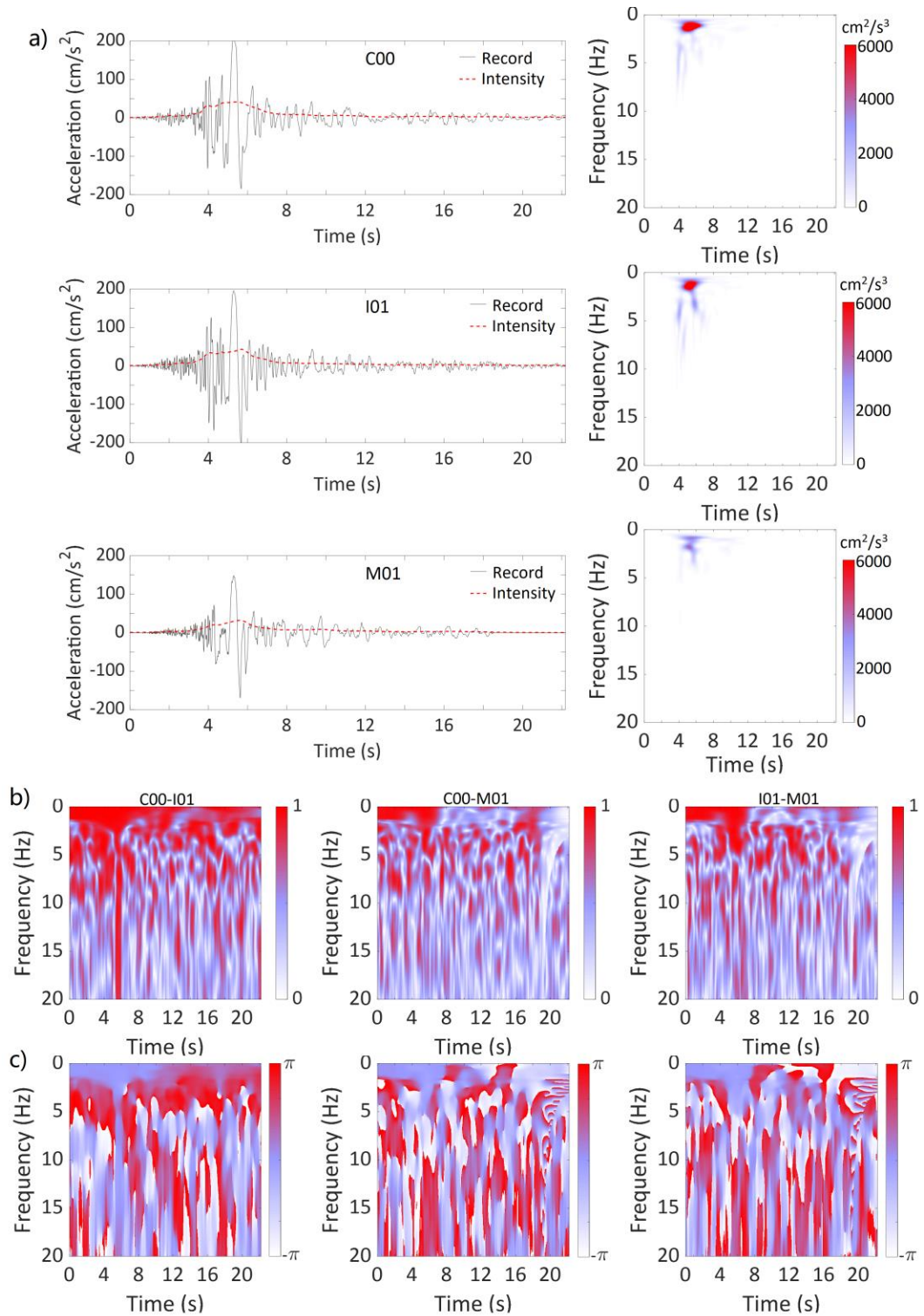


**Figure 5.6:** Records from the stations C00, I01, and M01 for the event SE-2, and estimated TFPSD and lagged coherence functions: a). Records and their TFPSD function (unit:  $\text{cm}^2/\text{s}^3$ ), b) lagged coherence function, and c) wrapped phase angles.

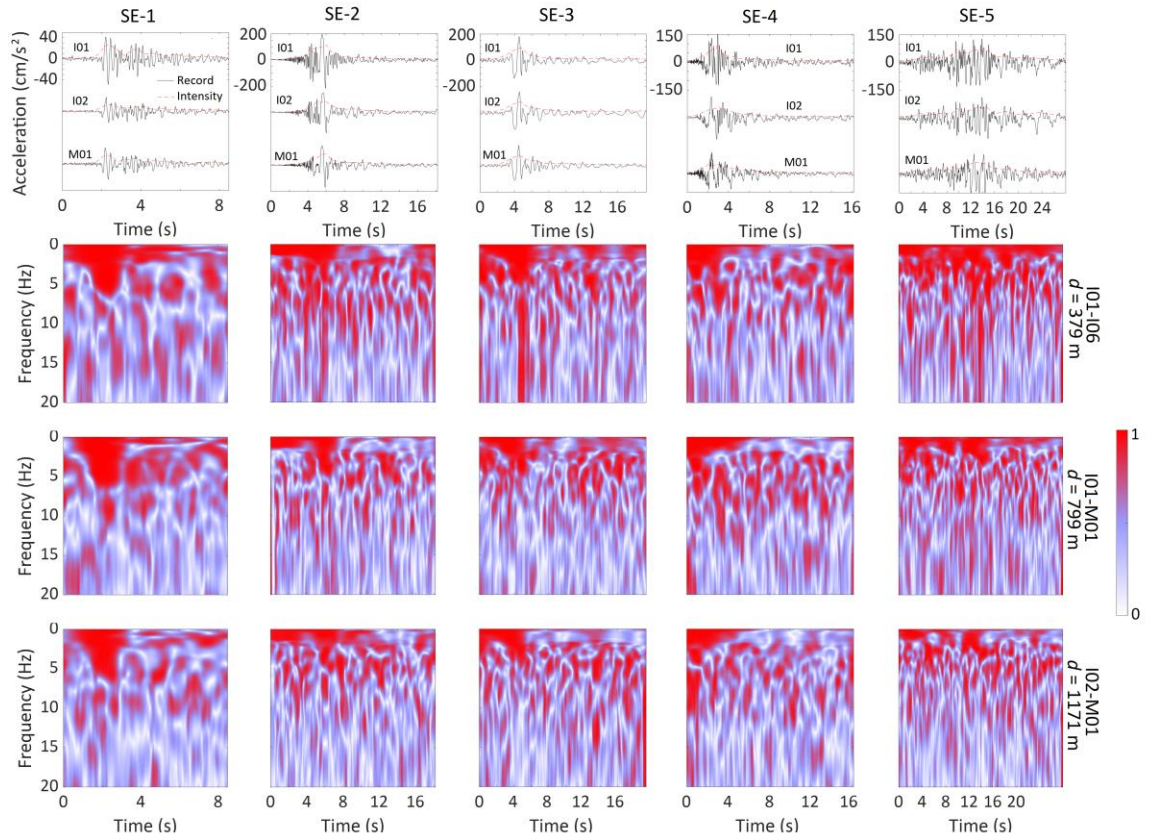


**Figure 5.7.** Records at stations I01, I06 and M01 from each of the 5 events listed in Table 1, and the calculated values of the lagged coherence.

### 5.3.3 Proposed TF-dependent lagged coherence model

Results in the previous section indicate that the lagged coherence depends on the intensity, which is a function of time. This is unlike the well-known models proposed in the literature (see introduction) that are obtained based on FT. The results shown in Figures 5.5 to 5.7 also indicate that the magnitude of the lagged coherence depends on  $I_{S_{n_1}}(\tau)$  as mentioned earlier.

To further investigate such a relation, first, it is noted that the scaling of the records by a constant does not alter the coherence function. Consider two records  $x_{n_1}(\tau)$  and  $x_{n_2}(\tau)$  with wave passage effect removed. Define the normalized time-varying ground motion intensity  $I_{N_{n_1 n_2}}(\tau)$  for the two records as

$$I_{N_{n_1 n_2}}(\tau) = \frac{1}{2} \left( \frac{I_{S_{n_1}}(\tau)}{\max(I_{S_{n_1}}(\tau))} + \frac{I_{S_{n_2}}(\tau)}{\max(I_{S_{n_2}}(\tau))} \right). \quad (5-15)$$

Based on this definition,  $I_{N_{n_1 n_2}}(\tau)$ , has a value within 0 and 1. Using this normalized intensity, the values of the estimated lagged coherence plotted in the  $f$ - $\tau$  domain in Figures 5.5 and 5.6 are replotted in the  $f$ - $I$  domain in Figure 5.8, where the simplifying notation  $I = I_{N_{n_1 n_2}}(\tau)$  is used. For the plotting, a squared box window is applied to provide a smoothed plot. The results presented in Figure 5.8 exhibit an identifiable pattern in the  $f$ - $I$  domain. It shows that the large magnitude of the lagged coherence is located in regions with low frequencies and high-intensity values and depends on the separation.

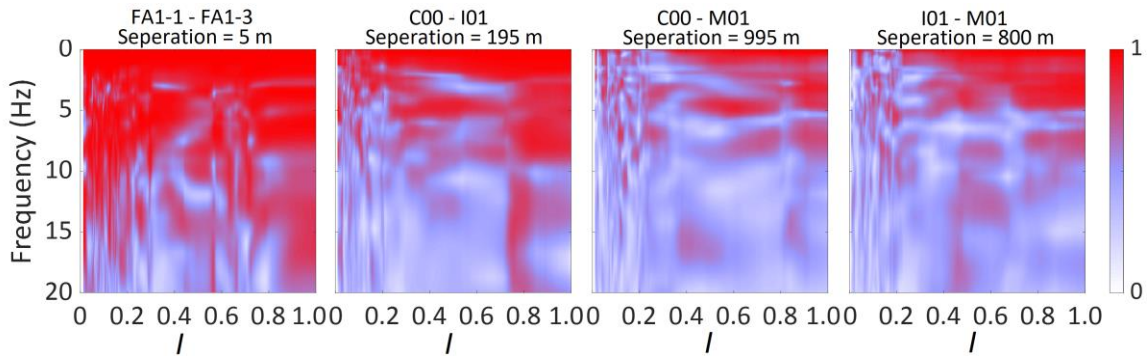


**Figure 5.8:** Lagged coherence shown in Figure 5.5 and 5.6 plotted in  $f$ - $I$  domain.

Based on the above observations, one could develop a lagged coherence model in terms of frequency and separation as well as  $I$  instead of time. In other words,



$|\gamma_{S_{n_1 n_2}}(f, \tau)|$  can be expressed as,

$$|\gamma_{S_{n_1 n_2}}(f, \tau)| = |\gamma_{S_n}(f, I, d)|, \quad (5-16)$$

where  $d = d_{n_1, n_2}$  in m denotes the separation between the recording sites for  $x_{n_1}(\tau)$  and  $x_{n_2}(\tau)$ .

As pointed out by Abrahamson et al. (1991), the statistical properties of lagged coherence  $|\gamma_{\mathcal{F}}(f)|$  are not simple even for stationary processes. The transformed  $|\gamma_{\mathcal{F}}(f)|$ ,  $\tanh^{-1}|\gamma_{\mathcal{F}}(f)|$ , is approximately normal with a bias that can be estimated and removed if  $|\gamma_{\mathcal{F}}(f)|$  is not very small (Enochson and Goodman 1965; Benignus 1969; Abrahamson et al. 1991).

Abrahamson et al. (1991) fitted  $h(f, d)$ , according to  $\tanh^{-1}|\hat{\gamma}_{\mathcal{F}}(f)| = h(f, d) + \zeta$  (see their equation (5-6)) where  $|\hat{\gamma}_{\mathcal{F}}(f)|$  is the estimated lagged coherence, and  $\zeta$  is the bias which depends on the width of the window used to smooth the spectra and was taken equal to 0.35. It is understood that the target lagged coherence to be used to simulate synthetic records should be  $\tanh(h(f, d))$ . Other studies (e.g. Hong and Liu 2014; Liu and Hong 2015, 2016) fitted  $h(f, d)$  directly to the samples of  $\tanh^{-1}|\hat{\gamma}_{\mathcal{F}}(f)|$ . In such a case, the target lagged coherence used for simulation should be  $\tanh[\max(h(f, \tau) - \zeta, 0)]$ . In this chapter, the fitting procedure given in Abrahamson et al. (1991) is followed to develop an empirical model for  $\tanh^{-1}|\gamma_{\mathcal{S}}(f, I, d)|$ .

For the development, first, the analysis that is carried out for a few record-pairs presented in Figure 5.8 is repeated but considering all the records from the events listed in Table 5.1. The estimated mean of the lagged coherence by considering the records is presented in Figure 5.9 for selected separation intervals (i.e.,  $0.9d$  to  $1.1d$ ). The plot shows that the mean of  $|\gamma_{\mathcal{S}}(f, I, d)|$  increases as  $I$  increases or  $f$  decreases. Such clear

trends facilitate the development of an empirical model for  $|\gamma_s(f, I, d)|$ . Since the number of events is so small no statistical analysis of the event to event statistical variability of  $|\gamma_s(f, I, d)|$  is carried out, although an inspection of the obtained results indicates that the estimated mean of  $|\gamma_s(f, I, d)|$  varies from event to event. This observation is consistent with the results obtained from the ordinary Fourier analysis (Liu and Hong 2016). By using the estimated lagged coherence from all events listed in Table 5.1, the estimated mean of  $|\gamma_s(f, I, d)|$  is shown in Figure 5.10a for selected separation intervals, while the estimated mean of  $\tanh^{-1}|\gamma_s(f, I, d)|$  is presented in Figure 5.10b. The results presented in Figure 5.10a confirm the trends mentioned for Figure 5.8. The estimated mean of  $\tanh^{-1}|\gamma_s(f, I, d)|$  also increases as  $I$  increases or  $f$  decreases. This is expected since  $\tanh^{-1}[\square]$  is a monotonic increasing transformation. Further inspection of the results shown in Figure 5.10 indicates that the mean of  $\tanh^{-1}|\gamma_s(f, I, d)|$  for fixed  $I$  and  $d$  follows an exponential decay as  $f$  increases. It remains almost constant for a given value of  $d$  that is around 20 m and for a given value of  $f$  that is less than about 5 Hz; this, however, is not the case for a given value of  $d$  that is greater than about 100 m. Also, the mean of  $\tanh^{-1}|\gamma_s(f, I, d)|$  is small and almost insensitive to the values of  $I, f$  and  $d$  for the region where  $f$  is higher than about 10 Hz, and  $d$  is larger than about 100 m.

Based on the above consideration and observations, the following functional form is used to fit  $\tanh^{-1}|\gamma_s(f, I, d)|$ ,

$$\tanh^{-1}|\gamma_s(f, I, d)| = h(f, I, d) + \zeta, \quad (5-17)$$

where,

$$h(f, I, d) = \exp\left[a_1 + a_2 d + (a_3 + a_4 d) f^b\right] \times \left[1 - (c_1 - c_2 I^{\lambda_I}) \left(1 - \exp(-(d/d_0)^{\lambda_d})\right)\right] \quad (5-18)$$

and  $[a_1, a_2, a_3, a_4, b, c_1, c_2, \lambda_I, d_0, \lambda_d]$  are model parameters to be determined through

regression analysis, and  $\zeta$  is set equal to 0.21 because the window width used to smooth the spectra in this chapter is wider than that used in Abrahamson et al. (1991). The estimated values of  $[a_1, a_2, a_3, a_4, b, c_1, c_2, \lambda_I, d_0, \lambda_d]$  through nonlinear regression analysis by considering the sampled means obtained by using the records from the listed events shown in Table 5.1 are  $[0.78, -3.14 \times 10^{-4}, -0.16, -2.25 \times 10^{-5}, 0.8, 0.54, 0.54, 1.84, 48.6, 5.0]$ . A comparison of the fitted model to the samples is shown in Figure 5.11 for a function of frequency and selected combinations of separation and intensity. It is observed that, in general, the fitted model represents well the trends of the samples. The deviation at low frequency is relatively large as compared to that for high frequencies. However, since the function  $\tanh(y)$  for  $y$  greater than about 1.5 is relatively insensitive to  $y$  (e.g.,  $\tanh(y)$  equals 0.91, 0.92, and 0.96 for  $y = 1.5, 1.6,$  and  $2,$  respectively), a relatively large deviation at high values of  $\tanh^{-1}|\gamma_s(f, I, d)|$  shown in Figure 5.11 is deemed acceptable. It should be noted that the consideration of  $f, I$  and  $d$  dependent residuals for the nonlinear regression analysis is of interest but beyond the scope of this chapter. Also, it should be understood that the target lagged coherence is to be calculated using  $\tanh(h(f, I, d))$  if the proposed model is adopted.



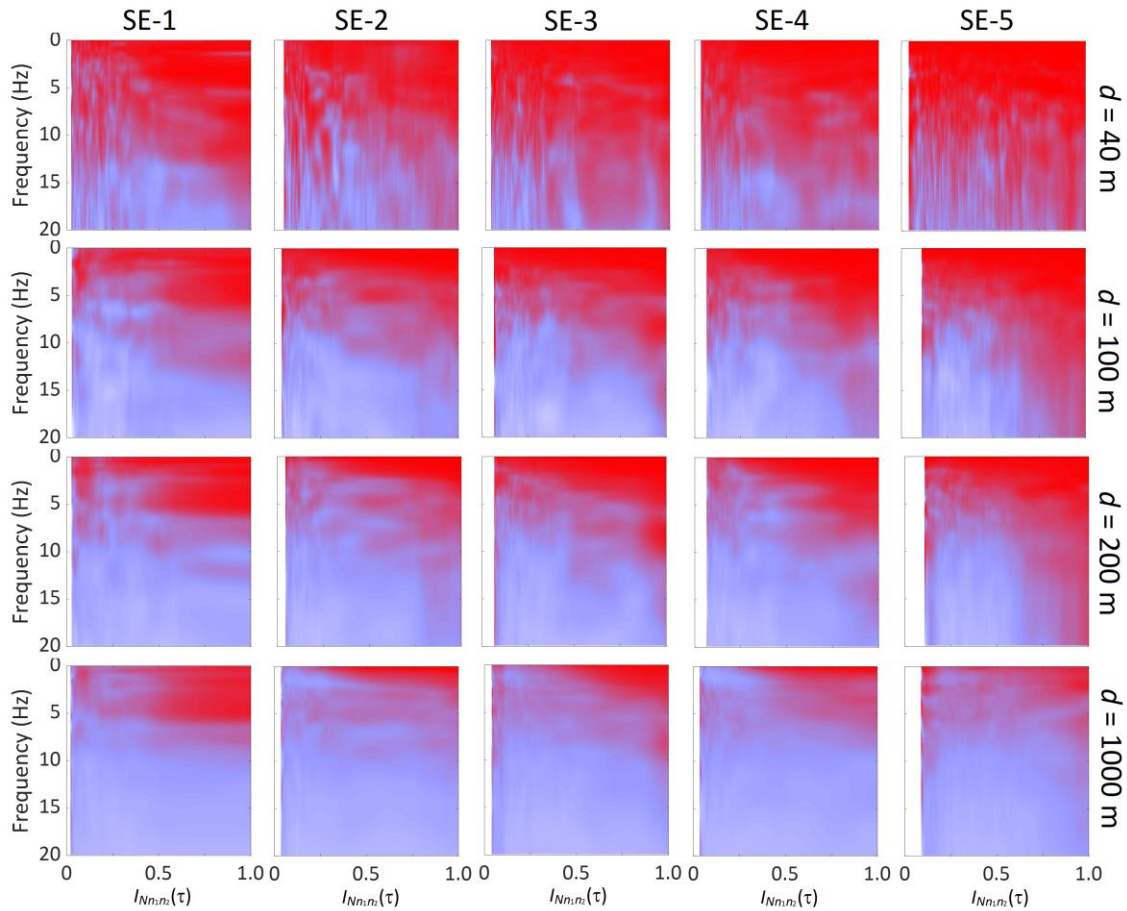


**Figure 5.9:** Mean of the estimated  $|\gamma_S(f, I, d)|$  by considering records from the events listed in Table 5.1 and for selected  $d$  values.

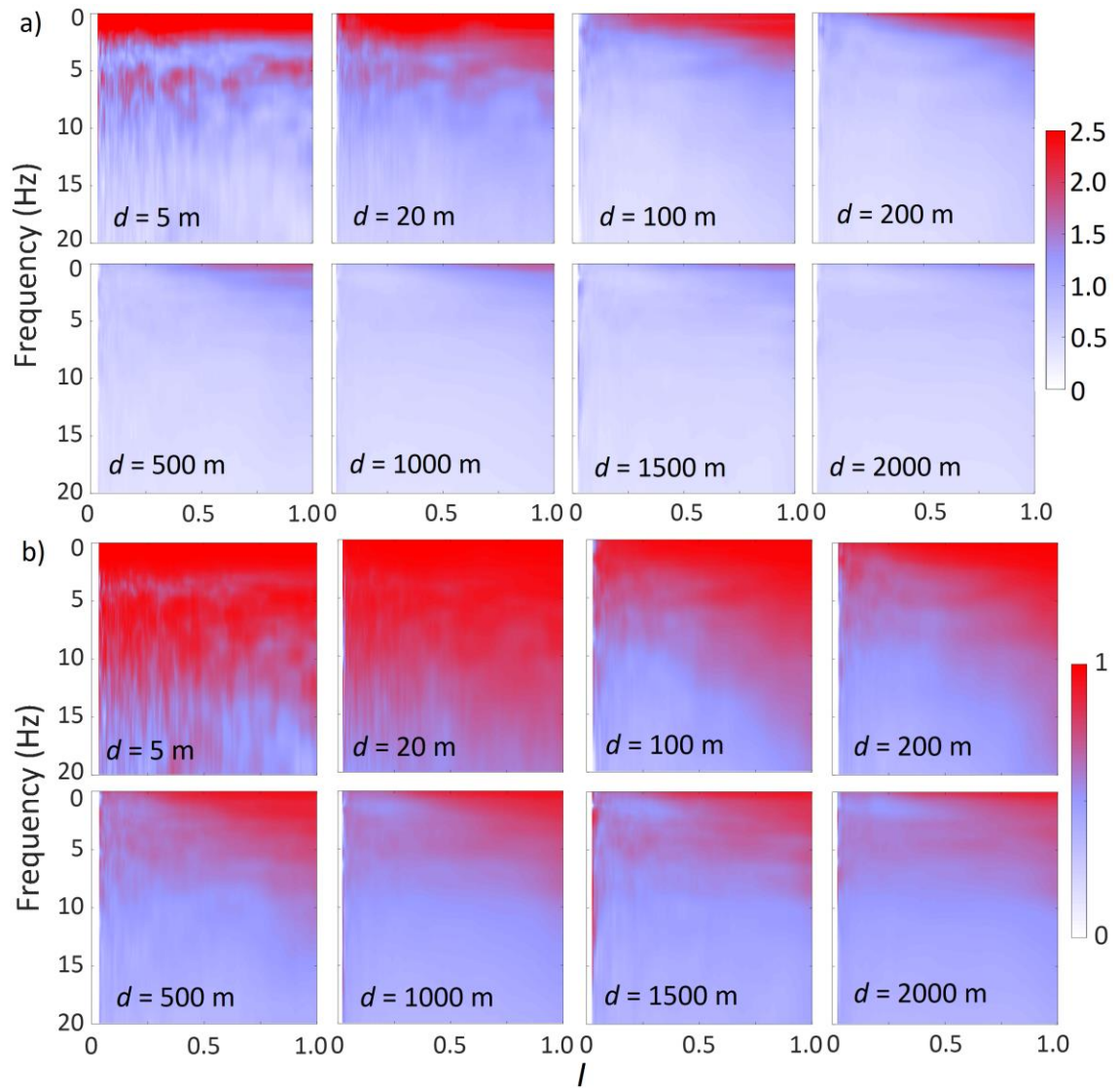


**Figure 5.10:** a) Mean of  $\tanh^{-1}|\gamma_S(f, I, d)|$ , and b) mean of  $|\gamma_S(f, I, d)|$  plotted in  $f$ - $I$  domain by considering records described in Table 5.1 for different  $d$  values ranging from 5 to 2000 m.

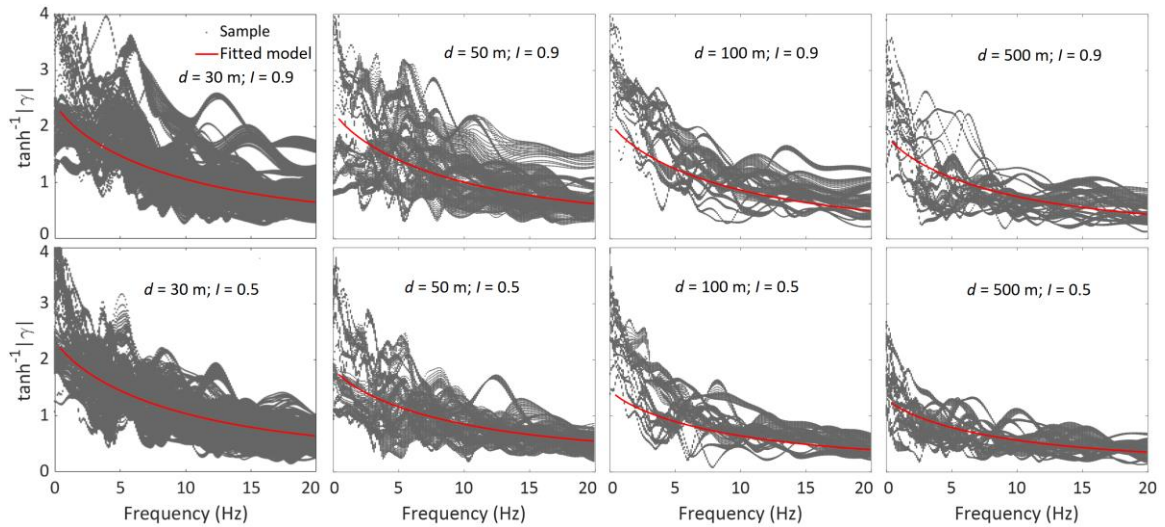


**Figure 5.11:** Comparison of the fitted model and samples for selected combinations of separation and intensity.

This developed empirical model is plotted in Figure 5.12. A comparison of the results shown in Figure 5.12 to those in Figure 5.10 indicates that the empirical model provides an adequate representation of the estimated lagged coherence from the actual records. Note that a simple plot of the developed TF-dependent lagged coherence model differs from the frequency-dependent coherence models. This is expected as the latter does not take into account the time-varying amplitude and frequency contents. The application of the developed TF dependent model is presented in the next section.

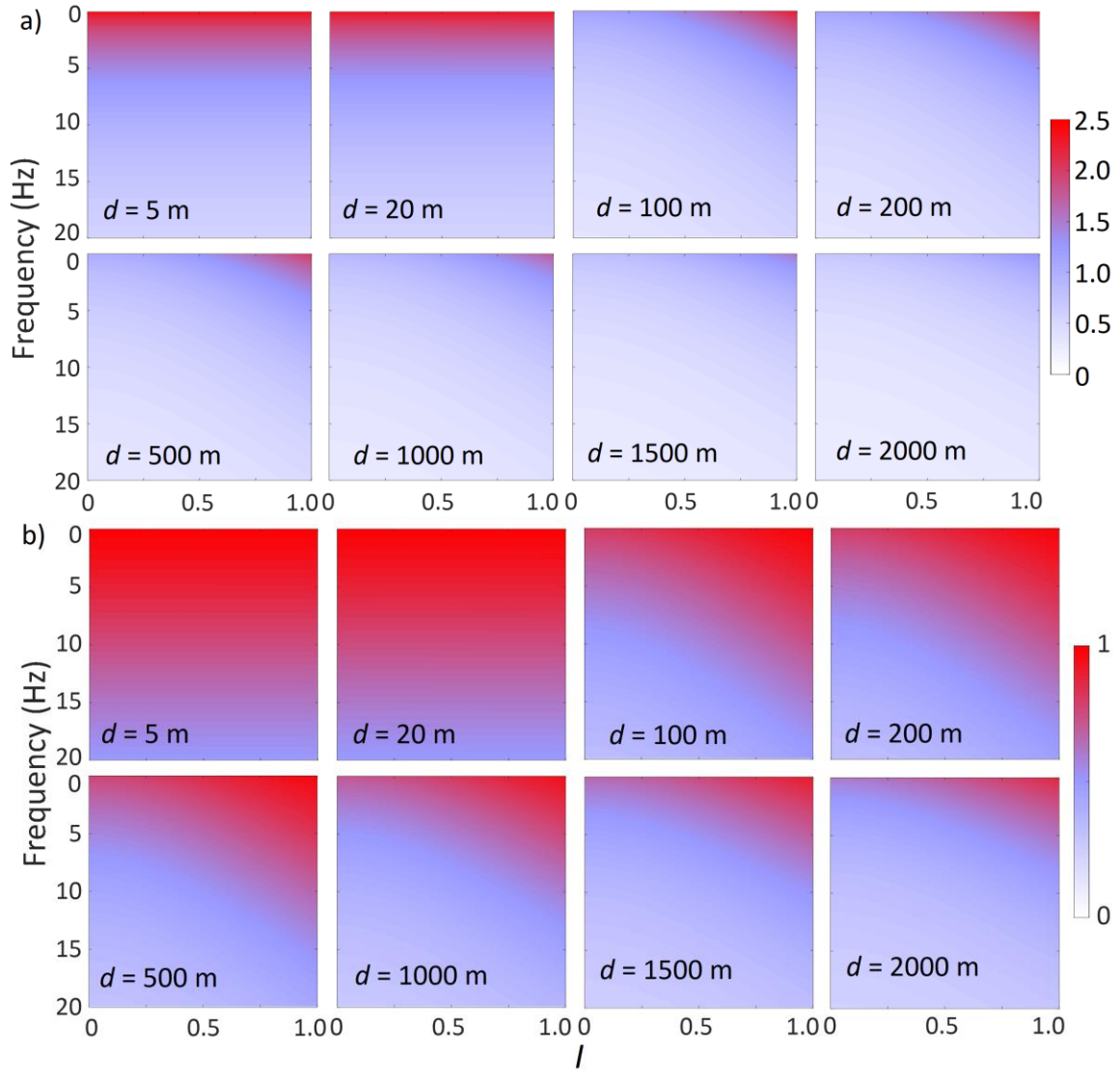


**Figure 5.12:** Predicted  $|\gamma_s(f, I, d)|$  and  $\tanh^{-1}|\gamma_s(f, I, d)|$  by using the empirical model shown in Eq. (5-17) with the estimated model parameters.

## 5.4 Numerical example applications

### 5.4.1 Method to simulate ground motions for given target TFPD functions

Given the target TFPD and the coherence functions for  $n$  points, the ground motion

records at multiple points can be simulated using a simulation model (i.e., time-frequency spectral representation method (TFSRM)) in chapter 3 that was developed based on the ST and DOST (Stockwell et al. 2003; Stockwell 2007). More specifically, let  $\mathbf{M}_{ST}(f, \tau)$  denote the  $n \times n$  TFPSD matrix with the  $(n_1, n_2)$ -th element denoted as  $S_{Tn_1n_2}(f, \tau)$  given by,

$$S_{Tn_1n_2}(f, \tau) = \gamma_{TSn_1n_2}(f, \tau, d_{n_1n_2}) \sqrt{S_{Tn_1n_1}(f, \tau) S_{Tn_2n_2}(f, \tau)}, \quad (5-19)$$

where  $n_1, n_2 = 1, \dots, n$ ,  $S_{n_1n_2}(f, \tau)$  with an additional subscript  $T$  is used to identify that it represents the target and is one-sided (which equals twice of doubled-sided value), and  $\gamma_{TSn_1n_2}(f, \tau, d_{n_1n_2})$  is the target coherence function.

Following the procedure given in chapter 3, the  $f$ - $\tau$  domain is discretized into cells according to the time and frequency localization of DOST. This discretization scheme and numbered cells for a given TFPSD are illustrated in Figure 5.13. The integral of  $S_{Tn_1n_2}(f, \tau)$  over the  $j$ -th cell's time and frequency domain is denoted as  $S_{Tn_1n_2}(j)$ . The matrix  $\mathbf{M}_{ST}(f, \tau)$  is then replaced by its corresponding matrix  $\mathbf{M}_{ST}(j)$  with the  $(n_1, n_2)$ -th element denoted  $S_{Tn_1n_2}(j)$ .  $\mathbf{M}_{ST}(j)$  is decomposed into  $\mathbf{L}(j)\mathbf{L}^H(j)$  based on Cholesky decomposition, where  $\mathbf{L}(j)$  is the lower triangle matrix and the superscript denotes the conjugate transpose (i.e., Hermitian matrix). The record at the  $n_1$ -th point is sampled initially using,

$$x_{init, n_1}(\tau_k) = \sqrt{2} \sum_{m=1}^{n_1} \sum_{j=1}^{N/2} \text{Re} \left[ L_{n_1m}(j) D_1(\tau_k; j) e^{i\theta_m(j)} \right], \quad \text{for } n_1 = 1, \dots, n, \quad (5-20)$$

where  $L_{n_1m}$  denotes the  $(n_1, m)$ -th element of  $\mathbf{L}(j)$ ,  $\theta_m(j)$  are independent and uniformly distributed between 0 and  $2\pi$ , and  $D_1(\tau_k; j)$  are the basis functions used in DOST (Stockwell 2007) in a single-index form. A total of  $N_T$  sets of  $\{x_{init, n_1}(\tau)\}$  is sampled, and the average of TFPSD of  $x_{init, n_1}(\tau)$ ,  $S_{ESn_1n_1}(f, \tau)$ , is calculated. Finally, the records

at the  $n_1$ -th point,  $x_{n_1}(\tau)$ , is then obtained using,

$$x_{n_1}(\tau_k) = IST \left[ \sqrt{S_{T_{n_1 n_1}}(f, \tau) / S_{ES, n_1 n_1}(f, \tau)} \square ST(x_{Init, n_1}(\tau_k)) \right], \quad (5-21)$$

where  $\square$  denotes the point by point multiplication operator in the  $f$ - $\tau$  domain. The use of Eq. (5-21) is aimed at enhancing the time-frequency representation of the simulated record.

To take into account the wave passage effect (Der Kiureghian 1996) in the simulated records in relation to a selected site, say the first site, one could simply apply  $IST \left[ ST(x_{n_1}(\tau_k)) \square \exp(i2\pi f d_{1n_1} / v_{ap}) \right]$  or  $IFT \left[ FT(x_{n_1}(\tau_k)) \square \exp(i2\pi f d_{1n_1} / v_{ap}) \right]$  to obtain the records that include the wave passage effect, where  $FT(\square)$  and  $IFT(\square)$  denote the Fourier transform and its inverse, respectively.

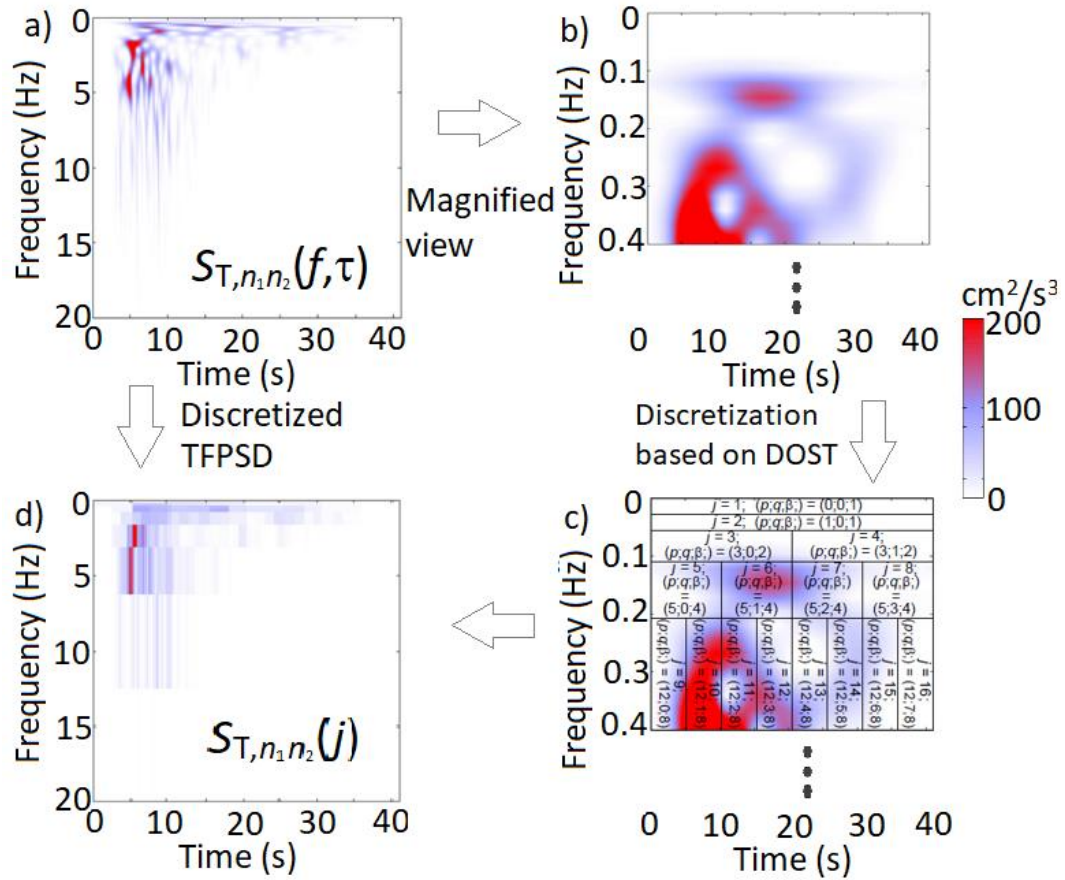


**Figure 5.13:** Illustration of mapping from  $S_{T,n_1,n_2}(f, \tau)$  to  $S_{T,n_1,n_2}(j)$ : a) Target TFPD function, b) Magnified view of TFPD function for a portion of low frequency, c) discretization according to the time and frequency localization of DOST, and d) TFPD associated with DOST representation.

#### 5.4.2 Numerical examples

For the numerical analysis, consider one is interested in simulate ground motions at eight supports for a bridge as illustrated in Figure 5.14 by considering a scenario strike-slip earthquake event with the moment magnitude 7, rupture distance equal to 50 km, and the shear wave velocity in the top 30 m equal to 450 m/s. It is considered that the seismic wave propagates from left to right (i.e., point 1 to point 8) with apparent wave velocity,

$v_{ap}$ , equals 2500 m/s. It is considered that  $\gamma_{TS}(f, \tau, d_{n_1 n_2})$  is defined based on the proposed empirical model shown in Eqs. (5-17) and (5-18), and  $S_{Tn_1 n_1}(f, \tau) = S_T(f, \tau) = S_{Tn_2 n_2}(f, \tau)$ , where,

$$\gamma_{TSn_1 n_2}(f, \tau, d_{n_1 n_2}) = \tanh \left| h \left( f, I_{Nn_1, n_2}(\tau), d_{n_1 n_2} \right) \right|, \quad (5-22)$$

and,

$$S_T(f, \tau) = \frac{E_T \lambda_0(\tau)}{f \sqrt{2\pi\eta(\tau)}} \exp \left[ -\frac{1}{2} \left( \frac{\ln f - \ln F_c(\tau) + \eta^2(\tau)/2}{\eta(\tau)} \right)^2 \right] \quad (5-23)$$

This adopted target  $S_T(f, \tau)$  is sampled based on the model given in chapter 4 for stick-slip earthquakes with the parameters  $E_T$ ,  $\eta(\tau)$ ,  $F_c(\tau)$ , and  $\lambda_0(\tau)$  for the considered scenario event presented in Table 5.2. Based on the adopted TFPSD function, the intensity function that is required for Eq. (5-15) can be calculated numerically using,

$$I_{S_{n_1 n_1}}(\tau) = \int_0^{+\infty} S_T(f, \tau) df \quad (5-24)$$

where  $n_1 = 1, \dots, 8$ . For this numerical example,  $I_{S_{n_1 n_1}}(\tau) = I_{S_{n_1 n_1}}(\tau)$  since  $S_{Tn_1 n_1}(f, \tau) = S_{Tn_2 n_2}(f, \tau)$ . The target TFPSD function for three selected sites and lagged coherence for three paired sites are depicted in Figures 5.15a and 5.15b. Figure 5.15a shows that the target TFPSD function contains the time-varying amplitude and frequency. Figure 5.15b illustrated that the target lagged coherence depends on the intensity, and it decreases as the separation increase.



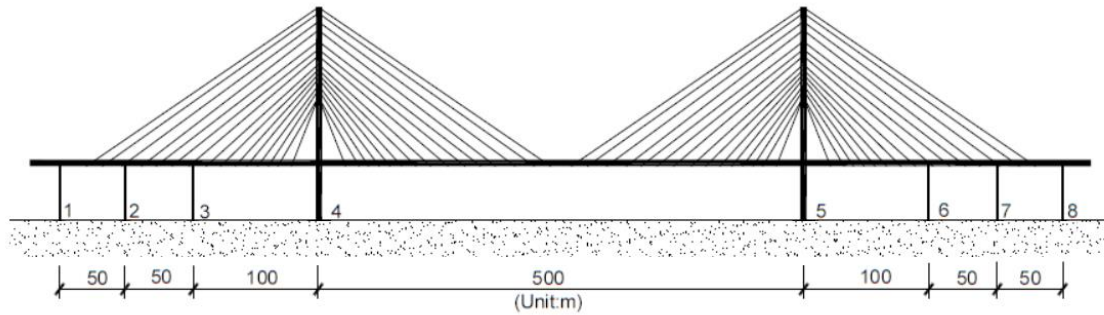


**Figure 5.14:** Layout of the sites for the numerical example.

Using TFSRM described in the previous section, 100 sets of records with  $\Delta\tau = 0.02$  s are simulated. A set of samples of  $x_{n_i}(\tau)$  is illustrated in Figure 5.16a, illustrating their similarity and time-varying amplitude. The calculated average values of the TFPSD function from the sets of the simulated records are shown in Figure 5.16b for three sites, and the calculated average of the lagged coherence for three paired stations are shown in Figure 5.16c. Figure 5.16b indicates that the mean of the TFPSD agrees well with its target. The lagged coherence presented in Figure 5.16c resembles closely to their target depicted in Figure 5.15b. This also corroborates the usefulness of TFSRM as well.

**Table 5.2:** Model parameters for the scenario event. The coefficients shown in the table represent a set of sampled coefficients simulated based on the ground motion model given in Chapter 4).

Model parameters in Eq. (23)	Coefficients
$E_T$ (cm <sup>2</sup> /s <sup>3</sup> )	$E_T = 30866$
$F_c(\tau) = c_1 \exp(-c_2 \tau/T) + c_3$ , where $c_1 = \frac{r_c^2 (F_{c,0} - F_{c,T})^2}{(2r_c - 1)(F_{c,0} - F_{c,T})}$ , $c_2 = -2 \ln\left(\frac{1-r_c}{r_c}\right)$ , and $c_3 = \frac{F_{c,0}F_{c,T} - F_{c,0}^2}{(2r_c - 1)(F_{c,0} - F_{c,T})}$	$r_c = 0.979$ $F_{c,0} = 11.061$ $F_{c,T} = 1.964$
$\eta(\tau) = \sqrt{\ln\left[1 + \left(\frac{F_b(\tau)}{F_c(\tau)}\right)^2\right]}$ , where $F_b(\tau) = b_1 \exp(-b_2 \tau/T) + b_3$ , $b_1 = \frac{r_b^2 (F_{b,0} - F_{b,T})^2}{(2r_b - 1)(F_{b,0} - F_{b,T})}$ , $b_2 = -2 \ln\left(\frac{1-r_b}{r_b}\right)$ , $b_3 = \frac{F_{b,0}F_{b,T} - F_{b,0}^2}{(2r_b - 1)(F_{b,0} - F_{b,T})}$	$r_b = 0.996$ $F_{b,0} = 8.425$ $F_{b,T} = 2.786$
$\lambda_0(\tau) = \frac{\delta T}{\sqrt{2\pi\tau(T-\tau)}} \exp\left[-\frac{1}{2}\left(\gamma + \delta \ln \frac{\tau}{T-\tau}\right)^2\right]$ Where $T = D / (v_{0.95} - v_{0.05})$ , $v_P = \frac{\exp\left[\left(\Phi^{-1}(P) - \gamma\right) / \delta\right]}{1 + \exp\left[\left(\Phi^{-1}(P) - \gamma\right) / \delta\right]}$ , and $\Phi^{-1}(\bullet)$ is the inverse of the normal distribution function.	$\delta = 1.25$ $\gamma = 1.50$

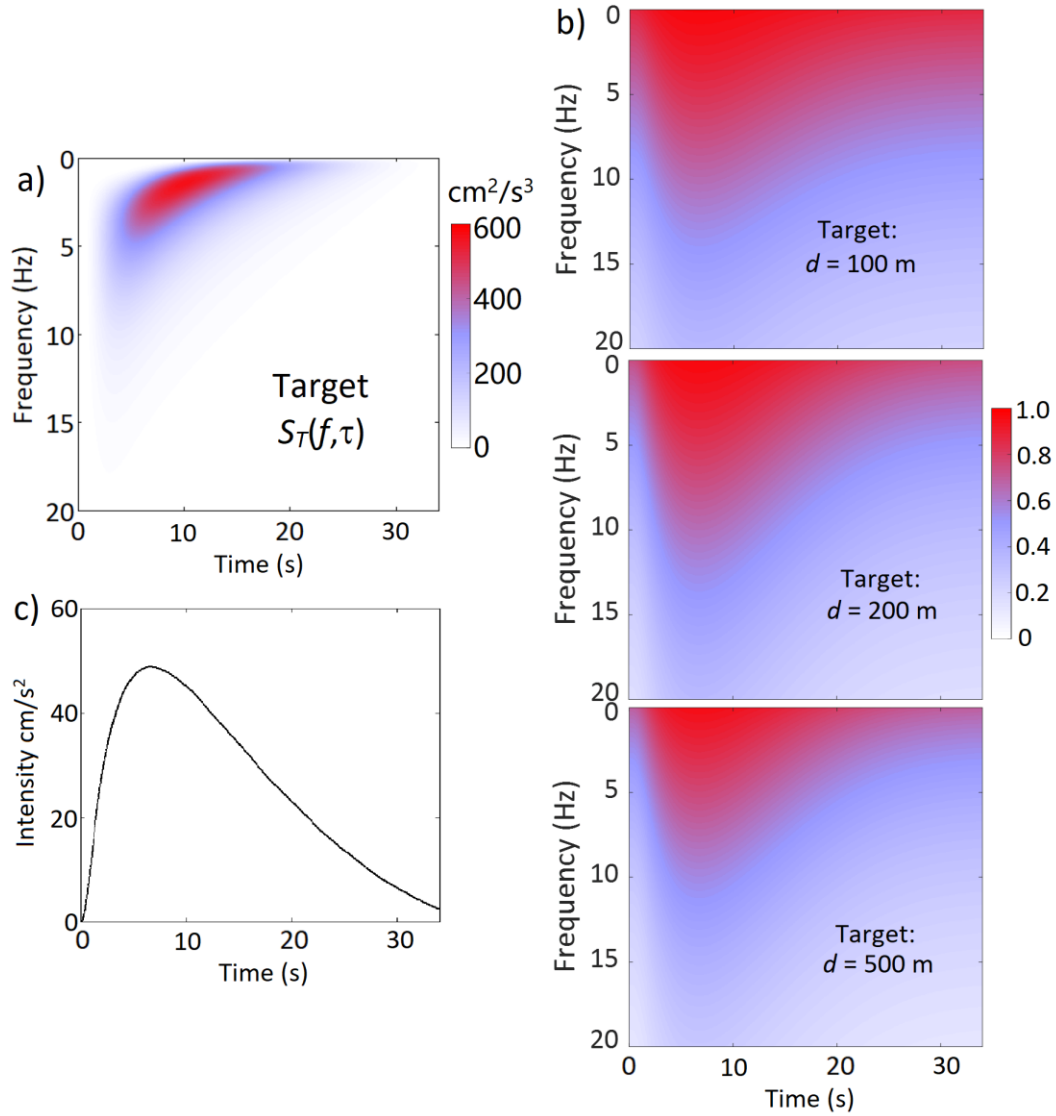


**Figure 5.15:** a) the target TFPSD; b) the target TF-dependent lagged coherence with  $d$  equal to 100m, 200m, and 500m. and c) normalized intensity.

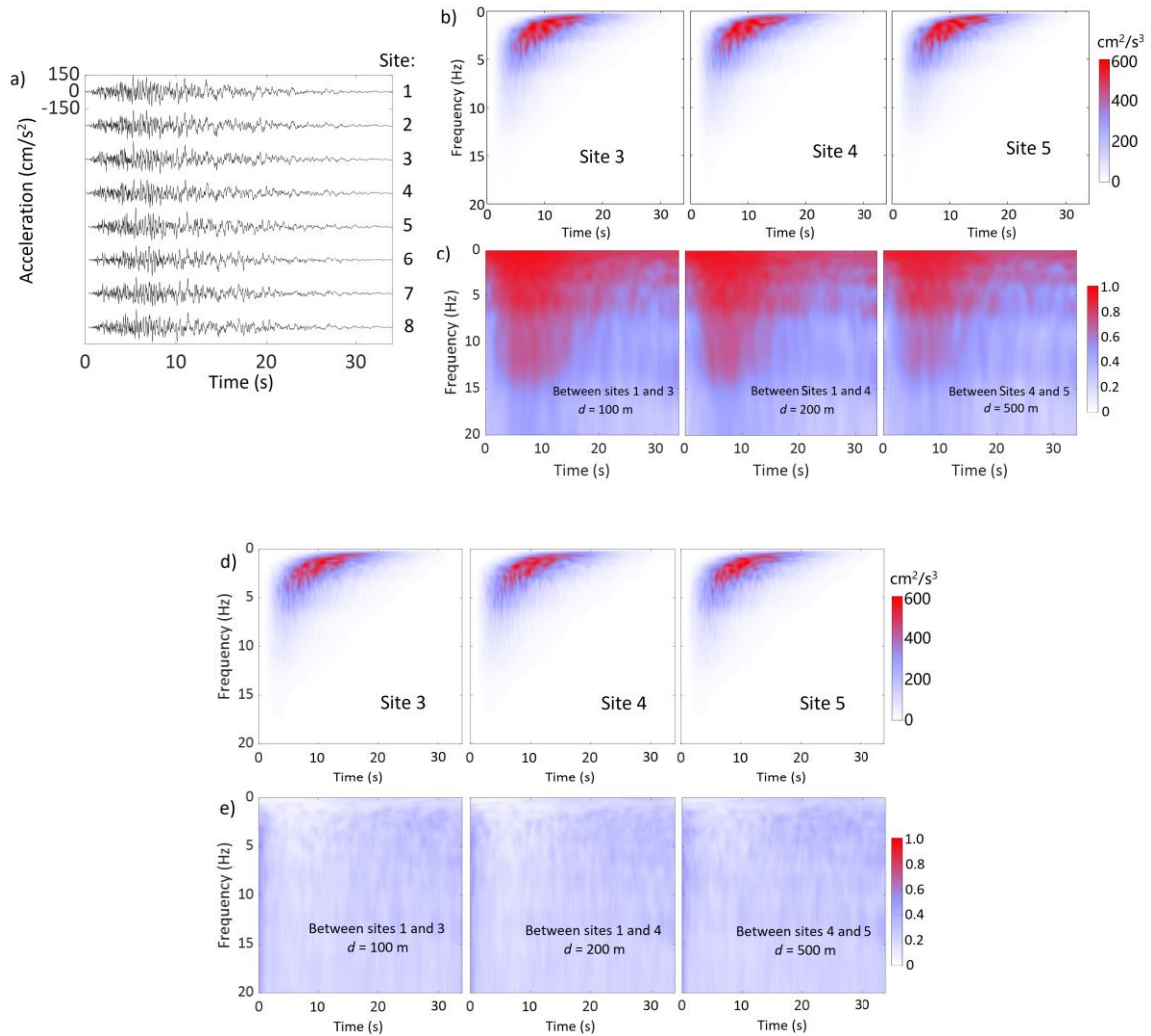


**Figure 5.16:** a) A set of sample of simulated records using Eq (5-20) and Eq (5-21) with wave-passage effect considered; b) mean of TFPSD samples of Sites 3, 4, and 5; c) mean of lagged coherence of simulated samples between 3 pairs of sites with  $d$  equal to 100m, 200m and 500m separately; d) standard deviation of TFPSD samples of Sites 3, 4, and 5; e) standard deviation of lagged coherence of simulated samples between 3 pairs of sites with  $d$  equal to 100m, 200m and 500m separately.

## 5.5 Summary and Conclusions

In this chapter, the time-frequency (TF) dependent (TF-dependent) lagged coherence model for the seismic ground motions is developed. The developed TF-dependent model

is first of its kind since existing models in the literature are frequency-dependent that is only adequate for stationary or amplitude modulation evolutionary process. The development is based on the time-frequency representation and the TF power spectral density function obtained from the S-transform - a TF-dependent windowed Fourier transform. The considered ground motion records for the development are those obtained from the dense arrays in Taiwan (i.e., Lotung Large Scale Seismic Test (LSST) Array and Strong Motion Array in Taiwan (SMART)).

The analysis results show that the lagged coherence decreases with increasing separation or increasing frequency, which is commonly observed based on ordinary Fourier analysis. Most importantly, it is shown that the TF-dependent lagged coherence varies with the time-varying intensity within the duration of the records; a higher normalized intensity corresponds to a higher lagged coherence. This striking feature is included in the developed empirical parametric TF-dependent lagged coherence model (see Eqs. (5-17) and (5-18)). The model is a function of the frequency, the separation between recording sites, and the normalized ground motion intensity that is a function of time. It must be noted that the proposed model is developed based on records from LSST and SMART-1, similar to other available time-independent lagged coherence models, it is assumed that it is applicable for other seismic regions. This assumption needs to be verified by using records from other regions when they become available.

The application of the developed TF-dependent lagged coherence model to simulated nonstationary ground motions at multiple points is presented by using the time-frequency spectral representation method that was developed based on the S-transform and discrete orthonormal S-transform.

## Reference

- Abbas, H., and Tezcan, J. (2019). Relevance vector machines modeling of nonstationary ground motion coherency. *Soil Dynamics and Earthquake Engineering*, 120, 262-272.
- Abbas, H., and Tezcan, J. (2020). Analysis and modeling of ground motion coherency at uniform site conditions. *Soil Dynamics and Earthquake Engineering*, 133, 106124.

- Abrahamson, N. A., Schneider, J. F., and Stepp, J. C. (1991). Empirical spatial coherency functions for application to soil-structure interaction analyses. *Earthquake spectra*, 7(1), 1-27.
- Battisti, U., and Riba, L. (1995). Window-dependent bases for efficient representations of the Stockwell transform. *Applied and Computational Harmonic Analysis*, 40(2), 292-320.
- Benignus, V. (1969). Estimation of the coherence spectrum and its confidence interval using the fast Fourier transform. *IEEE Transactions on Audio and Electroacoustics*, 17(2), 145-150.
- Chiu, H. C., Amirbekian, R. V., and Bolt, B. A. (1995). Transferability of strong ground-motion coherency between the SMART1 and SMART2 arrays. *Bulletin of the Seismological Society of America*, 85(1), 342-348.
- Clough, R. W., and Penzien, J. (1995). *Dynamics of structures*. Computers & Structures, Inc.
- Cohen, L. (1995). *Time-frequency analysis* (Vol. 778). Prentice hall.
- Conte, J. P., and Peng, B. F. (1997) Fully nonstationary analytical earthquake ground-motion model. *Journal of Engineering Mechanics*, 123(1), 15-24.
- Der Kiureghian, A. (1996). A coherency model for spatially varying ground motions. *Earthquake Engineering & Structural Dynamics*, 25(1), 99-111.
- Enochson, L. D., and Goodman, N. R. (1965). Gaussian approximations to the distribution of sample coherence (No. MAC-403-07). MEASUREMENT ANALYSIS CORP LOS ANGELES CA.
- Grigoriu, M., Ruiz, S. E., and Rosenblueth, E. (1988) The Mexico earthquake of September 19, 1985—Nonstationary models of seismic ground acceleration. *Earthquake Spectra*, 4(3),551-568.
- Hao, H., Oliveira, C. S., and Penzien, J. (1989) Multiple-station ground motion processing and simulation based on SMART-1 array data. *Nuclear Engineering and Design*, 111(3), 293-310.
- Harichandran, R. S., and Vanmarcke, E. H. (1986) Stochastic variation of earthquake ground motion in space and time. *Journal of Engineering Mechanics*, 112(2), 154-174.
- Heredia-Zavoni, E., and Santa-Cruz, S. (2000) Conditional simulation of a class of nonstationary space-time random fields. *Journal of engineering mechanics*, 126(4), 398-404.
- Hong, H.P. (2020) Response and first passage probability of SDOF systems subjected to nonstationary stochastic excitation modeled through S-Transform. Submitted to *Structural Safety*.
- Hong, H. P. (2016) Modeling of nonstationary winds and its applications. *Journal of Engineering Mechanics*, 142(4), 04016004.

- Hong, H. P., and Liu, T. J. (2014) Assessment of coherency for bidirectional horizontal ground motions and its application for simulating records at multiple stations. *Bulletin of the Seismological Society of America*, 104(5), 2491-2502.
- Konakli, K., Der Kiureghian, A., and Dreger, D. (2014) Coherency analysis of accelerograms recorded by the UPSAR array during the 2004 Parkfield earthquake. *Earthquake Engineering & Structural Dynamics* 43(5), 641-659.
- Liu, T. J., and Hong, H. P. (2015) Simulation of horizontal ground motions with spatial coherency in two orthogonal horizontal directions. *Journal of Earthquake Engineering* 19(5), 752-769.
- Liu, T. J., and Hong, H. P. (2016) Assessment of spatial coherency using tri-directional ground motions. *Journal of Earthquake Engineering* 20(5), 773-794.
- Luco, J. E., and Wong, H. L. (1986). Response of a rigid foundation to a spatially random ground motion. *Earthquake Engineering & Structural Dynamics*, 14(6), 891-908.
- Newland, D. E. (2012) *An introduction to random vibrations, spectral & wavelet analysis*. Courier Corporation.
- Pinnegar, C. R., and Mansinha L. (2003) A method of time-time analysis: The TT-transform. *Digital signal processing* 13(4), 588-603.
- Priestley, (1965) M. B. Evolutionary spectra and non - stationary processes. *Journal of the Royal Statistical Society: Series B (Methodological)* 27(2) 204-229.
- Priestley, M. B. (1988). *Non-linear and non-stationary time series analysis*. London: Academic Press.
- Priestley, M. B., and Tong, H. (1973) On the analysis of bivariate non - stationary processes. *Journal of the Royal Statistical Society: Series B (Methodological)* 35(2), 153-166.
- Qiao, D, Zhi, X, Fan, F., Hong, H.P. (2020) Estimation of Wavelet Coherence of Seismic Ground Motions. *Bulletin of the Seismological Society of America*; 110 (2): 613–628.
- Shinozuka, M., and Deodatis, G. (1996) Simulation of multi-dimensional Gaussian stochastic fields by spectral representation. *Applied mechanics review*, 49 (1).
- Shinozuka, M., and Jan, C-M. (1972) Digital simulation of random processes and its applications. *Journal of sound and vibration* 25(1), 111-128.
- Stockwell, R. G. (2007) A basis for efficient representation of the S-transform. *Digital Signal Processing* 17(1), 371-393.
- Stockwell, R. G., Mansinha L., and Lowe, R. P. (1996) Localization of the complex spectrum: the S transform. *IEEE transactions on signal processing* 44(4), 998-1001.
- Yan, Y., and Zhu, H. (2011) The generalization of discrete stockwell transforms. 19th *European Signal Processing Conference*, 1209-1213.

- Yeh, C-H., and Wen, Y. K. (1990) Modeling of nonstationary ground motion and analysis of inelastic structural response. *Structural Safety*, 8(1-4), 281-298.
- Zerva, A. (2009) Spatial variation of seismic ground motion. Modeling and engineering applications. *Nonlinear Dynamics*, 460.



## Chapter 6

# 6 An algorithm to simulate nonstationary and non-Gaussian stochastic processes at single or multiple sites

## 6.1 Introduction

Seismic ground motions vary in time and space. They can cause damages to structures and infrastructure systems. Since the actual ground motion records that match the configuration of the multiple supports of a structure, such as a bridge and a latticed shell structure (Lupoi et al. 2005; Zerva 2009; Li et al. 2014), are usually unavailable, simulated seismic ground motions are commonly employed to assess the structural responses.

The time-varying characteristics of the ground motions can be modeled using the evolutionary processes (Priestley 1965, 1981), as was done in Shinozuka and Deodatis (1991) and Deodatis (1996). The evolutionary process is defined based on an amplitude modulation function and the power spectral density (PSD) function of a stationary process. The amplitude modulation function may depend on time or frequency or both. The evolutionary process is known as the uniformly modulated evolutionary process if the amplitude modulation function depends only on time. The application of the evolutionary process results in that the PSD function of the evolutionary to be equal to the square of the amplitude modulation function multiplying the PSD function of the underlying stationary process. The simulation of the evolutionary process can be carried out by using the spectral representation methods (SRM) (Shinozuka and Jan 1972; Shinozuka and Deodatis 1991; Deodatis 1996; Liang et al. 2007), which is based on the ordinary Fourier transform. Some of the well-known PSD functions used to model the ground motions include the Kanai-Tajimi model, Clough-Penzien model, the model given in Sabetta and Pugliese (1996) and the model given in Pousse et al. (2006). The models in the last two mentioned studies are of interest, especially if one is interested in simulating ground motions for scenario seismic events.

The evolutionary process can be extended to vector processes, as described in Priestley and Tong (1973). They also showed that the lagged coherence between two evolutionary processes is time-independent. Therefore, if a time-independent lagged coherence model, such as the ones given in Luco and Wang (1986), Harichandran and Vanmarcke (1986), Hao et al. (1989), Abrahamson et al. (1991), and Liu and Hong (2015, 2016), is adopted, the use of the evolutionary process is adequate for simulating seismic ground motions. However, the study in chapter 5 showed that the lagged coherence is affected by the amplitude of the ground motions, and is time-dependent. In such a case, SRM cannot be used directly. To overcome this difficulty, the time-frequency (dependent) SRM (TFSRM) developed in chapter 3 to simulated ground motions based on the S-transform and discrete orthogonal S-transform (Stockwell et al. 1996; Pinnegar and Mansinha 2003; Stockwell 2007). TFSRM can cope with the time-dependent lagged coherence. The S-transform provides frequency-dependent resolution, and it can be viewed as a hybrid of continuous wavelet transform and short-time Fourier transform (Stockwell et al. 1996). Both the S-transform and the discrete orthogonal S-transform provide the time-frequency representation instead of the frequency only representation obtained by using the ordinary Fourier transform.

It should be noted that the application of SRM or TFSRM leads to a Gaussian stochastic process. However, the Gaussian assumption of the ground motions was questioned by Kafali and Grigoriu (2003), and Radu and Grigoriu (2018). Radu and Grigoriu (2018) analyzed a large number of ground motion records and concluded that the marginal probability distribution of the amplitude of ground motions is highly non-Gaussian. A simple and straightforward approach to simulate the stationary non-Gaussian process is to use SRM and the static probability distribution mapping (i.e., translation process) (Grigoriu 1998). One of the drawbacks of the approach is that the PSD of the simulated process may deviate from the target PSD function because of the probability distribution mapping. Several algorithms (Yamazaki and Shinozuka 1988; Gurley and Kareem 1997; Grigoriu 1998; Deodatis and Micaletti 2001) are proposed to correct this deviation. Masters and Gurley (2003) compared the performance of the algorithms; they also proposed an iterative spectral correction algorithm to simulate the stationary non-Gaussian processes. Their comparison indicates that the iterative spectral

correction algorithm outperforms the other considered algorithms in their study. It is worth noting that this iterative algorithm is similar to the iterative amplitude adjusted Fourier transform (IAAFT) algorithm (Schreiber and Schmitz 1996, 2000), which is designed to generate surrogate for a given signal for statistical hypothesis testing. Both of these algorithms are based on the ordinary Fourier transform. A clear difference between these two algorithms is how the prescribed target PSD function and cumulative distribution function (CDF) are calculated or assigned. The extension of IAAFT algorithm for generating a vector of surrogates is given in Schreiber and Schmitz (2000).

The translation process has been extended for the nonstationary non-Gaussian process (Ferrante et al. 2005; Shields and Deodatis 2013, Wu et al. 2018). Ferrante et al. (2005) focused on the simulation of a nonhomogeneous non-Gaussian field. Shields and Deodatis (2013) presented an iterative procedure to estimate the corresponding target PSD for a Gaussian process, given the target PSD function and the marginal CDF for a non-Gaussian process. By incorporating the time dependency in the probability distribution mapping for vector processes, a procedure is presented by Wu et al. (2018) to simulate nonstationary non-Gaussian ground motions. However, possible time-dependent lagged coherence cannot be taken into account because the algorithm is based on the evolutionary spectral theory, and the lagged coherence between evolutionary processes is time-independent, as mentioned earlier and explained in Priestley and Tong (1973). Also, an iterative power and amplitude correction (IPAC) algorithm was presented in Hong et al. (2020) to simulate nonstationary non-Gaussian process. The algorithm could be viewed as the extension of the spectral correction algorithm and IAAFT. But, it is based on the S-transform rather than the ordinary Fourier transform. The possibility of extending the IPAC algorithm to simulate nonstationary non-Gaussian vector processes with time-independent or time-dependent lagged coherence has not been explored.

For completeness, it should be noted that there are other available models to represent seismic ground motions in the literature, including the ones given by Yeh and Wen (1990), Fan and Ahmadi (1990), Conte and Peng (1997), and Rezaeian and Der Kiureghian (2010). The advantage of the model given by Yeh and Wen (1990) is that it

takes the frequency modulation into account, although the assessment of the frequency modulation function (or time transformation function) is associated with practical assumptions. The model given by Conte and Peng (1997) represents the ground motions by using the sum of multiple evolutionary processes. The model given by Fan and Ahmadi (1990) is essentially an extension of the model developed by Kanai-Tajimi in that, the filter is defined by a nonlinear dynamic system. The model presented by Rezaeian and Der Kiureghian (2010) considered that the ground motions are represented as a Duhamel integral with time-varying model parameters. However, the procedures for using these models for simulating nonstationary non-Gaussian vector processes are unavailable in the literature.

The main objective of this chapter is to extend the IPAC algorithm to simulate nonstationary non-Gaussian vector processes. The extension incorporates the essential features of the IAAFT algorithm for generating vector surrogates. It considers the time-independent or time-dependent lagged coherence. The numerical examples are focused on the simulation of the seismic ground motions, although the algorithm is equally applicable to the nonstationary non-Gaussian processes for other natural phenomena such as winds and waves. The remainder of this paper is organized as follows. In Section 2, a brief summary of ST, DOST, the corresponding definition of the energy distribution, and lagged coherence is given. It also serves the reader to familiarize our notations. Section 3 presents the extension of the IPAC algorithm to simulate the nonstationary non-Gaussian vector processes with time-independent or time-dependent lagged coherence. Several numerical examples for simulating the seismic ground motions are presented in Section 4 to illustrate the adequacy of the proposed algorithm. This is followed by some concluding remarks.

## 6.2 The S-transform, discrete orthonormal S-transform, and energy distribution

### 6.2.1 The S-transform and discrete orthonormal S-transform – a brief description

A brief review of the definition and relevant properties of the S-transform (ST) and discrete orthogonal S-transform (DOST) that are to be used in this chapter is summarized in this section. The term ST is also used for its continuous form and its discretized form that must be distinguished from the DOST. ST provides the time-frequency representation of a signal  $x(t)$  and is defined as (Stockwell et al. 1996; Pinnegar and Mansinha 2003),

$$x_S(f, \tau) = ST(x(t)) = \int_{-\infty}^{\infty} x(t)w(f, \tau-t)e^{-i2\pi ft} dt, \quad (6-1)$$

where  $x_S(f, \tau)$  is the ST coefficient,  $ST(\square)$  denotes ST of its argument, and  $\tau$  is the center of the window function  $w(f, \tau-t)$  defined as,

$$w(f, \tau-t) = \frac{|f|}{\sqrt{2\pi\kappa}} \exp\left(-\frac{f^2(\tau-t)^2}{2\kappa^2}\right). \quad (6-2)$$

with the parameter  $\kappa$  controls the effective width of the window in ST. Stockwell et al. (1996) showed that Eq. (6-1) can be re-written as,

$$x_S(f, \tau) = \int_{-\infty}^{\infty} \hat{x}(\phi + f) \exp\left(-\frac{1}{2}\left(\frac{2\pi\phi\kappa}{f}\right)^2\right) e^{i2\pi\phi\tau} d\phi, \quad (6-3)$$

and,

$$x(t) = IST(x_S(f, \tau)) = \int_{-\infty}^{\infty} \left[ \int_{-\infty}^{\infty} x_S(f, \tau) d\tau \right] e^{i2\pi ft} df, \quad (6-4)$$

where  $IST(\square)$  is the inverse ST (IST),  $\hat{x}(f)$  is the Fourier transform (FT) of  $x(t)$ . The amplitude of the ST coefficient is represented by  $|x_s(f, \tau)|$ ; the phase angle,  $\phi(f, \tau)$ , (rad) is given by,

$$\phi(f, \tau) = \tan^{-1} \left( \frac{\text{Im}(x_s(f, \tau))}{\text{Re}(x_s(f, \tau))} \right) \quad (6-5)$$

where  $\text{Im}()$  and  $\text{Re}()$  denote the imaginary and real parts.

Based on Eqs. (6-1) and (6-3), one has  $IST(ST(x(t))) = x(t)$ . However, for a given  $|x_s(f, \tau)|$ , and arbitrarily assigned phase angle  $\phi_A(f, \tau)$ , in general, the following is true,

$$x(t) = IST(|x_s(f, \tau)| e^{i\phi_A(f, \tau)}). \quad (6-6)$$

and,

$$ST(x(t)) = ST(IST(|x_s(f, \tau)| e^{i\phi_A(f, \tau)})) \neq |x_s(f, \tau)| e^{i\phi_A(f, \tau)}. \quad (6-7)$$

That is, for a randomly assigned phase angle  $\phi_A(f, \tau)$ ,  $|x_s(f, \tau)| e^{i\phi_A(f, \tau)}$  is not a legitimate ST coefficient because ST is a redundant transform. However, by letting  $x_{1s}(f, \tau) = ST(IST(|x_s(f, \tau)| e^{i\phi_A(f, \tau)}))$ , we have  $ST(IST(x_{1s}(f, \tau))) = x_{1s}(f, \tau)$ .

The discretized forms of Eqs. (6-3) and (6-4) are,

$$x(j\Delta_t) = IST(x_s(p\Delta_f, q\Delta_t)) = IFT_p \left( \Delta_t \sum_{k=0}^{N-1} x_s(p\Delta_f, k\Delta_t) \right), \text{ for } j = 0, \dots, N-1, \quad (6-8)$$

and,

$$x_s(p\Delta_f, q\Delta_t) = ST(x(q\Delta_t)) = IFT_j \left( \hat{x}((j+p)\Delta_f) \exp\left(-\frac{2\pi^2 j^2 \kappa^2}{p^2}\right) \right), \text{ for}$$

$$\begin{cases} p = -N/2+1, \dots, N/2 \\ q = 0, \dots, N-1 \end{cases}, \quad (6-9)$$

where the operator  $IFT(\square)$  denotes the inverse FT (IFT), and the subscript to this operators denotes the domain where the transform is carried out. Similarly, in the following, the operator  $FT(\square)$  will be used to represent FT. Eqs. (6-8) and (6-9) indicate that the evaluation of  $x(j\Delta_t)$  and  $x_s(p\Delta_f, q\Delta_t)$  can be carried out based on fast Fourier transform (FFT) (Battisti and Riba 2016).

Given the discrete samples  $\{x(j\Delta_t)\}_N$ , representing sampled  $x(j\Delta_t)$  for  $j = 0, \dots, N-1$ , its ST is represented by  $N \times N$  number of ST coefficients  $x_s(p\Delta_f, q\Delta_t)$ . This indicates that ST leads to a redundant representation. To have a more efficient non-redundant time-frequency representation based on ST, Stockwell (2007) proposed DOST. DOST has the maximum representation efficiency based on  $N$  orthonormal basis functions,  $D_{[\beta]}(k\Delta_t; p, q)$ , and is given by,

$$x_{\mathcal{D}\mathcal{S}}(p, q) = DOST(x(k\Delta_t)) = (1/N) \sum_{k=0}^{N-1} x(k\Delta_t) D_{[\beta]}(k\Delta_t; p, q), \quad (6-10)$$

and the inverse DOST is,

$$x(k\Delta_t) = IDOST(x_{\mathcal{D}\mathcal{S}}(p, q)) = \sum_{\text{for feasible } p, q} x_{\mathcal{D}\mathcal{S}}(p, q) D_{[\beta]}^*(k\Delta_t; p, q), \quad (6-11)$$

where  $x_{\mathcal{D}\mathcal{S}}(p, q)$  is the DOST coefficient, the superscript  $*$  indicates the complex conjugate,  $p$  (positive or negative) is an index of the center of a frequency band  $f_p = p\Delta_f$ ,  $\Delta_f = 1/(N\Delta_t)$ ,  $q$  is an index for the time localization, and

$$D_{[\beta]}(k\Delta_t; p, q) = \frac{ie^{-i\pi q} \{e^{-i2\pi(k/N-q/\beta)(p-\beta/2-1/2)} - e^{-i2\pi(k/N-q/\beta)(p+\beta/2-1/2)}\}}{\sqrt{\beta} 2\sin[\pi(k/N-q/\beta)]}, \quad (6-12)$$

in which  $\beta$  indicates the width of the frequency band centred at the frequency indexed by  $p$  (i.e.,  $f_p$ ); for positive  $p$ ,  $(p, q; \beta)$  are assigned according to (Stockwell 2007):  $(p; q; \beta)|_{m=0} = (0; 0; 1)$ ,  $(p; q; \beta)|_{m=1} = (1; 0; 1)$  and  $(p; q; \beta)|_{m=2, \dots, \log_2(N)-1} = (2^{m-1} + 2^{m-2}; 0, 1, \dots, 2^{m-1} - 1; 2^{m-1})$ , and  $m$  is the octave number. According to the assigned  $p$ ,  $q$ , and  $\beta$ , there are  $N_1 = N/2$  orthonormal basis functions (for non-negative  $p$ ). If the same  $\tau$  values are used, the vector of the basis functions for  $p$  is conjugate symmetric to the corresponding vector of the basis functions for  $-p$  (Wang and Orchard 2009). Moreover, similar to the ordinary Fourier transform, the DOST coefficients are conjugate symmetric about  $p = 0$  for a real-valued signal. Each cell defined by  $(p\Delta_f, q\Delta_t)$  covers a region in the time-frequency domain (Wang and Orchard 2009).

FT and DOST are non-redundant transforms. Therefore, by considering FT, for the randomly assigned phase angles  $\phi_A(f)$ , we have,

$$x(t) = IFT_f \left( |\hat{x}(f)| e^{i\phi_A(f)} \right), \quad (6-13)$$

and,

$$FT_t(x(t)) = FT_t \left( IFT_f \left( |\hat{x}(f)| e^{i\phi_A(f)} \right) \right) = |\hat{x}(f)| e^{i\phi_A(f)}, \quad (6-14)$$

If DOST is considered, for the randomly assigned phase angles  $\phi_A(p, q)$ , we have,

$$x(t) = IDOST \left( |x_{\mathcal{D}S}(p, q)| e^{i\phi_A(p, q)} \right), \quad (6-15)$$

and

$$DOST(x(t)) = DOST \left( IDOST \left( |x_{\mathcal{D}S}(p, q)| e^{i\phi_A(p, q)} \right) \right) = |x_{\mathcal{D}S}(p, q)| e^{i\phi_A(p, q)}, \quad (6-16)$$



This property shown in Eqs. (6-14) and (6-16) is not enjoyed by the redundant ST, as indicated in Eq. (6-7).

## 6.2.2 Energy distribution and lagged coherence

Consider two processes  $x(t)$  and  $y(t)$ . The two-sided cross periodogram or PSD defined based on FT is (Zerva 2009),

$$S_{\mathcal{F}XY}(f) = \hat{x}(f)\hat{y}^*(f)/T, \quad (6-17)$$

where  $\hat{x}(f)$  and  $\hat{y}(f)$  are FT of  $x(t)$  and  $y(t)$ , and  $T$  is the duration of  $x(t)$  and  $y(t)$ .  $S_{\mathcal{F}XX}(f)$  and  $S_{\mathcal{F}YY}(f)$  are the PSD of  $x(t)$  and  $y(t)$ , respectively. The coherence is defined as,

$$\Gamma_{XY}(f) = \mathcal{S}[S_{\mathcal{F}XY}(f)] / \sqrt{\mathcal{S}[S_{\mathcal{F}XX}(f)]\mathcal{S}[S_{\mathcal{F}YY}(f)]}, \quad (6-18)$$

where  $\mathcal{S}[\cdot]$  is a smoothing operator and the requirement for smoothing is explained in Zerva (2009).  $|\Gamma_{XY}(f)|$  is known as lagged coherence.

The ST based two-sided cross time-frequency power spectral density (TFPSD) function,  $S_{sXY}(f, \tau)$  is defined as,

$$S_{sXY}(f, \tau) = \left( x_s(f, \tau) / \sqrt{D_\kappa |f|} \right) \left( y_s(f, \tau) / \sqrt{D_\kappa |f|} \right)^*, \quad (6-19)$$

where  $D_\kappa = \int_{-\infty}^{\infty} (1/|\zeta|) \times \exp\left(- (2\pi\kappa(\zeta-1))^2\right) d\zeta$ . The above definition leads to energy preservation (Hong 2020). The two-sided TFPSD function  $S_{sXX}(f, \tau)$  and  $S_{sYY}(f, \tau)$  is defined similarly. Based on the TFPSD functions, the coherence,  $\Gamma_{sXY}(f, \tau)$ , is defined as,

$$\Gamma_{sXY}(f, \tau) = \frac{\mathcal{S}[S_{sXY}(f, \tau)]}{\sqrt{\mathcal{S}[S_{sXX}(f, \tau)]\mathcal{S}[S_{sYY}(f, \tau)]}}, \quad (6-20)$$

The requirement for smoothing applied in Eq. (6-20) is elaborated in chapter 5, and similar to the use of FT (Zerva 2009) and wavelet transform (Cohen and Walden 2010). The absolute value of  $\Gamma_{\mathcal{S}XY}(f, \tau)$ ,  $|\Gamma_{\mathcal{S}XY}(f, \tau)|$ , is known as lagged coherence.

The two-sided cross TFPSD function,  $S_{\mathcal{D}SXY}(p, q)$ , and the coherence,  $\Gamma_{\mathcal{D}SXY}(p, q)$ , based on DOST, are defined as, which is the same as in chapter 3 but in different index,

$$S_{\mathcal{D}SXY}(p, q) = x_{\mathcal{D}S}(p, q)y_{\mathcal{D}S}^*(p, q) \quad , \quad (6-21)$$

and,

$$\Gamma_{\mathcal{D}SXY}(p, q) = \frac{\mathcal{S}[S_{\mathcal{D}SXY}(p, q)]}{\sqrt{\mathcal{S}[S_{\mathcal{D}SXX}(p, q)]\mathcal{S}[S_{\mathcal{D}SY}(p, q)]}} \quad , \quad (6-22)$$

The smoothing in Eq. (6-22) is applied to the  $p$  and  $q$  according to their location in the time-frequency domain as discussed in chapter 3.  $|\Gamma_{\mathcal{D}SXY}(p, q)|$  is the lagged coherence. The lagged coherence calculated based on Eqs. (6-20) and (6-22) agree well in the time-frequency domain but the use of Eq. (6-20) leads to a better fidelity than that provided by Eq. (6-22).

### 6.2.3 Sampling coherent noise

Consider  $N_p$  stochastic vector processes  $x_k(t)$  for  $k = 1, \dots, N_p$ . If the processes are defined by  $S_{\mathcal{F}X_k X_k}(f)$  and the lagged coherence  $|\Gamma_{X_k X_l}(f)|$  for  $k, l = 1, \dots, N_p$ , samples of  $x_k(t)$  can be simulated using the SRM (Shinozuka and Jan 1972; Deodatis 1996). In particular, if  $S_{\mathcal{F}X_k X_k}(f)$  equals constant (e.g., one), the simulated  $x_k(t)$  represents coherent noises. Note that SRM cannot be used to simulate vector processes if the prescribed lagged coherence is time-dependent. This is because that the SRM is developed for the stationary processes and evolutionary processes whose lagged coherence is time-independent (Priestley and Tong 1973).

For the case with time-dependent lagged coherence, TFSRM proposed in chapter 3 can be employed. In TFSRM, first, the prescribed  $S_{S_{X_k X_k}}(f, \tau)$  and  $|\Gamma_{S_{X_k X_l}}(f, \tau)|$  of the vector processes are used to evaluate  $S_{\mathcal{D}S_{X_k X_k}}(p, q)$  and  $\Gamma_{\mathcal{D}S_{X_k X_l}}(p, q)$  according to the time and frequency location of DOST. The  $N_p \times N_p$  spectral matrix of the vector processes in the DOST domain,  $\mathbf{S}(p, q)$ , is then defined with its  $(k, l)$ -th element  $S_{\mathcal{D}S_{X_k X_l}}(p, q) = |\Gamma_{\mathcal{D}S_{X_k X_l}}(p, q)| \sqrt{S_{\mathcal{D}S_{X_k X_k}}(p, q) S_{\mathcal{D}S_{X_l X_l}}(p, q)}$ . As the wave passage effect is not included in  $\mathbf{S}(p, q)$ , its effect may be added after the processes are simulated (Der Kiureghian 1996). The application of Cholesky decomposition to  $\mathbf{S}(p, q)$  results in  $\mathbf{L}(p, q) \mathbf{L}^H(p, q)$ , where  $\mathbf{L}(p, q)$  is the lower triangle matrices, and the superscript H denotes Hermitian matrix. The sample of the  $k$ -th process is then given by,

$$x_k(j\Delta_t) = \sqrt{2} \sum_{m=1}^k \sum_{\text{for feasible } p, q} \text{Re} \left[ L_{km}(p, q) D_{[\beta]}^*(j\Delta_t; p, q) e^{i\theta_m(p, q)} \right], \quad (6-23)$$

where  $k = 1, \dots, N_p$ ,  $L_{km}(p, q)$  denotes the  $(k, m)$ -th element of the lower triangle matrix  $\mathbf{L}(p, q)$  and  $\theta_m(p, q)$  are independent and uniformly distributed between 0 and  $2\pi$ . If  $S_{S_{X_k X_k}}(f, \tau)$  equals a constant, Eq. (23) provides time-dependent coherent noise.

### 6.3 Extension of IPAC algorithm to simulate nonstationary non-Gaussian vector processes

The IPAC algorithm (Hong et al. 2020) for a nonstationary non-Gaussian process can be viewed as an extension of the well-known IAAFT algorithm (Schreiber and Schmitz 1996, 2000) and the spectral correction algorithm (Masters and Gurley 2003), which are developed for stationary process and based on FT. The following provides a rough procedure of IPAC, and for more details about IPAC, the reader is referred to the Appendix C. Given target TFPSD function  $S_{S_{XX}}(f, \tau)$  and target marginal CDF of  $x(t)$ ,  $F_{X,t}(x(t))$ , that depends on the time-varying standard deviation  $\sigma(t)$ , the use of the IPAC algorithm to obtain  $\{x(j\Delta_t)\}_N$  based on ST is as follows:

- a) Sample  $\{u(j\Delta_t)\}_N$  based on a random number generation algorithm for a uniformly distributed random variable between 0 and 1. Assign  $\{p(j)\}_N$  equal to the ascendingly sorted  $\{u(j\Delta_t)\}_N$ . Calculate the intensity function  $|x_S(f, \tau)| = \sqrt{S_{SXX}(f, \tau) D_k |f|}$ , and the time-dependent variance,

$$\sigma^2(t) = \int_{-\infty}^{\infty} S_{SXX}(f, t) df, \quad (6-24)$$

- b) Sample a sequence of Gaussian white noise,  $w(t)$ , of length  $N$ , calculate  $e^{i\phi(f, \tau)} = \eta(ST(w(t)))$ , where  $\eta(C) = C/|C|$  for  $C$  not equal to zero and  $\eta(C) = 0$  if  $C$  equals zero;
- c) Calculate  $x_{PC}(j\Delta_t) = IST(|x_S(f, \tau)| e^{i\phi(f, \tau)})$  (see Eq. (6)),  $p_{PC}(j\Delta_t) = F_{X,t}(x_{PC}(j\Delta_t))$ , and find the rank of  $p_{PC}(j\Delta_t)$ , denoted as  $r_j$ , for  $j = 0, \dots, N-1$ ;
- d) Assign  $x_{AC}(j\Delta_t) = F_{X,j\Delta_t}^{-1}(p(r_j))$ , for  $j = 0, \dots, N-1$ ; and calculate  $e^{i\phi(f, \tau)} = \eta(ST(x_{AC}(j\Delta_t)))$ ;
- e) Repeat Steps c) to d) until the convergence criterion is satisfied.

Step c) serves to adjust the energy distribution, and Step d) provides the correction to match the marginal distribution. As pointed out in Hong et al. (2020), some simplification can be made, and computational efficiency can be gained if the probability distribution of  $x(t)/\sigma(t)$  remains unchanged.

It is noted that the IAAFT algorithm was extended by Schreiber and Schmitz (2000) to generate surrogates for several coherent time series, where the phase angle for each target process are calculated using the FT. The extension is based on the fact that by adding the same phase to the Fourier coefficients of the processes at frequency  $f$ , the cross power spectral density (PSD) is preserved (Prichard and Theiler 1994). More specifically, based on FT and Eq. (6-13), for  $N_p$  processes, one has,

$$x_k(t) = IFT_f \left( |\hat{x}_k(f)| e^{i\phi_k(f)} \right), \text{ for } k = 1, \dots, N_p, \quad (6-25)$$

where  $\hat{x}_k(f) = |\hat{x}_k(f)| e^{i\phi_k(f)}$  denotes the Fourier coefficient for the  $k$ -th process, and  $|\hat{x}_k(f)|$  and  $\phi_k(f)$  represent the Fourier amplitude and phase angle of the Fourier coefficient. The cross-product of the Fourier coefficients for  $x_j(t)$  and  $x_k(t)$  is given by,

$$\hat{x}_k(f) \hat{x}_l(f) = |\hat{x}_k(f)| |\hat{x}_l(f)| e^{i[\phi_k(f) - \phi_l(f)]}, \quad (6-26)$$

which only involves the phase difference. Therefore, the cross-spectra is preserved by adding the same phase to the Fourier coefficients of each of the processes at the frequency  $f$ . Hence, the cross-correlation functions are preserved as well, according to the Wiener-Khintchine theorem.

A variant of the IAAFT algorithm given by Schreiber and Schmitz (2000) was presented in Borgnat et al. (2012) by using phase angles obtained from simulated coherent processes (or correlated noises) that have a constant variance. By considering the salient features of the IPAC algorithm for a single process and the IAAFT algorithm for vector processes, an extension to the IPAC algorithm to simulate the nonstationary and non-Gaussian vector processes is proposed below.

Before describing the algorithm, we note that for the vector processes, based on ST and Eq. (6-6), we can write,

$$x_k(t) = IST \left( |x_{s,k}(f, \tau)| e^{i\phi_k(f, \tau)} \right) \text{ for } k = 1, \dots, N_p, \quad (6-27)$$

where  $\phi_k(f, \tau)$  represents the phase of the ST coefficients. Therefore, the essential idea is to use a set of simulated  $\phi_k(f, \tau)$  according to the prescribed lagged coherence to define the processes and iteratively adjusting the phase by adding the same phase to the ST coefficients of each of the processes at the same  $(f, \tau)$ , one can simulate  $x_k(t)$  with prescribed lagged coherence, TFPSD and marginal CDF. The phase adjustment is determined by satisfying the target TFPSD and marginal CDF requirements.

Based on these considerations, for given target TFPSD function,  $S_{S X_k X_k}(f, \tau)$ , target marginal CDF,  $F_{X_k, t}(x_j(t))$ , with its time-varying variance  $\sigma_k^2(t) = \int_{-\infty}^{\infty} S_{S X_k X_k}(f, t) df$ , and target lagged coherence function ( $|\Gamma_{X_k X_k}(f)|$  or  $|\Gamma_{S X_k X_k}(f, \tau)|$ ) (or the target cross-correlation function), the steps to simulate,  $\{x_k(j\Delta_t)\}_N$ , are illustrated in Figure 6.1 and detailed as follows:

- 1) Sample  $\{u_k(j\Delta_t)\}_N$  for  $k = 1, \dots, N_p$ , based on a random number generation algorithm for a uniformly distributed random variable between 0 and 1. Assign  $\{p_k(j)\}_N$  equal to the ascendingly sorted  $\{u_k(j\Delta_t)\}_N$ . Calculate the intensity function  $|x_{S, k}(f, \tau)| = \sqrt{S_{S X_k X_k}(f, \tau) D_{\kappa} |f|}$ ,
- 2) Sample  $w_k(t)$  of length  $N$ , for  $k = 1, \dots, N_p$ , based on SRM if the target lagged coherence is time-independent or based on Eq. (6-23) if the target lagged coherence is time-dependent, where PSD function is a constant. Alternatively, if the target cross-correlation function is given,  $w_k(t)$  could be sampled by using the circulant embedding method (Wood and Chan 1994) with unit variance. Also, sample a Gaussian white noise  $\{w_0(j\Delta_t)\}_N$ . Calculate  $e^{i\theta_k(f, \tau)} = \eta(ST(w_k(j\Delta_t)))$  and  $e^{i\theta_0(f, \tau)} = \eta(ST(w_0(j\Delta_t)))$  (noting that  $f$  can be positive and negative); assign  $\phi_k(f, \tau) = \theta_k(f, \tau) + \theta_0(f, \tau)$ ;
- 3) For  $k = 1, \dots, N_p$ ,
  - 3.1) Calculate  $x_{PC, k}(j\Delta_t) = IST(|x_{S, k}(f, \tau)| e^{i\phi_k(f, \tau)})$ ,  $p_{PC, k}(j\Delta_t) = F_{X_k, t}(x_{PC, k}(j\Delta_t))$ , and find the rank of  $p_{PC, k}(j\Delta_t)$ , denoted as  $r_{k, j}$ , for  $j = 0, \dots, N-1$ ;
  - 3.2) Let  $x_{AC, k}(j\Delta_t) = F_{X_k, t}^{-1}(p_k(r_{k, j}))$ , for  $j = 0, \dots, N-1$ ; and calculate  $e^{i\phi_k(f, \tau)} = \eta(ST(y_{AC, k}(j\Delta_t)))$ ;

4) Calculate  $\alpha(f, \tau)$  using

$$\tan \alpha(f, \tau) = \frac{\sum_{k=1}^{N_p} \sin(\theta_k(f, \tau) - \phi_k(f, \tau))}{\sum_{k=1}^{N_p} \cos(\theta_k(f, \tau) - \phi_k(f, \tau))} , \quad \text{and set}$$

$$\phi_k(f, \tau) = \theta_k(f, \tau) + \alpha(f, \tau) , \quad \text{and}$$

5) Repeat Steps 3) to 4) until the convergence criterion is achieved.

For this chapter, the convergence criterion is based on the ratio,  $r_c$ , defined as the sum of the  $(x_{AC,k} - x_{PC,k})^2$  to the sum of the squared  $x_{PC,k}$  for  $k = 1, \dots, N_p$ ; the value of  $r_c$  less than 0.2% is used for numerical analysis to be carried out and the convergence is achieved usually within five iterations.

In Step 2), the phases for coherent processes are randomized by using  $\phi_k(f, \tau) = \theta_k(f, \tau) + \theta_0(f, \tau)$ . However, at the end of each iteration, only the relative phase differences are kept. The calculation of  $\alpha(f, \tau)$  in Step 4) is based on the equation given by Schreiber and Schmitz (2000) for the IAAFT algorithm, which is used to ensure that the cross power spectral density (PSD) function remains to be the same. The variate of the IAAFT algorithm given in Borgnat et al. (2012) neglects the requirement of such a consistent phase shift (i.e., neglect Step 4).

If the distribution type,  $F_{X_k,t}(x_k(t))$ , remains unchanged in time and only depends on  $\sigma_k(t)$  (i.e., if the marginal probability distribution of  $x_k(t) / \sigma_k(t)$  is identical), similar to the case of simulating a single nonstationary non-Gaussian process by using the IPAC algorithm (Hong et al. 2020), the above algorithm can be modified to gain efficiency according to the modifications given in Table 6.1. The output of the algorithm can be the power spectra density matched time series or amplitude matched time series (i.e.,  $x_{PC,k}(j\Delta_t)$  or  $x_{AC,k}(j\Delta_t)$ ), which are equivalent if the convergence criterion is satisfied.

**Table 6.1:** Simplification to the algorithm for the case where the marginal probability distribution of  $x_k(t) / \sigma_k(t)$  is identical.

Modifications	
Step 1	Calculate $\{\zeta_k(j) = \Phi^{-1}(p_k(j))\}_N$ after $\{p_k(j)\}_N$ is determined
Step 3.1	Calculate $p_{PC,k}(j\Delta_t) = y_{PC,k}(j\Delta_t) / \sigma_k(j\Delta_t)$ instead of $p_{PC,k}(j\Delta_t) = F_{X_{k,t}}(y_{PC,k}(j\Delta_t))$
Step 3.2	Calculate $x_{AC,k}(j\Delta_t) = \zeta(r_{k,j})\sigma_k(j\Delta_t)$ instead of $x_{AC,k}(j\Delta_t) = F_{X_{k,t}}^{-1}(p_k(r_{k,j}))$

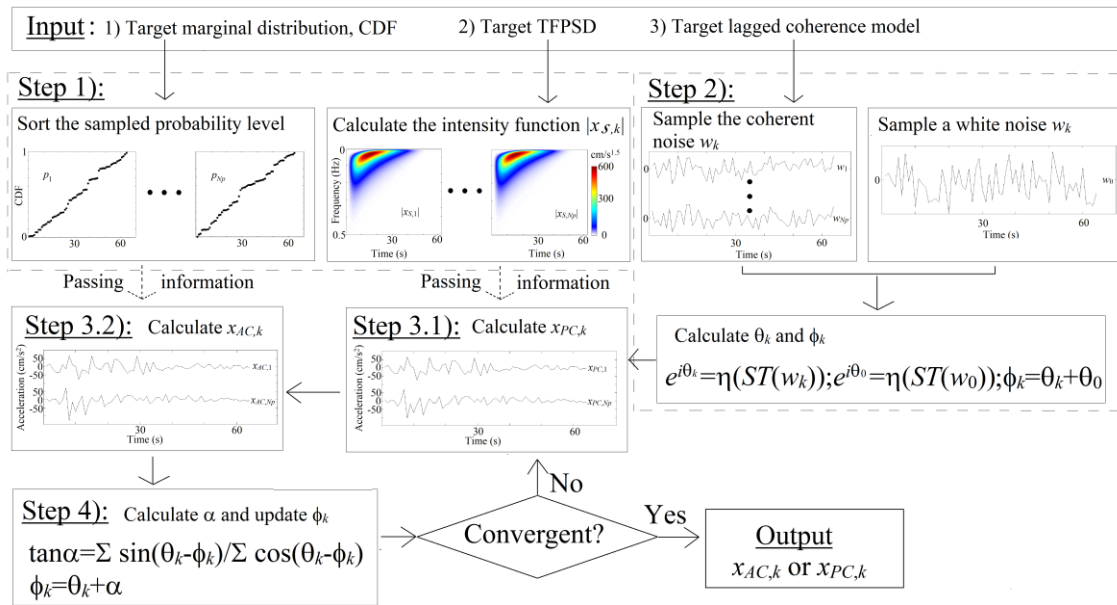


**Figure 6.1:** IPAC algorithm to simulate nonstationary and non-Gaussian vector processes.

## 6.4 Numerical validation and application of IPAC algorithm

### 6.4.1 Numerical validation for the case with time-independent lagged coherence

For the numerical validation, consider a scenario event, same as the event used in the example illustration of chapter 5, defined as a strike-slip earthquake with the moment magnitude 7. It is assumed that the rupture to site distance equals 50 km, and the shear wave velocity in the top 30 m of the site equals 450 m/s. For the considered scenario



events, it is assumed that the TFPSD of the zero-mean nonstationary ground motions,  $S_s(f, \tau)$ , for all considered sites shown in Figure 6.2a can be modeled using,

$$S_s(f, \tau) = \frac{\lambda_0(\tau)}{f\sqrt{2\pi}\eta(\tau)} \exp\left[-\frac{1}{2}\left(\frac{\ln f - \ln F_c(\tau) + \eta^2(\tau)/2}{\eta(\tau)}\right)^2\right], \quad (6-28)$$

where  $\tau \in [0, T]$ ,  $T = 34s$ , and the parameters  $\eta(\tau)$ ,  $F_c(\tau)$ , and  $\lambda_0(\tau)$  are given by,

$$\eta(\tau) = \sqrt{\ln\left[1 + \left[(5.64\exp(-11.03\tau/34) - 8.49)/F_c(\tau)\right]^2\right]}, \quad (6-29)$$

$$F_c(\tau) = 9.10\exp(-7.68\tau/34) - 11.55, \quad (6-30)$$

and,

$$\lambda_0(\tau) = 1311805 \exp\left[-0.5\left(1.5 + 1.25\ln\left(\tau/(T-\tau)\right)\right)^2\right] / \left[\sqrt{2\pi}\tau(T-\tau)\right]. \quad (6-31)$$

The used TFPSD function  $S_s(f, \tau)$  is the same as that used in the example of chapter 5. This TFPSD function is presented in Figure 6.2b. Also, the time-varying standard deviation that equals  $\sqrt{\lambda_0(\tau)}$  is shown in the figure.

Furthermore, it is assumed that the spatial lagged coherence can be modeled using,

$$\left|\Gamma_{X_k X_l}(f)\right| = \tanh\left(\tanh^{-1}\left(\left|\Gamma_{Bias X_k X_l}(f)\right|\right) - \varsigma\right), \quad (6-32)$$

where  $\varsigma$  denotes the bias factor that is taken equal to 0.2 in estimating the lagged coherence by using the Hamming window with a width of about 30 for smoothing,  $\left|\Gamma_{Bias X_k X_l}(f)\right|$  denotes the model given by Liu and Hong (2016) that is fitted to the calculated lagged coherence without removing the bias in estimating the lagged coherence (Abrahamson et al. 1991).  $\left|\Gamma_{Bias X_k X_l}(f)\right|$  is expressed as,

$$|\Gamma_{BiasX_l X_l}(f)| = A \exp\left(-\frac{2d_{kl}}{\alpha_0 \theta(f)}(1-A+\alpha_0 A)\right) + (1-A) \exp\left(-\frac{2d_{kl}}{\theta(f)}(1-A+\alpha_0 A)\right), \quad (6-33)$$

in which  $d_{kl}$  (m) is the separation between the  $k$ -th and  $l$ -th sites;  $\theta(f) = k(1+(f/f_0)^B)^{-1/2}$ ,  $A = 0.5$ ,  $\alpha_0 = 1.60 \times 10^{-4}$ ,  $k = 3.00 \times 10^7$ ,  $f_0 = 2.5$  and  $B = 5.7$ .

This target spatial lagged coherence is plotted in the  $\tau$ - $f$  domain as shown in Figure 6.3a. Based on this adopted target lagged coherence function, a typical set of simulated coherent noises by using the SRM is shown in Figures 6.3b. The lagged coherence of the simulated noise calculated based on ST (see Eq. (6-20)) is shown in Figure 6.4. For the lagged coherence calculation, Eq. (6-20) is used, and the smoothing is carried out by using a box window with  $30 \times 30$  points as discussed in chapter 5.

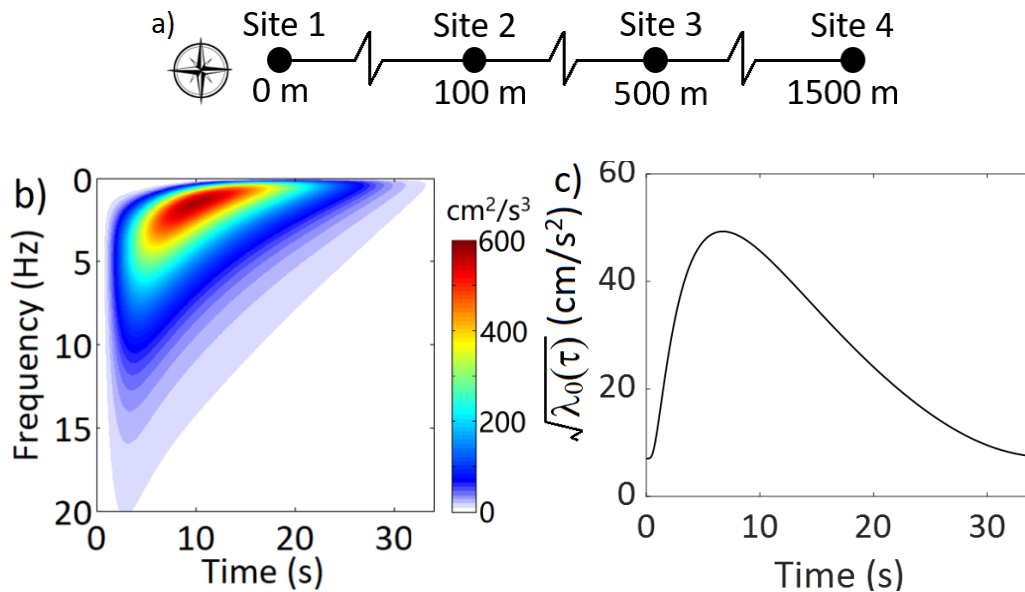


**Figure 6.2:** a). Layout of considered site; b) the target TFPSD; c) time-varying standard deviation that equals  $\sqrt{\lambda_0(\tau)}$ .

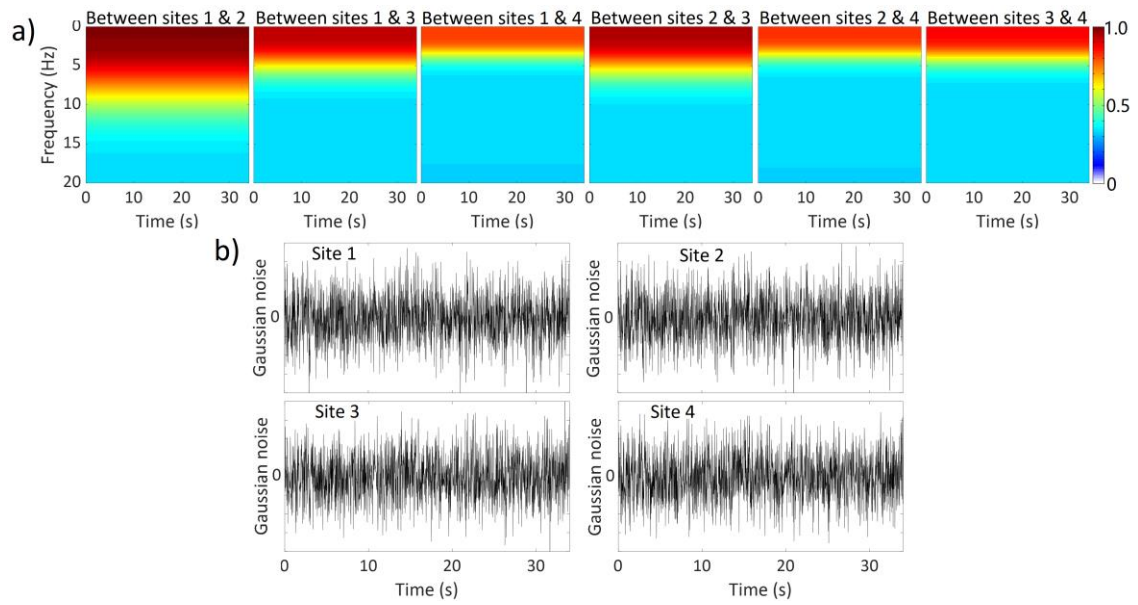


**Figure 6.3:** a) Target time-independent lagged coherence in the  $\tau$ - $f$  space and b) simulated coherent.

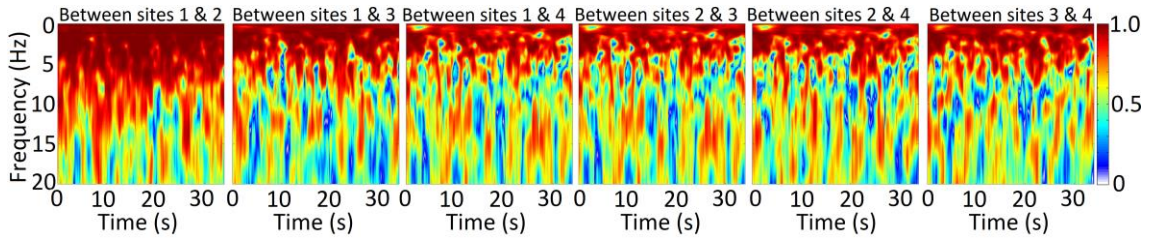


**Figure 6.4:** Lagged coherence between simulated noise shown in Figure 6.3b.

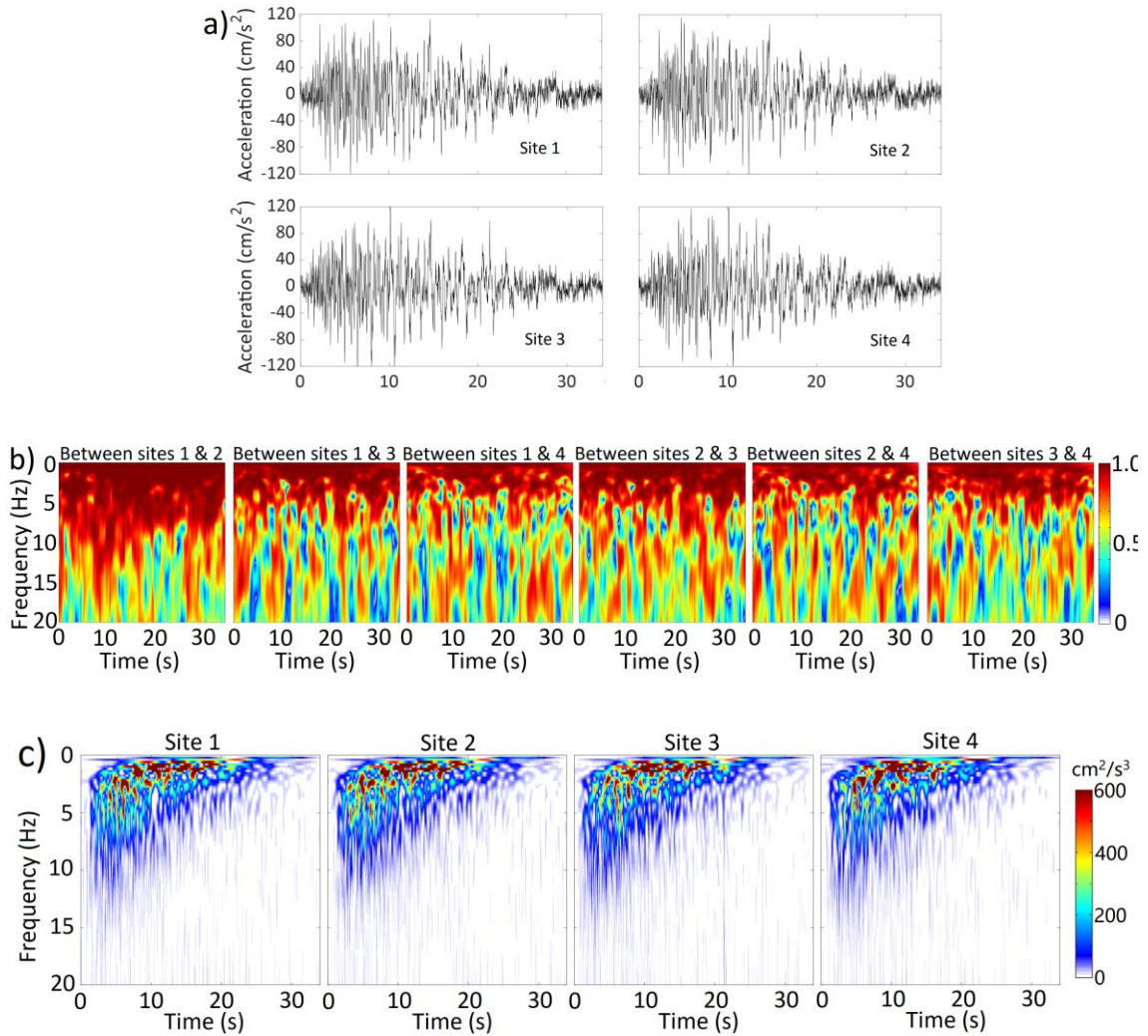


**Figure 6.5:** Simulated nonstationary Gaussian ground motions with time-independent lagged coherence and their spectral characteristics: a) sampled records, b) calculated lagged coherence; c) calculated TFPSD.

For the moment, consider that the ground motion is Gaussian. By applying the IPAC algorithm, with the phase angle  $\theta_k(f, \tau)$  obtained from the sampled coherent noise shown in Figure 6.3b, and the target TFPSD given in Eq. (6-28), the obtained ground motion time histories (based on  $x_{AC,k}(t)$ ) and their corresponding TFPSD for Sites 1 to 4 are shown in Figure 6.5a. The calculated TFPSD function and lagged coherence by using the simulated ground motions are shown in Figures 6.5b, and 6.5c, respectively. The calculated TFPSD presented in Figure 6.5b resembles that shown in Figure 6.2b. The lagged coherence presented in Figure 6.5c mimics well that shown in Figure 6.4,

indicating that the lagged coherence is maintained after the iteration. This partially validates the adequacy of the proposed extension to the IPAC algorithm. Since  $x_{AC,k}(t)$  are used as the simulated records, the amplitude matching (i.e., probability distribution matching) is ensured so no distribution comparison is presented.

As mentioned in the introduction, the ground motions may not be Gaussian (Kafali and Grigoriu 2003; Radu and Grigoriu 2018). Radu and Grigoriu (2018) showed that the kurtosis coefficient of the amplitude (positive and negative) of the ground motions deviates from that of a Gaussian random variable, which equals 3. A probability distribution fitting analysis carried out in Hong et al. (2020) for some historical records indicates that  $x(t)/\sigma(t)$  could be adequately modeled using the generalized Gaussian distribution (GGD) (Nadarajah 2005). This suggests that the marginal probability density function of  $x(t)$ ,  $f_{x,t}(x(t))$ , can be modeled using GGD,

$$f_{x,t}(x(t)) = \frac{\beta_0}{2\beta_1\Gamma(1/\beta_0)} e^{-(|x(t)-\mu|/\beta_1)^{\beta_0}}, \quad (6-34)$$

where  $\mu$  denotes the mean that equals zero for the zero-mean process,  $\beta_0$  and  $\beta_1$  are positive model parameters, and  $\Gamma(\square)$  denotes the gamma function. If  $\beta_0$  equals 2, it represents the normal distribution. The tail of the GGD is lighter and heavier than that of the normal distribution for  $\beta_0 > 2$  and  $< 2$ , respectively. The variance and kurtosis coefficients of GGD are equal to  $\beta_1^2\Gamma(3/\beta_0)/\Gamma(1/\beta_0)$  and  $\Gamma(5/\beta_0)\Gamma(1/\beta_0)/\Gamma^2(3/\beta_0)$ , respectively.

By considering that the target marginal CDF of  $x(t)$  is defined by Eq. (6-34) with  $\beta_0$  equal to 3, the analysis that is carried out for the Gaussian case is repeated by using the extended IPAC algorithm with the target TFPSD and lagged coherence as shown Eqs. (6-28) and (6-32). More specifically, by using the same sampled coherent noises shown in Figure 6.3b, the sampled nonstationary and non-Gaussian ground motions are illustrated in Figure 6.6a. As can be observed from the plots in Figures 6.5a and 6.6a, the Gaussian and non-Gaussian records differ. The difference is not very large because of the

relatively small difference between the considered GGD and Gaussian distribution. The calculated TFPSD function and lagged coherence for the sample records are shown in Figures 6.6b and 6.6c, respectively. Again, the TFPSD functions of the sampled records resemble the target shown in Figure 6.2b. Also, the comparison of the lagged coherence shown in Figures 6.4 and 6c indicates that the lagged coherence is maintained after using the extended IPAC algorithm, suggesting that the IPAC algorithm alters the lagged coherence of the simulated coherent noises only slightly.

Rather than illustrating a single realization of the vector processes, the analysis carried out for the results presented in Figures 6.4b, 6.5, and 6.6 is repeated 500 cycles. The mean and standard deviation of the sampled noises and records are shown in Figure 6.7. The mean of lagged coherence shown in Figure 6.7 in all cases agrees well with that shown in Figure 6.3a. Moreover, the means of the lagged coherence for the Gaussian and Non-Gaussian records calculated from the simulated ground motions agree well with those calculated from the simulated coherent noises. The standard deviation of the lagged coherence for the simulated Gaussian and non-Gaussian ground motions are similar to those of simulated coherent noises as well. These observations indicate the adequacy of the extended IPAC algorithm to simulate time-independent coherent nonstationary Gaussian or non-Gaussian processes.

The mean and the standard deviations of the TFPSD functions estimated from the sampled records for Site 1 are shown in Figure 6.8. The results for other sites are not shown because all sites have the same target TFPSD function. The mean of the TFPSD function from the simulated records is consistent with its corresponding target. Although the standard deviation of TFPSD is significant, the coefficient of variation of TFPSD is about one-half of that shown in Liu and Hong (2015, 2016), which is obtained from the simulated records by using SRM.

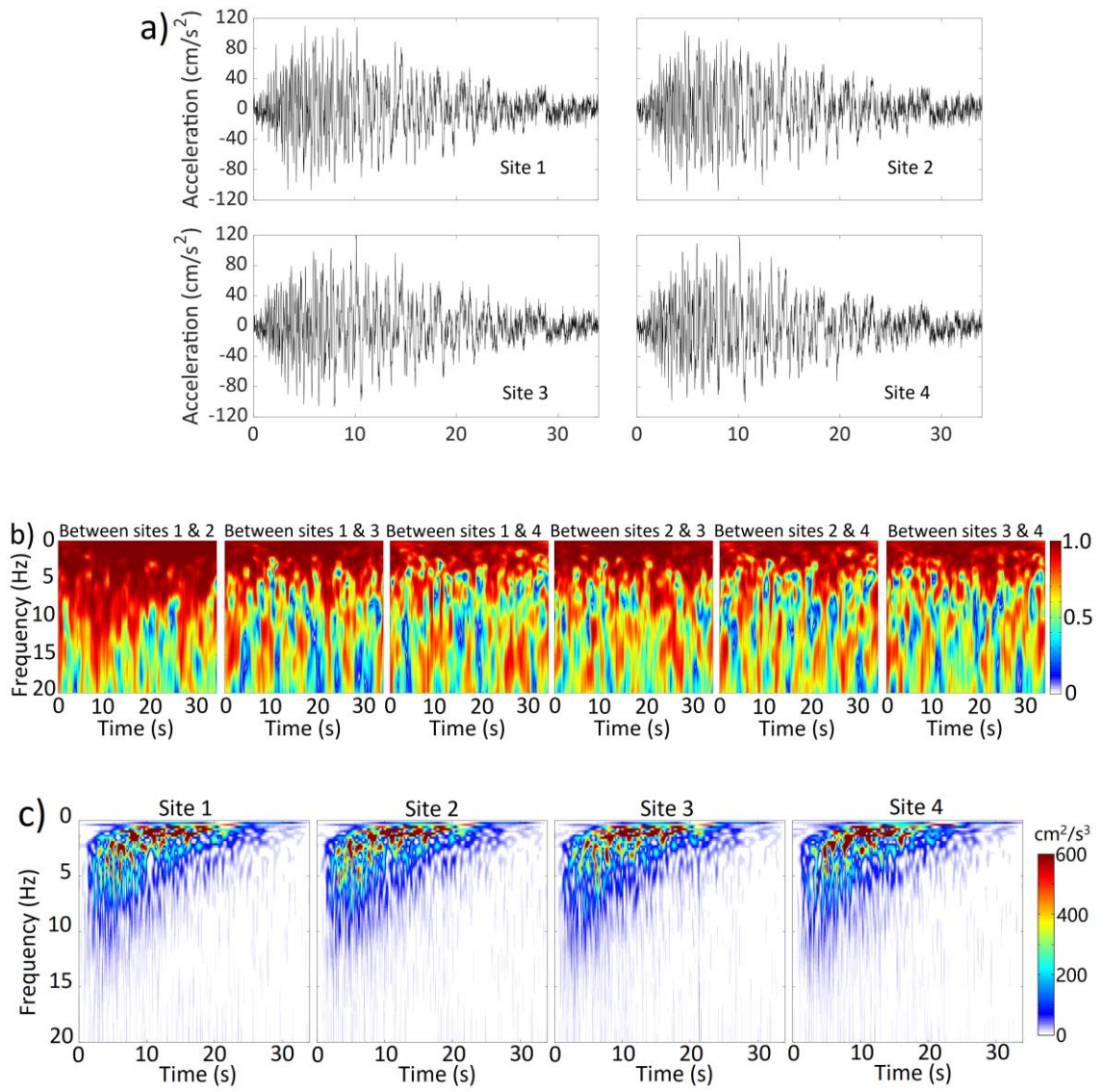


**Figure 6.6:** Simulated nonstationary Non-Gaussian ground motions with time-independent lagged coherence and their spectral characteristics: a) sampled records, b) calculated lagged coherence; c) calculated TFPD.



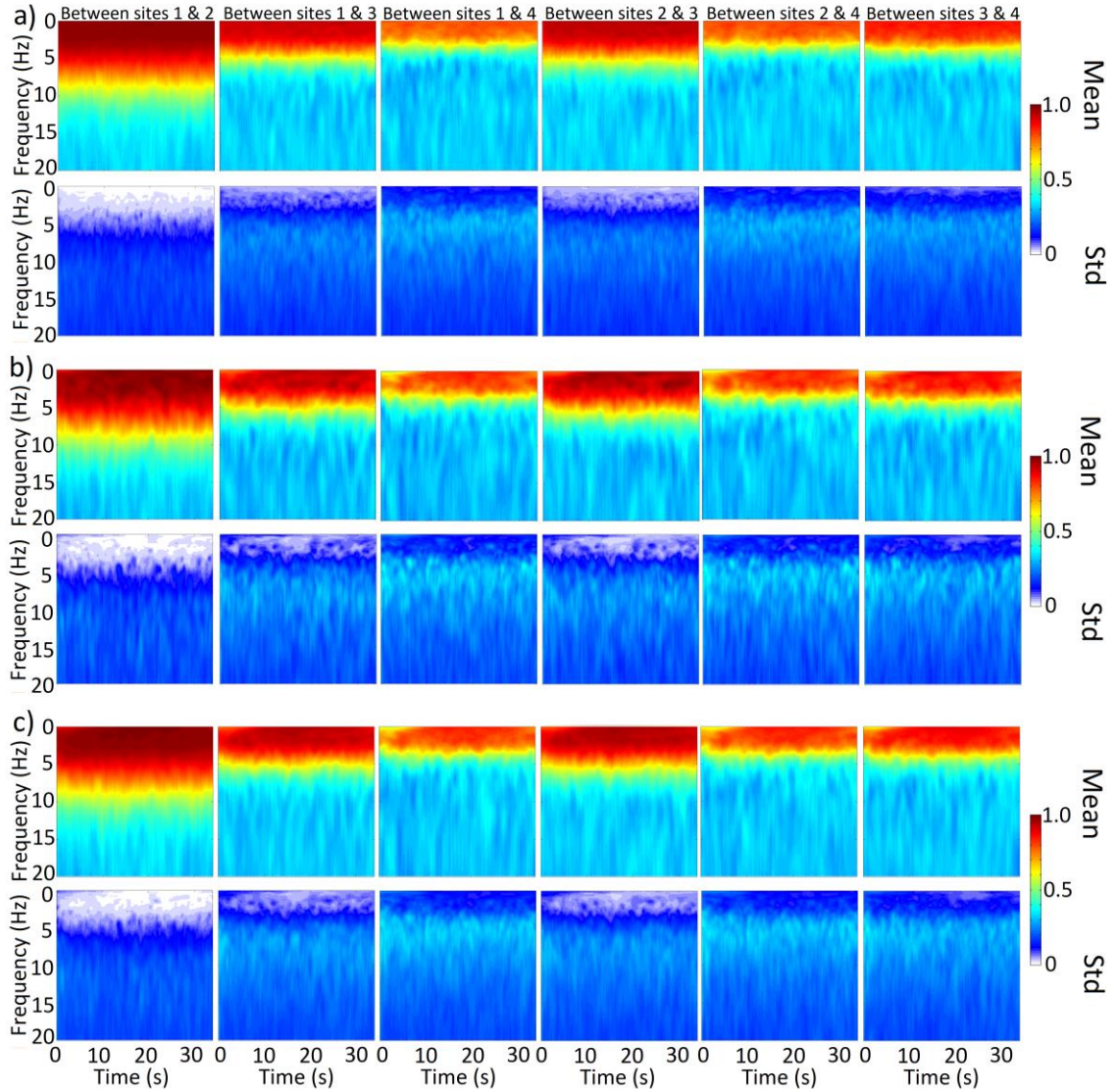


**Figure 6.7:** Estimated statistics of the lagged coherence from the sampled noises and records: a) for coherence noises; b) for nonstationary Gaussian records, and c) for nonstationary non-Gaussian noises.



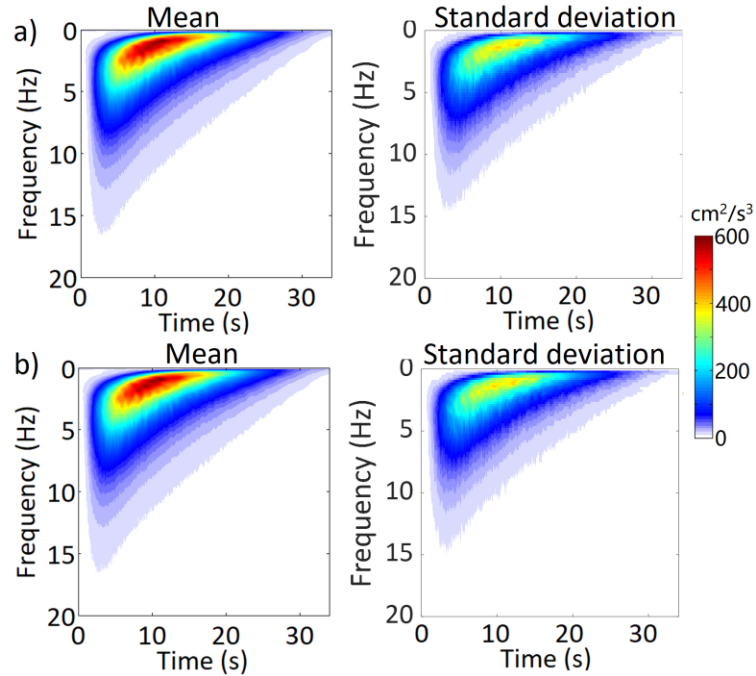


**Figure 6.8:** Estimated statistics of the TFPSD functions of the simulated ground motions: a) for simulated nonstationary Gaussian ground motions, and b) for simulated nonstationary non-Gaussian ground motions.

#### 6.4.2 Numerical validation for the case with time-dependent lagged coherence

In this section, the simulation of the vector processes by considering the time-dependent lagged coherence is carried out. For the simulation, the adopted time-dependent lagged coherence model is (see chapter 5),

$$|\Gamma_{sX_k X_l}(f, \tau)| = \tanh \left[ \frac{\exp \left[ a_1 + a_2 d_{kl} + (a_3 + a_4 d_{kl}) f^b \right]}{\times \left[ 1 - (c_1 - c_2 I_{kl}(t)^{\lambda_l}) \left( 1 - \exp(-d_{kl} / d_0)^{\lambda_d} \right) \right]} \right], \quad (6-35)$$

where  $[a_1, a_2, a_3, a_4, b, c_1, c_2, \lambda_l, d_0, \lambda_d]$  are model parameters that are equal to  $[0.78, -3.14 \times 10^{-4}, -0.16, -2.25 \times 10^{-5}, 0.8, 0.54, 0.54, 1.84, 48.6, 5.0]$ , and  $I_{kl}(t)$ , and

$$I_{kl}(t) = \frac{1}{2} \left( \frac{\sigma_k(t)}{\max(\sigma_k(t))} + \frac{\sigma_l(t)}{\max(\sigma_l(t))} \right). \quad (6-36)$$

The adopted time-varying lagged coherence is illustrated in Figure 6.9a. By using this adopted time-dependent lagged coherence, a typical simulated set of coherent noises is shown in Figure 6.9b.

By using the simulated coherence noises presented in Figure 6.9b, and the adopted target TFPSD shown in Figure 6.2b (see Eq. (28)), the analysis that is carried out for the results presented in Figures 6.4, 6.5, and 6.6 is repeated, and the obtained results are presented in Figures 6.10 to 6.12. An inspection of the results presented in the figures indicates that the observations made in the previous section are equally applicable to the results presented in Figures 6.10 to 6.12. Most importantly, the time-dependent coherence for the simulated ground motions are similar to those of simulated coherent noises, and they are consistent with their targets. The TFPSD functions of the simulated records agree with the target TFPSD function.

To have a statistical-based comparison, the above-described analysis is repeated 500 cycles. The obtained mean and standard deviation of the time-dependent lagged coherence are presented in Figures 6.13a to 6.13c; the obtained mean and standard deviation of TFPSD function are shown in Figures 6.14a and 6.14b. Again, in all cases, the mean of lagged coherence and the mean of the TFPSD functions calculated from the simulated vector processes agree well with their corresponding targets. Also, the observations made for Figures 6.7 and 6.8 in the previous section are equally applicable to the results presented in Figures 6.13 and 6.14.

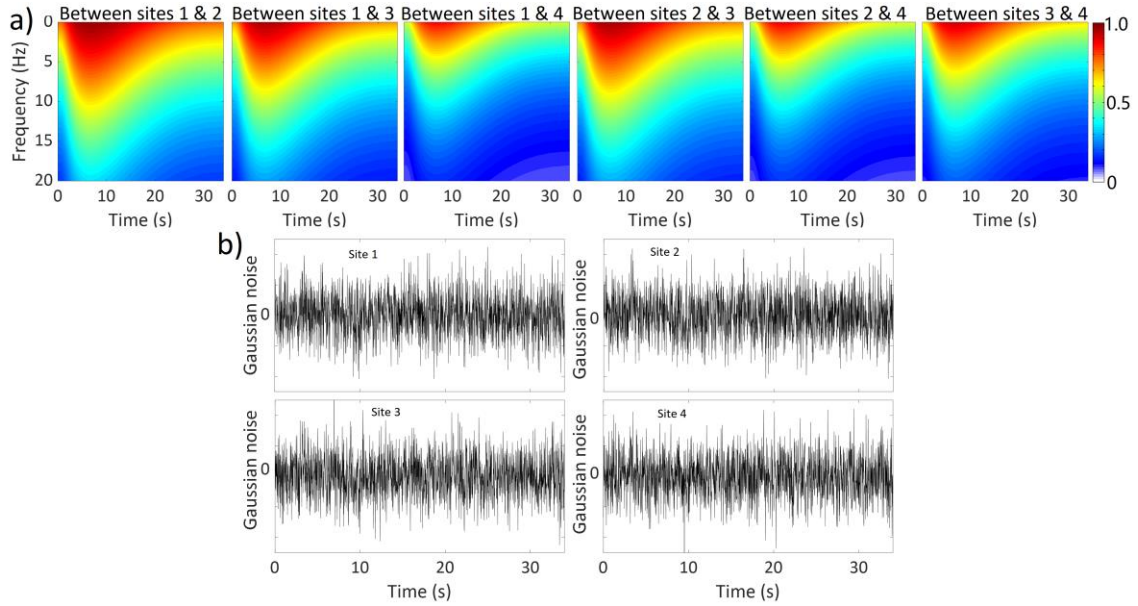


**Figure 6.9:** Target time-dependent lagged coherence and typical sampled noises with time-dependent coherence: a) target time-dependent lagged noise, and b) typical set of sampled noises.

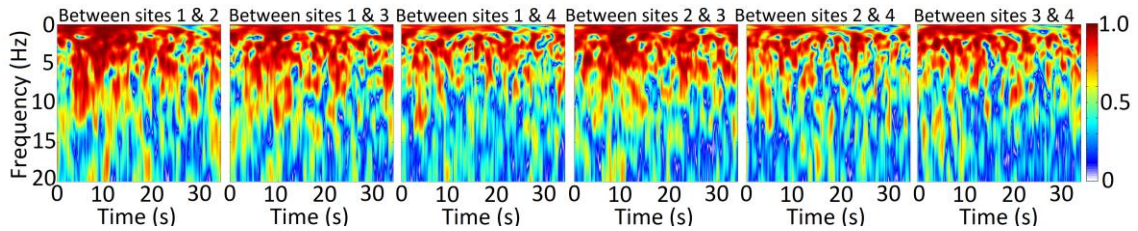


**Figure 6.10:** Calculated lagged coherence by using the sampled noises shown in Figure 6.9b.

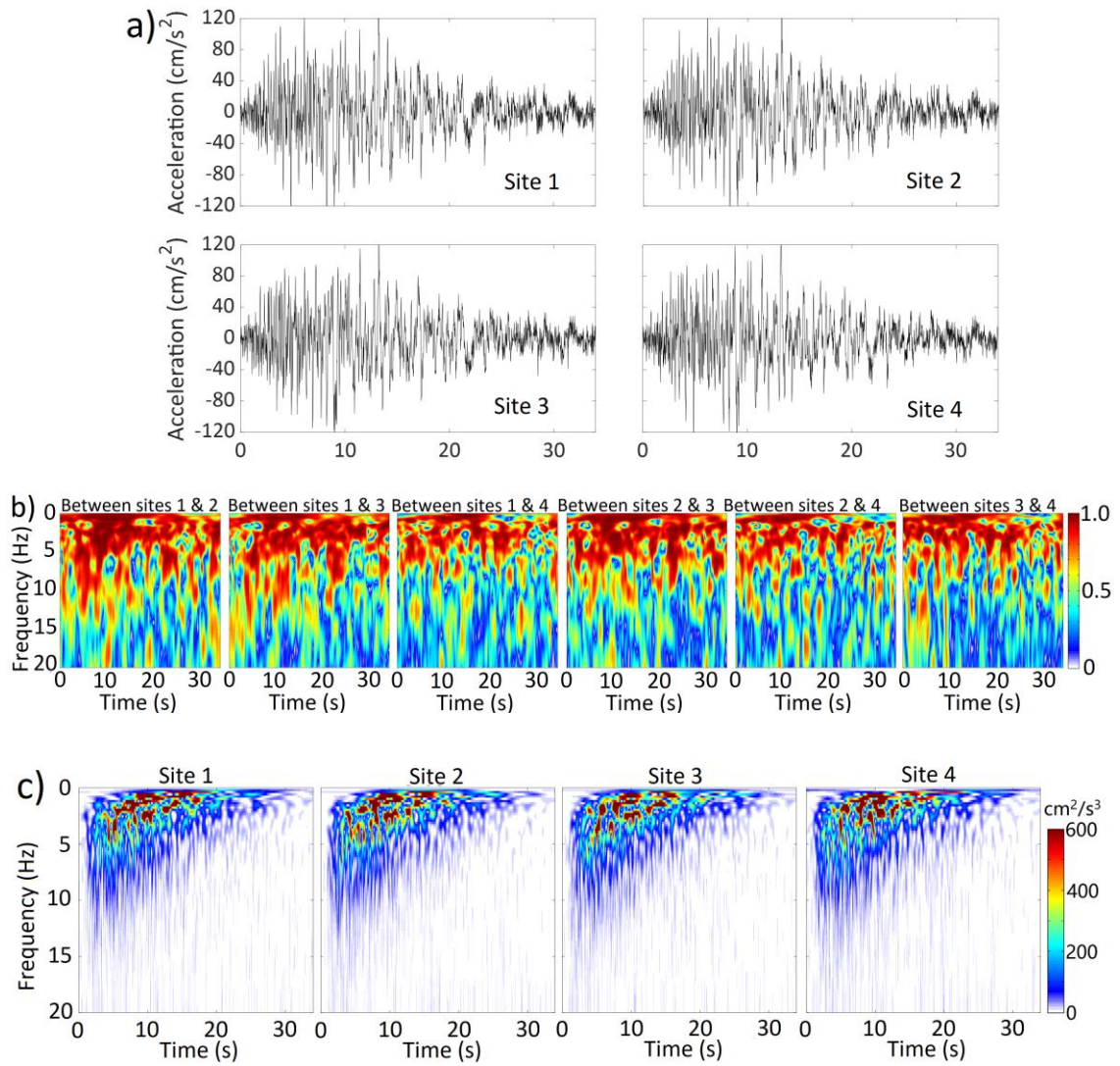


**Figure 6.11:** Simulated nonstationary Gaussian ground motions with time-dependent lagged coherence and their spectral characteristics: a) sampled records, b) calculated lagged coherence; c) calculated TFPSD.

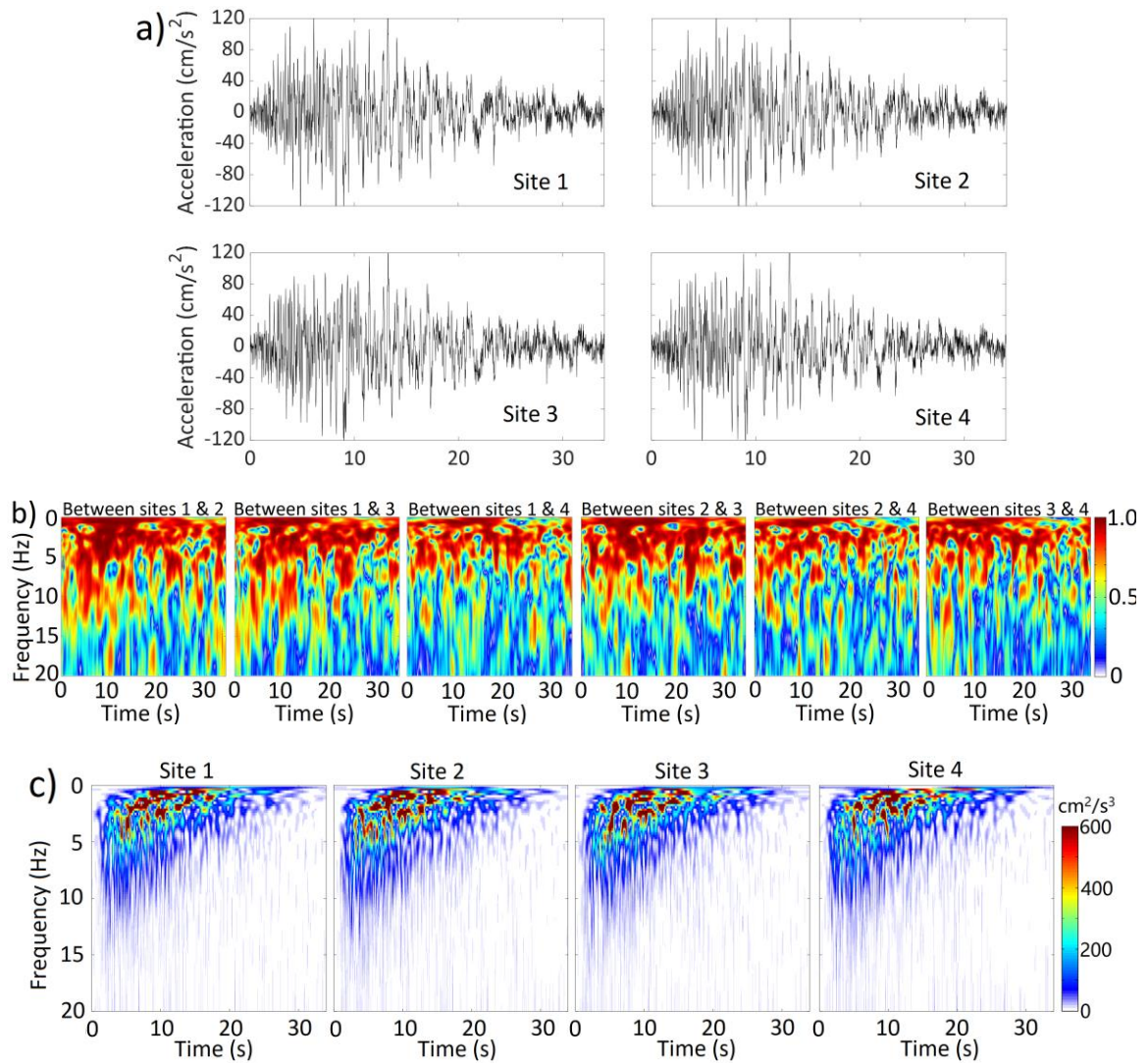


**Figure 6.12:** Simulated nonstationary non-Gaussian ground motions with time-dependent lagged coherence and their spectral characteristics: a) sampled records, b) calculated lagged coherence; c) calculated TFPSD.



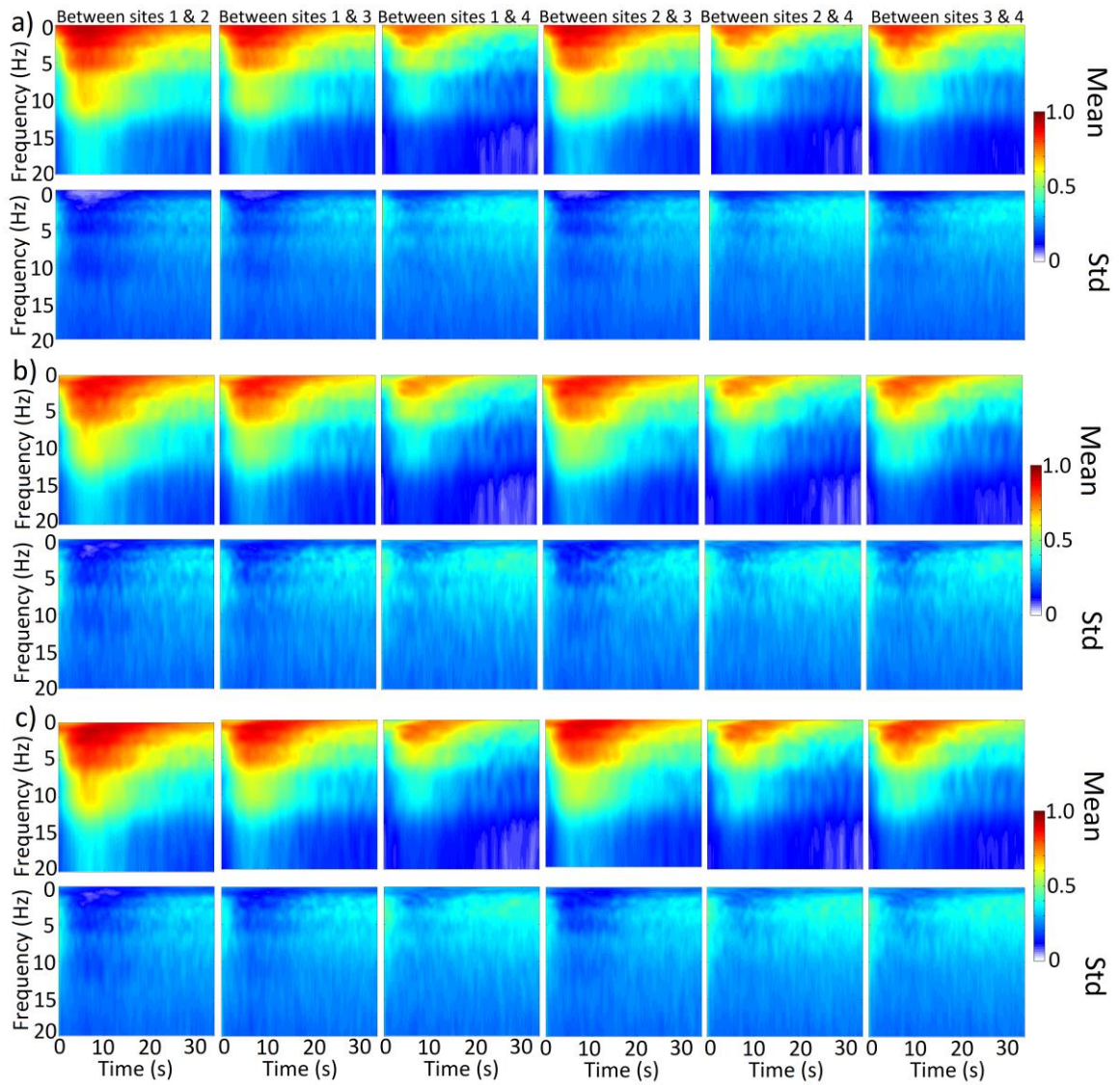


**Figure 6.13:** Estimated statistics of the lagged coherence from the sampled noises and ground motion records considering time-dependent target lagged coherence: a) for coherence noises; b) for nonstationary Gaussian records, and c) for nonstationary non-Gaussian noises;.

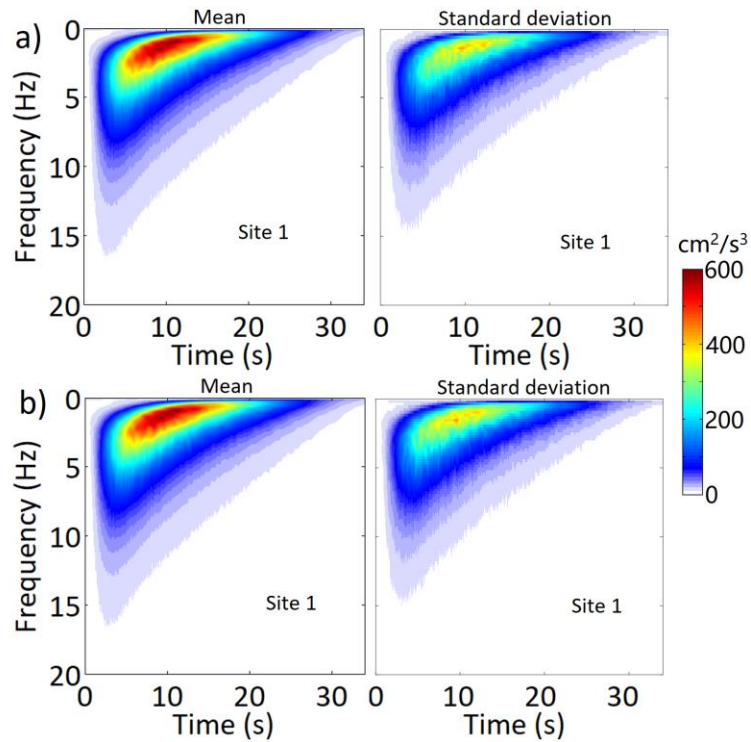


**Figure 6.14:** Estimated statistics of the TFPD functions using the simulated ground motions: a) for simulated nonstationary Gaussian ground motions, and b) for simulated nonstationary Gaussian ground motions.

## 6.5 Summary and conclusions

Natural phenomena such as the seismic ground motions could be considered nonstationary non-Gaussian. Their spatial lagged coherence could be time-dependent.

An algorithm for simulating nonstationary non-Gaussian vector processes with time-dependent lagged coherence is proposed in this chapter. The algorithm is an extension of the iterative power and amplitude correction algorithm developed for a single nonstationary non-Gaussian process. The algorithm first simulates coherent noises for given target lagged coherence, and then iteratively adjusts phases of the processes by using the same phase adjustment for all the considered processes at each time-frequency point in the transform domain. The phase adjustment is determined by the time-frequency power spectral matching, and the marginal probability distribution matching.

The algorithm is successfully validated and illustrated numerically by simulating nonstationary Gaussian and non-Gaussian vector of ground motions with time-independent as well as time-dependent lagged coherence.

Although the application of the algorithm in this chapter is focused on the seismic ground motions, the algorithm is equally applicable to other nonstationary non-Gaussian vector processes.

## Reference

- Abrahamson, N. A., Schneider, J. F., and Stepp, J. C. (1991). Empirical spatial coherency functions for application to soil - structure interaction analyses. *Earthquake spectra*, 7(1), 1-27.
- Borgnat, P., Abry, P., and Flandrin, P. (2012). Using surrogates and optimal transport for synthesis of stationary multivariate series with prescribed covariance function and non-Gaussian joint-distribution. In *2012 IEEE International Conference on Acoustics, Speech and Signal Processing (ICASSP)* (pp. 3729-3732). IEEE.
- Conte, J.P., and Peng, B.F. (1997). Fully nonstationary analytical earthquake ground-motion model. *Journal of Engineering Mechanics*, 123(1), 15-24.
- Cohen, E. A., and Walden, A. T. (2010). A statistical study of temporally smoothed wavelet coherence. *IEEE Transactions on Signal Processing*, 58(6), 2964-2973.
- Der Kiureghian A. (1996). A coherency model for spatially varying ground motions. *Earthquake Engineering & Structural Dynamics*, 25(1), 99-111.
- Deodatis, G., and Micaletti, R. C. (2001). Simulation of highly skewed non-Gaussian stochastic processes. *Journal of engineering mechanics*, 127(12), 1284-1295.
- Deodatis, G. (1996). Non-stationary stochastic vector processes: seismic ground motion applications. *Probabilistic Engineering Mechanics*, 11(3), 149-167.
- Ferrante, F., Arwade, S., and Graham-Brady, L. (2005). A translation model for non-stationary, non-Gaussian random processes. *Probability Engineering Mechanics*, 20(3), 215-228.
- Fan, F. G., and Ahmadi, G. (1990). Nonstationary kanai-tajimi models for el centro 1940 and mexico city 1985 earthquakes. *Probabilistic Engineering Mechanics*, 5(4), 171-181.
- Gurley, K., & Kareem, A. (1997). Analysis interpretation modeling and simulation of unsteady wind and pressure data. *Journal of Wind Engineering and Industrial Aerodynamics*, 69, 657-669.
- Grigoriu, M. (1998). Simulation of stationary non-Gaussian translation processes. *Journal of engineering mechanics*. 124(2), 121-126.



- Hao, H., Oliveira, C. S., and Penzien, J. (1989). Multiple-station ground motion processing and simulation based on SMART-1 array data. *Nuclear Engineering and Design*, 111(3), 293-310.
- Harichandran, R.S., and Vanmarcke, E.H. (1986). Stochastic variation of earthquake ground motion in space and time. *Journal of Engineering Mechanics*, 112(2), 154-174.
- Hong, H.P., Cui, X.Z. and Qiao, D. (2020). An algorithm to simulate nonstationary and non-Gaussian stochastic processes. Submitted to *Journal of Engineering Mechanics*.
- Kafali, C., and Grigoriu, M. (2003). Non-Gaussian model for spatially coherent seismic ground motions. *Proceedings of the ICASP9*.
- Lupoi, A., Franchin, P., Pinto, P. E., and Monti, G. (2005). Seismic design of bridges accounting for spatial variability of ground motion. *Earthquake engineering & structural dynamics*, 34(4 - 5), 327-348.
- Li, Y. G., Fan, F., and Hong, H. P. (2014). Effect of support flexibility on seismic responses of a reticulated dome under spatially correlated and coherent excitations. *Thin-Walled Structures*, 82, 343-351.
- Liang, J., Chaudhuri, S. R., and Shinozuka, M. (2007). Simulation of nonstationary stochastic processes by spectral representation. *Journal of Engineering Mechanics*, 133(6), 616-627.
- Liu, T.J. and Hong, H.P. (2015). Simulation of horizontal ground motions with spatial coherency in two orthogonal horizontal directions. *Journal of Earthquake Engineering*, 19(5), 752-769.
- Liu, T. J., and Hong, H. P. (2016). Assessment of spatial coherency using tri-directional ground motions, *Journal of Earthquake Engineering*, 20(5), 773-794.
- Luco, J. E., and Wong, H. L. (1986). Response of a rigid foundation to a spatially random ground motion. *Earthquake Engineering & Structural Dynamics*, 14(6), 891-908.
- Masters, F., and Gurley, K. R. (2003). Non-Gaussian simulation: cumulative distribution function map-based spectral correction. *Journal of engineering mechanics*, 129(12), 1418-1428.
- Nadarajah, S. (2005). A generalized normal distribution. *Journal of Applied Statistics*, 32(7), 685-694.
- Pinnegar, C.R., and Mansinha, L. (2003). The S-transform with windows of arbitrary and varying shape. *Geophysics*, 68(1), 381-385.
- Pousse, G., Bonilla, L. F., Cotton, F., and Margerin, L. (2006). Nonstationary stochastic simulation of strong ground motion time histories including natural variability: Application to the K-net Japanese database. *Bulletin of the Seismological Society of America*, 96(6), 2103-2117.
- Priestley, M. B., and Tong, H. (1973). On the analysis of bivariate non - stationary processes. *Journal of the Royal Statistical Society: Series B*, 35(2), 153-166.

- Priestley, M. B. (1965). Evolutionary spectra and non - stationary processes. *Journal of the Royal Statistical Society: Series B*, 27(2), 204-229.
- Priestley, M.B. (1981). *Spectral analysis and time series*, New York: Academic.
- Prichard, D., and Theiler, J. (1994). Generating surrogate data for time series with several simultaneously measured variables. *Physical review letters*, 73(7), 951.
- Qiao, D., Zhi, X., Fan, F., and Hong, H. (2020). Estimation of Wavelet Coherence of Seismic Ground Motions. *Bulletin of the Seismological Society of America*, 110(2), 613-628.
- Rezaeian, S., and Der Kiureghian, A. (2010). Simulation of synthetic ground motions for specified earthquake and site characteristics. *Earthquake Engineering & Structural Dynamics*, 39(10), 1155-1180.
- Shinozuka, M., and Deodatis, G. (1991). Simulation of Stochastic Processes by Spectral Representation. *Applied mechanical review (ASCE)*, 44(4): 191–204.
- Shinozuka, M., and Jan, C. M. (1972). Digital simulation of random processes and its applications. *Journal of sound vibration*, 25(1), 111-128.
- Sabetta, F., and Pugliese, A. (1996). Estimation of response spectra and simulation of nonstationary earthquake ground motions. *Bulletin of the Seismological Society of America*, 86(2), 337-352.
- Schreiber, T., and Schmitz, A. (1996). Improved surrogate data for nonlinearity tests. *Physical review letters*, 77(4), 635.
- Schreiber, T., and Schmitz, A. (2000). Surrogate time series. *Physica D: Nonlinear Phenomena*, 142(3-4), 346-382.
- Shields, M. D., and Deodatis, G. (2013). Estimation of evolutionary spectra for simulation of non-stationary and non-Gaussian stochastic processes. *Computer & Structures*, 126, 149–163.
- Stockwell, R. G. (2007). A basis for efficient representation of the S-transform. *Digital Signal Processing*, 17(1), 371-393.
- Stockwell, R. G., Mansinha, L., and Lowe, R. P. (1996). Localization of the complex spectrum: the S transform. *IEEE Transactions on Signal Processing*, 44(4), 998-1001.
- Wang, Y., and Orchard, J. (2009). Fast discrete orthonormal Stockwell transform, *SIAM Journal on Scientific Computing*, 31(5), 4000-4012.
- Wood, A. T., and Chan, G. (1994). Simulation of stationary Gaussian processes in  $[0, 1]^d$ . *Journal of computational and graphical statistics*, 3(4), 409-432.
- Wu, Y., Gao, Y., Zhang, N., and Zhang, F. (2018). Simulation of spatially varying non-gaussian and nonstationary seismic ground motions by the spectral representation method. *Journal of Engineering Mechanics*, 144(1), 04017143.
- Yamazaki, F., and Shinozuka, M. (1988). Digital generation of non-Gaussian stochastic fields. *Journal of Engineering Mechanics*, 114(7), 1183-1197.

- Yeh, C.H., and Wen, Y.K. (1990). Modeling of nonstationary ground motion and analysis of inelastic structural response, *Structural safety*, 8(1-4), 281–298.
- Zerva, A. (2009). Spatial variation of seismic ground motion: Modeling and engineering applications. *Nonlinear Dynamics*, 460.

## Chapter 7

### 7 Summary remarks and future work

#### 7.1 Summary remarks

In this thesis, a new simulation method for nonstationary ground motions at single or multiple sites consider time-independent, or time-dependent coherence is first illustrated. Then a new time-frequency power spectral density model for ground motion records and a time-dependent coherence model are proposed. Further, the simulation of nonstationary non-Gaussian ground motions at single or multiple sites is explored and shown. The proposed models and simulation algorithms can be used to simulate ground motion records for specific scenarios for single or multiple sites. The remarks from each chapter are summarized in the following:

We started to develop a very simple to use record-based approach to simulate ground motion records based on the DOST in Chapter 2. It is shown that although the time-frequency resolution obtained from DOST for the recorded ground motions is coarse as compared to that obtained using the S-transform, its use clearly identifies the energy distribution in time and frequency. The comparison of the time-frequency resolution, Fourier spectrum, time-varying power distribution, and response spectrum of the simulated and seed records indicates that the proposed simulation equation is useful for practical applications.

We then extended the model, called the time-frequency spectral representation method (TFSRM), to simulate ground motions for single and multiple sites for given time-frequency power spectral density function or matrix. Most importantly, we showed that the model is adequate to simulate ground motions with prescribed time-dependent lagged coherence. This is new and unavailable in the literature. It is shown that TFSRM can be used to conditionally simulate ground motions as well. In addition, an updating procedure is proposed to further enhance the fidelity of the time-frequency representation of the simulated ground motions.

To develop a time-frequency power spectral density (TFPSD) function model of the ground motions, extensive statistical analysis is carried out using an extensive set of actual ground motions for strike-slip fault earthquake in Chapter 4. The developed TFPSD model has 10 model parameters and can be used for scenario seismic events. The use of the proposed TFPSD function to simulate ground motions for seismic source and site conditions is illustrated by applying the simulation technique developed in Chapters 2 and 3. The adequacy of the proposed TFPSD function for the ground motions is investigated by comparing the spectral acceleration estimated from the simulated record components to the predicted PSA by using ground motion models from NGA-West2 and to the pseudo-spectral acceleration from the considered historical records. The comparison shows that they agree well.

Although there are indications that the lagged coherence of the ground motions is time-frequency dependent (TF-dependent), yet such a model is unavailable in the literature. By using records from dense arrays, a new parametric model for the TF-dependent lagged coherence model is proposed in Chapter 5. The model is first of its kind. The TF-dependent lagged coherence varies with the (time-varying) intensity within the duration of the records; a higher normalized intensity corresponds to a higher lagged coherence. The model is a function of the frequency, the separation between recording sites, and the normalized ground motion intensity that is a function of time. The use of the proposed model to simulate ground motions at multiple sites is illustrated.

Chapter 6 is focused on the simulation of non-stationary and non-Gaussian processes. An efficient iterative algorithm for simulating nonstationary non-Gaussian vector processes with time-dependent lagged coherence is proposed. The algorithm is an extension of the iterative power and amplitude correction algorithm developed for a single nonstationary non-Gaussian process. The algorithm is successfully validated and illustrated numerically by simulating nonstationary Gaussian and non-Gaussian vector of ground motions with time-independent as well as time-dependent lagged coherence.

## 7.2 Future work

Some potential future investigations envisaged are given below:

1. The simulation of time-dependent coherent ground motions is based on DOST whose resolution is less than that of the S-transform. Although the coherence between ground motion calculated based on DOST and S-transform is very close, the direct use of the S-transform to simulation spatially coherent ground motions could be an interesting and challenging topic.
2. Although the standard deviation of interevent and intraevent of the developed TFPSD model is given, the correlation between the intraevent residual is unknown. This correlation may be dependent on the  $M$ ,  $R_{rup}$ , and  $V_{S30}$ . The investigation of such correlation could lead to an improved model characterization.
3. During the investigation of time-dependent coherence model, it was observed that the coherence might depend on the earthquake magnitude. This aspect deserves further consideration if the data become available in the near future.
4. The proposed iterative power and amplitude correction algorithm for simulating ground motions is proposed. The algorithm is efficient. Several aspects of the algorithms deserve further consideration, including the selection of convergence criterion, further improvement of efficiency and robustness.

## Appendix

### Appendix. A Expectation of TFPSD function of the proposed models for a single site

To simplify the notation for the proof that the expected TFPSD function of the nonstationary processes described by the proposed Model-1 and Model-2 is equal to its target value, let  $D_{1R}(t_k; j) = \text{Re}(D_1(t_k; j))$  and  $D_{1I}(t_k; j) = \text{Im}(D_1(t_k; j))$ . The expectation of the time-frequency spectrum of Model-1 can be written as,

$$\begin{aligned}
 E\{X_{1\mathcal{D}\mathcal{S}}(l)X_{1\mathcal{D}\mathcal{S}}^*(m)\} &= \\
 2 \times \frac{2}{N^2} E &\left\{ \sum_{k_1=0}^{N-1} D_1(t_{k_1}; l) \sum_{j_1=1}^{N_1} \sqrt{S(j_1)} \text{Re}\left[D_1(t_{k_1}; j_1) e^{i\theta(j_1)}\right] \right. \\
 &\left. \times \sum_{k_2=0}^{N-1} D_1^*(t_{k_2}; m) \sum_{j_2=1}^{N_1} \sqrt{S(j_2)} \text{Re}\left[D_1(t_{k_2}; j_2) e^{i\theta(j_2)}\right] \right\} \quad (\text{A-1}) \\
 &= 2 \times \frac{2}{N^2} \sum_{k_1=0}^{N-1} \sum_{k_2=0}^{N-1} D_1(t_{k_1}; l) D_1^*(t_{k_2}; m) \sum_{j_1=1}^{N_1} \sqrt{S(j_1)} E \left\{ \sum_{j_2=1}^{N_1} \sqrt{S(j_2)} E\{CS\} \right\}
 \end{aligned}$$

where,

$$E\{CS\} = E \left\{ \begin{aligned} &\left[ D_{1R}(t_{k_1}; j_1) \cos(\theta(j_1)) - D_{1I}(t_{k_1}; j_1) \sin(\theta(j_1)) \right] \\ &\times \left[ D_{1R}(t_{k_2}; j_2) \cos(\theta(j_2)) - D_{1I}(t_{k_2}; j_2) \sin(\theta(j_2)) \right] \end{aligned} \right\} \quad (\text{A-2})$$

Using the condition that  $\theta(j)$  are independent and uniformly distributed between 0 and  $2\pi$ , the expectation in Eq. (A-1) becomes,

$$E \left\{ \sum_{j_2=1}^{N_1} \sqrt{S(j_2)} E\{CS\} \right\} = \frac{\sqrt{S(j_1)}}{2} \left\{ D_{1R}(t_{k_1}; j_1) D_{1R}(t_{k_2}; j_1) + D_{1I}(t_{k_1}; j_1) D_{1I}(t_{k_2}; j_1) \right\} \quad (\text{A-3})$$

Substituting Eq. (A-3) into Eq. (A-1) results in,

$$\begin{aligned}
& E\{X_{1\mathcal{D}\mathcal{S}}(l)X_{1\mathcal{D}\mathcal{S}}^*(m)\} \\
&= \frac{2}{N^2} \sum_{k_1=0}^{N-1} \sum_{k_2=0}^{N-1} D_1(t_{k_1}; l) D_1^*(t_{k_2}; m) \sum_{j_1=1}^{N_1} S(j_1) \{D_{1R}(t_{k_1}; j_1) D_{1R}(t_{k_2}; j_1) + D_{1I}(t_{k_1}; j_1) D_{1I}(t_{k_2}; j_1)\} \\
&= \frac{2}{N^2} \sum_{j_1=1}^{N_1} S(j_1) \sum_{k_1=0}^{N-1} D_1(t_{k_1}; l) \left\{ \begin{aligned} & D_{1R}(t_{k_1}; j_1) \sum_{k_2=0}^{N-1} D_{1R}(t_{k_2}; j_1) D_1^*(t_{k_2}; m) \\ & + D_{1I}(t_{k_1}; j_1) \sum_{k_2=0}^{N-1} D_{1I}(t_{k_2}; j_1) D_1^*(t_{k_2}; m) \end{aligned} \right\} \quad (\text{A-4}) \\
&= \frac{2}{N^2} \sum_{j_1=1}^{N_1} S(j) \left\{ \begin{aligned} & (I_{RR}(j, m) - iI_{RI}(j, m))(I_{RR}(j, l) + iI_{RI}(j, l)) \\ & + (I_{IR}(j, m) - iI_{II}(j, m))(I_{IR}(j, l) + iI_{II}(j, l)) \end{aligned} \right\}
\end{aligned}$$

where the index function,

$$I_{UV}(j, l) = \sum_{k=0}^{N-1} D_{1U}(t_k; j) D_{1V}(t_k; l), \quad (\text{A-5})$$

in which  $U$  and  $V$  equal  $R$  or  $I$ . Since the basis functions in DOST are orthonormal,  $I_{UV}(j, l) = 1/2$  if  $U = V$  and  $j = l$ , otherwise it equals zero. The use of this in Eq. (A-4) leads to,

$$E\{X_{1\mathcal{D}\mathcal{S}}(l)X_{1\mathcal{D}\mathcal{S}}^*(m)\} = \frac{2}{N^2} \sum_{j=1}^{N_1} S(j) \{I_{RR}(j, m)I_{RR}(j, l) + I_{II}(j, m)I_{II}(j, l)\}. \quad (\text{A-6})$$

which becomes,

$$E\{X_{1\mathcal{D}\mathcal{S}}(j)X_{1\mathcal{D}\mathcal{S}}^*(j)\} = S(j). \quad (\text{A-7})$$

if  $l = m = j$ . This completes the proof for Eq. (14) in chapter 3.

For Model-2, the expectation of the TFPSD function can be written as,



$$\begin{aligned}
E\{X_{1\mathcal{D}S}(l)X_{1\mathcal{D}S}^*(m)\} &= \frac{2}{N^2} E \left\{ \sum_{k_1=0}^{N-1} D_1(t_{k_1}; l) \sum_{j_1=1}^{N_1} [A_{j_1} D_{1R}(t_{k_1}; j_1) + B_{j_1} D_{1I}(t_{k_1}; j_1)] \right. \\
&\quad \left. \times \sum_{k_2=0}^{N-1} D_1^*(t_{k_2}; m) \sum_{j_2=1}^{N_1} [A_{j_2} D_{1R}(t_{k_2}; j_2) + B_{j_2} D_{1I}(t_{k_2}; j_2)] \right\} \quad .(A-8) \\
&= \frac{2}{N^2} \sum_{k_1=0}^{N-1} \sum_{k_2=0}^{N-1} D_1(t_{k_1}; l) D_1^*(t_{k_2}; m) \sum_{j_1=1}^{N_1} S(j_1) [D_{1R}(t_{k_1}; j_1) D_{1R}(t_{k_2}; j_1) + D_{1I}(t_{k_1}; j_1) D_{1I}(t_{k_2}; j_1)]
\end{aligned}$$

Since the last equality in Eq. (A-8) is the same as the second equality shown in Eq. (A-4), consequently, the solution given in Eq. (A-6) also apply to Eq. (A-8), indicating that the expectation of the TFPSD function of the nonstationary stochastic process by Model-2 equal to the target TFPSD function  $S(j)$ .

## Appendix. B Expectation of TFPSD function of the proposed models for multiple-support

Let the DOST of  $X_{n_1}(t)$  and  $X_{n_2}(t)$  be denoted as  $X_{n_1, \mathcal{D}\mathcal{S}}(j)$  and  $X_{n_2, \mathcal{D}\mathcal{S}}(j)$  (i.e.,  $\sqrt{2}X_{n_1, \mathcal{D}\mathcal{S}}(p, q)$  and  $\sqrt{2}X_{n_2, \mathcal{D}\mathcal{S}}(p, q)$ ). The application of DOST to  $X_{n_1}(t)$  shown in Eq. (21) in chapter 3 results in,

$$X_{n_1, \mathcal{D}\mathcal{S}}(l) = \frac{2}{N} \sum_{k_1=0}^{N-1} D_1(t_{k_1}; l) \sum_{m_1=1}^{n_1} \sum_{j_1=1}^{N_1} \text{Re} \left[ L_{n_1 m_1}(j_1) D_1(t_{k_1}; j_1) e^{i\theta(m_1, j_1)} \right], \quad (\text{B-1})$$

and  $X_{n_2, \mathcal{D}\mathcal{S}}(j)$  can be written in a similar fashion. The expectation of the TFPSD function of the nonstationary processes defined by Model-1 shown in Eq. (21) in chapter 3 for  $n_1 \leq n_2$  is then given by,

$$\begin{aligned} E \left\{ X_{n_1, \mathcal{D}\mathcal{S}}(l) X_{n_2, \mathcal{D}\mathcal{S}}^*(m) \right\} &= \frac{4}{N^2} E \left\{ \sum_{k_1=0}^{N-1} D_1(t_{k_1}; l) \sum_{m_1=1}^{n_1} \sum_{j_1=1}^{N_1} \text{Re} \left[ L_{n_1 m_1}(j_1) D_1(t_{k_1}; j_1) e^{i\theta(m_1, j_1)} \right] \right. \\ &\quad \left. \times \sum_{k_2=0}^{N-1} D_1^*(t_{k_2}; m) \sum_{m_2=1}^{n_2} \sum_{j_2=1}^{N_1} \text{Re} \left[ L_{n_2 m_2}(j_2) D_1(t_{k_2}; j_2) e^{i\theta(m_2, j_2)} \right] \right\} \\ &= \frac{4}{N^2} \sum_{k_1=0}^{N-1} \sum_{k_2=0}^{N-1} D_1(t_{k_1}; l) D_1^*(t_{k_2}; m) \times \\ &\quad E \left\{ \sum_{m_1=1}^{n_1} \sum_{j_1=1}^{N_1} \text{Re} \left[ L_{n_1 m_1}(j_1) D_1(t_{k_1}; j_1) e^{i\theta(m_1, j_1)} \right] \sum_{m_2=1}^{n_2} \sum_{j_2=1}^{N_1} \text{Re} \left[ L_{n_2 m_2}(j_2) D_1(t_{k_2}; j_2) e^{i\theta(m_2, j_2)} \right] \right\} \end{aligned} \quad (\text{B-2})$$

After some algebraic manipulations and considering that the phase angles  $\theta(m, j)$  are independent and uniformly distributed between 0 to  $2\pi$  and the basis functions in DOST are orthonormal, Eq. (B-2) becomes,

$$E \left\{ X_{n_1, \mathcal{D}\mathcal{S}}(l) X_{n_2, \mathcal{D}\mathcal{S}}^*(m) \right\} = 0. \quad (\text{B-3})$$

if  $l \neq m$ , and,

$$\begin{aligned}
& E\left\{X_{n_1 1 \mathcal{D}\mathcal{S}}(j)X_{n_2 1 \mathcal{D}\mathcal{S}}^*(j)\right\} \\
&= \frac{1}{2} \sum_{m_1=1}^{n_1} \left[ L_{n_1 m_1}^*(j) L_{n_2 m_1}(j) + L_{n_2 m_1}(j) L_{n_1 m_1}^*(j) \right] = S_{n_1 n_2}(j).
\end{aligned} \tag{B-4}$$

if  $l = m = j$ . The last equality is based on the Cholesky decomposition of the matrix  $\mathbf{S}(j)$ . Eq. (B-4) indicates that the expectation of the TFPSD function of the sampled records from Model-2 equal to the target TFPSD matrix  $\mathbf{S}(j)$ .

For Model-2 shown in Eq. (22) in chapter 3, the expectation of the TFPSD function can be written as,

$$\begin{aligned}
E\left\{X_{n_1 1 \mathcal{D}\mathcal{S}}(l)X_{n_2 1 \mathcal{D}\mathcal{S}}^*(m)\right\} &= \frac{2}{N^2} E \left\{ \sum_{k_1=0}^{N-1} D_1(t_{k_1}; l) \sum_{j_1=1}^N \left[ A_{n_1 j_1} D_{1R}(t_{k_1}; j_1) \right. \right. \\
&\quad \left. \left. + B_{n_1 j_1} D_{1I}(t_{k_1}; j_1) \right] \right. \\
&\quad \left. \times \sum_{k_2=0}^{N-1} D_1^*(t_{k_2}; m) \sum_{j_2=1}^N \left[ A_{n_2 j_2} D_{1R}(t_{k_2}; j_2) \right. \right. \\
&\quad \left. \left. + B_{n_2 j_2} D_{1I}(t_{k_2}; j_2) \right] \right\}. \tag{B-5} \\
&= \frac{2}{N^2} \sum_{k_1=0}^{N-1} \sum_{k_2=0}^{N-1} D_1(t_{k_1}; l) D_1^*(t_{k_2}; m) \sum_{j_1=1}^N S_{n_1 n_2}(j_1) \left[ D_{1R}(t_{k_1}; j_1) D_{1R}(t_{k_2}; j_1) \right. \\
&\quad \left. + D_{1I}(t_{k_1}; j_1) D_{1I}(t_{k_2}; j_1) \right]
\end{aligned}$$

Following the same steps as shown in Eqs. (A-4) to (A-7), it can be shown that

$$E\left\{X_{n_1 1 \mathcal{D}\mathcal{S}}(l)X_{n_2 1 \mathcal{D}\mathcal{S}}^*(m)\right\} = \begin{cases} 0, & l \neq m \\ S_{n_1 n_2}(m), & l = m \end{cases} \tag{B-6}$$

Note that the right-hand side of the first equality in Eq. (B-5) represents the application of double DOST but one with the conjugate basis functions (DOST\*) to the correlation function of  $X_{n_1}(t_{k_1})$  and  $X_{n_2}(t_{k_2})$ ,  $R(t_{k_1}, t_{k_2})$ . This indicates that for the considered models of the nonstationary stochastic processes, the double DOST to the correlation function of two processes equals the expected value of the product of DOST of a process and DOST\* of another process. The product equals the quantity given in Eq. (B-6), reflecting the orthogonality of energy in different non-overlapping cells in the time-frequency domain.

## **Appendix. C An algorithm to simulate nonstationary and non-Gaussian stochastic processes**

### **C.1 Introduction**

Observed time histories of the seismic ground motions (Newmark and Rosenblueth 1976), wind velocity (Simiu and Scanlan 1996), wave height (Ochi 2005), etc. fluctuate randomly in time and space. The time histories are used as the input to carry out the structural analysis. Since the available recorded time histories of the random phenomena are limited, their synthetics are generated and used in practice. The simulation is based on the theory of stochastic processes (Lutes and Sarkani 2004; Li and Chen 2009; Cramér and Leadbetter 2013).

For stationary Gaussian processes, and evolutionary processes (Priestley 1965), the simulation can be carried out using the spectral representation method (Shinozuka and Jan 1972; Liang et al. 2007), developed based on the ordinary Fourier transform (FT). A stationary process is defined by its power spectral density (PSD) function, and an evolutionary process is defined by the evolutionary PSD that is a function of an amplitude modulation function. The evolutionary process with time-dependent amplitude modulation is widely used in generating seismic ground motions (Deodatis 1996; Boore 2009) and fluctuating wind velocity for high-intensity wind events (Chen and Letchford 2007; Kwon and Kareem 2009; Huang and Chen 2009; Hong 2016).

Masters and Gurley (2003) proposed an iterative spectral correction algorithm to simulate the stationary non-Gaussian processes, where the spectral representation method is used in each iteration to generate the time history. They showed that their algorithm outperforms the SRM-based simulation techniques presented in Yamazaki and Shinozuka (1988), Gurley and Kareem (1997), Grigoriu (1998), and Deodatis and Micaletti (2001). It is noted that an algorithm similar to the spectral correction algorithm, namely the iterative amplitude adjusted Fourier transform (IAAFT) algorithm, was proposed by Schreiber and Schmitz (1996, 2000) in the context of generating surrogate for statistical hypothesis testing. The use of the translation process for the stationary non-Gaussian

process proposed in Grigoriu (1998) was extended for the nonstationary processes by others, including Ferrante et al. (2005) and Shields et al. (2011).

The evolutionary PSD is often assessed using (time-dependent) windowed Fourier transform, such as the short-time Fourier transform (Cohen 1995). The resolution of such a transform is controlled by the width of the window. As the width of the window increases, a better resolution is obtained at the low frequencies, and the resolution in time deteriorates. A good resolution in both time and frequency (i.e., scale) can be obtained by applying the continuous wavelet transforms (WT) (Daubechies 1992; Percival and Walden 2006). A procedure to estimate the evolutionary PSD by applying the continuous WT was proposed by Spanos and Failla (2004). However, an algorithm that directly applies the continuous WT to simulate the nonstationary stochastic processes with a prescribed wavelet spectrum or time-scale PSD was unavailable. Recently, an iterative algorithm was presented by Chavez and Cazelles (2019) to generate surrogate for statistical hypothesis testing. We will point out, in the following sections, a potential weakness of the algorithm, as well as the link between this algorithm and an interesting way of defining nonstationary processes in the wavelet domain introduced by Maraun et al. (2007). The lack of continuous WT-based algorithm to simulate time histories is partly due to that the use of continuous WT does not lead to the decomposed signal to be represented by a set of orthogonal basis functions. Rather than using the continuous WT, the application of the discrete WT and wavelet packet transform that have sets of orthogonal basis functions is presented in Gurley and Kareem (1999), and Yamamoto and Baker (2013). The resolution obtained by using these discrete transforms is less refined than that obtained by using the continuous WT.

The phase information in WT is local, while the phase information in the Fourier transform refers to the harmonics at zero time (Stockwell 2007). Stockwell et al. (1996) (see also Pinnegar and Mansinha 2003) developed the S-transform (ST) that provides the time-frequency representation of the analyzed signal. It is a hybrid of continuous WT and windowed FT. The S-transform provides frequency-dependent resolution. Similar to the continuous WT, ST does not lead to a decomposed signal to be represented by a set of orthogonal basis functions. Stockwell (2007) proposed a discrete orthonormal S-

transform. The simulation of the seismic ground motions by using the discrete orthonormal S-transform or combination with ST was presented in Cui and Hong (2020) and Hong and Cui (2020). These studies argued that the time-frequency PSD obtained based on ST should not be used as the evolutionary PSD since the former could include the time-varying frequency. However, an algorithm by using ST alone to simulate nonstationary stochastic processes has not been reported in the literature.

There are other techniques used to simulate the nonstationary processes. These include the application of autoregressive moving-average (Samaras et al. 1985), Karhunen–Loève expansion (Spanos and Ghanem 1989; Phoon et al. 2002; Spanos et al. 2007), and polynomial chaos (Sakamoto and Ghanem 2002), and Hilbert-Huang transform (Wen and Gu 2004). A review of these simulation procedures is beyond the presented study since these techniques involve varieties of mathematical concepts and algorithms.

In the present study, we exam and extend the definition of the nonstationary processes in the transform domain. We proposed an iterative power and amplitude correction (IPAC) algorithm to simulate nonstationary and non-Gaussian processes. The algorithm could be viewed as an extension of IAAFT (Schreiber and Schmitz 1996) and the spectral correction algorithm (Masters and Gurley 2003) and is rooted in the concept of defining the stochastic processes in the transform domain. In particular, we provide details of using the proposed algorithm with FT, ST and WT, where the energy distribution in the transform domain that satisfies energy preservation is prescribed, and the marginal probability distribution function of the process is given. We provide numerical examples to show the proposed algorithm and compare the simulated time histories obtained by using the ST-based and (continuous) WT-based approach.

## **C.2 Fourier transform, S-transform, and wavelet transforms**

This section summarizes some basic properties of FT (Cohen 1995; Newland 2012), ST (Stockwell et al. 1996; Pinnegar and Mansinha 2003), and continuous WT (Daubechies 1992). Only the continuous WT, including its discretized form (which differs from the discrete wavelet transform), is used in the present study. Unless

otherwise indicated, WT is used to refer to the continuous WT and its discretized form in the following. The summary provides the basis for the proposed iterative simulation algorithm to be described in the next sections.

Let  $x(t)$  denote a sample of a stochastic process such as the ground motion record,  $X(t)$ . FT of  $x(t)$ , and its inverse (IFT) can be expressed as

$$\hat{x}(f) = FT_t(x(t)) = \int_{-\infty}^{+\infty} x(t)e^{-i2\pi ft} dt, \quad (C-1)$$

and,

$$x(t) = IFT_f(\hat{x}(f)) = \int_{-\infty}^{+\infty} \hat{x}(f)e^{i2\pi ft} dt \quad x(t) = IFT_f(\hat{x}(f)) = \int_{-\infty}^{+\infty} \hat{x}(f)e^{i2\pi ft} dt, \quad (C-2)$$

where  $FT(\square)$  and  $IFT(\square)$  denote the FT and IFT operations, the subscript associated with these operators indicates the domain or the index where the operation is carried out;  $\hat{x}(f)$  denotes FT of  $x(t)$ ;  $f$  is the frequency in Hz,  $\hat{x}(f) = \hat{x}^*(-f)$ , and  $*$  denotes the complex conjugate. A symbol or function with a circumflex is used to represent its FT throughout the present study. If  $x(t)$  is given in the discrete form  $x(j\Delta_t)$ ,  $j = 0, \dots, N-1$ , with a sampling time interval  $\Delta_t$  and the duration  $T$ ,  $T = N\Delta_t$ , the (discretized) FT pair is given by,

$$x(j\Delta_t) = IFT_p(\hat{x}(p\Delta_f)) = \frac{1}{N\Delta_t} \sum_{k=0}^{N-1} \hat{x}(k\Delta_f) e^{i\frac{2\pi}{N}kj}, \quad (C-3)$$

and,

$$\hat{x}(p\Delta_f) = FT_j(x(j\Delta_t)) = \Delta_t \sum_{k=0}^{N-1} x(k\Delta_t) e^{-i\frac{2\pi}{N}pk}, \quad (C-4)$$

where  $p = 0, \dots, N-1$ ,  $\Delta_f = 1/T$ , and the operators  $FT(\square)$  and  $IFT(\square)$  that are used for continuous FT are used for discrete FT as well. It is considered implicitly in the following that the numerical calculations of  $\hat{x}(p\Delta_f)$  and  $x(j\Delta_t)$  are to be carried by

using the fast Fourier transform (FFT) (Newland 2012) for computational efficiency. Moreover, the notation  $\{\square\}_N$  is used for the collection of its argument of length  $N$ . For example,  $\{x(j\Delta_t)\}_N$  represents all  $x(j\Delta_t)$  for  $j = 0, \dots, N-1$ .

ST of  $x(t)$  is defined as (Stockwell et al. 1996; Pinnegar and Mansinha 2003),

$$x_S(f, \tau) = ST(x(t)) = \int_{-\infty}^{\infty} x(t)w(f, \tau-t)e^{-i2\pi ft} dt, \quad (\text{C-5})$$

where  $x_S(f, \tau)$  is the ST coefficient,  $ST(\square)$  denotes the S-transform of its argument, and  $\tau$  is the center of the window function  $w(f, \tau-t)$  defined as,

$$w(f, \tau-t) = \frac{|f|}{\sqrt{2\pi\kappa}} \exp\left(-\frac{f^2(\tau-t)^2}{2\kappa^2}\right). \quad (\text{C-6})$$

The parameter  $\kappa$  in Eq. (C-6) controls the effective width of the window in ST. It can be shown (Stockwell et al. 1996) that,

$$x_S(f, \tau) = \int_{-\infty}^{\infty} \hat{x}(\phi + f) \exp\left(-\frac{1}{2}\left(\frac{2\pi\phi\kappa}{f}\right)^2\right) e^{i2\pi\phi\tau} d\phi, \quad (\text{C-7})$$

and,

$$x(t) = IST(x_S(f, \tau)) = \int_{-\infty}^{\infty} \left[ \int_{-\infty}^{\infty} x_S(f, \tau) d\tau \right] e^{i2\pi ft} df, \quad (\text{C-8})$$

where  $IST(\square)$  is the inverse S-transform (IST). Using Eqs. (C-7) and (C-8), the discretized version of  $x(t)$  and  $x_S(f, \tau)$ , represented by  $x(j\Delta_t)$  and  $x_S(q\Delta_f, p\Delta_t)$  pair, can be written as,

$$x(j\Delta_t) = IST(x_S(p\Delta_f, q\Delta_t)) = IFT_p \left( \Delta_t \sum_{k=0}^{N-1} x_S(p\Delta_f, k\Delta_t) \right), \text{ for } j = 0, \dots, N-1, \quad (\text{C-9})$$



and,

$$x_s(p\Delta_f, q\Delta_t) = ST(x(q\Delta_t)) = IFT_j \left( \hat{x}((j+p)\Delta_f) \exp\left(-\frac{2\pi^2 j^2 \kappa^2}{p^2}\right) \right), \quad \text{for}$$

$$p, q = 0, \dots, N-1, \quad (\text{C-10})$$

indicating that the evaluation of the ST coefficients at  $(p\Delta_f, q\Delta_t)$  and its inverse at  $j\Delta_t$  based on FT (Battisti and Riba 2016).

WT is defined as (Daubechies 1992; Percival and Walden 2006),

$$x_w(s, \tau) = WT(x(t)) = \frac{1}{\sqrt{|s|}} \int_{-\infty}^{\infty} x(t) \psi^* \left( \frac{t-\tau}{s} \right) dt, \quad (\text{C-11})$$

where  $x_w(s, \tau)$  is the wavelet coefficient, the operator  $WT(\square)$  denotes WT,  $\psi(\cdot)$  is the mother wavelet and,  $s$  is the scaling or dilation factor, and  $\tau$  is the translation or position parameter. Eq. (C-11) can be expressed as (Daubechies 1992; Percival and Walden 2006),

$$x_w(s, \tau) = \sqrt{|s|} \int_{-\infty}^{\infty} \hat{x}(f) \hat{\psi}^*(sf) e^{i2\pi f\tau} df, \quad (\text{C-12})$$

to facilitate its computation by using FFT for signals given in the discretized form. If the admissibility condition  $0 < C_\psi < \infty$  is satisfied, where  $C_\psi = \int_{-\infty}^{\infty} (1/|f|) \times |\hat{\psi}(f)|^2 df$ ,  $x(t)$  can be obtained using the following inverse WT (Daubechies 1992),

$$x(t) = IWT(x_w(s, \tau)) = \frac{1}{C_\psi} \int_{-\infty}^{\infty} \int_{-\infty}^{\infty} x_w(s, \tau) \frac{1}{\sqrt{|s|}} \psi \left( \frac{t-\tau}{s} \right) \frac{1}{s^2} d\tau ds, \quad (\text{C-13})$$

where  $IWT(\square)$  is the inverse of  $WT(\square)$ . If  $\psi(t) = \psi^*(-t)$ , Eq. (C-13) becomes,

$$x(t) = \frac{2}{C_\psi} \int_0^\infty \int_{-\infty}^\infty x_w(s, \tau) \frac{1}{\sqrt{s}} \psi\left(\frac{t-\tau}{s}\right) \frac{1}{s^2} d\tau ds. \quad (\text{C-14})$$

Moreover, if the analytical wavelet – complex-valued wavelet function that has no negative frequency components – is used, Eq. (C-13) can be expressed in Morlet formulation (Shenza 1992),

$$x(t) = \text{Re} \left( \frac{2}{C_{1\psi}} \int_0^\infty \frac{1}{s^{3/2}} x_w(s, t) ds \right), \quad (\text{C-15})$$

$$\text{where } C_{1\psi} = \int_0^\infty (\hat{\psi}^*(f)/|f|) df.$$

There are several well-known wavelet families (Daubechies 1992; Percival and Walden 2006; Olhede and Walden 2002), including Daubechies wavelets, generalized Morse wavelets, and Morlet wavelets.

Eq. (C-14), (C-15) and (C-13) can be written in the following discretized form,

$$x(j\Delta_t) = \frac{2\Delta_t \ln s_0}{C_\psi} \sum_{k=0}^K \sum_{r=-L_t}^{L_t} x_w(c_0 s_0^k, r\Delta_t) \frac{1}{(c_0 s_0^k)^{3/2}} \psi\left(\frac{j\Delta_t - r\Delta_t}{c_0 s_0^k}\right), \text{ for } j = 0, \dots, N-1, (\text{C-16})$$

$$x(j\Delta_t) = \text{Re} \left( \frac{2 \ln s_0}{C_{1\psi}} \sum_{k=0}^K \frac{x_w(c_0 s_0^k, j\Delta_t)}{\sqrt{c_0 s_0^k}} \right), \text{ for } j = 0, \dots, N-1, \quad (\text{C-17})$$

and,

$$x_w(c_0 s_0^p, q\Delta_t) = \sqrt{|c_0 s_0^p|} \times \text{IFT}_k \left( \hat{x}(k\Delta_f) \hat{\psi}^*(c_0 s_0^p k\Delta_f) \right), \text{ for } p = 0, \dots, K, \text{ and } q = 0, \dots, N-1 (\text{C-18})$$

where  $c_0$  and  $s_0$  are parameters for the numerical computation;  $K$  is the total number of scales considered for the numerical integration;  $T_L = -L_t \Delta_t$  and  $T_U = L_t \Delta_t$  define the

lower and upper limit for the integral over time  $\tau$ , and  $C_{1\psi} = \int_0^\infty (\hat{\psi}^*(f)/|f|) df$ . In the

following, we restrict ourselves to the real-valued signal and the analytical wavelets or wavelets with  $\psi(t) = \psi^*(-t)$ .

### C.3 Gaussian process, power spectral density, and defining process in the transform domain

According to the spectral representation method (Shinozuka and Jan 1972) with the use of FFT (Yang 1972), a sample of a Gaussian stationary process,  $x(t)$ , can be simulated by transforming Gaussian white noise  $w(t)$  to the Fourier domain, multiplying it with an intensity function  $|\hat{y}(f)|$ , and transforming it back to the time domain. That is,

$$x(t) = IFT_f \left( |y(f)| e^{i\theta_y(w(t))} \right), \quad (\text{C-19})$$

where  $e^{i\theta_y(w(t))} = \eta(FT(w(t)))$ , in which the function  $\eta(C) = C/|C|$  is introduced to normalize the complex number  $C$ . Based on FT pair,  $\hat{x}(f) = |y(f)| e^{i\theta_y(w(t))}$ . Since, by definition, the double-sided PSD function of the process  $x(t)$  with duration  $T$ ,  $S_{\mathcal{F}_x}(f)$ , is given by,

$$S_{\mathcal{F}_x}(f) = \hat{x}(f)\hat{x}^*(f)/T, \quad (\text{C-20})$$

it indicates that given the target PSD function  $S_{\mathcal{F}_x}(f)$ , one could define a stationary Gaussian process in the Fourier domain by assigning  $|\hat{y}(f)| = |\hat{x}(f)| = \sqrt{S_{\mathcal{F}_x}(f)T}$ . The samples of the process so defined can be obtained using,

$$x(t) = IFT_f \left( |\hat{x}(f)| e^{i\theta_x(w(t))} \right), \quad (\text{C-21})$$

and the expected PSD of the sampled signals equals the prescribed  $S_{\mathcal{F}_x}(f)$ . The use of the definition given in Eq. (C-20) preserves the energy of  $x(t)$  according to Parseval's theory.

We note that by assigning  $|\hat{y}(f)|$  equal to  $M(f)|\hat{x}(f)|$ , Eq. (C-19) becomes,

$$x(t) = IFT_f \left( M(t) \times |\hat{x}(f)| e^{i\theta_{\hat{x}}(w(t))} \right) = M(t) \times IFT_f \left( |\hat{x}(f)| e^{i\theta_{\hat{x}}(w(t))} \right), \quad (\text{C-22})$$

which simulates a uniformly amplitude modulated evolutionary process (Priestley 1965). Such a process has an evolutionary PSD function equals  $|M(t)|^2 \left( \hat{x}(f) \hat{x}^*(f) / T \right)$ , and  $M(t)$  is the amplitude modulation function, which will be considered to be positive. However, the use of  $|y(f)|$  equal to  $M(t, f) |\hat{x}(f)|$  in Eq. (C-19) does not lend itself to be interpreted as a proper inverse Fourier transform because the modulation function depends on the frequency. This reduces the computational efficiency that otherwise can be gained by using FFT; it also makes the distinction between the modulation function and intensity function more blurred. We will concentrate only on the case where the modulation function is defined outside of the transform domain. However, the consideration of modulation that depends on variables in the transform domain could be a valid assumption.

Maraun et al. (2007) emphasized the usefulness of using Eq. (C-19) to obtain samples of stationary Gaussian process, and extended it to define a class of nonstationary Gaussian processes in the wavelet domain by the wavelet multipliers  $|y_w(s, \tau)|$ , stating that “an individual process is defined by its multipliers and a synthesizing wavelet pair...” Samples of  $x(t)$  based on such a definition are then given as,

$$x(t) = IWT \left( |y_w(s, \tau)| e^{i\theta_w(w(t))} \right), \quad (\text{C-23})$$

where  $e^{i\theta_w(w(t))} = \eta(WT(w(t)))$ . We use the intensity function  $|y_w(s, \tau)|$  and  $e^{i\theta_w(w(t))}$  in Eq. (C-23) instead of using  $y_w(s, \tau)$  and  $WT(w(t))$  as suggested in Maraun et al. (2007). The use of  $e^{i\theta_w(w(t))}$  instead of  $WT(w(t))$  is aimed at not biasing the energy arising from the intensity function since  $[WT(w(t))][WT(w(t))]^*$  is not a constant in the wavelet domain by using WT defined in Eq. (C-12). The use of  $|y_w(s, \tau)|$  (as well as  $|\hat{y}(f)|$  in Eqs. (C-21) and (C-22)) is more restrictive than  $y_w(s, \tau)$  but is adequate for the proposed algorithm in the following section since we are focused on real-valued signals. However,

a negatively valued intensity and complex-valued intensity may be considered for other applications.

Similar to the use of  $M(t)$  in defining the uniformly modulated evolutionary process mentioned earlier, we include  $M(t)$  in Eq. (C-23),

$$x(t) = IWT \left( M(t) |y_w(s, \tau)| e^{i\theta_w(w(t))} \right) = M(t) \times IWT \left( |y_w(s, \tau)| e^{i\theta_w(w(t))} \right), \quad (\text{C-24})$$

to define a **modulated and intensity function adjusted (MODIF)** process. The intensity function gives time-scale characteristics of the process, and the modulation function provides additional time-varying characteristics of the process.

We further extend the concept of defining the MODIF process in the time-frequency domain according to ST, denoted as the S-domain, where samples of  $x(t)$  are given as,

$$x(t) = IST \left( M(t) \times |y_s(f, \tau)| e^{i\theta_s(w(t))} \right) = M(t) \times IST \left( |y_s(f, \tau)| e^{i\theta_s(w(t))} \right), \quad (\text{C-25})$$

where  $y_s(f, \tau)$  is an intensity function in the S-domain, and  $e^{i\theta_s(w(t))} = \eta(ST(w(t)))$ .

It is noted that besides the above-mentioned transforms, there are other transforms used for signal analysis and modeling; for example, the generalized Fourier family transforms (Brown et al. 2009). Therefore, it is relevant and straightforward to conceptually generalize the approach in defining the MODIF processes in the transform domain if other transform pair is considered. The definitions lend themselves to an easily understandable and almost trivial algorithm to simulate stochastic processes:

- A) Sample Gaussian white noise,  $w(t)$ , and calculate the normalized coefficients of  $w(t)$  in the transform domain (e.g.,  $e^{i\theta_f(w(t))}$ , or  $e^{i\theta_w(w(t))}$ , or  $e^{i\theta_s(w(t))}$  if FT, or WT, or ST is used, respectively).
- B) Apply the inverse transform to the product of the intensity function and the normalized coefficients obtained in Step A).
- C) Apply the modulation function to the simulated signal from Step B).

Step C) is separated from Steps A) and B) and is not affected by the selected transformation. A critical issue of applying the MODIF process with prescribed target energy distribution is that the energy distribution of the sampled signals for given intensity function may not be readily established, except for the case where FT is used (i.e., transforms with non-redundant representation). This is because unlike the FT, both WT and ST provide redundant representation. The redundant representation results in that, in general,  $|y_w(s, \tau)|e^{i\theta_w(w(t))}$  and  $|y_s(s, \tau)|e^{i\theta_s(w(t))}$  do not represent the proper coefficients of WT and ST, respectively. In other words,  $|y_w(s, \tau)|e^{i\theta_w(w(t))}$  and  $|y_s(s, \tau)|e^{i\theta_s(w(t))}$  are not equal to  $x_w(s, \tau) = WT\left(IWT\left(|y_w(s, \tau)|e^{i\theta_w(w(t))}\right)\right)$  and  $x_s(f, \tau) = ST\left(IST\left(|y_s(s, \tau)|e^{i\theta_s(w(t))}\right)\right)$ , respectively.

To see the impact of this inequality on the simulated MODIF process by using Eq. (C-24), we note that we can define the double-sided time-scale PSD (TSPSD) function of the simulated process  $x(t)$ ,  $S_{w_x}(s, \tau)$ , as,

$$S_{w_x}(s, \tau) = \left( \frac{x_w(s, \tau)}{s\sqrt{C_\psi}} \right) \left( \frac{x_w(s, \tau)}{s\sqrt{C_\psi}} \right)^* \quad (\text{C-26})$$

The use of this definition leads to energy preservation since the integral of  $S_{w_x}(s, \tau)$  in the wavelet domain equals the integral of  $|x(t)|^2$  in the time domain (see Proposition 2.4.1 in Daubechies (1992)). Consequently, even we assign  $|y_w(s, \tau)|$  equals  $\sqrt{S_{w_x}(s, \tau)C_\psi}|s|$  and  $M(t) = 1$  for the simulation, the average energy of the sampled signals according to Eq. (C-24) will likely deviate from the specified target  $S_{w_x}(s, \tau)$ .

Consider that we simulate the MODIF process using Eq. (C-25). We can define the double-sided time-frequency PSD (TFPSD) function of the simulated process,  $S_{s_x}(f, \tau)$ , as,

$$S_{s_x}(f, \tau) = \left( x_s(f, \tau) / \sqrt{D_\kappa |f|} \right) \left( x_s(f, \tau) / \sqrt{D_\kappa |f|} \right)^*, \quad (\text{C-27})$$

since the use of this definition leads to energy preservation (Hong 2020), where

$$D_\kappa = \int_{-\infty}^{\infty} (1/|\zeta|) \times \exp\left(- (2\pi\kappa(\zeta-1))^2\right) d\zeta. \text{ However, the average energy of the sampled}$$

signals by using Eq. (C-25) with  $|y_s(f, \tau)|$  equal to  $|x_s(f, \tau)| = \sqrt{S_{s_x}(f, \tau) D_\kappa |f|}$  and  $M(t) = 1$  will likely deviate from the specified target.

In addition to the discussed energy distortion, the application of the MODIF process is likely to lead to the samples obtained from Eqs. (C-22), (C-24) and (C-25) to follow a marginal cumulative distribution function (CDF) that deviates from the prescribed marginal CDF of the zero-mean process  $F_{x,t}(x(t))$ . An iterative process is proposed in the following sections to simulate the nonstationary and non-Gaussian with prescribed target PSD and CDF. The PSD functions that satisfy the energy preservation by considering the selected transform are used as the basis to describe the proposed algorithm to maintain consistency. Although this could become clumsy in some instances, it is useful in checking that a consistent transform pair is employed.

## C.4 Iterative power and amplitude corrected algorithm

### C.4.1 IAAFT algorithm

To develop the proposed iterative algorithm, we note that, given the observed  $\{x(j\Delta_t)\}_N$ , the IAAFT algorithm was proposed by Schreiber and Schmitz (1996, 2000) in the context of generating surrogates for statistical hypothesis testing. The algorithm repeatedly uses FT and IFT, and ranked data. This algorithm is explained using the ranking of  $x(j\Delta_t)$  in the following.

The PSD function  $S_{\mathcal{F}_x}(f)$  of  $\{x(j\Delta_t)\}_N$  is calculated using Eq. (C-19) with possible

smoothing. The objective of IAFFT is to generate surrogates that match the calculated  $S_{\mathcal{F}_x}(f)$  and shuffled  $\{x(j\Delta_t)\}_N$ . A similar algorithm - the spectral correction algorithm - was independently designed by Masters and Gurley (2003) to simulate non-Gaussian processes for the given target  $S_{\mathcal{F}_x}(f)$  and target marginal CDF  $F_X(x(t))$ . A subtle difference between these two algorithms is on how the prescribed target PSD function and CDF are obtained or assigned. For example,  $\{x(j\Delta_t)\}_N$  is obtained through distribution mapping in the spectral correction algorithm. In IAFFT,  $\{x(j\Delta_t)\}_N$  is given and shuffled. This shuffling, in the spectral correction method, can be viewed as matching the prescribed probability distribution. Once  $\{x(j\Delta_t)\}_N$  is prescribed and  $S_{\mathcal{F}_x}(f)$  is calculated, by letting  $\{\xi(j)\}_N$  equal to the ascendingly sorted  $\{x(j\Delta_t)\}_N$ , the steps of the IAFFT algorithm are:

1. Sample a sequence of Gaussian white noise,  $w(t)$ , of length  $N$ , calculate  $e^{i\phi_p} = \eta(FT(w(t)))$ ;
2. Calculate  $x_{PC}(j\Delta_t) = IFT_p\left(\left|\sqrt{S_{\mathcal{F}_x}(p\Delta_f)}T\right|e^{i\phi_p}\right)$  and find the rank of  $x_{PC}(j\Delta_t)$ ,  $r_j$ , for  $j = 0, \dots, N-1$ , based on the ascending order;
3. Set  $x_{AC}(j\Delta_t) = \xi(r_j)$ , for  $j = 0, \dots, N-1$ ; and calculate  $e^{i\phi_p} = \eta(FT_j(x_{AC}(j\Delta_t)))$ ;
4. Repeat Steps 2) to 3) until the convergence criterion is achieved.

Steps 1) and 2) are the same as Steps A) and B) described earlier that simulates a Gaussian process, except an additional ranking of  $x_{PC}(j\Delta_t)$  is carried out, which is equivalent to define the CDF as a preparation for the iteration. In general, Step 2) leads to  $x_{PC}(j\Delta_t)$  with the PSD correction but  $x$  may deviate from the target CDF assigned by  $\{\xi(j)\}_N$ , and Step 3) leads to the sampled  $x_{AC}(j\Delta_t)$  with the amplitude correction (i.e., matching CDF assigned based on  $\{\xi(j)\}_N$ ) but may deviate from the target PSD. The iteration adjusts the PSD and CDF of the sampled time series to their corresponding



targets. The tolerable differences between  $x_{PC}(j\Delta_t)$  and  $x_{AC}(j\Delta_t)$  can be used as the convergence criterion. Once convergence is achieved  $x_{PC}(j\Delta_t)$  or  $x_{AC}(j\Delta_t)$  can be used as the sampled time series.

The IAAFT algorithm is designed for stationary processes. For the shuffling of  $\{x(j\Delta_t)\}_N$  to simulation stationary process, it is implicitly considered that the marginal CDF of  $x(t)$  at any given time remains to be the same. Also, the PSD function for the stationary process is time-independent. The IAAFT algorithm or the spectral correction method is not applicable to simulate the nonstationary processes as they have time-varying PSD and CDF.

#### ***C.4.2 Iterative power and amplitude correction algorithm***

In this section, we describe the proposed iterative power and amplitude correction (IPAC) algorithm to simulate the time history  $\{x(j\Delta_t)\}_N$  of a zero-mean nonstationary non-Gaussian process. The proposed algorithm could be viewed as an extension to the IAAFT algorithm. For the simulation, it is considered that, for  $M(t) = 1$ , the PSD function of the process that is characterized based on FT, or ST, or WT is given, and the distribution type for the marginal CDF of  $x(t)$ ,  $F_{X,t}(x(t))$ , is known. Moreover, it is considered that  $F_{X,t}(x(t))$  can be completely defined by the zero-mean, the time-varying standard deviation,  $\sigma(t)$ , and other prescribed distribution parameters if they are required (since, in some cases, a CDF with more than two parameters may be considered).

If FT is considered for a stationary process, the standard deviation  $\sigma(t)$  equals  $\sqrt{\lambda_{\mathcal{F}_x}}$  which is time-independent, where  $\lambda_{\mathcal{F}_x}$ , equals the integral of  $S_{\mathcal{F}_x}(f)$  over the frequency domain. Since  $S_{\mathcal{S}_x}(f, \tau)$  provides the energy distribution over the time-frequency domain, the integral of  $S_{\mathcal{S}_x}(f, \tau)$  over the frequency domain provides the energy distribution in the time domain,  $\lambda_{\mathcal{S}_x}(\tau)$ ,

$$\lambda_{S_x}(\tau) = \int_{-\infty}^{\infty} S_{S_x}(f, \tau) df, \quad (\text{C-28})$$

and the integral of  $S_{S_x}(f, \tau)$  over the time domain provides the energy distribution in the frequency domain,  $S_{S_x}(f)$ . Analogously to the statistics for the stationary process,  $\lambda_{S_x}(\tau)$  represents the variance of  $x(\tau)$ , and  $\sigma(t)$  equals  $\sqrt{\lambda_{S_x}(t)}$ . Similarly, for the given  $S_{W_x}(s, \tau)$ , the time-varying variance  $\lambda_{W_x}(\tau)$  is given by,

$$\lambda_{W_x}(\tau) = \int_{-\infty}^{\infty} S_{W_x}(s, \tau) df, \quad (\text{C-29})$$

and the integral of  $S_{W_x}(s, \tau)$  over the time domain provides the energy distribution in the scale domain,  $S_{W_x}(f)$ .  $\sigma(t)$ , equals  $\sqrt{\lambda_{W_x}(t)}$ .

Let  $u(t)$  be a uniformly distributed random variable between 0 and 1 with its marginal CDF denoted as  $U(u(t))$ . The relation between  $u(t)$  and  $x(t)$  can be established based on the probability transformation,  $U(u(t)) = F_{X,t}(x(t))$ . The steps in the IPAC algorithm in a pseudo-code form are shown in the flowchart depicted in Figure C.1 and are described as follows:

D) Prescribe the targets and initiate the simulation process:

Sample  $\{u(j\Delta_t)\}_N$  based on a random number generation algorithm for a uniformly distributed random variable between 0 and 1. Assign  $\{p(j)\}$  equal to the ascendingly sorted  $\{u(j\Delta_t)\}_N$ , and the intensity function  $|y_{\mathcal{F}_t}(\bar{s}_p)|$  according to the considered transform pair  $(Tf(\square), ITf(\square))$ , where

- a) For  $(Tf(\square), ITf(\square)) = (FT(\square), IFT(\square))$ ,  $|y_{\mathcal{F}_t}(\bar{s}_p)| = |y_{\mathcal{F}}(f)| = \sqrt{S_{\mathcal{F}_x}(f)T}$ , and  $\sigma(t) = \sqrt{\lambda_{\mathcal{F}_x}}$  which is time-independent,

b) For  $(Tf(\square), ITf(\square)) = (ST(\square), IST(\square))$ ,  $|y_{\mathcal{F}}(\bar{s}_p)| = |y_s(f, \tau)| = \sqrt{S_{s_x}(f, \tau) D_\kappa |f|}$ , and  $\sigma(t) = \sqrt{\lambda_{s_x}(t)}$ ,

c) For  $(Tf(\square), ITf(\square)) = (WT(\square), IWT(\square))$ ,  $|y_{\mathcal{F}}(\bar{s}_p)| = |y_w(s, \tau)| = \sqrt{S_{w_x}(s, \tau) C_\psi |s|}$ , and  $\sigma(t) = \sqrt{\lambda_{w_x}(t)}$ .

The calculated  $\sigma(t)$  is used to fully specify  $F_{x,t}(x(t))$ .

II) Iteration steps:

II.1) Sample a sequence of Gaussian white noise,  $w(t)$ , of length  $N$ , calculate

$$e^{i\phi_{\mathcal{F}}(\bar{s}_p)} = \eta(Tf(w(t)));$$

II.2) Calculate  $x_{PC}(j\Delta_t) = ITf\left(|y_{\mathcal{F}}(\bar{s}_p)| e^{i\phi_{\mathcal{F}}(\bar{s}_p)}\right)$ ,  $p_{PC}(j\Delta_t) = F_{x,t}(x_{PC}(j\Delta_t))$ , and find the rank of  $p_{PC}(j\Delta_t)$ , denoted as  $r_j$ , for  $j = 0, \dots, N-1$ ;

II.3) Set  $x_{AC}(j\Delta_t) = F_{x,t}^{-1}(p(r_j))$ , for  $j = 0, \dots, N-1$ ; and calculate

$$e^{i\phi_{\mathcal{F}}(\bar{s}_p)} = \eta(Tf(x_{AC}(j\Delta_t)));$$

II.4) Repeat Steps 2) to 3) until the convergence criterion is satisfied.

II.5)  $x(j\Delta_t) = M(j\Delta_t) \times x_{AC}(j\Delta_t)$ .

The algorithm essentially simulates the MODIF process and iteratively corrects the PSD and CDF. The intensity function and the transform pair are used from Steps I) to II.4), while the modulation function only affects the assignment of the final results in Step II.5). Since  $x_{AC}(j\Delta_t)$  is used in Step II.5), the distribution match (i.e., matching samples of  $F_Z(z(t))$ ,  $\{z(j\Delta_t)\}_N$ ) is ensured by design. One could replace Step II.5) with  $x(j\Delta_t) = M(j\Delta_t) \times x_{PC}(j\Delta_t)$  without altering the results if a stringent convergence

criterion is employed. As can be observed from the steps of the IPAC algorithm, the analysis, as well as the simulation, is carried out within the same transform pair. It avoids the need to map the obtained results from one type of transform into a different kind of transform (e.g., obtaining the spectrum using continuous WT and then transform it into evolutionary PSD). Note that it may be attempting to replace the uniform distribution with the normal distribution for  $u(t)$ . However, by doing so, it requires the use of the inverse distribution transformation in Steps II.2 and II.3) and increases computing demand.

The algorithm can be simplified if  $F_{x,t}(x(t))$  remains unchanged and only depends on  $\sigma(t)$ , that is, the marginal probability distribution of  $z(t) = x(t)/\sigma(t)$ ,  $F_Z(z(t))$ , is time-independent and  $z(t)$  has zero mean and unit variance. In such a case, we calculate  $\{\zeta(j)\}_N = \{F_Z^{-1}(p(j))\}_N$  in Step I); we replace “ $p_{PC}(j\Delta_t) = F_{x,t}(x_{PC}(j\Delta_t))$ ” in Step II.2) and “ $x_{AC}(j\Delta_t) = F_{x,t}^{-1}(p(r_j))$ ” in Step II.3) with “ $p_{PC}(j\Delta_t) = x_{PC}(j\Delta_t)/\sigma(j\Delta_t)$ ” and “ $x_{AC}(j\Delta_t) = \zeta_{r_j}\sigma(j\Delta_t)$ ”, respectively. This avoids the use of probability distribution function during the iteration to gain extra computational efficiency. This simplified version can also be used to generate surrogate for observed  $\{x(j\Delta_t)\}_N$ , which has the effect of the modulation function already removed. This is done by calculating  $\{z(j\Delta_t)\}_N = \{x(j\Delta_t)/\sigma(j\Delta_t)\}_N$ , and letting  $\{\zeta(j)\}_N$  equal to the ascendingly sorted  $\{z(j\Delta_t)\}_N$  in Step I.1) (instead of  $\{\zeta(j)\}_N = \{F_Z^{-1}(p(j))\}_N$ ), where  $\sigma(j\Delta_t)$  is to be calculated based on the PSD function estimated from  $\{x(j\Delta_t)\}_N$  by using a preferred transform.

The usefulness of surrogate in the context of wind engineering was presented in McCullough and Kareem (2013). The proposed algorithm, when used with WT to generate surrogate, differs from that given in Chavez and Cazelles (2019) for testing time-localized coherence, in that the time-varying  $\sigma(j\Delta_t)$  is neglected in their algorithm (i.e., the amplitude adjustment is based on  $\{x(j\Delta_t)\}_N$  rather than its normalized version

in the IPAC algorithm). This is convenient and may likely speed up the convergence of the algorithm. However, the basis for the shuffling of  $\{x(j\Delta_t)\}_N$  is unclear if the marginal probability distribution of  $x(j\Delta_t)$  for a nonstationary process is assumed to be time-varying.

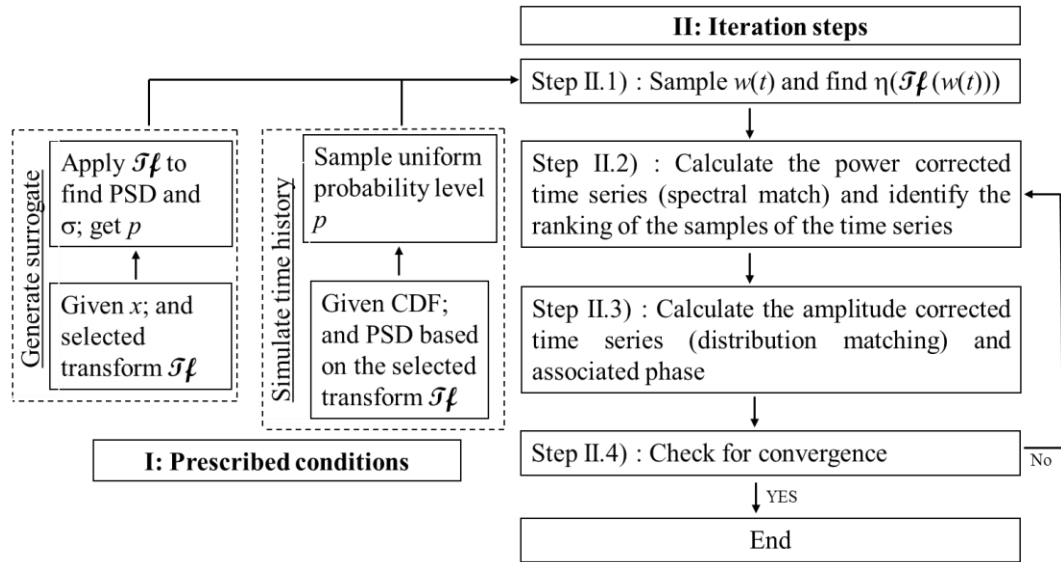


**Figure C.1:** Iterative power and amplitude corrected algorithm to simulate nonstationary and non-Gaussian processes ( $\mathcal{T}_f$  denotes the selected transform in this figure).

## C.5 Numerical examples

In this section, we illustrate the proposed algorithm by generating surrogate for a given ground motion record and for a given fluctuating component of wind velocity time history of a high-intensity wind event. We apply the algorithm to sample nonstationary ground motions for prescribed target PSD, where the target is defined based on a set of ground motion records, and the CDF is assumed to be Gaussian and non-Gaussian. The test of the proposed algorithm for esoteric mathematical models is beyond the consideration of the present study.

### *C.5.1 Generating surrogate for an earthquake record*

Consider the record shown in Figure C.2. By applying ST with the window parameter  $\kappa = 1$  (see Eq. (C-6)), the obtained TFPSD function is shown in Figure C.3a, and the calculated time-varying  $\sigma(t)$  is presented in Figure C.3b, showing that the TFPSD varies in time and frequency.

By applying the IPAC algorithm, a surrogate is simulated and shown in Figure C.3b. The TFPSD of this surrogate is depicted in Figure C.3c. The figure shows that the surrogate resembles the given record, and its TFPSD function resembles well that shown in Figure C.3a. As  $x_{AC}(t)$  is used for generating surrogate (see Step II.5 in IPAC algorithm), the amplitude (or probability distribution) matching is certain, so no plot is provided. Additional test runs indicate that the convergence is usually achieved within five iterations, depending on the adopted convergence criterion. It was noted that the average TFPSD function from multiple generated surrogates tends to be smoother as compared to the TFPSD of the observed record, which is expected since the observed as well as a single sampled record are realizations of stochastic processes.

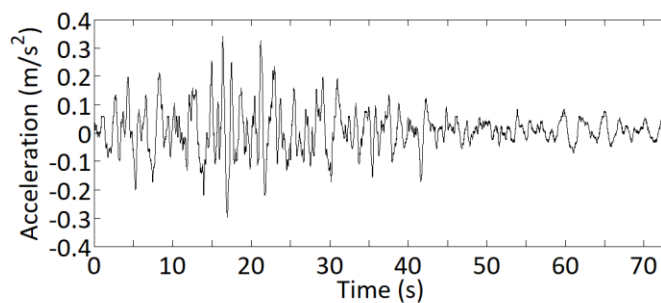


**Figure C.2:** Ground motions recorded at the CU station, UNAM, Mexico, for the Michoacán earthquake that occurred on September 19, 1985.

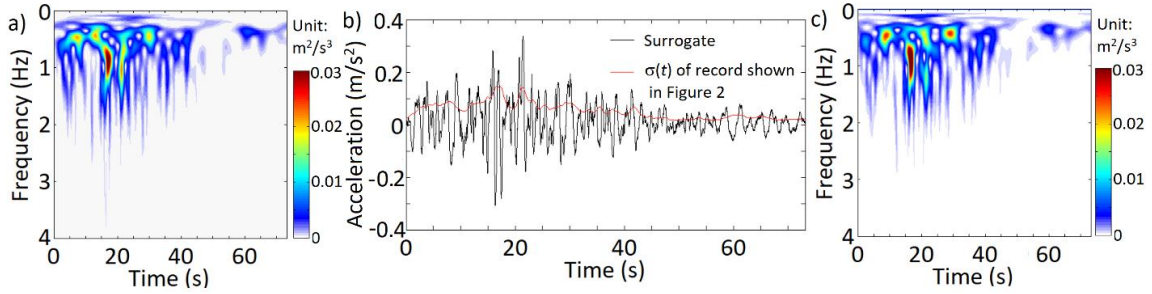


**Figure C.3:** Results by using ST for the given record shown in Figure C.2: a) TFPSD of the given record, b) a generated surrogate and  $\sigma(t)$  of the given record, and c) TFPSD of the generated surrogate shown in Figure C.3b

The analysis based on ST is repeated but by applying WT using the GMWs (Olhede and Walden, 2002),

$$\hat{\psi}_{0,\beta,\gamma}(f) = U(f) a_{\beta,\gamma} (2\pi f)^\beta e^{-(2\pi f)^\gamma}, \quad (\text{D-30})$$

where  $U(\omega)$  is the Heaviside function,  $a_{\beta,\gamma} = 2(e\gamma/\beta)^{\beta/\gamma}$ , and  $\beta$  and  $\gamma$  are model parameters. The GMW is an analytical wavelet, and it was used to evaluate the coherence of the seismic ground motions (Qiao et al. 2020). For the numerical analysis,  $\beta = 20$  and  $\gamma = 3$  are employed since these values are suggested as the default values for the algorithm implemented in MATLAB (Version 2019a). The obtained TSPSD and  $\sigma(t)$  of the record are shown in Figures C.4a and C.4b, respectively. A generated surrogate is also shown in Figure C.4b with its corresponding TSPSD function depicted in Figure C.4c. An inspection of the surrogate depicted in Figure C.4b and the original record presented in Figure C.2 indicates that they exhibit similar temporal trends. The TSPSD of the surrogate resembles that of the given record. Again, the convergence is achieved within a few iterations. A comparison of  $\sigma(t)$  shown in Figures C.3b and C.4b indicates that they are almost identical. The minor differences between them are due to that ST and WT have different time-frequency (or time-scale) decomposition.

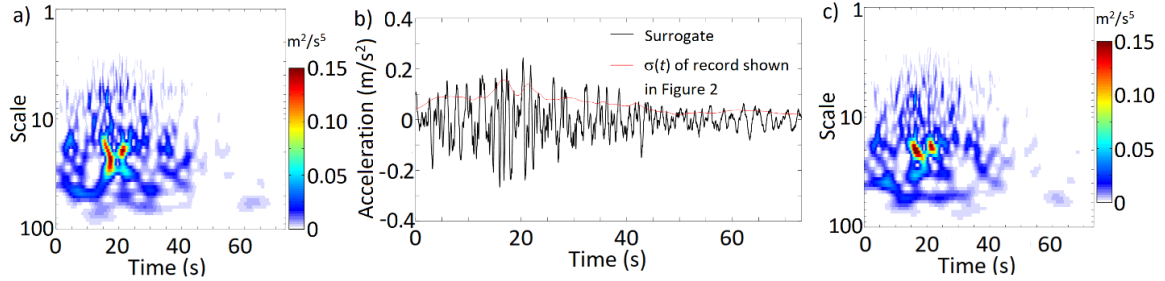


**Figure C.4:** Results by using WT for the given record shown in Figure C.2: a) TSPSD of the given record, b) a generated surrogate and  $\sigma(t)$  of the given record, and c) TSPSD of the generated surrogate shown in Figure C.3b

### C.5.2 Generating surrogate for a wind record

Now, consider a wind record presented in Figure C.5a. For simplicity, the box window with a width of 32 samples is used to find the mean wind velocity of the time-varying wind record. By removing the mean, the fluctuating component of the wind is presented in Figure C.5b.

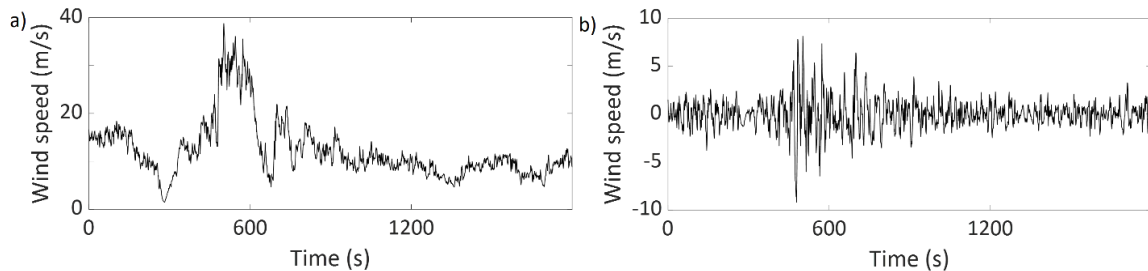


**Figure C.5:** Wind velocity record from Tower 4 and 10 m height of the rear-flank downdraft that occurred during the evening on June 4, 2002, near Lubbock, Texas (Gast and Schroeder 2003; Orwig and Schroeder 2007): a) the wind record, and b) the fluctuating component of the record.

By applying ST and WT, and following the same analyses that are carried out for the



ground motion record shown in the previous section, the obtained results are presented in Figures C.6 and C.7. In general, the observations that can be drawn from this example are similar to those presented in the previous section for the ground motion record.

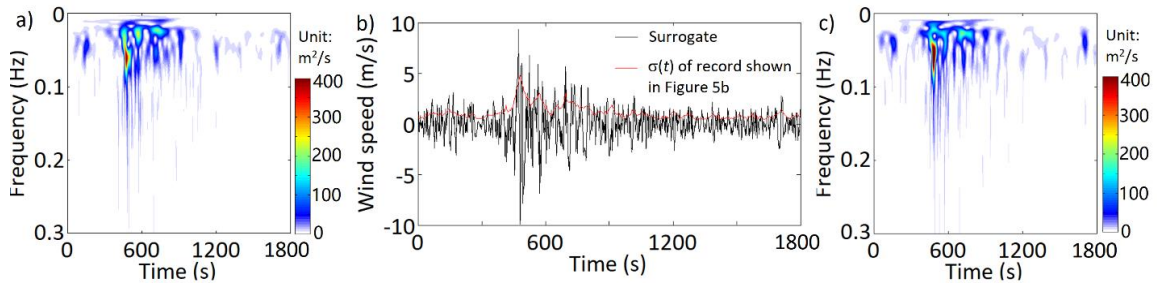


**Figure C.6:** Results by using ST for the wind record shown in Figure C.5b: a) TFPSD of the given record, b) a generated surrogate and  $\sigma(t)$  of the given record, and c) TFPSD of the generated surrogate shown in Figure C.6b.

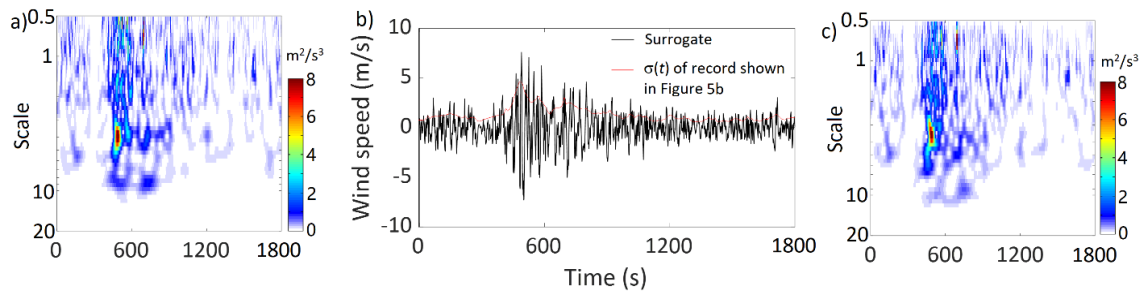


**Figure C.7:** Results by using WT for the wind record shown in Figure C.5b: a) TSPSD of the given record, b) a generated surrogate and  $\sigma(t)$  of the given record, and c) TSPSD of the generated surrogate shown in Figure C.7b.

### C.5.3 Simulating ground motions

Consider a set of 12 ground motion records oriented in the E-W direction for a seismic event that occurred on January 16, 1986, with a local magnitude of 6.1, focal depth of 10.2 km, and an epicentral distance of 25.2 km. These records are recorded by the LSST

array in Lotung, Taiwan, where the separation between any two recording sites is less than 100 m, as shown in Figure C.8a. Three records from the 15 recording sites seem to be corrupted and are not considered. The record obtained from FA-1 site is illustrated in Figure C.8b. To minimizing the wave passage effect, first, each of the remaining 11 records is time-shifted with respect to the record presented in Figure C.8b such that the sum of the product of a considered record and that shown in Figure C.8b is maximized after the shift.

It is assumed that the average PSD of the considered 12 records could provide a good representation of the ground motions, at least for such a type of seismic event. The calculated average TFPSD based on ST and the calculated average TSPSD based on WT are shown in Figures C.8c and C.8d, respectively. The calculated  $\sigma(t)$  by using the average TFPSD and the average TSPSD presented in Figures C.8c and C.8d are included in Figure C.8b. The obtained PSD and the standard deviation indicate the nonstationarity of the ground motions.  $\sigma(t)$  values obtained by using ST and WT are in very good agreement.

An assessment of the empirical probability distribution of the standardized variable  $z(t) = x(t) / \sigma(t)$  is carried out by considering all 12 records. The empirical distribution of  $z(t)$  by considering all 12 records is presented in Figure C.9, indicating that the empirical distribution can be fitted by a normal distribution only for the initial segment of the records. Moreover, the distribution shape is time-varying and non-Gaussian. The non-Gaussian behaviour of the ground motions is supported by the findings given in Radu and Grigoriu (2018), indicating that the Gaussian assumption for the seismic ground motions records included in the PEER NGA-West dataset may not always appropriate. However, for this particular set of records, the tail of the distribution is shorter than that of the normal distribution, which differs from the longer tail behaviour suggested by Radu and Grigoriu (2018).

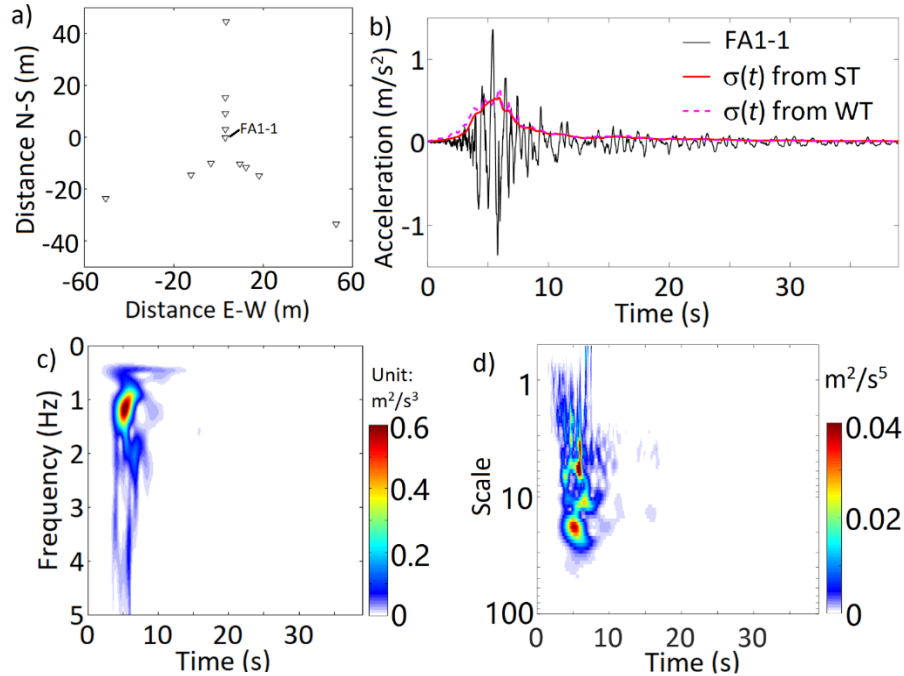


**Figure C.8:** a) The LSST array station of selected records, b) record at FA1-1 station, c) average TSPSD by using ST based on 12 records, and d) average TSPSD by using WT based 12 records.

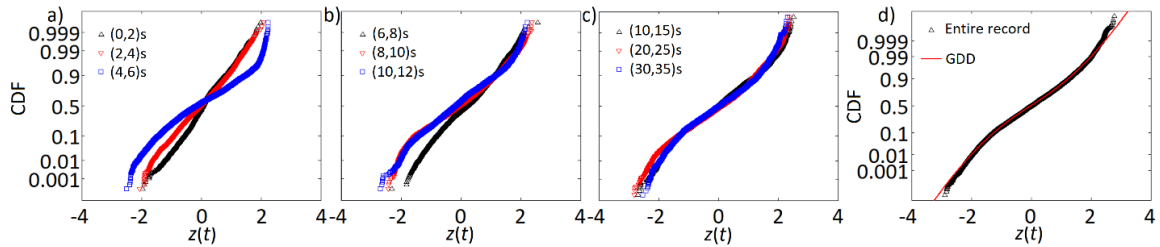


**Figure C.9:** Empirical distributions of the normalized time series of the considered ground motions. a): Time interval (0, 2), (2, 4), (4, 6); b): (6, 8), (8,10), (10, 12); c): (10, 15), (20, 25), (30, 35); d): entire duration and the fitted GGD with  $\beta_0 = 3.01$  and  $\beta_1 = 1.54$ .

For illustration purposes, it is assumed that the marginal probability density function of  $x(t)$  can be represented by the generalized Gaussian distribution (GGD) (Nadarajah

2005),

$$f_{x,t}(x(t)) = \frac{\beta_0}{2\beta_1\Gamma(1/\beta_0)} e^{-(|x(t)-\mu|/\beta_1)^{\beta_0}}, \quad (\text{D-31})$$

where  $\mu$  denotes the mean,  $\beta_0$  and  $\beta_1$  are positive model parameters, and  $\Gamma(\square)$  denotes the gamma function. If  $\beta_0$  equals 2, it represents the normal distribution. For  $\beta_0 > 2$  and  $< 2$ , the distribution tail is lighter and heavier than that of normal distribution. The variance equals  $\beta_1^2\Gamma(3/\beta_0)/\Gamma(1/\beta_0)$ , and the kurtosis coefficient equals  $\Gamma(5/\beta_0)\Gamma(1/\beta_0)/\Gamma^2(3/\beta_0)$ .

By considering  $\beta_0 = 2$  and  $\beta_1 = \sqrt{2}$  (i.e., standard Gaussian), we use ST and the average target TFPSD function shown in Figure C.8c to sample the records using the IPAC algorithm. Since a sampled record to sampled record comparison is irrelevant for  $x(t)$  represented as a nonstationary stochastic process, only a sampled record is illustrated in Figure C.10a. The average TPSD function obtained from the 1000 sampled records is presented in Figure C.10b, and the calculated spectral acceleration (SA) for a damping ratio of 5% is shown in Figure C.10c for the 1000 sampled records. Similarly, we use WT and the average target TFPSD function shown in Figure C.8d to carry out the simulation. The obtained results are presented in Figures C.10d to C.10f. The PSD functions shown in Figures C.10b and C.10e are almost identical to their corresponding targets presented in Figures C.8c and C.8d. The mean of SA values shown in Figures C.10c and C.10f are in good agreement. The standard deviation of SA obtained by using ST smaller than that obtained by using WT.

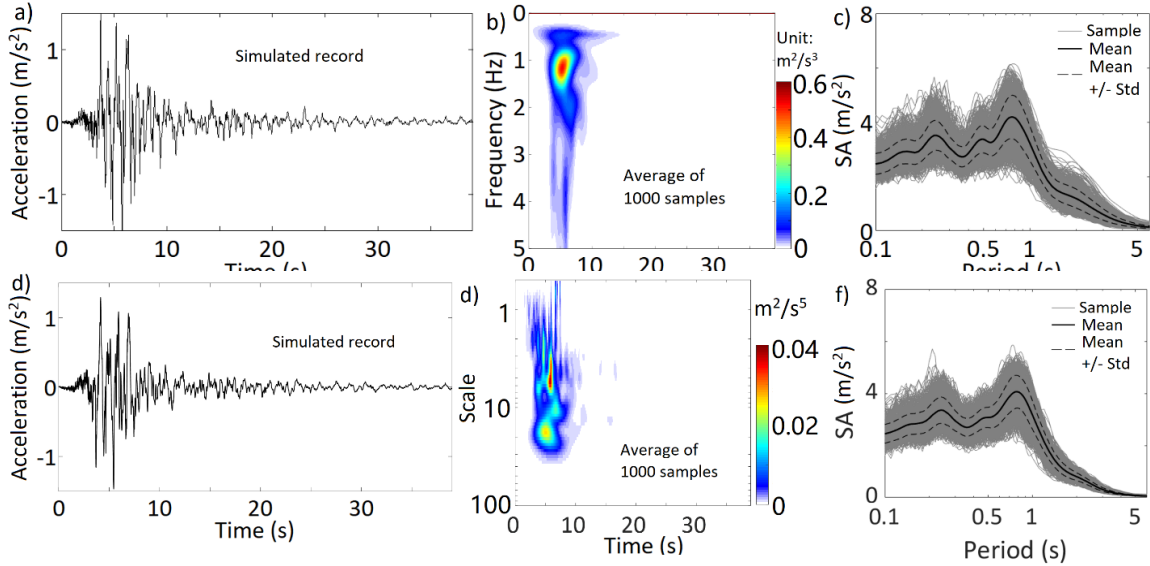


**Figure C.10:** Results based on simulated nonstationary Gaussian records by using ST and WT (the results presented in a) to c) are for ST, and the results presented in d) to f) are for WT): a) a sampled record based on ST, b) average TFPD of the 1000 sampled record, c) SA from 1000 sampled records using ST, d) a sampled record based on WT, e) average TSPD of the 1000 sampled record, f) SA from 1000 sampled records using WT.

We have tested the IPAC algorithm to simulate ground motions for additionally selected target PSD functions. It was observed that in some cases, when the initial or final segment of records has less than 0.5% of total energy, the algorithm may converge very slowly or may not converge. In such a case, it is suggested that such segments with negligible energy are to be truncated. This is in agreement with common practice in earthquake engineering.

To simulate the non-Gaussian process, we consider  $f_{X,t}(x(t))$  as shown in Eq. (D-31) but with  $\beta_0 = 3.01$  and  $\beta_1 = 1.54$  (i.e., a kurtosis coefficient of 2.4) since their use fit the data adequately, as depicted in the last plot in Figure C.9. We repeat the analysis that is carried out for the results presented in Figure C.10. The obtained results are presented in Figure C.11. A comparison of the results shown in Figures C.10 and C.11 indicates that the results follow the same trends. To assess the quantitative differences between the

obtained SA based on Gaussian and non-Gaussian assumptions, we calculate the ratio of the mean of SA shown in Figure C.11 (i.e., non-Gaussian case) to its corresponding value shown in Figure C.10 (i.e., Gaussian case). We do the same for the standard deviation of SA. The obtained values are presented in Figure C.12, indicating that the mean and standard deviation of SA for the non-Gaussian case with a lighter tail are smaller than those for the Gaussian case for most considered vibration periods, which is expected. The decrease in SA by considering non-Gaussian excitation is most noticeable for a shorter vibration period. This is because stiffer structures are more sensitive to peak acceleration values. In general, the ratio based on ST is smoother than that based on WT.

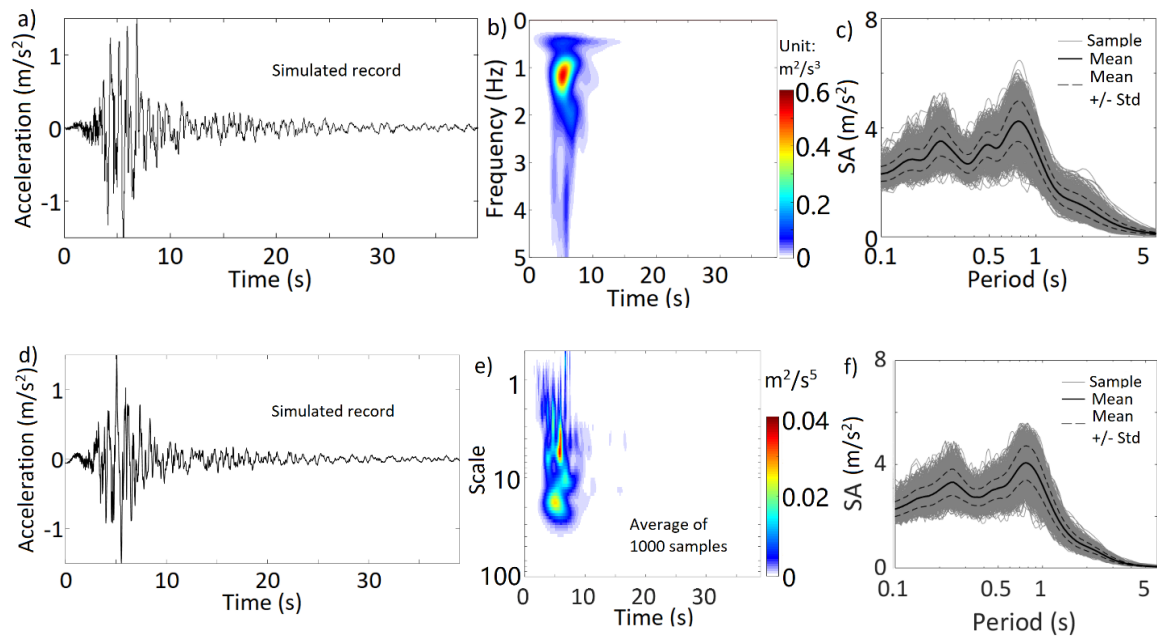


**Figure C.11:** Results based on simulated nonstationary non-Gaussian records by using ST and WT (the results presented in a) to c) are for ST, and the results presented in d) to f) are for WT): a) a sampled record based on ST, b) average TFPSD of the 1000 sampled record, c) SA from 1000 sampled records using ST, d) a sampled record based on WT, e) average TSPSD of the 1000 sampled record, f) SA from 1000 sampled records using WT.

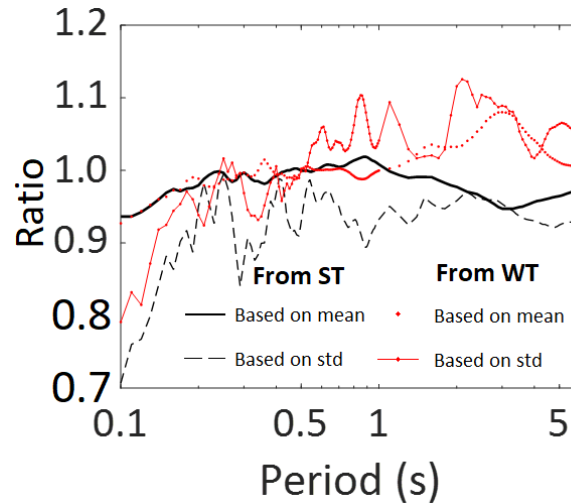


**Figure C.12:** Ratio of statistics of SA of simulated records with non-Gaussian and with Gaussian distribution assumptions.

## C.6 Summary and conclusions

We elaborated the concept of defining a modulated and intensity function adjusted (MODIF) stochastic process in the transform domain. The definitions of the stochastic processes in the transform domain lend themselves to an easily understandable and almost trivial algorithm to simulate stochastic processes. As such a simulated signal may not lead to the prescribed target PSD function and marginal cumulative distribution function of the process, we proposed a new iterative algorithm, called iterative power and amplitude corrected (IPAC) algorithm, so the sampled signal after the iteration have the prescribed properties. Besides simulating nonstationary and non-Gaussian processes, the proposed iterative algorithm can be used to generate surrogate. The algorithm can be used with Fourier transform, S-transform, and continuous wavelet transforms.

Practical illustrative numerical examples showed the applicability of the proposed algorithm by sampling surrogates for the ground motions and the fluctuating component of winds. The use of the IPAC algorithm to simulate nonstationary Gaussian and non-Gaussian ground motions based on S-transform (ST) and continuous wavelet transform (WT) is presented. The spectral accelerations are calculated using the simulated records.

In general, the mean and standard deviation of SA of the simulated records based on ST and based on WT agree well despite the differences between ST and continuous WT and between the frequency-dependent window used in ST and the generalized Morse wavelet used in the continuous WT.

## Reference

- Battisti, U., and Riba, L. (2016). “Window-dependent bases for efficient representations of the Stockwell transform.” *Applied and Computational Harmonic Analysis*, 40(2), 292-320.
- Boore, D. M. (2009). “Comparing stochastic point-source and finite-source ground-motion simulations: SMSIM and EXSIM.” *Bulletin of the Seismological Society of America*, 99(6), 3202-3216.
- Brown, R. A., Lauzon, M. L., and Frayne, R. (2009). A general description of linear time-frequency transforms and formulation of a fast, invertible transform that samples the continuous S-transform spectrum nonredundantly. *IEEE Transactions on Signal Processing*, 58(1), 281-290.
- Chavez, M., and Cazelles, B. (2019). Detecting dynamic spatial correlation patterns with generalized wavelet coherence and non-stationary surrogate data. *Scientific reports*, 9(1), 1-9.
- Chen, L., and Letchford, C. W. (2007). Numerical simulation of extreme winds from thunderstorm downbursts. *Journal of Wind Engineering and Industrial Aerodynamics*, 95(9-11), 977-990.;
- Cohen, L. (1995). *Time-frequency analysis*, Prentice-Hall, New Jersey, U.S.
- Cramér, H., and Leadbetter, M. R. (2013). *Stationary and related stochastic processes: Sample function properties and their applications*. Courier Corporation.
- Cui, X.Z. and Hong, H.P. (2020). Use of discrete orthonormal S-transform to simulate earthquake ground motions. *Bull. Seismol. Soc. Am.*, 110(2), 565-575.
- Daubechies, I. (1992). *Ten lectures on wavelets*, Siam, Philadelphia, U.S.
- Deodatis, G. (1996). Non-stationary stochastic vector processes: seismic ground motion applications. *Probabilistic Engineering Mechanics*, 11(3), 149-167.
- Deodatis, G., and Micaletti, R. C. (2001). Simulation of highly skewed non-Gaussian stochastic processes. *Journal of engineering mechanics*, 127(12), 1284-1295.
- Ferrante, F. J., Arwade, S. R., and Graham-Brady, L. L. (2005). A translation model for non-stationary, non-Gaussian random processes. *Probabilistic engineering mechanics*, 20(3), 215-228.
- Grigoriu M. Simulation of stationary non-Gaussian translation processes. *J Eng. Mech* 1998;124:121–6.



- Gurley, K., and Kareem, A. (1997). Analysis interpretation modeling and simulation of unsteady wind and pressure data. *Journal of Wind Engineering and Industrial Aerodynamics*, 69, 657-669.
- Gurley, K., and Kareem, A. (1999). Applications of wavelet transforms in earthquake, wind and ocean engineering. *Engineering structures*, 21(2), 149-167.
- Hong, H. P. (2016). Modeling of nonstationary winds and its applications. *Journal of Engineering Mechanics*, 142(4), 04016004.
- Hong, H. P. (2020). Response and first passage probability of SDOF systems subjected to nonstationary stochastic excitation modeled through S-Transform. Submitted to *Structural Safety*.
- Hong, H.P., and Cui, X.Z. (2020) Time-frequency spectral representation models to simulate nonstationary processes and their use to generate ground motions, *Journal of Mechanic Engineering, ASCE*, DOI: 10.1061/(ASCE)EM.1943-7889.0001827.
- Huang, G., and Chen, X. (2009). Wavelets-based estimation of multivariate evolutionary spectra and its application to nonstationary downburst winds. *Engineering Structures*, 31(4), 976-989.
- Kwon, D., and Kareem, A. (2009). Gust-front factor: new framework for wind load effects on structures, *J. Struct. Engrg., ASCE*, 135(6), 717-732.
- Li, J., and Chen, J. (2009). *Stochastic dynamics of structures*. John Wiley and Sons.
- Liang, J., Chaudhuri, S. R., & Shinozuka, M. (2007). Simulation of nonstationary stochastic processes by spectral representation. *Journal of Engineering Mechanics*, 133(6), 616-627.
- Lutes, L. D., and Sarkani, S. (2004). *Random vibrations: analysis of structural and mechanical systems*. Butterworth-Heinemann.
- Maraun, D., Kurths, J., and Holschneider, M. (2007). Nonstationary Gaussian processes in wavelet domain: synthesis, estimation, and significance testing. *Physical Review E*, 75(1), 016707.
- Masters, F., and Gurley, K. R. (2003). Non-Gaussian simulation: cumulative distribution function map-based spectral correction. *Journal of engineering mechanics*, 129(12), 1418-1428.
- McCullough, M., and Kareem, A. (2013). Testing stationarity with wavelet-based surrogates. *Journal of Engineering Mechanics*, 139(2), 200-209.
- Nadarajah, S. (2005). A generalized normal distribution. *Journal of Applied Statistics*, 32(7), 685-694.
- Newland, D. E. (2012). *An introduction to random vibrations, spectral and wavelet analysis*. Courier Corporation.
- Newmark, N.M., and Rosenblueth, E. (1971). *Fundamentals of Earthquake Engineering*, Prentice-Hall, Englewood Cliffs, N.J.

- Ochi, M. K. (2005). *Ocean waves: the stochastic approach* (Vol. 6). Cambridge University Press.
- Olhede, S. C., and Walden, A. T. (2002). Generalized morse wavelets. *IEEE Transactions on Signal Processing*, 50(11), 2661-2670.
- Percival, D.B., and Walden, A.T. (2000). *Wavelet Methods for Time Series Analysis*. Cambridge University Press.
- Phoon, K. K., Huang, S. P., and Quek, S. T. (2002). Simulation of second-order processes using Karhunen–Loeve expansion. *Computers and structures*, 80(12), 1049-1060.
- Pinnegar, C.R., and Mansinha, L. (2003). The S-transform with windows of arbitrary and varying shape. *Geophysics*, 68(1), 381-385.
- Priestley, M.B. (1965). Evolutionary spectra and non-stationary processes. *J. R. Stat Soc B.*, 27, 204–37.
- Qiao, D., Zhi, X., Fan, F., and Hong, H. (2020). Estimation of Wavelet Coherence of Seismic Ground Motions. *Bulletin of the Seismological Society of America*, 110(2), 613-628.
- Radu, A., and Grigoriu, M. (2018). A site-specific ground-motion simulation model: application for Vrancea earthquakes. *Soil Dynamics and Earthquake Engineering*, 111, 77-86.
- Sakamoto S, Ghanem R. Polynomial chaos decomposition for the simulation of non-Gaussian nonstationary stochastic processes. *J Eng Mech* 2002;128:190–201.
- Samaras, E., Shinzuka, M., and Tsurui, A. (1985). ARMA representation of random processes. *Journal of Engineering Mechanics*, 111(3), 449-461.
- Schreiber, T., and Schmitz, A. (1996). Improved surrogate data for nonlinearity tests. *Physical review letters*, 77(4), 635.
- Schreiber, T., and Schmitz, A. (2000). Surrogate time series. *Physica D: Nonlinear Phenomena*, 142(3-4), 346-382.
- Shensa, M. J. (1992). The discrete wavelet transform: wedding the a trous and Mallat algorithms. *IEEE Transactions on signal processing*, 40(10), 2464-2482.
- Shields, M. D., Deodatis, G., and Bocchini, P. (2011). A simple and efficient methodology to approximate a general non-Gaussian stationary stochastic process by a translation process. *Probabilistic Engineering Mechanics*, 26(4), 511-519.
- Shinozuka, M., and Jan, C. M. (1972). Digital simulation of random processes and its applications. *Journal of sound and vibration*, 25(1), 111-128.
- Simiu, E., and Scanlan, R.H., (1996). *Wind Effects on Structures: Fundamentals and Applications to Design*, third ed. Wiley, USA.
- Spanos P, Ghanem R. Stochastic finite element expansion for random media. *J Eng Mech* 1989;115:1035–53
- Spanos, P. D., and Failla, G. (2004). Evolutionary spectra estimation using wavelets. *Journal of Engineering Mechanics*, 130(8), 952-960.

- Spanos, P. D., Beer, M., and Red-Horse, J. (2007). Karhunen–Loève expansion of stochastic processes with a modified exponential covariance kernel. *Journal of Engineering Mechanics*, 133(7), 773-779.
- Stockwell, R. G. (2007). A basis for efficient representation of the S-transform. *Digit. Signal Process*, 17(1), 371-393.
- Stockwell, R. G., Mansinha, L., and Lowe, R. P. (1996). Localization of the complex spectrum: the S transform. *IEEE Trans. Signal Process.*, 44(4), 998-1001.
- Wen, Y. K., and Gu, P. (2004). Description and simulation of nonstationary processes based on Hilbert spectra. *Journal of Engineering Mechanics*, 130(8), 942-951.
- Yamamoto, Y., and Baker, J. W. (2013). Stochastic model for earthquake ground motion using wavelet packets. *Bulletin of the Seismological Society of America*, 103(6), 3044-3056.
- Yamazaki, F., and Shinozuka, M. (1988). Digital generation of non-Gaussian stochastic fields. *Journal of Engineering Mechanics*, 114(7), 1183-1197.
- Yang, J. N. (1972). Simulation of random envelope processes. *Journal of Sound and Vibration*, 21(1), 73-85.

## Curriculum Vitae

**Name:** Xizhong Cui

**Post-secondary Education and Degrees:** Harbin institute of technology (Weihai)  
Weihai, Shandong province, China  
2011-2015 B.Eng.

The University of Western Ontario  
London, Ontario, Canada  
2015-2016 M.Eng.

The University of Western Ontario  
London, Ontario, Canada  
2016-2020 Ph.D.

**Honors and Awards:** Graduate Scholarship in Structural Engineering  
2020

China Scholarship Council Scholarship for PhD student  
2017-2020

**Related Work Experience** Teaching Assistant  
The University of Western Ontario  
2016-2020

Research Assistant  
The University of Western Ontario  
2016-2020

**Publications:**  
**Journal (Published)**

**Cui, X.Z.**, Li, Y.G. and Hong, H.P. (2019). Reliability of stability of single-layer latticed shells with spatially correlated initial geometric imperfection modeled using conditional autoregressive model. *Engineering Structures*, 201, 109787.

**Cui, X.Z.** and Hong, H.P. (2020). Conditional Simulation of Spatially Varying Multicomponent Nonstationary Ground Motions: Bias and Ill Condition. *Journal of Engineering Mechanics*, 146(2), 04019129.

**Cui, X.Z.**, Li, Y.G. and Hong, H.P. (2020). Effect of spatially correlated initial geometric imperfection on reliability of spherical latticed shell considering global instability. *Structural Safety*, 82, 101895.

- Cui, X.Z.** and Hong, H.P. (2020). Use of Discrete Orthonormal S - Transform to Simulate Earthquake Ground Motions. *Bulletin of the Seismological Society of America*, 110(2), 565-575.
- Hong, H.P. and **Cui, X.Z.** (2020). Time-Frequency Spectral Representation Models to Simulate Nonstationary Processes and Their Use to Generate Ground Motions. *Journal of Engineering Mechanics*, 146(9), 04020106.
- Hong, H.P. and **Cui, X.Z.** (2020). On the estimation of power spectral density and lagged coherence of time transformed nonstationary seismic ground motions and their use to simulate synthetic records. *Journal of Earthquake Engineering*, <https://doi.org/10.1080/13632469.2020.1811176>.

### **Conference paper**

- Cui, X.Z.** and Hong, H.P. (2019). Simulating incoherent multicomponent nonstationary ground motions conditioned on observed records. In *12th Canadian Conference on Earthquake Engineering*, Quebec City, Canada.